Geological controls on the evolution of submarine channels in the Espírito Santo Basin, SE Brazil

Yongpeng Qin

Submitted in partial fulfilment of the requirements for the degree of Ph.D.

School of Earth and Ocean Sciences,

Cardiff University

September 2017

DECLARATION

This work has not been submitted in substance for any other degree or award at this or any other university or place of learning, nor is being submitted concurrently in candidature for any degree or other award.

Signed ………………………………………………… (candidate)   Date ………………………………….………

STATEMENT 1

This thesis is being submitted in partial fulfilment of the requirements for the degree of PhD

Signed ……………………………………………………… (candidate)   Date …………………………………………

STATEMENT 2

This thesis is the result of my own independent work/investigation, except where otherwise stated, and the thesis has not been edited by a third party beyond what is permitted by Cardiff University's Policy on the Use of Third Party Editors by Research Degree Students. Other sources are acknowledged by explicit references.   The views expressed are my own.

Signed …………………………………………………… (candidate)   Date …………………………………………

STATEMENT 3

I hereby give consent for my thesis, if accepted, to be available online in the University's Open Access repository and for inter-library loan, and for the title and summary to be made available to outside organisations.

Signed ……………………………………………..…….. (candidate)   Date …………………………………………

STATEMENT 4: PREVIOUSLY APPROVED BAR ON ACCESS

I hereby give consent for my thesis, if accepted, to be available online in the University's Open Access repository and for inter-library loans after expiry of a bar on access previously approved by the Academic Standards & Quality Committee.

Signed ……………………………………………..……… (candidate)   Date …………………………………………

Author note and status of publications

Two of the chapters in this thesis were published as research articles in peer-reviewed journals.

Chapter 4 was published as "Qin, Y., Alves, T., Constantine, J., Gamboa, D. 2016. Quantitative seismic geomorphology of a submarine channel system in SE Brazil (Espírito Santo Basin): Scale comparison with other submarine channel systems. *Marine and Petroleum Geology*, 78: 455-473."

Chapter 6 was published as "Qin, Y., Alves, T., Constantine, J., Gamboa, D. 2017. The role of mass wasting in the progressive development of submarine channels (Espírito Santo Basin, SE Brazil). *Journal of Sedimentary Research*, 87: 500-516."

Although the articles are co-authored with the supervisors, the work presented in the articles is the result of my own original research.

This thesis is dedicated to my grandmother

Acknowledgements

Table of Contents

List of Figures

Chapter 3

Abstract

Submarine channels are conduits that transfer sediment from continental shelves to the deep sea. They can form important hydrocarbon reservoirs when filled with sand-prone deposits and are, consequently, one of the most important hydrocarbon prospects on continental margins around the world. In this thesis, a 3D seismic volume from offshore Espírito Santo (SE Brazil) was used to analyse submarine channel systems near the modern sea floor. The aim of the thesis was to investigate the key controlling factors on variations in the morphology and architecture of submarine channel systems, at the same time, providing an analogue for modern and ancient depositional systems on continental slopes around the world.

This work shows significant variations in morphology and architectures along the investigated submarine channel systems. The spatial variations in both channel and valley morphology documented here suggest an important role of local factors (e.g. mass-wasting events, tributaries, substrate lithology and salt tectonics) in the development of channel systems. It also records in great detail the nature of the interaction between mass-transport deposits and turbidity currents at the early stages of channel evolution. Basal scars created by mass-wasting events can capture turbidity currents and facilitate flow channelisation, which is a key process for submarine-channel initiation. In addition, the replacement of MTDs by channel-fill deposits has profound implications for reservoir volumes and net-to-gross ratios in channel systems. Spatial variations in channel sinuosity observed in this work are interpreted as reflecting substrate erodibility beneath the channel system. Submarine channels will show higher sinuosity when encountering resistant substrates, and lower sinuosity when the substrate is more erodible. Temporal changes in channel sinuosity resulted from enhanced sediment discharge from tributaries. This work stresses the role of lateral channel migration as an important mechanism responding to factors such as sediment supply and ultimately, controlling the evolution of submarine channel systems.

Chapter 1

Introduction

1. Introduction

1.1 Thesis structure

This thesis is divided into eight Chapters. Chapter 1 presents background information on submarine channels and the aims of this thesis. This chapter includes: a) a brief history of submarine-channel research, b) an overview of current understanding about submarine channels, c) the rationale of this work, and d) the objectives of this thesis. Chapter 2 presents the seismic dataset used in this thesis, and introduces the principles behind the acquisition, processing and interpretation of seismic reflection data. Chapter 3 summarises: a) the Mesozoic–Cenozoic geological evolution and salt tectonics of the Espírito Santo Basin, b) the geological background of the area where the studied seismic volume located. Chapter 4 presents a quantitative analysis of submarine channel systems in terms of hierarchical framework. Chapter 5 shows spatial variations in the sediment dispersal pattern(s) of the channel systems. Chapter 6 describes mass-wasting related erosional and depositional features within the channel systems. Chapter 7 discusses: 1) controls on the morphology and sediment dispersal pattern of the channel systems, 2) the role of mass-wasting events in the initiation and development of submarine channels, 3) the impacts of salt diapirs on channel evolution, 4) channel stacking patterns within the channel system and its implications in channel evolution, and 5) the limitations of this thesis and future work. Chapter 8 summaries the main conclusions of the thesis.

1.2 Background and overview of submarine channels

1.2.1 Background

In the early 20th century, a multitude of submarine canyons were recognised on continental shelves and slopes due to the development of echo-sounding technology (e.g. Spencer, 1903; Hull, 1912; Veatch and Smith, 1939). Because submarine canyons reveal a similar morphology to rivers, and connect with river mouths at places, river entrenchment was proposed at the time as the main

mechanism forming submarine canyons on continental shelves and slopes (e.g. Spencer, 1903; Shepard et al., 1936). However, key limitations soon arose from this interpretation, including: 1) a lack of evidence for large-scale uplift on land allowing for river erosion on continental slopes, 2) the realisation that the extent of lowering sea level cannot explain submarine canyons located far below sea level, where fluvial rivers were unlikely to develop (e.g. Shepard et al., 1936; Shepard and Emery, 1941).

Ocean currents were also proposed to be a major factor forming submarine canyons. In fact, Daly (1936) suggested that during glacial periods when sea level is relatively low, wind, waves and tidal waves are capable of eroding mud and sands on the continental shelves. Sediment-loaded currents are thus formed and lead to the incision of submarine canyons. However, direct measurements of currents beneath the sea undertaken at that time (1936) did not confirm the existence of high energy flows (Shepard, 1936). Furthermore, it is difficult to imagine ocean currents capable of cutting submarine canyons through highly resistant rocks (e.g. granite, as sometimes recorded) on their flanks (e.g. Shepard, 1936).

Stimulated by Daly's (1936) density-flow hypothesis, many researchers carried out a series of tank experiments to study the importance of density flows in submarine environments. Their results have demonstrated the effect of sediment transport from onshore areas into the deep sea (Kuenen, 1937; Kuenen and Migliorini, 1950). At the same time, depositional products of turbidity currents were found, and studied at outcrop (e.g. Kuenen and Carozzi, 1953; Natland and Kuenen, 1951), and using sediment cores collected from deep-sea areas (e.g. Ericson et al., 1952; Phleger, 1951). The resulting observations supported, at the time, the theory that turbidity currents are capable of transporting sediment via submarine canyons. Heezen and Ewing (1952) further ascribed the break of submarine telegraph cables to slump-generated turbidity currents due to earthquakes. Based on these observations, turbidity currents were finally recognised as a major control on the geometry and evolution of submarine canyons (e.g. Shepard, 1951; Menard, 1955; Ericson et al., 1961).

In the middle 20th century, many submarine channels connected to submarine canyons were also recognised on the continental slopes and abyssal plains (e.g. Tolstoy, 1951; Ewing et al., 1953; Dietz, 1953; Dill et al., 1954; Menard, 1955; Laughton, 1960; Heezen et al., 1964). They show similar

characteristics to fluvial channel in subaerial settings, such as the presence of distributaries (e.g. Heezen et al., 1964) and the development of meandering patterns (e.g. Tolstoy, 1951; Dill et al., 1954).

Notwithstanding these efforts, difficulties in observing submarine canyons and channels still frustrated our understanding, and detailed knowledge was only significantly improved when seafloor-mapping technology, such as single- and multi-beam equipment and side-scan sonar, was fully developed (e.g. Normark and Piper, 1969; Damuth and Kumar, 1975; Garrison et al., 1982; Kastens and Shor, 1985, 1986; McHargue and Webb, 1986; Flood and Damuth, 1987; Hagen et al., 1994; Pirmez and Flood, 1995). These technology and data have formed, for the past few decades, the basic building blocks for our understanding of submarine canyons and channels.

With the development of hydrocarbon exploration on deep-water margins, seismic data, particularly high-resolution 3D seismic datasets, provided unprecedented detail about the internal architecture of submarine canyons and channels. New data gathered from 3D seismic volumes have enabled interpretation of both modern and ancient systems in a degree of detail never achieved before (e.g., Roberts and Compani, 1996; Kolla et al., 2001; Abreu et al., 2003; Posamentier and Kolla, 2003; Deptuck et al., 2003, 2007; Janocko et al., 2013).

To understand flow processes within submarine canyons and channels, a wide range of numerical and physical experiments were conducted to understand the flow properties of turbidity currents within and outside submarine canyons and channels (e.g., Komar, 1973; Imran et al., 1999; Peakall et al., 2000, 2007; Pirmez and Imran, 2003; Kane et al., 2008). Since the early 2000s, more direct observations derived from oceanographic moorings (e.g. Xu et al., 2002, 2004; Khripounoff et al., 2003; Vangriesheim et al., 2009) have filled the gap between numerical results and the 'true' flow parameters recorded in nature. Together with lithology and sedimentary structures observed from outcrop analogues (e.g. Normark and Piper, 1969; Piper, 1970; Walker, 1975; Mutti, 1977; Cronin, 1994; Clark et al., 1996; Piper et al., 1999; Abreu et al., 2003; Arnott, 2007; Pyles et al., 2012; Hubbard et al., 2014), the scientific community have recently gathered important insights on the interaction between turbidity currents and the sea floor.

1.2.2 Overview of submarine channels

Submarine channels are V- or U-shaped negative features on the seafloor. They are generally located on the middle-lower continental slope and abyssal plains, while submarine canyons are typically located on upper continental slope, some of canyons are markedly incising the shelf edge and being part of continental shelf. However, there is no clear dividing line between the characteristic that distinguishes a submarine canyon from a submarine channel as they usually merge with each other (e.g. Wynn et al., 2007). This thesis focuses on submarine channels, which are V- or U-shaped negative features typically located on the middle-lower continental slope and abyssal plains.

Submarine channels are conduits that transfer sediment from continental shelves to deep-sea depositional areas such as submarine fans. They link terrestrial and deep-marine environments and are considered as crucial components of mass distribution on Earth (e.g. Normark et al., 1993; Posamentier et al., 2003). To date, submarine channels have been widely recognised on continental slopes and submarine fan systems such as the Amazon Fan (Damuth and Kumar, 1975; Damuth et al., 1983; Pirmez and Flood, 1995), the Mississippi Fan (Garrison et al., 1982; Bouma et al., 1985; Kastens and Shor, 1985, 1986), the Bengal Fan (Emmel et al., 1985; Curray et al., 2003), the Indus Fan (McHargue and Webb, 1986; Kolla and Coumes, 1987; Clift et al., 2002), the Nile Fan (Kenyon et al., 1975; Mascle et al., 2001), and the Zaire Fan (Babonneau et al., 2002).

A key aspect of submarine channels is that they become major depositional features on continental slopes when filled with sediment. Understanding their distribution and evolution in response to various forcing mechanisms is thus essential for understanding source-to-sink dynamics, a sub-discipline that investigates the role of hinterland tectonics, climate, and sea level changes in sediment distribution. Moreover, submarine channels can form important hydrocarbon reservoirs when filled with sand (e.g. Mayall and Stewart, 2000; Mayall et al., 2006; McHargue et al., 2011), and are one of the most important hydrocarbon prospects on continental margins around the world. Understanding their evolution leads to more accurate predictions of reservoir distribution and heterogeneity within submarine channel systems.

1.3 Hierarchical framework and terminology associated with submarine channels

Previous studies have documented a range of hierarchical framework associated with submarine channels, in order to classify and synthesise genetically-related channel-form sand bodies from various settings, locations, and datasets (e.g. Mutti and Normark, 1987; Pickering et al., 1995; Campion et al., 2000; Gardner and Borer, 2000; Sprague et al., 2002, 2005; McHargue et al., 2011). For example, Mutti and Normark (1987) proposed five orders of spatial and temporal scales of turbidite deposits: complex, system, stage, sub-stage and beds. Pickering et al. (1995) applied the classification of zero to sixth order bounding-surface hierarchy to submarine environment. Some authors built hierarchical scales based on outcrop studies of submarine channels (e.g. Beaubouef et al., 1999; Gardner and Borer; 2000; Campion et al., 2003).

The hierarchical framework used in this thesis is similar to the classification of Sprague et al. (2002, 2005) and McHargue et al. (2011) (Fig. 1.1). Three orders of stratigraphic elements were used in this thesis, channel element, channel complex and channel complex set, all of which are extensively described and mostly used in the published literatures (e.g. Cronin, 1994; Clark and Pickering, 1996; Abreu et al., 2003; Di Celma et al., 2011; Thomas and Bodin, 2013; Bain and Hubbard, 2016).

Channel element is the fundamental element of the hierarchical framework (e.g. Sprague et al., 2002; McHargue et al., 2011). It consists of a channel-form erosional surface and the sediments fill within the erosional surface (McHargue et al., 2011) (Fig. 1.1A). Deposits within channels comprise channel-fill deposits. The term 'channel' here refers to V or U shaped, unfilled morphological feature on the seafloor. It indicates a present channel on the seafloor and is distinct from the 'channel element', which indicates an ancient channel. They are in the same order of hierarchical framework. Gully is generally straight and small-scale channels, i.e. tens of meters deep at most, tens to hundreds of meters wide (Field, et al., 1999; Surpless et al., 2009; Micallef and Mountjoy, 2011).

Channel complex is an architectural element of a higher order than the channel element. It is composed of two or more genetically related channel-fill episodes and is formed by lateral migration
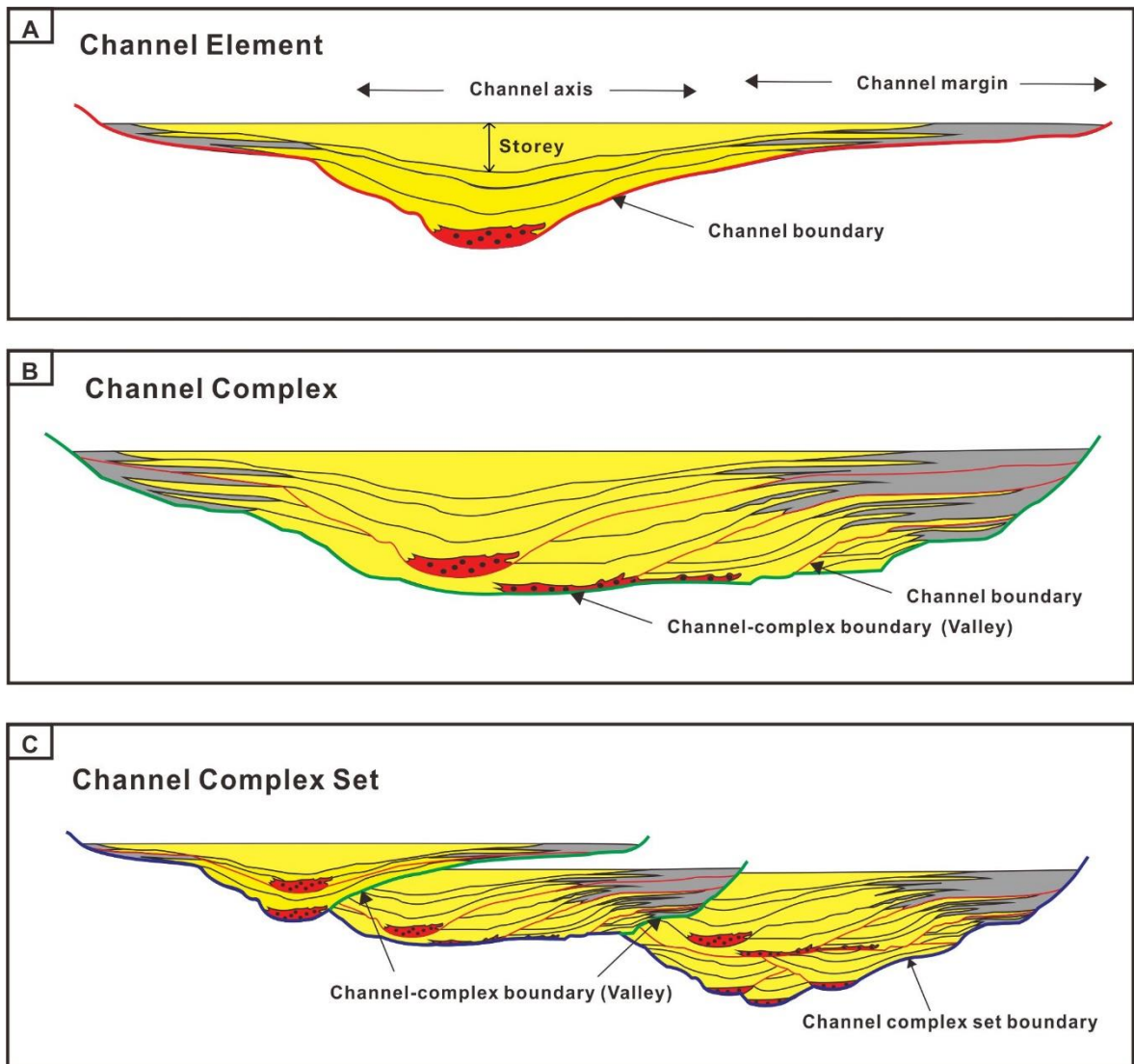
Figure 1.1. Schematic diagram showing the stratal hierarchy of submarine channels (from Di Celma et al., 2011). The channel element, the channel complex, and the channel complex set are commonly observed architectural elements of this hierarchical framework. Envelope shaped facies at the base of channel element is basal lag deposits.

and vertical stacking of a single channel element (e.g. Sprague et al., 2002; Abreu et al., 2003; McHargue et al., 2011; Thomas and Bodin, 2013) (Fig. 1.1B). It refers to channel belt in some studies (e.g. Deptuck et al., 2003; Posamentier, 2003; Catterall et al., 2010; Kane and Hodgson, 2011; Gamberi et al., 2013; Hansen et al., 2015; Jobe et al., 2016).

Valley is used here to refer to a composite erosional surface confining the channel complex, rather than a morphological feature on the seafloor (e.g. Posamentier and Kolla, 2003; Samuel et al., 2003; Deptuck et al., 2003; Babonneau et al., 2004; Kolla, 2007; Kolla et al., 2012; Sylevester et al., 2011; Janocko et al., 2013) (Fig. 1.1B). It is a time-transgressive erosional surface that is formed during lateral and vertical movement of a single channel. Similar erosional surfaces have also been described in previous studies as erosional fairway (Deptuck et al., 2003; Catterall et al., 2010), master erosion/incision surface (Gee et al., 2007), channel-belt erosion surface (Kane and Hodgson, 2011), or bounding erosion surface (Hansen et al., 2015).

Levees are overbank deposits with gull-wing geometries that converge away from the channel thalweg. External levees (outer levees sensu Deptuck et al., 2003, 2007; master-bounding levees sensu Posamentier, 2003) and internal levees (inner levee sensu Deptuck et al., 2003, 2007) are used to differentiate levees deposited outside and inside the valley (Kane and Hodgson, 2011).

The term channel system is used here to refer to all genetically-related morphological and depositional components. It is defined by channel complex plus the external levees.

Channel complex set is composed of multiple genetically related channel complexes (e.g. Sprague et al., 2002; McHargue et al., 2011) (Fig. 1.1C).

1.4 Geomorphology of submarine channels and channel complexes

1.4.1 Channel and channel-complex dimensions

1.4.1.1 Channel dimensions

The cross-section of a channel is commonly symmetrical when the channel is relatively straight; however, it is markedly asymmetric at meander bends (e.g. Kolla et al., 2001; Wynn et al., 2007; Deptuck et al., 2007). In these latter bends, the channel shows steeper margins on its outer bends

and gentler margins on its inner bends.

Morphological parameters such as channel width (i.e. the distance between internal levees or erosional banks of channels), height (i.e. the distance between levee crest or the top of erosional banks and channel thalweg), and cross-sectional area (CSA) have been widely used in previous studies (e.g. Flood and Damuth, 1987; Pirmez et al., 1995; Babonneau et al., 2002; Estrada et al., 2005; Antobreh and Krastel, 2006; Deptuck et al., 2007; Jobe et al., 2015) (Fig. 1.2). These parameters are recognised as being associated with changes in the dynamics of turbidity currents within submarine channels (e.g. Komar, 1969, 1973; Bowen et al., 1984; Klaucke et al., 1997; Babonneau et al., 2002; Pirmez and Imran, 2003; Estrada et al., 2005; Sequeiros, 2012; Konsoer et al., 2013; Jobe et al., 2015). For example, Pirmez and Imran (2003) reconstructed the characteristics of turbidity currents (e.g. flow velocity, thickness, concentration and duration) within the Amazon submarine channels based on channel morphology and depositional patterns. Konsoer et al. (2013) found that the size of submarine channels is related to bankfull discharge (i.e. the flow condition that turbidity current just spills over channel levees). Making use of chronostratigraphic constraints provided from high-resolution stratigraphic data, Jobe et al. (2015) correlated temporal variations in channel size to changes in sediment supply associated with sea level changes.

Submarine channels documented by literature are generally hundreds of meters wide, and tens of meters high (e.g. Normark, 1978; Walker, 1985; Shanmugam and Moiola, 1988; Clark and Pickering, 1996; Gardner et al., 2003; Deptuck et al., 2007; Di Celma et al., 2011; Moody et al., 2012; Sylvester et al., 2012; Jobe et al., 2015; Maier et al., 2012; Brunt et al., 2013; Figueiredo et al., 2013; Bain and Hubbard, 2016). However, kilometre-wide channels are also recorded in previous studies (Shanmugam and Moiola, 1988; Pirmez and Flood, 1995; Clark and Pickering, 1996; Babonneau et al., 2002). Jobe et al. (2016) collected morphological data of 21 submarine systems from seismic and outcrop studies. They found that channel width ranges from 400 m to 1200 m, whereas channel thickness ranges from 20-100 m (Jobe et al., 2016). However, morphological data collected by McHargue et al. (2011) shows smaller channels elements than Jobe et al. (2016). McHargue et al. (2011) showed that the mean value of channel width is ~ 300 m for outcrop data and ~ 200 m for seismic data, whereas the mean value of channel thickness is ~ 10 m. Therefore, more studies about
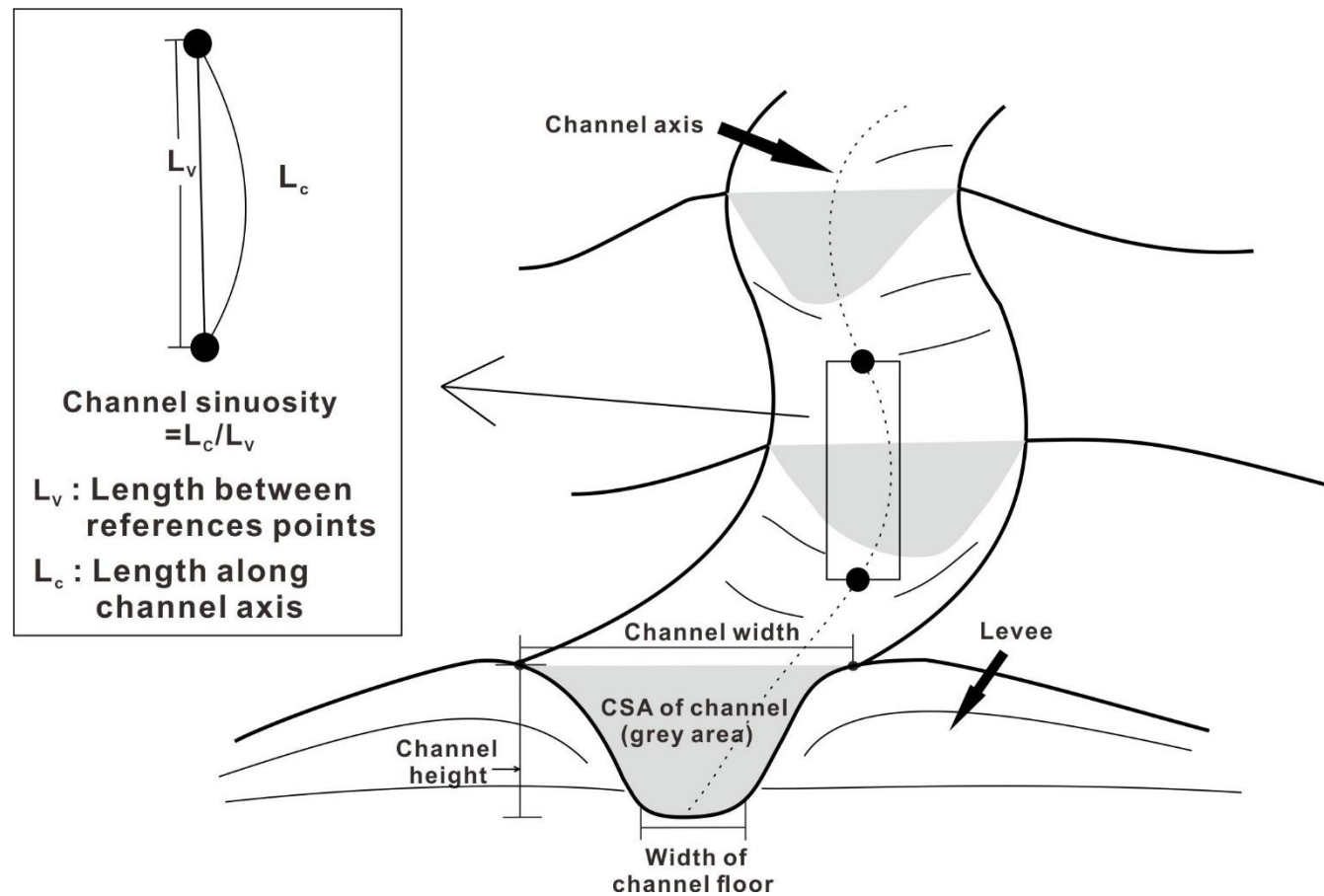
Figure 1.2. Schematic representation of morphological analyses commonly used in the interpretation submarine channels. Parameters analysed include the channel-floor width, channel width, height, and the calculation of cross-sectional area (CSA) and channel sinuosity.

channel dimensions are needed to truly correlate channel dimensions with the flow properties of turbidity currents.

Jobe et al. (2016) compiled morphological data from submarine and fluvial channels from a range of tectonic settings to find that the average thickness of channels and channel belts in the submarine realm is much larger than in sub-aerial settings. In addition, they also found that the aspect ratio of channel belts approaches a value of 9 for submarine channels, which is much smaller than the recorded value of 72 for fluvial channels (Jobe et al., 2016). These differences in thickness and aspect ratio between fluvial and submarine channels are interpreted as caused by distinct (and variable) flow properties, i.e. higher quantities of suspended sediment in the upper portions of turbidity currents promote levee growth and vertical aggradation in submarine channel systems (Jobe et al., 2016).

1.4.1.2 Channel-complex dimensions

Channel complexes documented in the literature show striking morphological variations. For example, channel complexes can be less than 1000 m wide and similar to the width of submarine channels (e.g. Gardner et al., 2003; Pyles et al., 2010; Thomas and Bodin, 2013; Macauley and Hubbard, 2013). In comparison, channel complexes wider than 3000 m have been recorded on seismic data (e.g. Samuel et al., 2003; Deptuck et al., 2007; Catteral et al., 2010; De Ruig and Hubbard, 2006; Kolla et al., 2012; Jolly et al., 2016), and at outcrop (e.g. Cronin et al., 2005b; Bain and Hubbard, 2016; Grecula et al., 2003). In the Indus fan, the valley can be up to 10 km wide (Deptuck et al., 2003). These marked variations are likely due to differences in the degree of lateral channel migration, and by channel kinematics influenced by local factors (e.g. Bain and Hubbard, 2016; Jobe et al., 2016).

1.4.1.3 Summary

To date, the majority of previous studies from seismic data have been focused on either the channel scale (e.g. Flood and Damuth, 1987; Clark et al., 1992; Pirmez and Flood, 1995; Babonneau et al., 2002; Antobreh and Krastel, 2006; Gee et al., 2007; Estrada et al., 2005; Clark and Cartwright,

2009; Peakallet al., 2012; Kolla et al., 2012; Georgiopoulou and Cartwright, 2013; Jobe et al., 2015; Reimchen et al., 2016) or the channel-complex scale (e.g. Catterall et al., 2010; Wood and Mize-Spansky, 2009). Few published papers addressing the morphological characteristics of both scales in the same channel system (e.g. Wonham et al., 2000; Deptuck et al., 2007; Wood and Mize-Spansky, 2009).

Outcrops of submarine channel systems have shown stratigraphic elements of distinct sizes, from small-scale channel elements to large-scaled channel complexes and channel complex sets (e.g. Grecula et al., 2003; Lien et al., 2003; Cronin et al., 2005b; Vigorito et al., 2006; Hubbard et al., 2008, 2009, 2014; Thomas and Bodin, 2013; Gamberi et al., 2013; Macauley and Hubbard, 2013; Bain and Hubbard, 2016). They have revealed the size of channel complexes and channel complex sets to be similar to the seismic scale, allowing for comparisons between seismic and outcrop data (e.g. Lien et al., 2003; Vigorito et al., 2006; Thomas and Bodin, 2013; Bain and Hubbard, 2016). However, to further bridge the gap between seismic and outcrop studies, new morphological data are increasingly needed from high-quality seismic volumes, especially when addressing spatial changes in channel-associated stratigraphic elements.

1.4.2 Channel sinuosity

Sinuosity is a prominent planform characteristic of submarine channels (Fig. 1.2). It can be formed either at early incision stages, or at subsequent aggradation stages (e.g. Mayall et al., 2006). Various forms of channel sinuosity, including downstream or upstream translation, lateral expansion, or a combination of all these, have been found in submarine channels (e.g. Chough and Hesse, 1976; Droz and Bellaiche, 1985; Pirmez and Flood, 1995; Kolla et al., 2001, 2007; Abreu et al., 2003; Wynn et al., 2007; Janocko et al., 2013).

Quantitative analyses have been used to address the relationship between channel sinuosity and valley slope in submarine settings, such as the Amazon Fan (Flood and Damuth, 1987; Pirmez and Flood, 1995), the Indus Fan (Amir, 1992), the Mississippi Fan (Weimer, 1991), Mediterranean Sea (Cronin et al., 1995), Peru-Chile forearc (Hagen et al., 1994), West Africa (Babonneau et al. 2002; Ferry et al., 2005; Gee et al., 2007), and offshore Japan (Soh et al., 1990; Soh and Tokuyama, 2002;

Noda et al., 2008). For example, Flood and Damuth (1987) first documented a positive relationship between channel sinuosity and valley slope on the Amazon fan, i.e. channel sinuosity increases as valley slope increases and channel sinuosity decreases as valley slope decreases. This relationship was later confirmed by more detailed morphological studies on the Amazon fan undertaken by Pirmez and Flood (1995), and other studies from the Indus Fan (Amir, 1992), the Zaire fan in west Africa (Babonneau et al. 2002), Almeria canyon in the Mediterranean Sea (Cronin et al., 1995), and the Boso Canyon from offshore Japan (Soh et al., 1990). Clark et al. (1992) further compiled morphological data from a range of submarine fans and found similar trends to the curves obtained from flume experiments conducted by Schumm and Khan (1972). The curves show that channel sinuosity increases as valley slope increases until a threshold slope is reached, after which channel sinuosity decreases (Clark et al., 1992).

Not all previous studies documented a positive relationship between valley slope and channel sinuosity (e.g. Ferry et al., 2005; Noda et al., 2008). For example, both negative and positive relationships have been observed on the Angolan continental margin (Gee et al., 2007). In addition, in the Tenryu Canyon offshore Japan, correlations are unclear between valley slope and channel sinuosity (Soh and Tokuyama, 2002). The absence of positive relationships in these studies is probably due to diverse factors, such as: 1) the existence of a threshold slope gradient (i.e. a gradient that above which channels can follow a more direct course rather than a more sinuous course downslope). For example, channel sinuosity decreases when channel gradient is higher than threshold slope gradient (Clark et al., 1992; Gee et al., 2007); 2) different measurement intervals adopted by researchers, resulting in erroneous scenarios as the measured intervals can be too large (or too small) to capture the actual variations in sinuous loops with valley slope (e.g. Wynn et al., 2007). For example, channel sinuosity measured at 10 km, 20 km, and 30 km intervals shows different patterns at places in the Bengal fan (Kolla et al., 2012); 3) channels can be in a state of adjustment (i.e. out of equilibrium) rather than having reached their local equilibrium state (Pirmez and Flood, 1995; Ferry et al., 2005); 4) channel sinuosity is affected by other factors such as tectonic controls and sediment supply (e.g. Cronin, 1994; Clark and Cartwright, 2011; Babonneau et al., 2002).

Wood and Mize-Spansky (2009) found a positive relationship between seafloor gradient and sinuosity. However, in some regions with similar seafloor gradient, channels may display different sinuosity (e.g. Maier et al., 2013; Zucker et al., 2017; Hansen et al., 2017), a character suggesting that seafloor gradient is not the key factor controlling channel sinuosity.

Sediment supply (e.g. grain size, density and frequency of turbidity current) is also suggested to be an important factor affecting channel sinuosity (e.g. Weimer, 1991; Babonneau et al., 2002; Kolla et al. 2007; Wynn et al., 2007; Hansen et al., 2017). For example, Babonneau et al. (2002) suggest that decreases in flow energy and erosive power downslope result in a decrease in channel sinuosity. However, it is difficult to evaluate the relationship between sediment supply and channel sinuosity without lithological data.

Additionally, some authors suggest that channel sinuosity increases with time, with meander cut-offs forming during this process (e.g. Deptuck et al., 2003; Gee et al., 2007; Wynn et al., 2007; Babonneau et al., 2010; Maier et al., 2013). Babonneau et al. (2010) attributed the increases in irregularity and complexity of meandering shape to the maturity of channel. They suggest that meander cut-off, asymmetrical and composite meander shape show a longer evolutionary history compared to less sinuous channels (Babonneau et al., 2010). Furthermore, Gee et al. (2007) and Maier et al. (2013) proposed an evolutionary model in which submarine channels developed from relatively straight to more sinuous pathways. Flow frequency maybe is important in this process as flow frequency increases with time within a specific channel, thus resulting in increased channel sinuosity.

Previous studies have also linked the variations of channel sinuosity to other factors such as Coriolis force (e.g. Peakall et al., 2012; Wells and Cossu, 2013). Peakall et al. (2012) found that more sinuous channels tend to be located in low latitudinal areas, while less sinuous channels tend to be located in higher latitudinal area. They attributed such variations in channel sinuosity to the Coriolis force, which changes with latitude and leads to variations in intra-channel flow and subsequent channel sinuosity (Peakall et al. 2012).

Substrate is also proposed to be one of factors affect channel sinuosity (e.g. Hansen et al., 2017). However, related studies are still lacking because of difficulties in obtaining information

about lithological variations beneath channels. Seafloor topography (e.g. Mayall et al., 2006; Clark and Cartwright, 2011) is another factor influencing channel pathways and associated sinuosity. The role of this factor is discussed in Section 1.7.1.

1.4.3 Longitudinal profile of submarine channels

The thalweg-depth profiles (i.e. longitudinal profile) of submarine channels are generally measured at the channel thalweg (i.e. the deepest point of a channel) along the channel axis. Three types of longitudinal profiles, convex, slightly concave, and very concave profiles, were documented by Covault et al. (2011) (Fig. 1.3), and indicate variations in continental slope settings and local structures. For example, convex-upward profiles generally develop in passive margins affected by tectonic deformation and active convergent margins. Slightly concave-upward profiles commonly occur in mature passive continental margins not subjected to significant tectonic deformation (Covault et al., 2011).

Despite variations in channel longitudinal profiles, an equilibrium profile exists for submarine channels along their paths because turbidity currents tend to seek a balance between erosion and deposition (Normark and Piper, 1969; Pirmez et al., 2000) (Fig. 1.4). It is an equilibrium condition for deep-water channels that prevailing sediment discharge is carried through the channels with minimum aggradation or degradation (Pirmez et al., 2000). Georgiopoulou and Cartwright (2013) further defined the concept of equilibrium profiles from the perspective of flow energy. They suggested that a slope in equilibrium is the most energy-efficient route (i.e. the path of least resistance) for flows, which tend to conserve as much energy as possible and bypass the slope without erosion or deposition. However, it is usually difficult to generalise the form of equilibrium profiles of submarine channels because of a wide range of factors, such as temporal and spatial changes in flow properties (Kneller, 2003), and modifications in seafloor topography induced by local tectonic structures (e.g. Pirmez et al., 2000; Georgiopoulou and Cartwright, 2013).
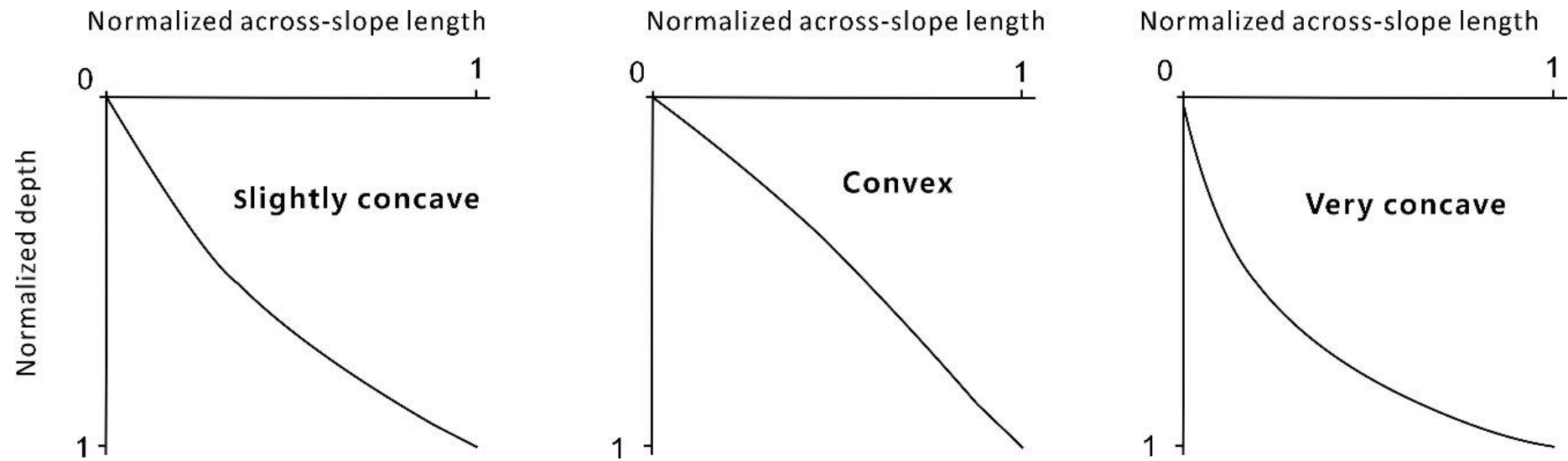
Figure 1.3. Three types of longitudinal-profile shape, slightly concave, convex and very concave profiles (Covault et al., 2011).
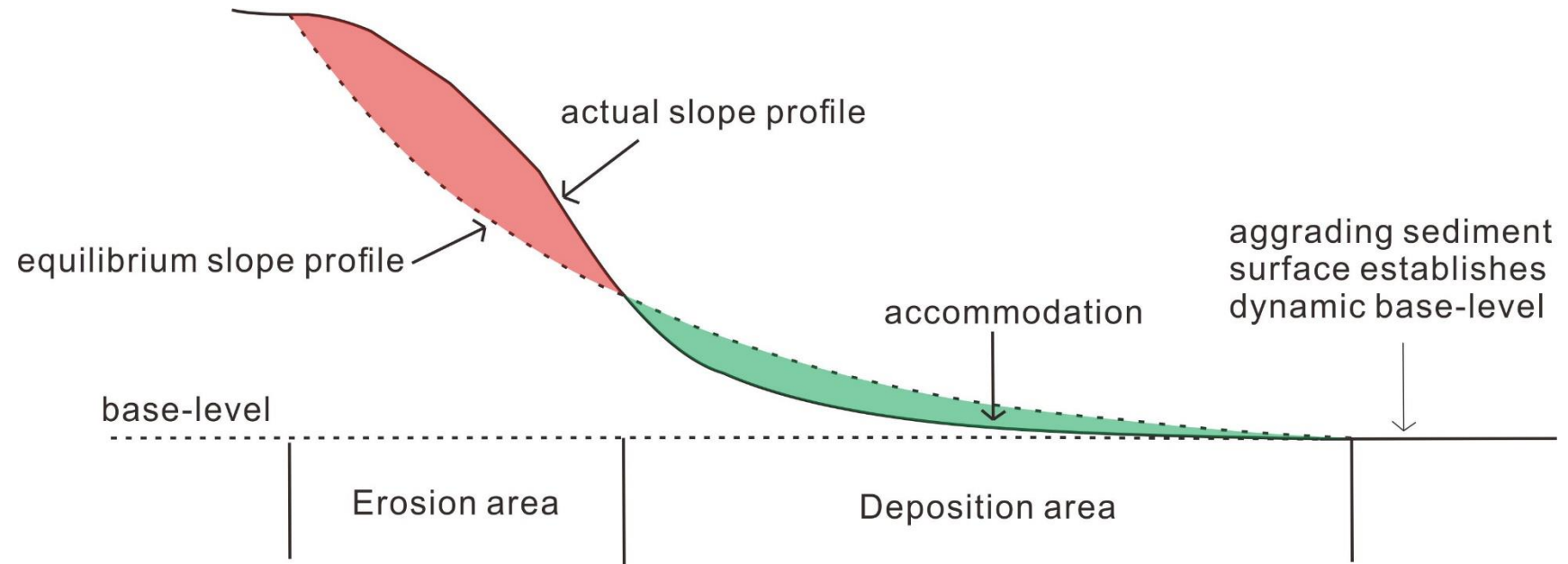
Figure 1.4. Schematic illustration of equilibrium slope profiles for submarine channels, and associated erosional and depositional processes (from Kneller, 2003). Base level is defined as the deepest point in the basin that can be reached by gravity flows (Carter, 1988; Pirmez et al., 2000).

1.5 Architectural elements in submarine channels systems

In order to build a conceptual framework for comparing modern and ancient turdidite systems Mutti and Normark (1987) introduced the concept of 'element', which includes channels, overbank deposits, lobes, channel/lobe transition features, and scours, to provide a characterization of facies assemblage. The term 'architectural element' was later borrowed from fluvial system to build a hierarchical classification of depositional elements in turbidite system (Miall, 1989). An architectural element is a depositional body defined by its geometry, scale and facies (Miall, 1989; Pickering et al., 1995). It is formed by a particular process or series of processes within a depositional system (Miall, 1989).

Previous studies have documented a variety of architectural elements associated with submarine channel systems such as internal and external levees, thalweg deposits, slump/slide deposits, and deposits associated with lateral channel migration (e.g. Mutti and Ricci Lucchi, 1975; Pickering, 1982; McHargue and Webb, 1986; Shanmugam and Moiola, 1988; Mutti and Normark, 1991; Normark et al., 1993; Cronin, 1994; Clark and Pickering, 1996; Kolla et al., 2001; Abreu et al., 2003; Deptuck et al., 2003; Mayall et al., 2006; Kane and Hodgson, 2011; Janocko et al., 2013).

1.5.1 Deposits associated with lateral migration

In submarine channels, two types of migration, discrete and continuous migration, have been widely documented in the literature from high-resolution subsurface data (e.g. Kolla et al., 2001; Abreu et al., 2003; Deptuck et al., 2003, 2007; Maier et al., 2012) (Fig. 1.5). They are interpreted to result from variations in flow properties (Kolla et al., 2001, 2007). Steady and surge-type turbidity currents result in varying degrees of discrete and continuous channel migration, while steadier flows cause subtler and more continuous lateral channel migration than surge flows (Kolla et al., 2001, 2007).
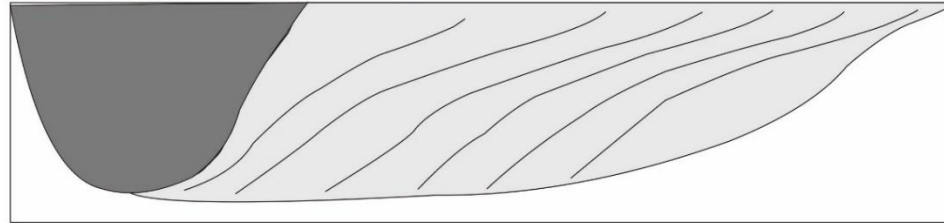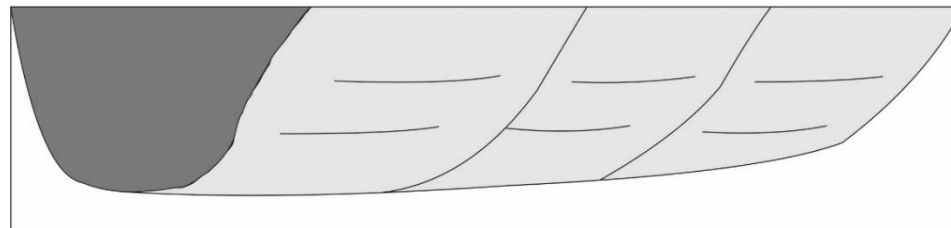
Figure 1.5. Comparison between continuous and discrete lateral migration in submarine channels (modified from Abreu et al., 2003). Continuous migration is characterised by inclined strata, while discrete migration is characterised by sub-horizontal strata.

1.5.1.1 Continuous migration

Continuous migration has been observed in submarine channels, as shown by Lateral Accretion Packages (LAPs) on seismic data from West Africa (e.g. Abreu et al., 2003; Flood et al., 2009; Jancko et al., 2013) (Fig. 1.5). These LAPs are located at the inner bends of channels, and are characterised by: a) inclined seismic reflections dipping towards the channels axis in vertical seismic profiles, and b) "scroll bar" geometries on horizon slices (Abreu et al., 2003).

They represent the lateral accretion of sediments formed by lateral migration of the channel thalweg, in a process similar to the formation of point-bars in fluvial channels (Abreu et al., 2003) (Fig. 1.6).

Lateral-accretion deposits, which correspond to LAPs on seismic data, have been documented at outcrop (e.g. Cronin, 1994; Elliott et al., 2000; Abreu et al., 2003; Pyles et al., 2010; Arnott, 2007; Wynn et al., 2007; Dykstra and Kneller, 2009). Lithofacies associated with these deposits range from conglomerates and coarse-sandstones, to sandy and muddy turbidites (Cronin, 1994; Abreu et al., 2003). Fining-upward trends (e.g. Abreu et al., 2003; Wynn et al., 2007; Janocko et al., 2013) and coarsening-upward profiles (Pyles et al., 2012) are both found in 'point bars' of submarine channels. Arnott (2007) documented two repeating and interstratified types of strata: a) coarse-grained deposits consisting of strata as coarse as granule conglomerates, and b) fine-grained deposits composed of thin- to medium-bedded fine-grained turbidites. The dip angles of lateral-accretion surfaces range from 4° to 26° on seismic data (Abreu et al., 2003; Kolla et al., 2007; Janocko et al., 2013), and from 7° to 16° at outcrop (Cronin, 1994; Arnott, 2007; Abreu et al., 2003).

1.5.1.2 Discrete migration

The discrete migration of submarine channels occurs in the form of cut-and-fill processes that involve the infilling of the channel before shifting its position, with flows eroding the channel banks and generating remnant channel-fill deposits (e.g. Deptuck et al., 2007; Maier et al., 2012) (Fig. 1.7). During this process, turbidity currents can erode the inner or outer banks of previous channels, resulting in lateral migration with no clear patterns (Fig. 1.8). Deptuck et al. (2007) suggest that the position of channels re-incision is strongly influenced by the thickness of channel-fill deposits. For
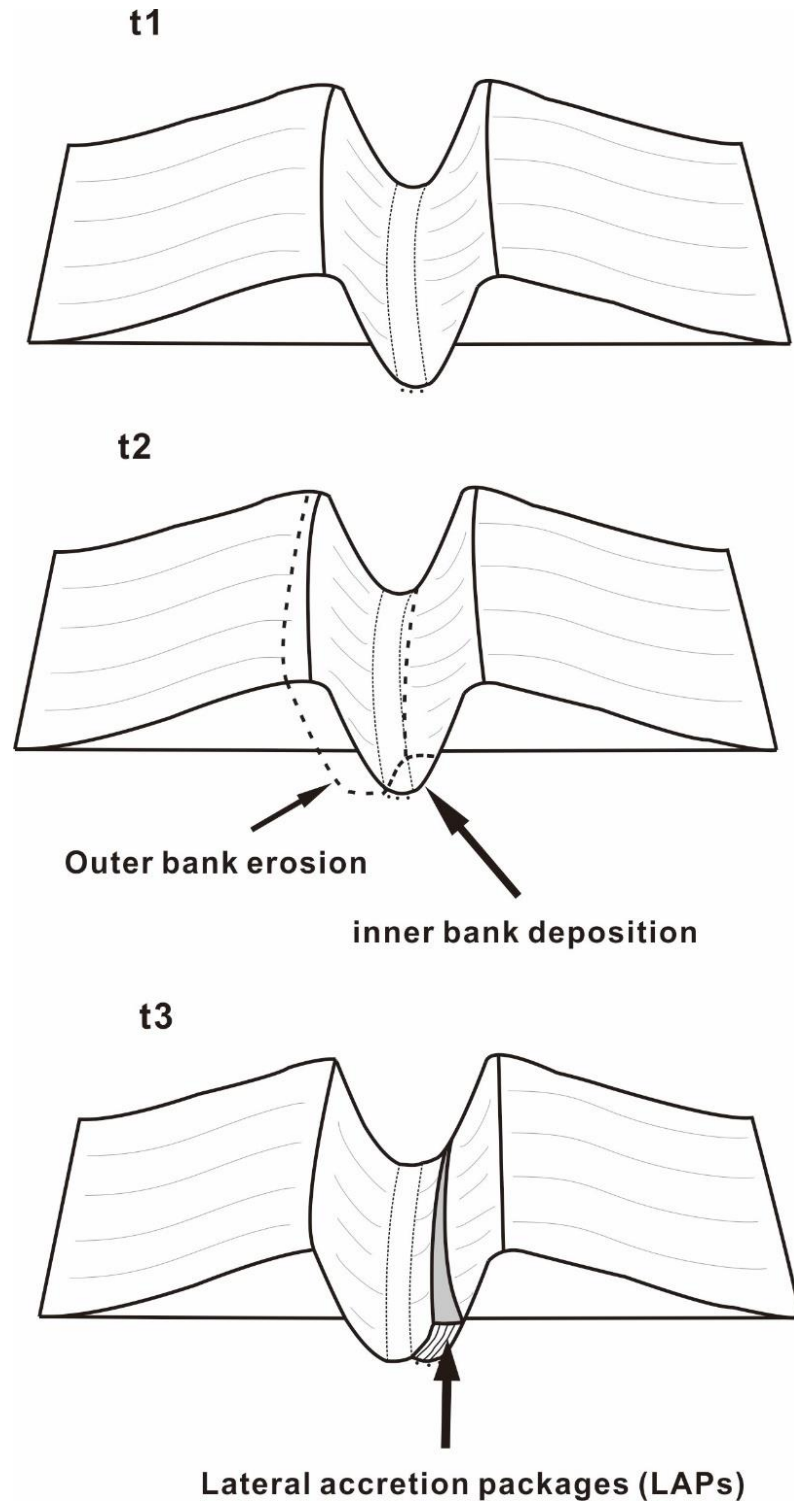
Figure 1.6. Continuous lateral migration within submarine channels. This process is similar to the formation of point-bars in fluvial channels and is characterised by the accumulation of Lateral Accretion Packages (LAPs).
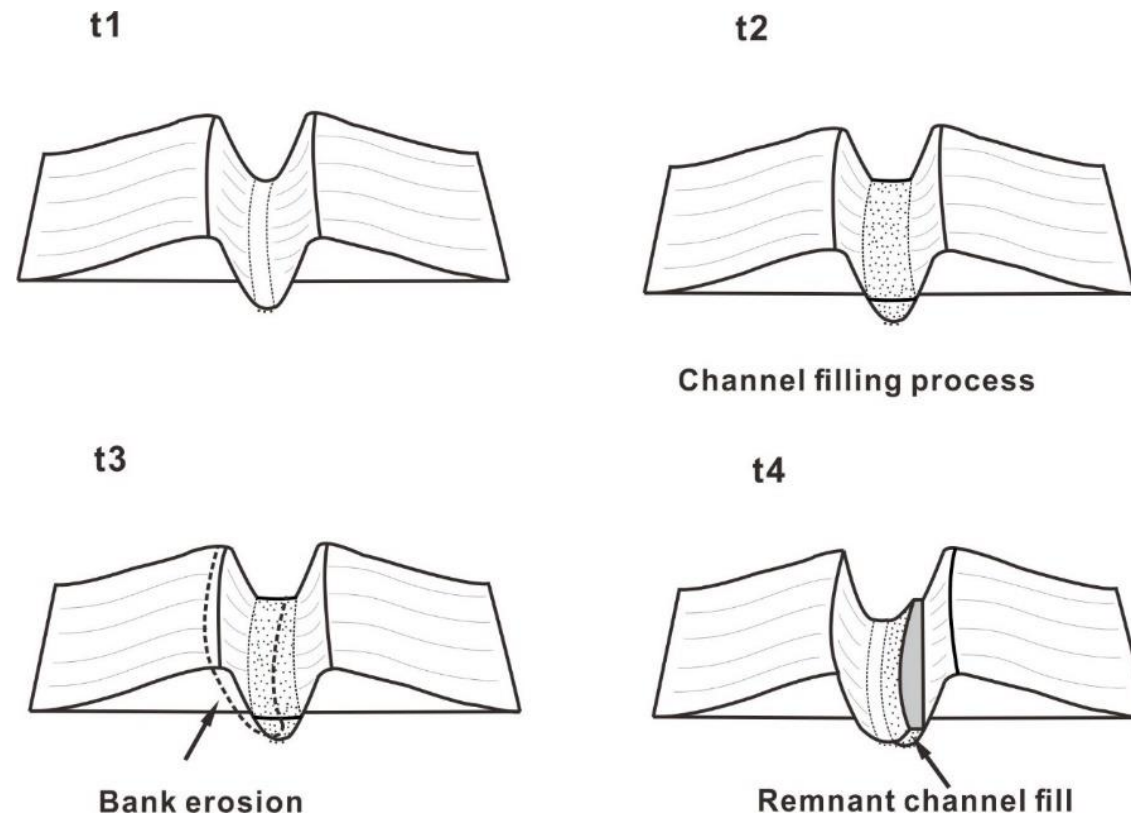
Figure 1.7. Discrete lateral migration within submarine channels (modified from Maier et al., 2012). This figure illustrates a cut-and fill process involving the total infill of the channel before the channel shifts its position, with flows eroding the channel banks and generating remnant channel-fill deposits.
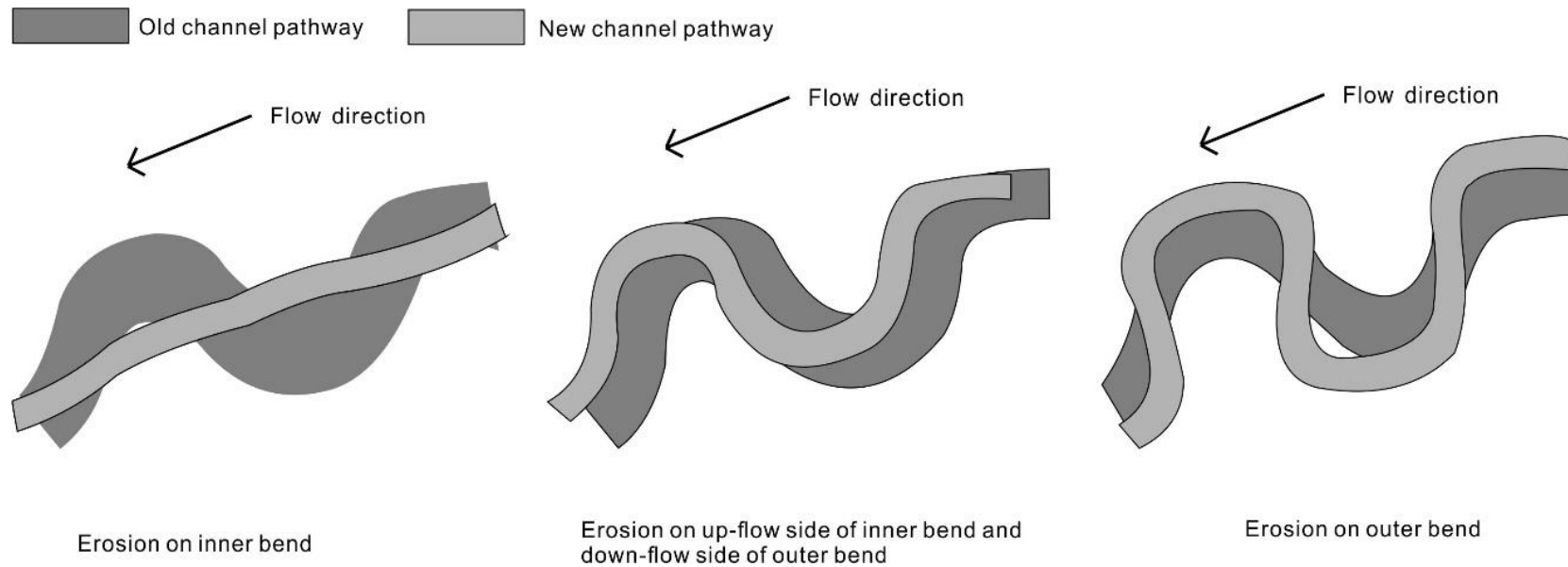
Figure 1.8. Variation in channels migration patterns (Deptuck et al., 2007). This variation is associated with flow parameters and the morphology of the old channels.

example, thicker channel-fill deposits result in the reduced confinement of subsequent 'erosive' flows - these flows are thus less likely to follow their previous pathway(s) (Deptuck et al., 2007).

1.5.2 Basal lags

Basal lags are deposits accumulated on the channel floor when turbidity currents bypass channels (e.g. Normark et al., 1993; Mayall et al., 2006). There are, at least, three types of basal-lag depositional facies recorded in the literature: 1) coarse sands and conglomerates, 2) mud-clast conglomerates, and 3) shale drapes (Mayall et al., 2006). The occurrence of these three types of basal lag result in different reservoir properties of channel bases (Mayall et al., 2006). For example, coarse sands and conglomerates form high permeability zones and mud-clast conglomerates and shale drapes form permeability barriers (Mayall et al., 2006).

Basal lags in channels are often interpreted as High Amplitude Reflections (HARs) on seismic data which are discontinuous, high amplitude seismic reflections (Damuth et al., 1983; Stelting and DSDP Leg 96 shipboard scientists, 1985; McHargue and Webb, 1986; Deptuck et al., 2003; Catterall et al., 2010; Wynn et al., 2007).

1.5.3 Bank failures

Bank failures can be recognised by the presence of amphitheatre-shaped scars on the banks of channel systems (e.g. Deptuck et al., 2003; Cronin et al., 2005a; Janocko et al., 2013; Hansen et al., 2017). Their corresponding deposits are usually composed of a muddy matrix, and muddy to clean sands, and show a contorted internal structure (e.g. Cronin et al., 1998; Mayall et al., 2006). On seismic data, mass-failure deposits are characterised by the presence of discordant to chaotic, transparent to high-amplitude, hummocky reflections (e.g. Embley, 1980; Kastens and Shor, 1985; McHargue and Webb, 1986; Hess and Rakofsky, 1992; Mayall et al., 2006; Gaudin et al., 2006; Gee et al., 2007; Janocko et al., 2013). In some cases, reflections within rotational slide blocks are inclined towards the sidewalls, which may be correlated with adjacent undeformed strata (e.g.

Deptuck et al., 2003, Catterall et al., 2010).

Excess overpressures are thought to be the main cause for mass failures on channel margins. These overpressures are often generated during the rapid deposition of low-permeability, fine-grained sediment such as levee deposits (Dugan and Sheahan, 2012; Sawyer et al., 2013). Sawyer et al. (2013) studied the relationship between levee height and bank failure using numerical models. Their results show that rapid levee deposition above the channel banks can generate high fluid pressures in near-seafloor strata, reducing effective stresses within the strata and promoting mass failures above a critical bank height (Sawyer et al., 2013). In addition, local oversteepening of channel walls resulting from undercutting is another mechanism capable of causing bank failures (e.g. Deptuck et al., 2003; Noda et al., 2008; Catterall et al., 2010).

1.5.4 Levees

Levees are formed by the overspilling and flow stripping of turbidity currents from the channel onto its overbank (e.g. Buffington, 1952; Komar, 1973; Piper and Normark, 1983; Hübscher et al., 1997; Skene et al., 2002). They are often recognised as high- to low-amplitude, continuous, parallel to subparallel, wedge-shaped reflections on seismic data (e.g. McHargue and Webb, 1986; Deptuck et al., 2003; Gee et al., 2007; Catterall et al., 2010; Kane and Hodgson, 2011; Janocko et al., 2013). There are two scales of levees documented within submarine channel systems: external levees (outer levees *sensu* Deptuck et al., 2003, 2007) or master-bounding levees (*sensu* Posamentier, 2003) that confine submarine channel complexes; and internal levees (inner levee *sensu* Deptuck et al., 2003, 2007) that confine submarine channels (Kane and Hodgson, 2011). Within submarine complexes, accommodation space for internal-levee deposition is often provided by features such as erosional terraces, abandoned meander loops and slumps or slides (e.g. Deptuck et al., 2003; Babonneau et al., 2004, 2010).

In the published literature, sediment waves have been recognised on the external levees of submarine channel systems (e.g. Nakajima et al., 1998; Wynn et al., 2002, 2007; Posamentier and Kolla, 2003). They are symmetrical to asymmetrical wave-like bedforms observed in unconfined

submarine environments, and are formed by spillover and flow stripping due to super-elevation of turbidity currents associated to centrifugal forces (Piper and Normark, 1983; Normark et al., 2002).

1.5.5 Last-stage channel fills

Last-stage channel fill deposits record the abandonment stage of submarine channels (Clark et al., 1996; Kneller, 2003; Wynn et al., 2007; Janocko et al., 2013). They vary from sand– to mud-prone, high- to low-amplitude (continuous) horizontal seismic reflections (e.g. Janocko et al., 2013), and commonly show convex-upward "hat" shapes after compaction (Posamentier, 2003). Such a geometry is ascribed to the differential compaction of the axial sandy fill deposited adjacent to muddy deposits (Posamentier, 2003).

1.5.6 Cyclic steps

When turbidity currents hit a change in seafloor gradient, increasingly downward-directed stresses and associated turbulence lead to sea bed erosion and the occurrence of a hydraulic jump (Menard, 1964; Van Andel and Komar, 1969; Komar, 1971; Mutti and Normark, 1987; Garcia and Parker, 1989; Kostic and Paker, 2006; Covault et al., 2016). At the seafloor slope transition areas, the turbidity currents change from supercritical flows (Froude number > 1) on the steeper slope area to subcritical flows (Froude number < 1) on the gentler slope areas (Van Andel and Komar, 1969; Komar, 1971). Froude number (Fr_d) can be shown as (Van Andel and Komar, 1969; Covault et al., 2016):

$$Fr_d = U / \sqrt{\frac{\Delta\rho}{\rho} gh} \quad \text{---------------------------------------} \text{ (Eq. 1.1)}$$

where U is the depth-averaged velocity of currents, g is the gravitational acceleration, $\Delta\rho/\rho$ is the submerged specific gravity of the currents, and h is the current thickness.

Hydraulic jumps are associated with the presence of cyclic steps, which are step-like bed forms

and have been recorded in several areas such as offshore California (e.g. Fildani et al., 2006; Normark et al., 2009; Covault et al., 2016), the Espírito Santo Basin (Heiniö and Davies, 2009), Niger Delta (Armitage et al., 2012) and South China Sea (Zhong et al., 2015). A series of linear cyclic steps are suggested to be relate to the initiation of submarine channels (Fildani et al, 2006; Covault et al., 2013).

1.5.7 Summary

The distribution of channel-associated deposits provides information about depositional processes and associated flows dynamics, as well as the assessment of reservoir quality (e.g. Mayall et al., 2006; Peakall and Sumner, 2015). However, sedimentation within submarine channels is still lacking due to difficulties in direct observations and measurements of on-going depositional processes within submarine channels. Current understanding about sedimentation and associated flow processes are mainly from experimental and numerical modelling (e.g. Komar, 1973; Imran et al., 1999; Peakall et al., 2000, 2007; Pirmez et al., 2003; Kane et al., 2008). For example, deposition in inner- and outer-bends is both observed within sinuous submarine channels (Abreu et al., 2003; Nakajima et al., 2009; Kane et al., 2008). The sedimentation processes of such deposits mainly depend on the degree of confinement; the higher degree of confinement results in strongly bypassing flows and sedimentation in inner bend, while a relatively lower degree of confinement results in weakly bypassing flows and sedimentation in outer bend (Kane et al., 2008).

High-resolution 3D seismic data allows the detailed interpretation of sediment types and quantification of sediment volume within submarine channel systems. However, there is still less attention has been paid on the quantification of sediment-dispersal patterns within submarine channel systems. More quantitative work from seismic data is needed to explore sedimentation processes within submarine channels and associated flow processes.

1.6 The influence of mass-transport deposits (MTDs) on submarine-channel development

Mass-wasting processes have a significant impact on seafloor morphology and sediment distribution on continental slopes (e.g. Nardin et al., 1979; Embley, 1980; Damuth and Embley, 1981; Hampton et al., 1996; McAdoo et al., 2000; Kneller et al., 2016). They evacuate large volumes of sediment and are capable of changing seafloor topography, ultimately controlling the distribution of turbidites that may form important reservoirs for hydrocarbons (e.g. Cronin et al., 1998; Pickering and Corregidor, 2005; Armitage et al., 2009; Jackson and Johnson, 2009; Joanne et al., 2010; Hansen et al., 2013; Olafiranye et al., 2013; Ortiz-Karpf et al., 2015; Turner, 2015; Kneller et al., 2016; Corella et al., 2016).

The relationship between accommodation space and the geometry and internal structure of mass-transport deposits (MTDs), the common product of mass-wasting events, has been addressed using seismic data (e.g. Kertznus, 2009; Bernhardt et al., 2012; Hansen et al., 2013; Olafiranye et al., 2013; Ortiz-Karpf et al., 2015; Masalimova et al., 2015; Kneller et al. , 2016) and outcrop data (Cronin et al., 1998; Pickering and Corregidor, 2005; Shultz et al., 2005; Lucente and Pini, 2008; Armitage et al., 2009; Jackson and Johnson, 2009; Eggenhuisen et al., 2010), bathymetric data (Corella et al., 2016), well and core data (Eggenhuisen et al., 2010; Corella et al., 2016), and numerical models (Stright et al., 2013).

A variety of turbidity-current responses to pre-existing MTDs have been recorded in previous studies. For example, the irregular top surfaces of MTDs can create ponded accommodation space for subsequent turbidites (e.g. Cronin et al., 1998; Shultz et al., 2005; Moscardelli et al., 2006; Moscardelli and Wood, 2008; Alves, 2010; Armitage et al., 2009; Jackson and Johnson, 2009; Olafiranye et al., 2013). Armitage et al. (2009) further established a surface hierarchy based on the vertical and lateral scale of topographic irregularities on MTD top surfaces (Tiers 1 to 3; Fig. 1.9). Tier 1 relates to the presence of topographic features of several meters in their horizontal and vertical dimensions, and is associated with cohesive freezing (Embley, 1980) or buckling of MTDs (Olafiranye et al., 2013). Tier 2 is one order of magnitude larger (i.e., tens of metres) in the two dimensions than Tier 1. Features associated with Tier 2 include rafted blocks with different size(s),
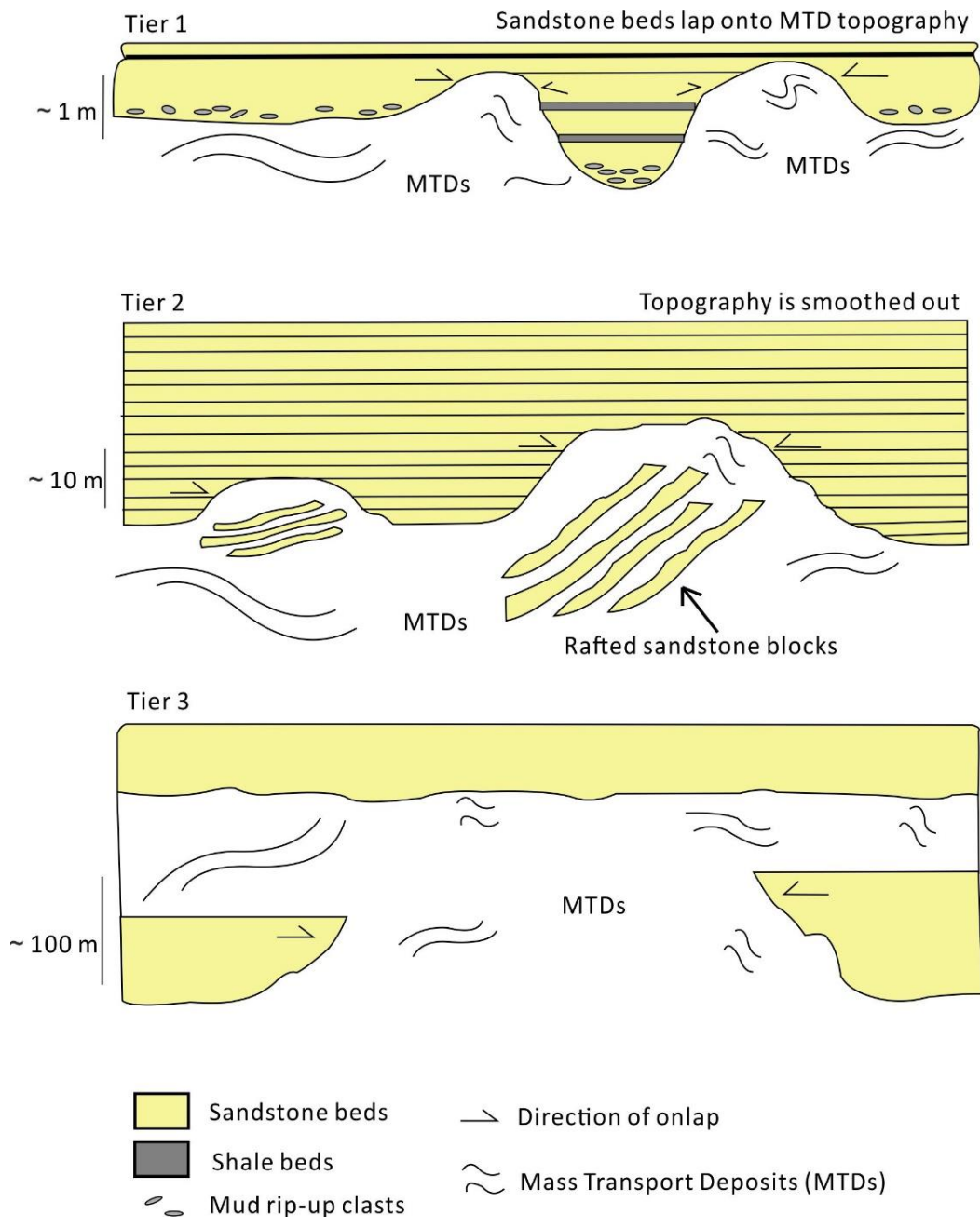
Figure 1.9. Conceptual diagram showing MTD surface-topography hierarchy (from Armitage et al., 2009). Three distinct tiers are identified based on the vertical and lateral scale of the irregularities on MTDs top surfaces: Tier 1 (metres to several metres), Tier 2 (10 m to several tens of metres), and Tier 3 (100m to several hundreds of metres).

and the degree to which they protrude above the top surface at the time of deposition, being important to analyse their impact on subsequent depositional systems (Armitage et al., 2009; Olafiranye et al., 2013). Tier 3 is hundreds of metres or more in at least two dimensions, and is interpreted to be the result of individual MTDs (or outsized rafted blocks) and large-scale hummocky topography on the MTD top surface (Armitage et al., 2009). Such a topographic hierarchy leads to diverse sediment distribution patterns (Armitage et al., 2009), as variations in the volume of accommodation space on top of MTDs often depend on the internal structure of the MTDs; particularly on the distribution of megaclasts, or blocks, and orientation and scale of faults within MTDs (Armitage et al., 2009; Alves 2010; Olafiranye et al., 2013; Ortiz-Karpf et al., 2015; Kneller et al., 2016). Folds and pressure ridges within MTDs also contribute to the generation of irregularities on the top surfaces of MTDs (Olafiranye et al., 2013; Kneller et al., 2016).

In addition, turbidity currents can deposit upstream and above MTDs (e.g. Jacobi, 1976; Jansen et al., 1987; Dam and Sønderholm, 1994; Henrich et al., 2008; Bernhardt et al., 2012; Ortiz-Karpf et al., 2015; Corella et al., 2016) or, instead, can be erosive to create large-scale scours (e.g. Shultz et al., 2005). Furthermore, turbidity currents can be diverted by topographic highs created by MTDs, leading to the generation of new sediment routes (e.g. Droz and Bellaiche, 1985; Hansen et al., 2013; Masalimova et al., 2015; Kertznus, 2009; Corella et al., 2016). Large-scale mass-wasting events can, therefore, modify the geometry of sedimentary basins and result in rapid shifts in the location of depocentres on continental slopes (Lucente and Pini, 2008). Kneller et al. (2016) further pointed out that the deflection (and reflection) of turbidity currents, and associated erosion, bypass, and deposition processes, are controlled by: a) the scale and geometry of MTD-associated topographic relief, and b) turbidity currents properties, e.g. thickness, grain-size distribution, and variations in the vertical density of flows (Kneller et al., 2016; Kneller and McCaffrey, 1999).

Previous studies focused mainly on the channel location and pathways influenced by MTDs (e.g. Kertznus, 2009; Hansen et al., 2013; Masalimova et al., 2015; Kneller et al., 2016; Corella et al., 2016), but less attention has been paid to the initiation and development of submarine channels affected by MTD-related topography. The presence of MTDs at the base of channel systems has been documented on both seismic (e.g. Deptuck et al., 2003; Mayall et al., 2006) and outcrop data

(e.g. Cronin et al., 2005b; Macauley and Hubbard, 2013; Bain and Hubbard, 2016), leading some authors to suggest that seafloor roughness produced by mass-wasting processes can capture and accelerate turbidity currents, facilitating the formation of channels (e.g. Deptuck et al., 2003; Gee et al., 2007; Abdurrokhim and Ito, 2013). In fact, flow-capture processes associated with mass wasting have recently been documented in the Gulf of Mexico and the Nile Delta (e.g. Kertznus, 2009; Kneller et al., 2016). For example, evacuation zones created by mass failure on the upper and middle slope can capture flows derived from shelf areas, focusing subsequent flows into conduits created by mass-failure events (Hackbarth and Shew, 1994; Shultz et al., 2005; Kneller et al., 2016). However, the role of mass-wasting processes in channel initiation and development is still poorly understood due to the lack of good-quality seismic and stratigraphic data.

1.7 The role of tectonic structures in submarine-channel evolution

1.7.1 The responses of submarine channels to tectonic structures

The behaviours of turbidity currents, such as erosion, bypassing or deposition, are closely related to variations in seafloor gradient, the development of submarine channels is thus strongly influenced by variable seafloor topography generated by active faults, folds, and gravity tectonics such as mud and salt diapirs (e.g. Graham and Bachman, 1983; Droz and Bellaiche, 1985; Cronin, 1995; Pirmez et al., 2000; Huyghe et al., 2004; Ferry et al., 2005; Gee and Gawthorpe, 2006; Mayall et al., 2006, 2010; Clark and Cartwright, 2011). Studies of channel adjustment in response to tectonic structures commonly help to reconstruct the deformation history of these structures and predict sediment distribution patterns on continental slopes.

A wide variety of submarine-channel responses have been documented in the literature. For example, Clark and Cartwright (2009) identified four types of responses of submarine channels to tectonic structures: confinement, diversion, deflection and blocking (Fig. 1.10). Detailed responses of submarine channels to seafloor deformation induced by tectonic structures, documented by previous studies, are as follows:
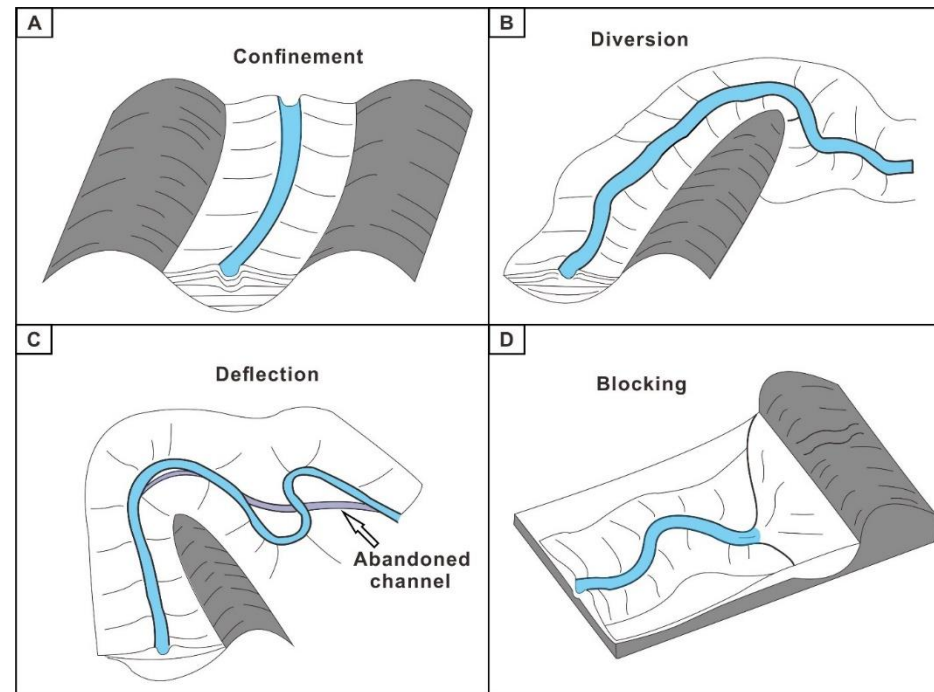
Figure 1.10. Schematic representation of the four end-member interaction between submarine-channel development and underlying deformation (from Clark and Cartwright, 2009). A: Confinement is defined as the restriction of channel courses and channel deposits because of pre-existing structures. B: Diversion is defined as changes in channel courses due to pre-existing structures obstructing flow pathways by modifying the seafloor gradient. C: Deflection is defined as progressive shifts in channel courses away from adjacent growing structures. D: Blocking is defined as termination of channel courses due to structures orientated at a high angle to channel courses.

1.7.1.1 Variations in channel pathways

Active tectonic structures change seafloor gradient by generating topographic highs and lows. Turbidity currents are preferentially transported in a down-dip direction towards topographic lows, and the diversion and deflection of channels caused by structures have been widely documented in the literature (e.g. Cronin, 1995; Posamentier and Kolla, 2003; Gee and Gawthorpe, 2006; Mayall et al., 2006, 2010; Clark and Cartwright, 2009; Zucker et al., 2017). In some cases, submarine channels can be confined by fault-related topography and their pathways can, as a result, show similar orientations to the faults (e.g. Antobreh and Krastel, 2006; Chiang et al., 2006; Clark and Cartwright, 2009).

1.7.1.2 Variations in channel morphology

Variations in channel gradient and the presence of knickpoints are widely documented along channel pathways near tectonic structures (e.g. Pirmez et al., 2000; Huyghe et al., 2004; Ferry et al., 2005; Mitchell, 2006; Heiniö and Davies, 2007; Georgiopoulou and Cartwright, 2013). As channels attempt to reach the equilibrium profile by incision or aggradation due to base-level change caused by tectonic deformation, increases in channel gradient and convex-upward longitudinal profiles are commonly observed near active uplifting structures such as fold and thrusts faults (e.g. Huyghe et al., 2004; Deptuck et al., 2007; Heiniö and Davies, 2007; Noda et al., 2008). They are interpreted to result from deep incision of turbidity currents in response to local uplift (Huyghe et al., 2004; Deptuck et al., 2007; Noda et al., 2008).

In addition to channels gradient, variations in channel sinuosity and dimension have also been associated with tectonic structures (e.g. Pirmez et al., 2000; Deptuck et al., 2007; Clark and Cartwright, 2011; Posamentier and Kolla, 2003). For example, a narrow channel with relatively high sinuosity was observed downstream of a sill (i.e. a horizontal or gently-dipping sheet intrusion of igneous rock) when compared to upstream areas (Posamentier and Kolla, 2003). Mayall et al. (2006) documented a narrower and deeper channel system when crossing an anticline.

1.7.1.3 Variations in the architectural elements within channels systems

Erosion and deposition associated with gradient changes caused by active tectonic deformation, lead to variations in the architectural elements of submarine channel systems. For instance, erosional terraces may be formed due to channel incision caused by tectonic uplift (e.g. Pirmez et al., 2000; Deptuck et al., 2003; Huyghe et al., 2004; Noda et al., 2008), whereas bank failures may be triggered by fault activity (e.g. Antobreh and Krastel, 2006). Additionally, variations in levee morphology and distribution have been documented next to tectonic structures (e.g. Wood and Mize-Spansky, 2009; Catterall et al., 2010; Clark and Cartwright, 2009, 2011). Wood and Mize-Spansky (2009) found that the morphology of channel levees is associated with the regional tilting directions of basins in the Caribbean Sea. Levees are higher and wider on the south side than on the north side of channel, with regional basin slope tilting southward (Wood and Mize-Spansky, 2009). In addition, Clark and Cartwright (2011) show that levee morphology and distribution is also controlled by deformation patterns of adjacent structures (Fig. 1.11). For example, the internal reflections of levees downlap onto the flank of uplifted structures when the uplift occurs before channel development, whereas levees are folded due to adjacent growing structures when the deformation of structures coeval with or occur after channel development (Clark and Carwright, 2011) (Fig. 1.11).

Because submarine channels tend to migrate to topographic lows when relative seabed uplift occurs (e.g. Clark and Carwright, 2009; Mayall et al., 2010), the architecture of channel systems usually changes with the patterns of deformation (e.g. deformation rate) near the sea floor and the frequency and/or magnitude of turbidity currents (e.g. Kane et al., 2010, 2012) (Fig. 1.12). For instance, submarine channels developed on the flanks of salt structures avulse downslope during salt growth (Fig. 1.12A-D), and show aggradation patterns during periods of salt withdrawal and subsidence (Kane et al., 2010, 2012) (Fig. 1.12F).

1.7.1.4 Channel spacing

Gamboa et al. (2012) documented a close relationship between the topographic confinement imposed by growing salt diapirs and channel spacing. They found that channel spacing decreases
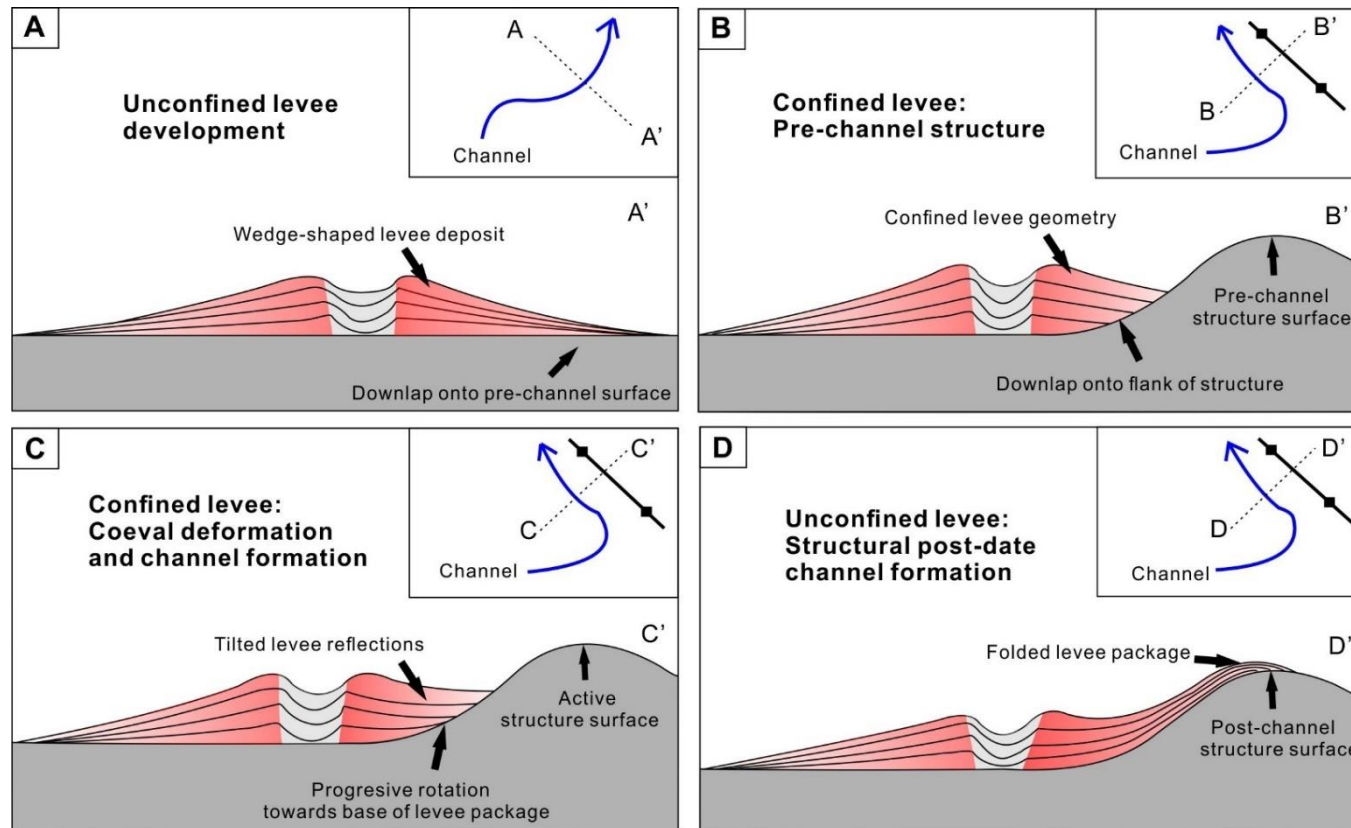
Figure 1.11. Schematic representation of the responses of levee morphology to the effects of tectonic deformation (from Clark and Cartwright, 2009).
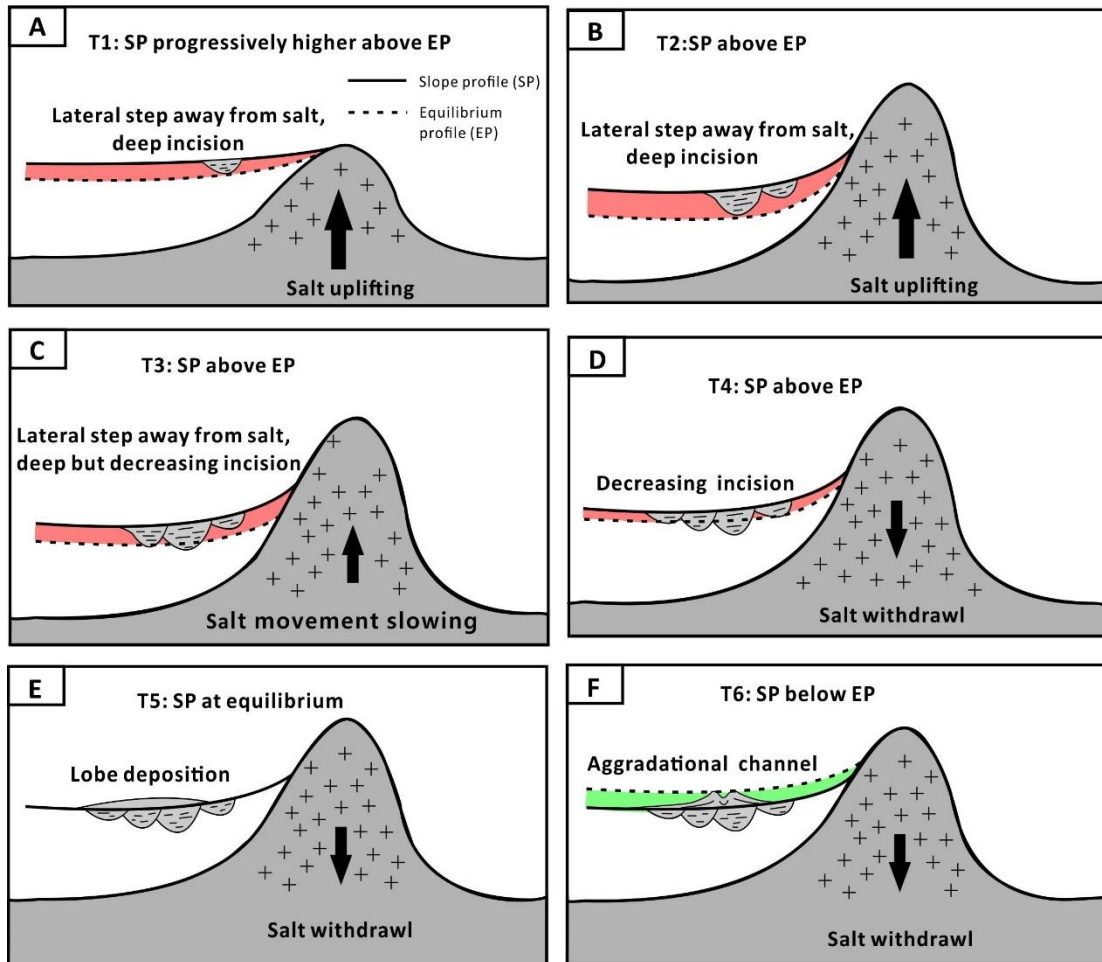
Figure 1.12. Schematic illustrations showing channel evolution in response to the movement of nearby salt structures with time (T1-T5). SP indicates actual channel slope profile, and EP is the equilibrium profile channels attempt to reach. Channel incision and aggradation are related to the relative movement of salt structure. Its longitudinal profile moves downwards (A-D) or upwards (F) in order to achieve a stable equilibrium profile (from Kane et al., 2012).

from unconfined regions of the slope to topographically confined regions delimited by salt diapirs (Gamboa et al., 2012).

1.7.1.5 Factors controlling channel response(s) to tectonic structures

Several factors are related to channel adjustment in response to tectonic structures: 1) the location, geometry, number, and deformation time and rates of tectonic structures, and 2) the relative rates of channel deposition and erosion (Clark and Cartwright, 2011; Mayall et al., 2010; Kane et al., 2012; Oluboyo et al., 2013). For example, whether channels are able to cut through a growing structure such as folds is dependent on the uplift rate of structures, the susceptibility of the substrate to erosion and the erosive power of turbidity currents associated with the frequency, vigour and duration of flows (Huyghe et al., 2004; Mitchell et al., 2006; Noda et al., 2008; Mayall et al., 2010; Clark and Cartwright, 2011; Chiang et al., 2012; Jolly et al., 2016). Submarine channels deflect away from growing structures if the incision rate of turbidity currents cannot keep pace with the uplift rate of the structures (e.g. Clark and Cartwright, 2009; Mayall et al., 2010). However, if the incision rate of turbidity currents is higher than the rates of tectonic uplift, channels will cut across structures such as growing folds (e.g. Morgan et al., 2004; Huyghe et al., 2004; Mayall et al., 2010; Jolly et al., 2016).

1.7.2 The role of salt tectonics on submarine channels

Salt structures such as salt diapirs and salt walls, and associated faults are widely documented on continental margins around the world. Key study areas where salt structures have been documented together with submarine channels include the Gulf of Mexico (e.g. Tripsanas et al., 2004; Carter et al., 2016), the Nile fan (e.g. Loncke et al., 2009), offshore Angola (e.g. Gee et al., 2006; Oluboyo et al., 2013), and offshore Brazil (e.g. Alves et al., 2009; Gamboa et al., 2012; Gamboa and Alves, 2015). Salt structures modify the seafloor morphology by generating topographic highs and lows, leading to variations in seafloor slope. These variations, in turn, result in major changes in sediment routes and sediment distribution (e.g. Gamboa and Alves, 2015; Alves et al., 2009; Gee

et al., 2006; Mayall et al., 2010; Oluboyo et al., 2013). In the Espírito Santo Basin of SE Brazil, for example, Gamboa and Alves (2015) analysed the spatial and dimensional relationships of depositional elements in the basin. They found that the dimension of depositional elements changes with the distance between these elements and evolving salt ridges. Next to salt ridges, there are larger variations in dimension, and lower continuity of depositional elements such as submarine channels and turbidite lobes (Gamboa and Alves, 2015).

Apart from the location and distribution of salt structures, the relative movement of salt structures also affects depositional elements on other continental margins. For instance, Kane et al. (2012) suggest that the cycles of salt growth and withdrawal may result in distinct cycles of channel evolution, from entrenched channels and/or channels migrating away from growing structures, to marked backfilling when salt growth slows down and ceases. Previous studies indicated that interactions between salt structures and turbidity currents are associated with the size, shape, uplift rate of salt structures, incidence angle between regional flow direction and structural strike (Mayall et al., 2010; Kane et al., 2012; Oluboyo et al., 2013; Carter et al., 2016).

1.8. Flows within submarine channels

Turbidites, which are deposits of turbidity currents, are characterised by graded bedding (Kuenen and Migliorini, 1950) and Bouma sequence that consists of five divisions (A, B, C, D, and E) (Bouma, 1962). Such deposits have been extensively described around the world from outcrops (e.g. Kuenen and Carozzi, 1953; Walker, 1975; Mutti and Ricci Lucchi, 1975; Pickering et al., 1986; Shanmugam and Moiola, 1988; Cronin, 1994; Piper et al., 1999; Abreu et al., 2003; Wynn et al., 2007). Many numerical and experimental studies were also conducted to provide insights into flow processes of turbidity currents within submarine channels (e.g. Imran et al., 1999; Peakall et al., 2000, 2007; Pirmez and Imran, 2003; Kane et al., 2008). Despite the fact that debris-flow deposits were also recognised in ancient channel systems at outcrop (e.g. Mutti and Ricci Lucchi, 1975; Pickering et al., 1986; Shanmugam and Moiola, 1988; Cronin, 1994; Clark and Pickering, 1996; Beaubouef, 2004; Mayall et al., 2006), the majority of channel-fill deposits is turbidity current-

deposits, suggesting that turbidity currents are predominant within the submarine channels.

Three main types of initiation processes for turbidity currents have been proposed by previous studies (e.g. Normark and Piper, 1991; Piper and Normark, 2009; Meiburg and Kneller, 2010): a) transformation of failed sediment, which can be triggered by earthquakes and volcanic eruptions, b) hyperpycnal flows from rivers, and c) resuspension of sediment near the shelf edge due to oceanographic processes (e.g., storms, tides and internal waves).

Direct measurements of turbidity currents have been conducted in submarine canyons and channels (e.g. Hay, 1987; Khripounoff et al., 2003; Xu et al., 2004). They show distinct turbidity currents within submarine canyons and channels such as 1) high-magnitude and short duration gravity currents; 2) low-magnitude and high-frequency currents; 3) erosive and sandy turbidity currents; 4) sluggish and muddy turbidity currents (Arzola et al., 2008; Vangriesheim et al., 2009; Mas et al., 2010; Mulder et al., 2012; Jobe et al. 2011). Conway et al. (2012) suggest that flow properties vary not only from one event to another, but also within the time frame of single event.

Apart from turbidity currents, low-energy, tide-initiated hydrodynamic events have also been observed within canyons (Masson et al., 2011; Mulder et al., 2012). Normandeau et al., (2014) further suggested that slope failure and internal tides/waves are frequent enough to remobilise in-situ sediment within the canyon. Consequently, gravity flows sourced from adjacent shores and shelves may not a prerequisite for the activity of canyons.

1.9 Stratigraphic evolution of submarine channels

The stratigraphic evolution of submarine channels from early incision to later-stage aggradation has been documented from both outcrop studies (e.g. Normark and Piper, 1969; Walker, 1975; Mutti and Normark, 1987; Clark and Pickering, 1996; Cronin, 1994; Hodgson et al., 2011; Figueiredo et al., 2013; Hubbard et al., 2014; Covault et al., 2016) and subsurface data (e.g. Samuel et al., 2003; Deptuck et al., 2003, 2007; Cross et al., 2009; Janocko et al., 2013). This cycle of erosion and deposition may occur repeatedly during channel evolution (e.g. Mutti and Normark, 1987; Cronin, 1994; Clark and Pickering, 1996). In addition, a period of sediment bypass has been

interpreted between early erosion and final deposition based on the internal architecture of channel-fill deposits (e.g. Walker, 1975; Mutti and Normark, 1987, 1991; Cronin, 1994; Beaubouef, 2004; McHargue et al., 2011; Stevenson et al., 2013; Hubbard et al., 2014).

McHargue et al. (2011) suggest that the cycle of degradation-aggradation is caused by waxing-waning cycles, which alter flow energy, the volume and calibre (i.e. grain size) of turbidity currents, and lead to the rise and fall of the equilibrium profile of submarine channels (Fig. 1.13). For example, increases in flow thickness and density remove accommodation space for sediment, leading to the fall of equilibrium profile and the generation of erosional channels (Fig. 1.13A). Decreases in flow thickness and density create accommodation space and result in the rise of equilibrium profile and the generation of aggradational channels (Kneller, 2003; McHargue et al., 2011) (Fig. 1.13C).

There are a range of external and internal factors, such as sediment supply, sea-level changes and local basin morphology, suggested as important for channel evolution (e.g. Shanmugam and Moiola, 1982; Samuel et al., 2003; Posamentier and Kolla, 2003; Kneller, 2003; Kolla, 2007; McHargue et al., 2011) (Fig. 1.14). For example, flows tend to be sand rich during relative sea-level rises, resulting in degradation, while flows tend to be mud rich during relative sea-level falls, leading to aggradation (Posamentier and Kolla, 2003). However, modelling results from Sylvester et al. (2011) suggest that the architectures of most submarine channel-levee systems can also reflect a simpler model involving a single channel form that evolves from incision and migration to aggradation without large temporal variations in flow magnitude. Sylvester and Covault (2016) further found that internal factors such as the process of meander cutoff, can lead to the retreat of knickpoints and complexity of submarine-channel architectures.

The architecture of channel systems is associated with the interaction between lateral and vertical movements in individual channel element (e.g. Mutti and Normark, 1987; Weimer, 1991; Clark and Pickering, 1996; Deptuck et al., 2003; Sylvester et al., 2011; Jobe et al., 2016). Lateral migration with no or little aggradation at early stage of channel evolution has been recorded in West Africa (e.g. Deptuck et al., 2003; Janocko et al., 2013; Covault et al., 2016). This type of lateral migration led to the formation of highly-amalgamated sheet deposits at the base of channel systems (e.g. Sameul et al., 2003; Mayall et al., 2006) and suggests that the channels are in equilibrium state,
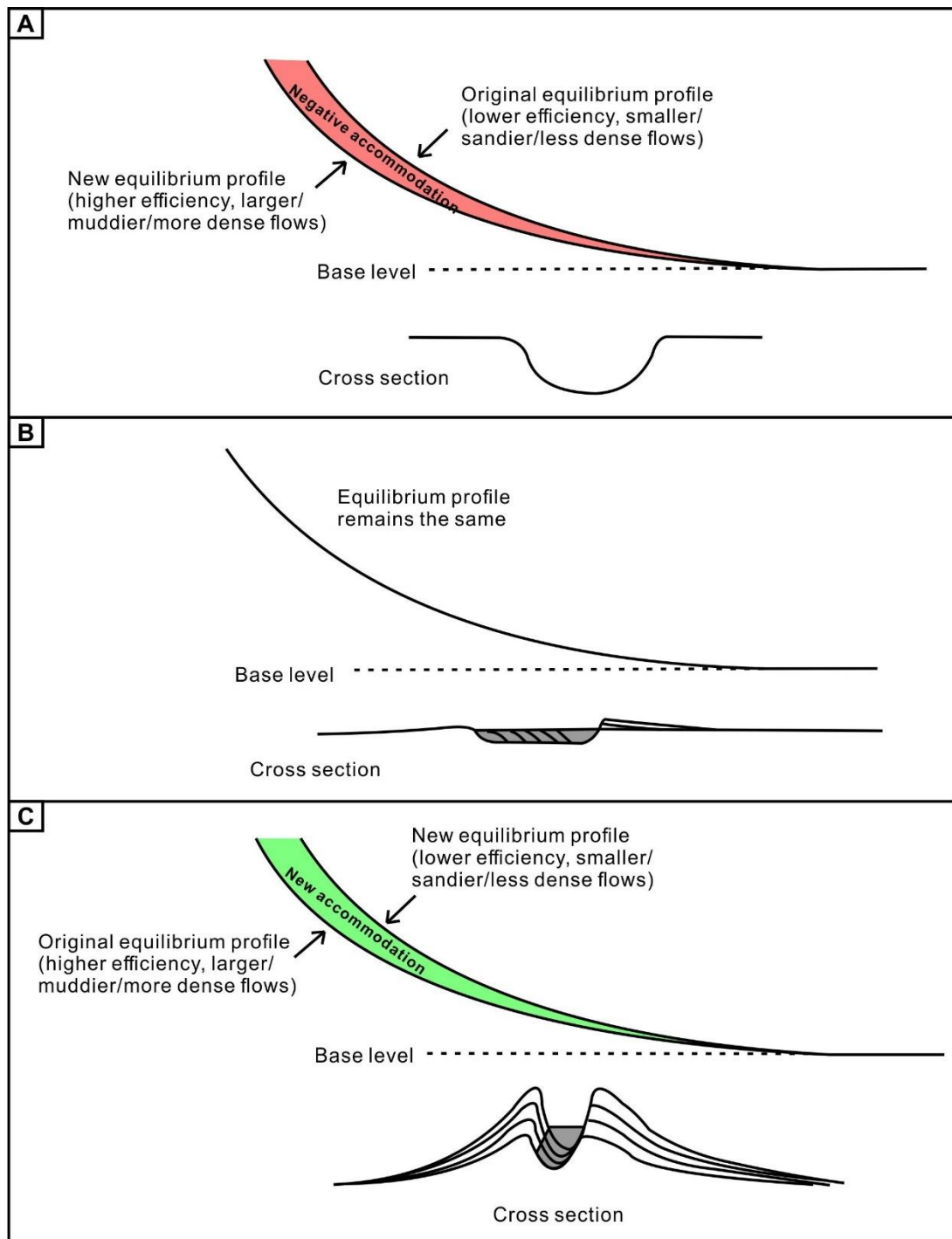
Figure 1.13. Schematic diagram showing the response of submarine channels to variations in sediment supply (Modified from Kneller, 2003).
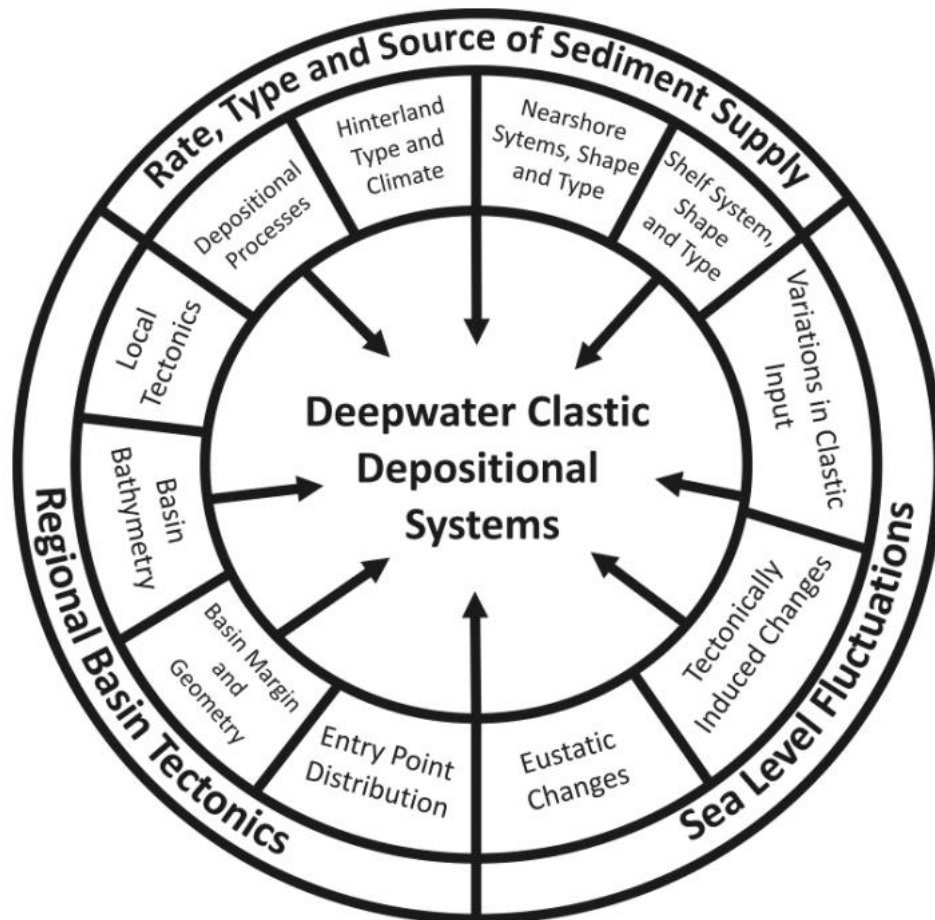
Figure 1.14. Flow chart summarising external and internal controls on deep-water depositional systems (Richards et al., 1998).

in which state channel migrates within a plane parallel to the equilibrium profile (Kneller, 2003). However, lateral migration may occur at any stage of channel evolution (e.g. Samuel et al., 2003; Deptuck et al., 2007; Janocko et al., 2013; Jobe et al., 2015), and occur with either degradation (e.g. Jobe et al., 2015) or aggradation (e.g. Kolla et al., 2001; Deptuck et al., 2007; Janocko et al., 2013). Such variations in the occurrence of lateral migration make the drivers of lateral migration difficult to understand.

1.10 Rationale

Despite the significant advances made in the past decades, controlling factors for stratigraphic evolution of submarine channels are still under debate, such as the cause for a switch from incision to aggradation and the cause for lateral channel migration (e.g. McHargue et al., 2011; Sylvester et al., 2011). The quantitative analysis of temporal stacking patterns of submarine channels is a key point to improve our understanding of external and internal factors affecting channel evolution (e.g. Jobe et al., 2016).

This work provides an example of a submarine channel system developed near the modern sea floor. This submarine channel system preserved the most recent erosional and depositional features without experiencing the effect of diagenesis (e.g. compaction). High resolution 3D seismic data used in this study allows a detailed characterisation of the modern channel system in terms of its morphology and stacking patterns. Studies of modern channel systems often provide valuable insights on ancient submarine channel systems. In addition, quantitative analyses of modern submarine channel systems help to understand and predict variations sediment budgets at different locations of sediment routing systems, as well as the prediction of reservoir distribution in deep-water margins.

1.11 Aims of this study

The aims and objectives of this thesis are as follows:

1) To document the quantitative seismic geomorphology of submarine channel systems by:

   A) Conducting quantitative analyses of submarine channel systems at channel and valley scales.

B) Undertaking a comparison between the studied channel system and other channel systems around the world.

2) To investigate the evolution of submarine channel systems by:

A) Identifying architectural elements within the study channel system developed on the seafloor.

B) Investigating temporal variations in the morphology and architectures of channel systems.

C) Evaluating the relationship among the morphology and internal architectures of the channel systems.

3) To understand the controlling factors for the evolution of submarine channel systems by:

A) Assessing the direct and indirect impacts of salt diapirs on channel evolution.

B) Assessing the role of MTD-associated topography in turbidity currents and channel evolution.

C) Investigating other possible geological and oceanographic factors controlling channel evolution.

Chapter 2

Seismic data and methods

2. Seismic data and methods

2.1 Introduction

This chapter presents the seismic reflection data used in this study, including the principles behind the acquisition, processing and interpretation of seismic-reflection data, and is followed by a brief introduction of the seismic dataset used in this thesis.

2.2 Seismic-data acquisition

Marine seismic data are acquired by creating an acoustic pulse using airgun arrays on ships (Fig. 2.1). The sound wave travels down through the sea water into subsurface rocks. Some of the sound waves are reflected back to the sea surface whenever interfaces with changes in physical properties are found (e.g. density and velocity changes). The reflected waves are then received and recorded by a series of hydrophones on the ships (Fig. 2.1). The time seismic wave travel from the source (i.e. airguns) to the receivers (i.e. geophones) is measured in two-way travel time (TWTT).

2.3 Seismic waves

Despite many types of waves that travel through the Earth, most seismic datasets use compressional waves or P-waves. The key variables defining the shape of a wave are amplitude, period, frequency and wavelength (Fig. 2.2). The wave display changes in amplitude, which can be represented by a maximum (i.e. peak) and a minimum value (i.e. trough) (Fig. 2.2). The separation (in time) between two successive peaks or troughs is the wave period (T) (Fig. 2.2). The frequency of a wave is the number of cycles, i.e. peaks or troughs that pass through a specific point in a specific period. For example, 40 Hz indicates that 40 peaks or troughs pass through a specific point in one second. The wave frequency can also be shown as the inverse of the period:

$$F = 1/T \text{ --(Eq. 2.1)}$$
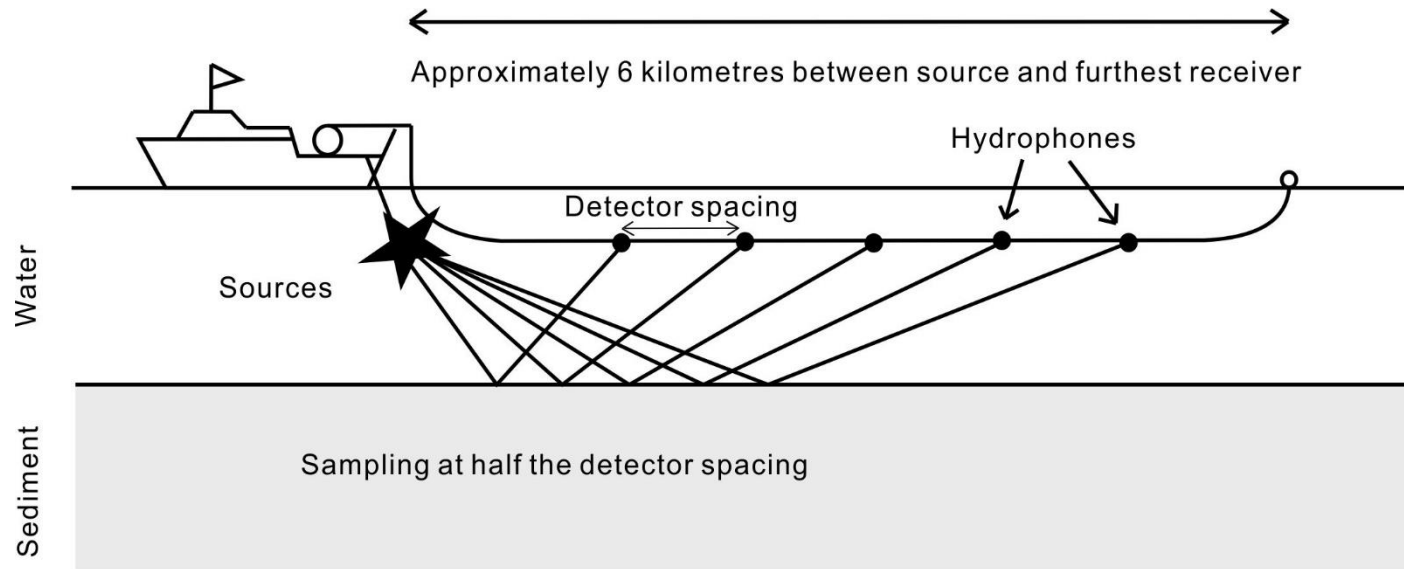
Figure 2.1. Schematic diagram showing the common geometry of a marine seismic survey. An acoustic source mounted on a boat emits a sound wave into the water. When the acoustic properties of the rock change, the P-waves are reflected back to the surface and detected by hydrophones in a long cable towed behind the boat (streamer) (modified from Bacon et al. 2003).
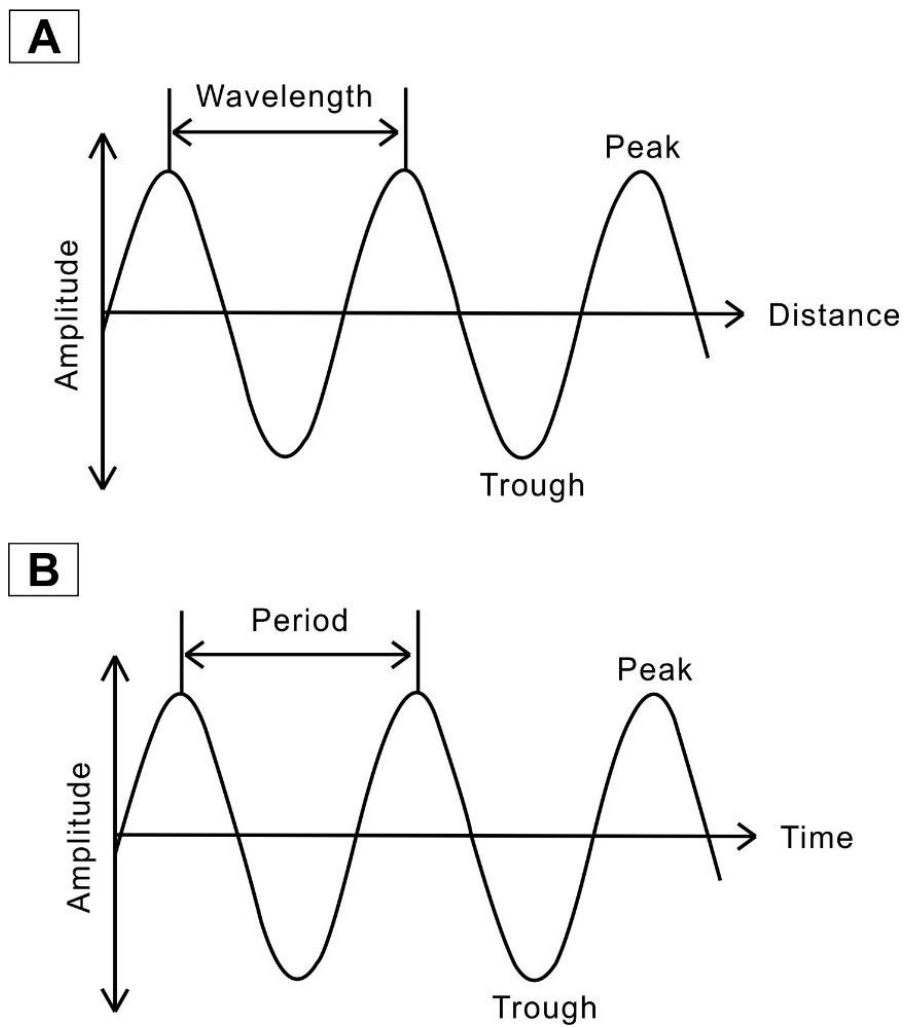
Figure 2.2. A simple cosine geometry illustrating traveling waves in distance A) and time B) (from Hart, 2011).

The wavelength is the distance between successive repetitions of the waveform (e.g., troughs or peaks) (Fig. 2.2). It is a function of the frequency (f) and velocity (v) in which waves travel through rocks:

$$\lambda = v/f \quad \text{---}\textbf{(Eq. 2.2)}$$

However, as seismic waves commonly contain a range of frequencies, the dominant frequency is generally used to calculate wavelength.

The energy of the P-waves is reflected at interfaces where changes in acoustic impedance are recorded (Z). Acoustic impedance is a function of the rocks' P-wave velocity (v) and density (ρ):

$$Z = v \times \rho \quad \text{---}\textbf{(Eq. 2.3)}$$

In this equation, velocity and density are associated with rock physical properties such as texture, porosity and fluid content.

The relative amplitude of the reflected wave can be predicted by the zero-offset reflection coefficient (R_0):

$$R_0 = \frac{Z_2 - Z_1}{Z_2 + Z_1} \quad \text{---}\textbf{(Eq. 2.4)}$$

where Z_1 and Z_2 are the acoustic impedances of the layer above and below the interface, respectively.

2.4 Data resolution

The vertical resolution of seismic data is defined as the vertical distance between two seismic reflections that can be resolved separately, and this separation relates to the distance between two interfaces (Hart, 2011). A value of $\lambda/4$ is generally considered to define the vertical resolution of seismic data (Fig. 2.3). Therefore, the higher the frequency and lower the velocity of the wave, the

Bed thickness
> Tuning thickness

Bed thickness
= Tuning thickness

Bed thickness
< Tuning thickness

Limit of separability

No separability

$$\frac{\lambda}{4} = \frac{T}{2}$$

Limit of visibility

Amplitude boosted
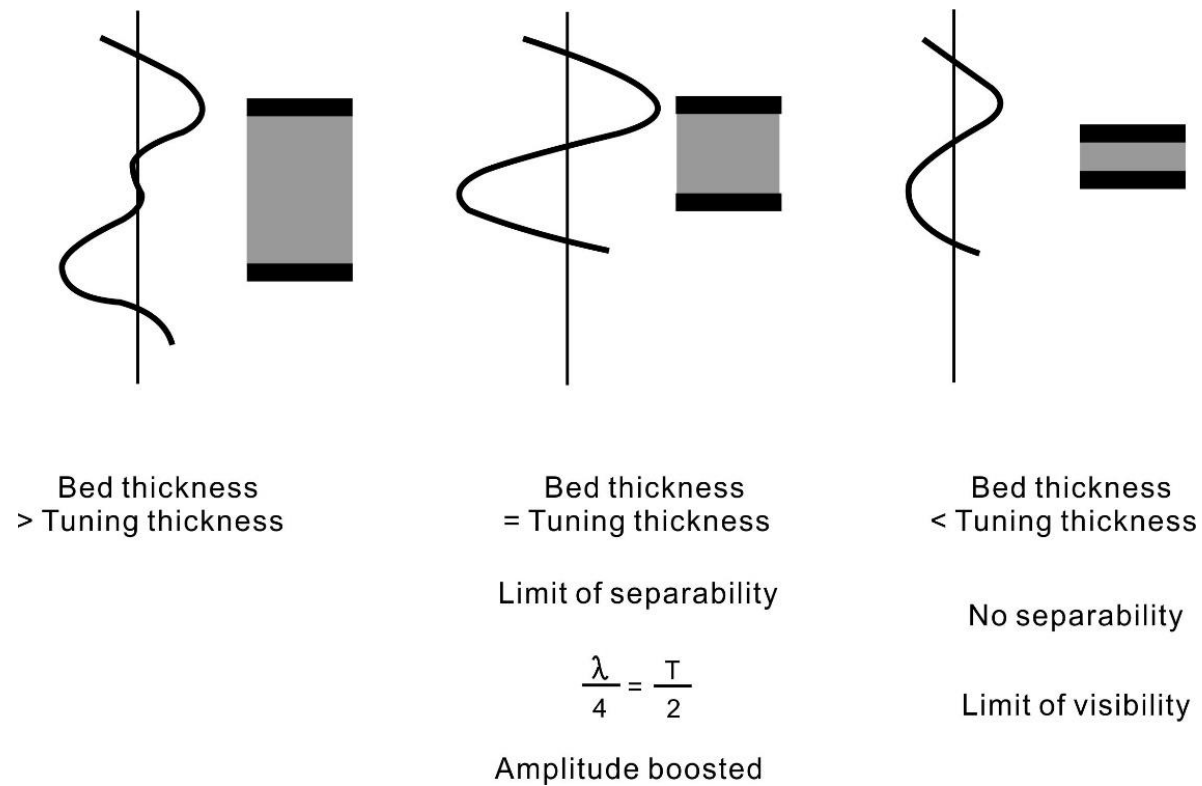
Figure 2.3. The relationship between bed thickness and tuning thickness. The tuning thickness is the bed thickness that two reflections become indistinguishable in time. The vertical resolution is related to the interaction between two closely spaced wavelets (from Brown, 2004).

better will be the vertical resolution.

However, as velocity increases and frequency decreases with depth, vertical resolution decreases. In addition, constructive interference or tuning occurs when the interfaces of layers spaced more closely than $\lambda/4$, leading to the overlap of reflections and boosted seismic signals (Fig. 2.3).

Lateral resolution of seismic data is associated with the Fresnel zone (Fig. 2.4). Because the seismic energy travels as wave fronts, the region where the seismic energy is reflected constructively is known as the Fresnel zone. The width of an object equal or greater than the diameter of Fresnel Zone can be resolved in seismic data. The diameter of Fresnel zone depends on the average velocity down to a specific horizon (v), two-way travel time (t) and frequency (f) (Hart, 2011):

$$D_F = v\sqrt{\frac{t}{f}}$$ ---**(Eq. 2.5)**

2.5 Seismic-data visualisation

Three-dimensional (3D) seismic volumes can be considered as a series of data cubes, or voxels (Hart, 2000). Each voxel consists of four pieces of information: the x, y, and z showing the location and an amplitude value. The x-y dimension is associated with bin space during data acquisition and is represented by inlines and crosslines during interpretation, whereas the z dimension reflects the location in the depth direction (Hart, 2000). Arbitrary lines comprise a single transect or multiple transects extracted from the data set, in order to image structural or stratigraphic features oriented obliquely to the inline or crossline. Apart from seismic cross sections, 3D seismic data can also provide plan views of features by using time slices, and flattened time slices, allowing the detailed imaging of geological features.

For example, seismic attributes are extensively used in the seismic interpretation of stratigraphy, structural geology, and reservoir properties. Submarine channels can be clearly imaged on attribute maps because of their linear and sinuous aspects. In this thesis, dip, RMS amplitude and variance maps are used to document the variations in pathways of submarine channels.

Pre-migration Fresnel zone

$$= V \sqrt{\frac{T}{F}} = 2260 \text{ ft}$$

T = 2 s
F = 25 Hz
V = 8000 ft/s

V is average velocity

Post-migration Fresnel zone

$$\frac{\lambda}{4} = \frac{T}{4F} = 80 \text{ ft}$$
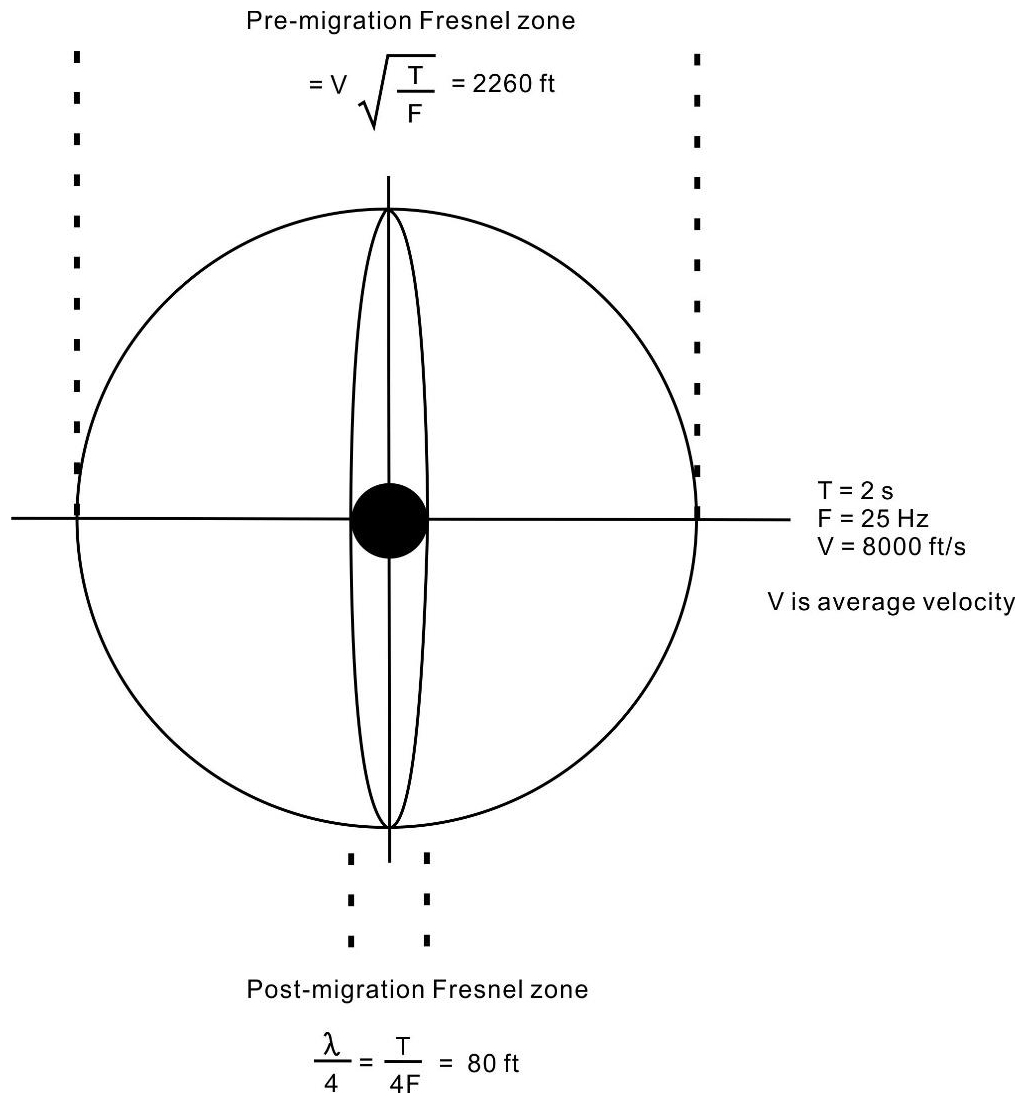
Figure 2.4. The effect of pre-and post-migration on Fresnel-zone size (from Brown, 2004).

Dip maps show gradient changes by comparing the time or depth value between adjacent points in 3D seismic data. It is a good indicator of slope changes in a reference horizon. The banks of submarine channel are highlighted in dip maps because they are generally steeper than the dip of adjacent strata (Fig. 2.5).

Amplitude maps highlight lateral variations in acoustic impedance that are related to changes in the rock physical properties and fluid content of the horizon (Brown, 2004). Root-Mean Square (RMS) amplitude maps highlight high-amplitude reflections on seismic data in comparison with low-amplitude 'background' strata. They can be extracted along a specific horizon or within a defined time window. Because the basal lags of submarine channels are commonly coarse-grained and generate high-amplitude reflections, submarine channels can be clearly identified on amplitude maps due to their high amplitude, sinuous reflections (Fig. 2.6).

Variance maps are calculated based on discontinuities by comparing how similar are adjacent waveforms in a picked horizon, in contrast with coherence map that calculates continuities of seismic data. They are generally used for imaging lateral extent of geological features. The discontinuities shown in the variance map may be stratigraphic (e.g. channels) or fault discontinuities. For example, channel banks are erosional truncations on seismic data, they can be well defined on variance maps based on the higher variance value of channel banks (Fig. 2.7). The variance map is generally extracted from a variance volume that computed based on a reference horizon. This reference horizon can be a time slice from seismic volume or a flattened interpreted horizon.

Isochron maps highlight the variations in thickness (in TWTT) between two reference horizons. They provide detailed information on the thickness and lateral extent of sedimentary units. For example, isochron maps were used to quantify variations in sediment dispersal patterns in the studied channel systems, and to assess the role of sediment supply from tributaries in the sediment distribution within the channel system.

2.6 Seismic-data interpretation

The mapping of structural and stratigraphic features is commonly undertaken by manual
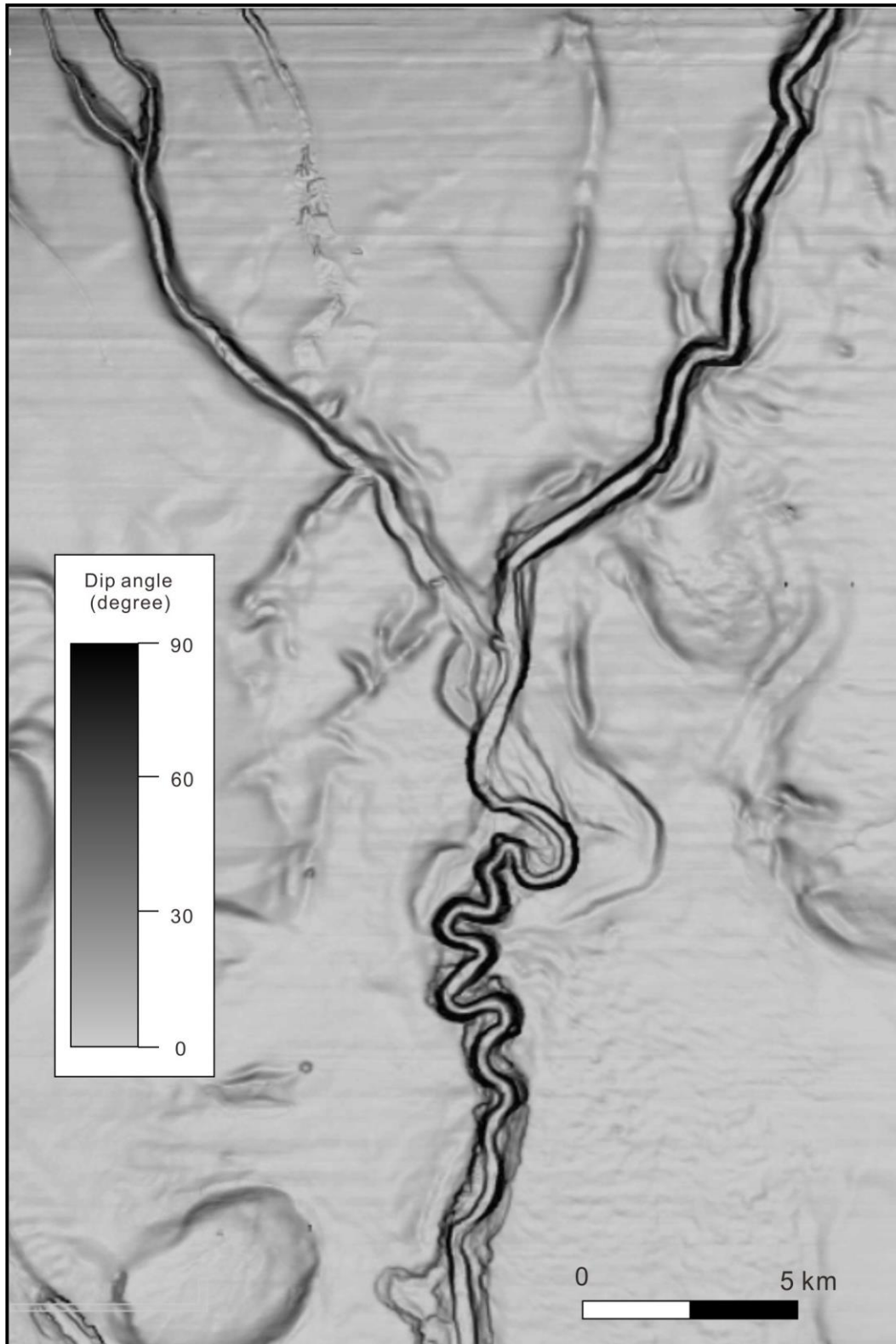
Figure 2.5. Dip map highlighting submarine channels with steep banks.
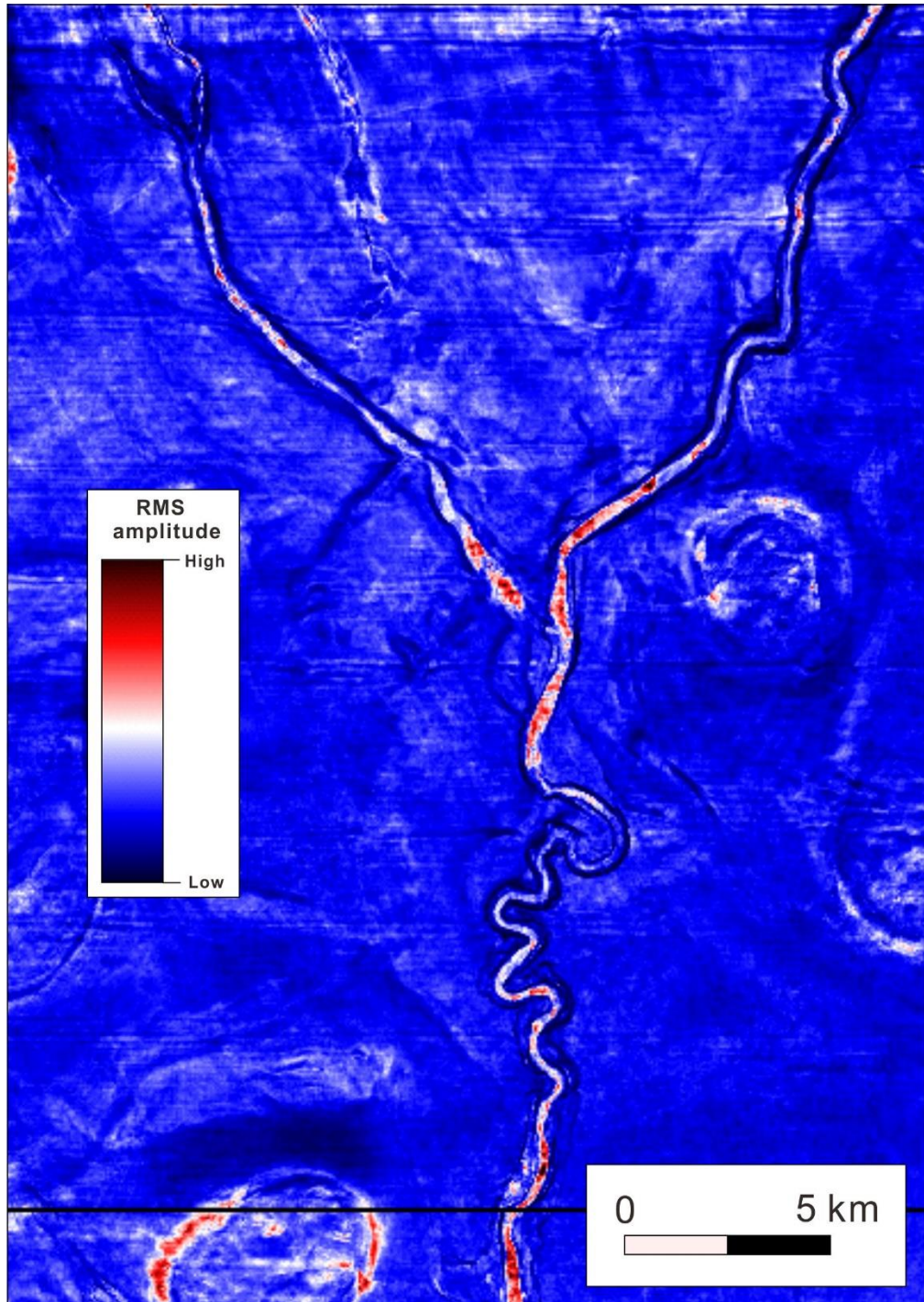
Figure 2.6. Root-Mean Square (RMS) amplitude map highlighting submarine channels with higher-amplitude reflections compared to lower-amplitude slope strata. High-amplitude reflections are also shown surrounding salt diapirs.
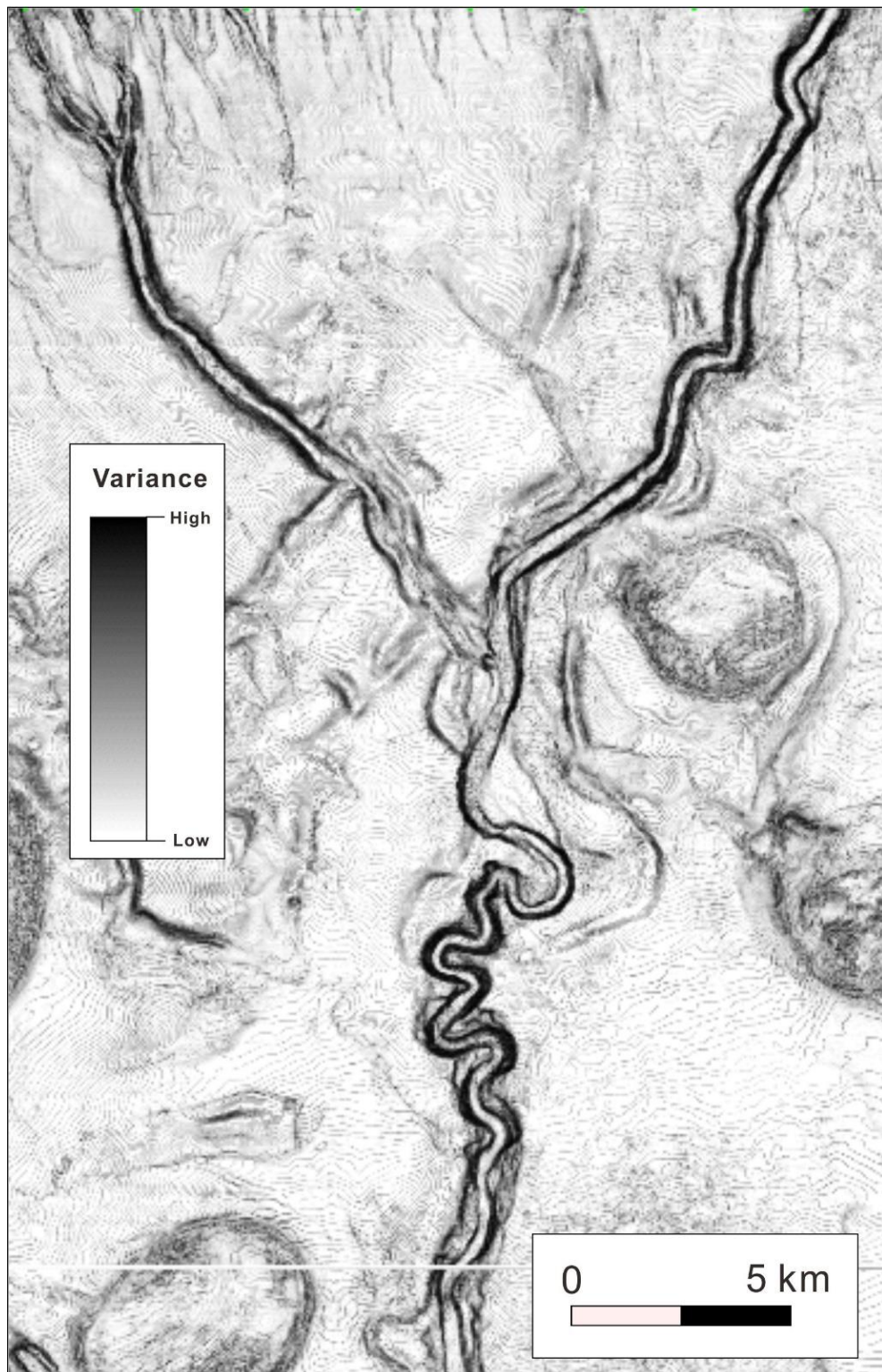
Figure 2.7. Variance map highlighting submarine channels with banks of higher variance.

picking and/or autotracking of relevant reflections, combined with an analysis of seismic facies based on the geometry, continuity and amplitude of reflections. The main principles of such an analysis follow concepts in Mitchum et al. (1977) (Fig. 2.8).

Four types of seismic facies associated with submarine channels were interpreted based on their seismic amplitude, reflection continuity, reflection geometry, and termination patterns against adjacent strata (Fig. 2.9). The interpretation of seismic facies was based on widely accepted criteria for deep-water settings (e.g. Posamentier and Kolla, 2003; Mayall et al., 2006; Catterall et al., 2010; Deptuck et al., 2003; Janocko et al., 2013).

Seismic Facies 1 is characterised by high-amplitude, continuous to discontinuous seismic reflections (Fig. 2.9A), and is usually confined within V- or U-shaped erosional surfaces (Fig. 2.9B–E). This facies is interpreted as comprising the basal lags of submarine channels (e.g. Deptuck et al., 2003; Mayall et al., 2006; Catterall et al., 2010). It corresponds to coarse-grained sediments accumulated at the base of submarine channels (e.g. McHargue and Webb, 1986; Mayall et al., 2006).

Seismic Facies 2 consists of low- to high-amplitude, subparallel and continuous seismic reflections (Fig. 2.9A). This facies may have different origins: channel deposits accumulated in a channel-abandonment stage (e.g. Deptuck et al., 2003; Catterall et al., 2010; Janocko et al., 2013), or overbank deposits, some of which show a wedge-shaped geometry (Fig. 2.9B–E). These latter are interpreted as levee deposits (e.g. Posamentier and Kolla, 2003; Deptuck et al., 2003; Catterall et al., 2010; Janocko et al., 2013).

Seismic Facies 3 is composed of variable-amplitude, chaotic, discontinuous seismic reflections (Fig. 2.9A). This facies represents mass-transport deposits (MTDs) and is attributed to processes such as slides, slumps and debris flows (e.g. Posamentier and Kolla, 2003; Mayall et al., 2006; Janocko et al., 2013). Blocks with high-amplitude, parallel reflections are observed in the MTDs (Figs. 2.9B and C).

Seismic Facies 4 is composed of low-amplitude, parallel, continuous seismic reflections interpreted as background hemipelagic sediment (Fig. 2.9).

Upper boundary

Erosional truncation

Toplap

Top concordance

Lower boundary

Onlap

Downlap

Base concordance

Figure 2.8. Stratal relationships within depositional sequences (from Mitchum, 1977). Erosional truncation highlights strata along a stratigraphic unconformity. Toplap highlights strata against an overlying surface. Top concordance represents strata that do not terminate against an upper boundary. Onlap shows horizontal strata terminate against an inclined surface. Downlap indicates strata terminate against an inclined surface. Base concordance shows strata do not terminate against a lower boundary.

Figure 2.9. A) Description and interpretation of seismic facies observed in the channel system. B, C, D, E) Uninterpreted and interpreted seismic sections highlighting the seismic facies interpreted in the channel system.

2.7 3D seismic volume used in the thesis

The interpreted 3D seismic volume is located in the northern part of the Espírito Santo Basin (Fig. 2.10). It covers an area of 1600 km^2.

The seismic data were acquired by a dual airgun array and a 6 x 5700 m array of streamers. The survey has a bin spacing of 12.5 m by 12.5 m and a 2 ms vertical sampling interval, later resampled at 4 ms together with the application of an anti-aliasing filter. Data processing included resampling, spherical divergence corrections, and zero-phase conversions undertaken prior to stacking, 3D prestack time migration using the Stolt algorithm, and one-pass 3D migration. The polarity of data is SEG normal i.e., positive amplitude reflections (red) on the seismic profiles represent an increase in acoustic impedance.

The vertical resolution of the data is ~10 m at the depth of analysis in this study, based on a dominant frequency of 40 Hz and a P-wave velocity of 1600 m/s for near-seafloor strata.

Petrel provided by Schlumberger is the software used for interpretation of seismic data in this thesis.
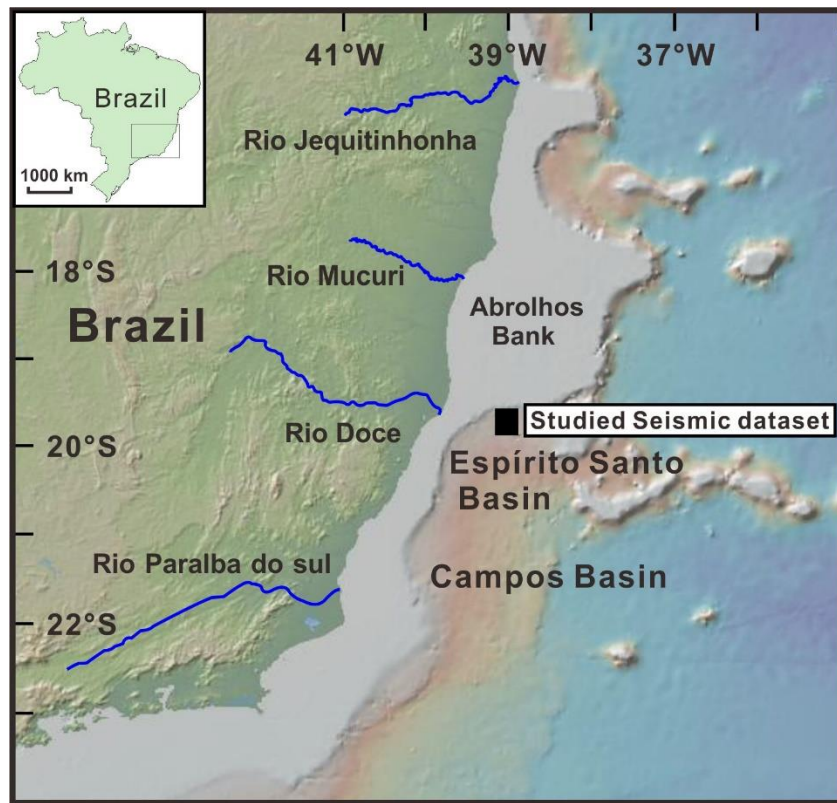
Figure 2.10. Regional map of the SE Brazilian margin (Bathymetric data from GeoMapApp, http://www.geomapapp.org; Amante and Eakins, 2009), showing the location of Espírito Santo Basin and the studied 3D seismic volume in the Espírito Santo Basin.

Chapter 3

Geological setting

3. Geological setting

3.1 Introduction

To better understand the impact of local geological setting on channel evolution, this chapter starts with geological setting of the Espírito Santo Basin, where study area is located (Fig. 3.1). This section includes: 1) tectono-sedimentary evolution of the Espírito Santo Basin; 2) salt tectonics in the Espírito Santo Basin; 3) submarine channel system in the Espírito Santo Basin. The second section of this chapter shows a brief introduction of study area, including: 1) seismic stratigraphy of study area, 2) salt tectonics in the study area, 3) seafloor morphology of study area, 4) studied channel system in the thesis, and 5) possible sediment sources for the seafloor channel.

3.2 Geological setting of the Espírito Santo Basin

3.2.1 Tectono-sedimentary evolution of the Espírito Santo Basin

The Espírito Santo Basin is located on the continental margin of SE Brazil in the area between the Abrolhos Bank and the Campos Basin (Fig. 3.1). The basin covers approximately 41, 500 km^2 in area, of which 300 km^2 are located onshore (França et al., 2007). The width of the Espírito Santo Basin's continental shelf increases from 50-60 km in the south of the study area, to 240 km on the Abrolhos Bank to the north (Bastos et al., 2015) (Fig. 3.1). The modern shelf break varies in depth from 40 to 80 m (Knoppers et al., 1999; Bastos et al., 2015).

The basement of the Espírito Santo Basin is part of the São Francisco Craton, which is composed of migmatites, granulites and granitoids (França et al., 2007). The development of the Espírito Santo Basin is closely related to the breakup of Gondwana supercontinent (Ojeda, 1982; Mohriak, 2008). Four tectono-sedimentary stages have been interpreted in the Espírito Santo Basin by Ojeda (1982) and Mohriak et al. (2008): pre-rift, syn-rift, transition and drift stages (Fig. 3.2). However, Chang et al. (1992) and França et al. (2007) did not recognized deposits of 'pre-rift' stage in the Espírito Santo Basin.
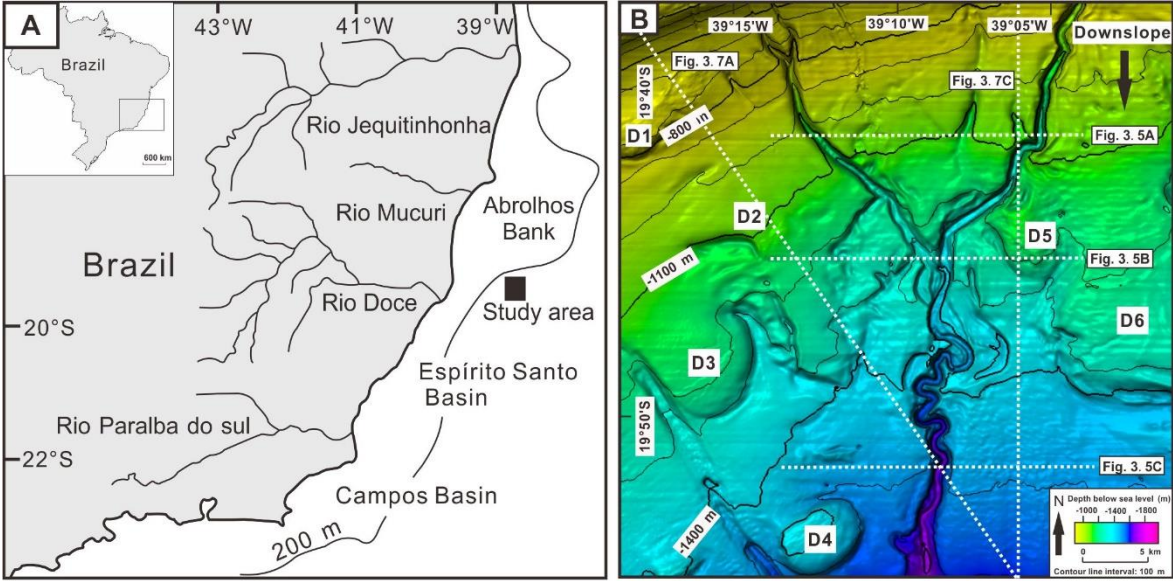
Figure 3.1. A) Regional map of the SE Brazilian margin showing the location of the studied 3D seismic volume from the Espírito Santo Basin. B) Contoured seafloor map of the study area generated from the interpreted seismic volume. It highlights the location of the modern channel relatively to salt diapirs D1 to D6.
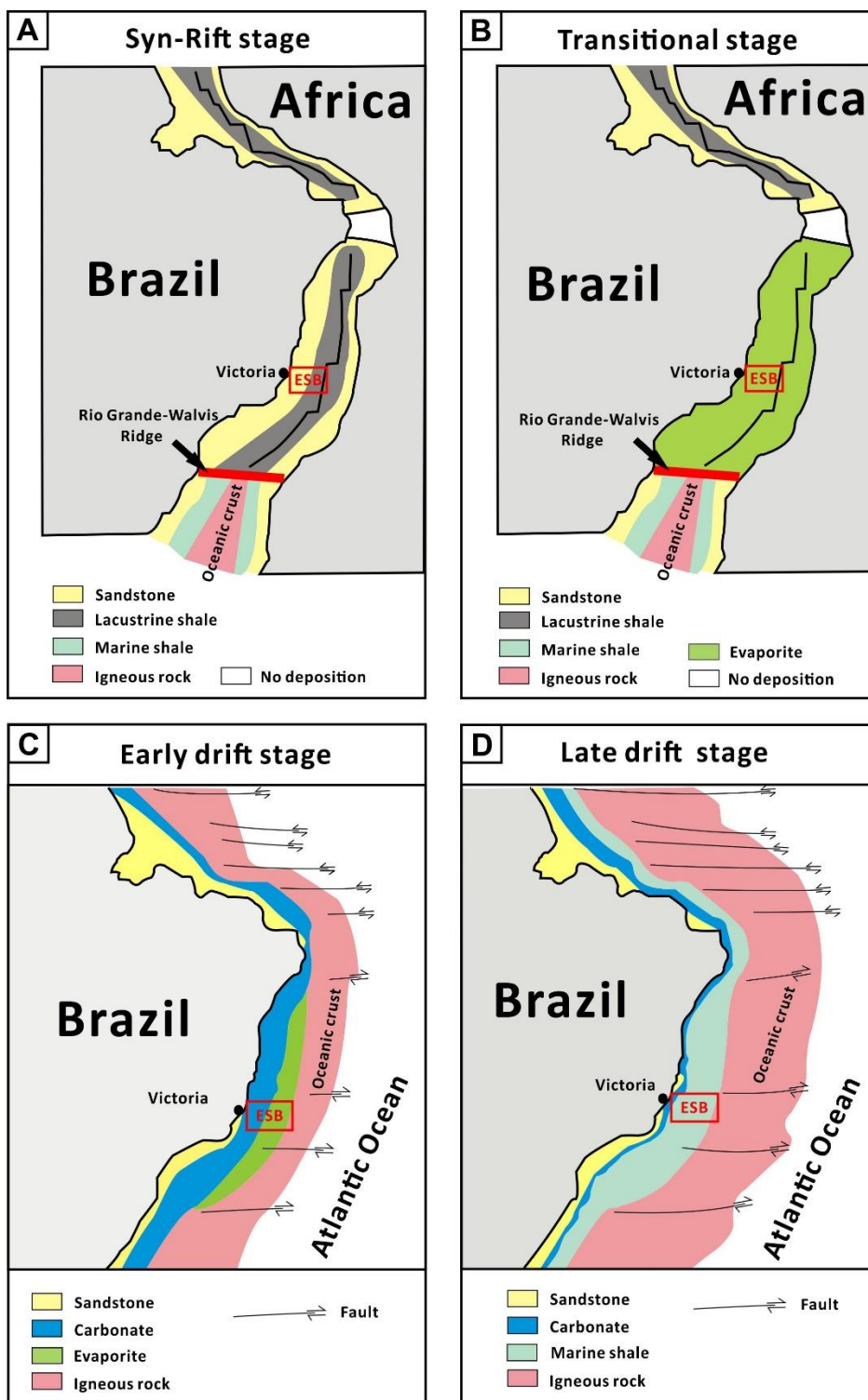
Figure 3.2. Schematic diagram showing major tectonic stages of the Brazilian margin (redrawn from Ojeda, 1982). The location of the Espírito Santo Basin (ESB) is highlighted by the red box. A) Syn-rift phase dominated by continental environments. B) Transitional phase characterised by the deposition of evaporites. C) Early drift phase, with the formation of shallow-marine carbonate platforms. D) Late drift phase characterised by open marine sedimentation.

The 'pre-rift' stage spans the Late Jurassic to Early Cretaceous, when the breakup of Gondwana supercontinent started (Mohriak et al., 2008). This stage is marked by a small degree of asthenospheric uplift and lithospheric thinning. These processes resulted in normal faulting and the formation of local depocentres (Mohriak et al., 2008). A thin sedimentary sequence was deposited within these depocentres during this period. It is mainly located in the Barreirinhas and Sergipe-Alagoas basins offshore Brazil (Ojeda, 1982; Mohriak et al., 2008), but is likely absent in the Espírito Santo Basin (França et al., 2007). This thin sequence comprises fluvial and alluvial-fan deposits, together with lacustrine deposits (Ojeda, 1982).

The 'syn-rift' stage developed from the Late Berriasian to Early Aptian. This stage is characterised by an increased degree of asthenospheric uplift and lithospheric thinning (Mohriak et al., 2008). In the basins located in the south-southeastern part of offshore Brazil, such as the Espirito Santo Basin, the presence of Neocomian tholeiitic basalts overlying the Precambrian basement marks increased lithospheric stretching (Ojeda, 1982; Chang et al., 1992; Mohriak et al., 2008). This magmatic event was followed by intense normal faulting, and the formation of a series of half grabens and rift valleys (Mohriak et al., 2008). This stage records the widespread formation of rift sub-basins in the Espírito Santo Basin, in which fluvial-lacustrine sediments were accumulated (Ojeda, 1982; Chang et al., 1992) (Fig. 3.2). These fluvial-lacustrine sediments are interbedded with volcaniclastic intervals (Chang et al., 1992; França et al., 2007), comprising the lower-Cretaceous Cricaré Formation (França et al., 2007) (Fig. 3.3). The terrestrial deposits in this formation change from conglomerates and coarse sandstones in the proximal region to fine-grained mudstones and shales in more distal regions of the basin (França et al., 2007). The lacustrine shales of the Cricaré Formation are the main source rock of the basin (Estrella, 1984). The Cricaré Formation is overlain by the Mucuri Member, which changes from alluvial fan and fluvial deposits to lacustrine deposits and associated sabkha deposits (França et al., 2007) (Fig. 3.3).

By the end of this stage, a relative increase in lithospheric extension resulted in the reactivation of large faults and the formation of a regional breakup unconformity (Mohriak and Fainstein, 2012). This unconformity separates continental fluvial-lacustrine sediments from microbialites (pre-salt units) and overlying evaporates, and marks the beginning of the transitional stage, which spanned the Middle Aptian to Late Aptian/Early Albian. The deposition of thick evaporite sequences and
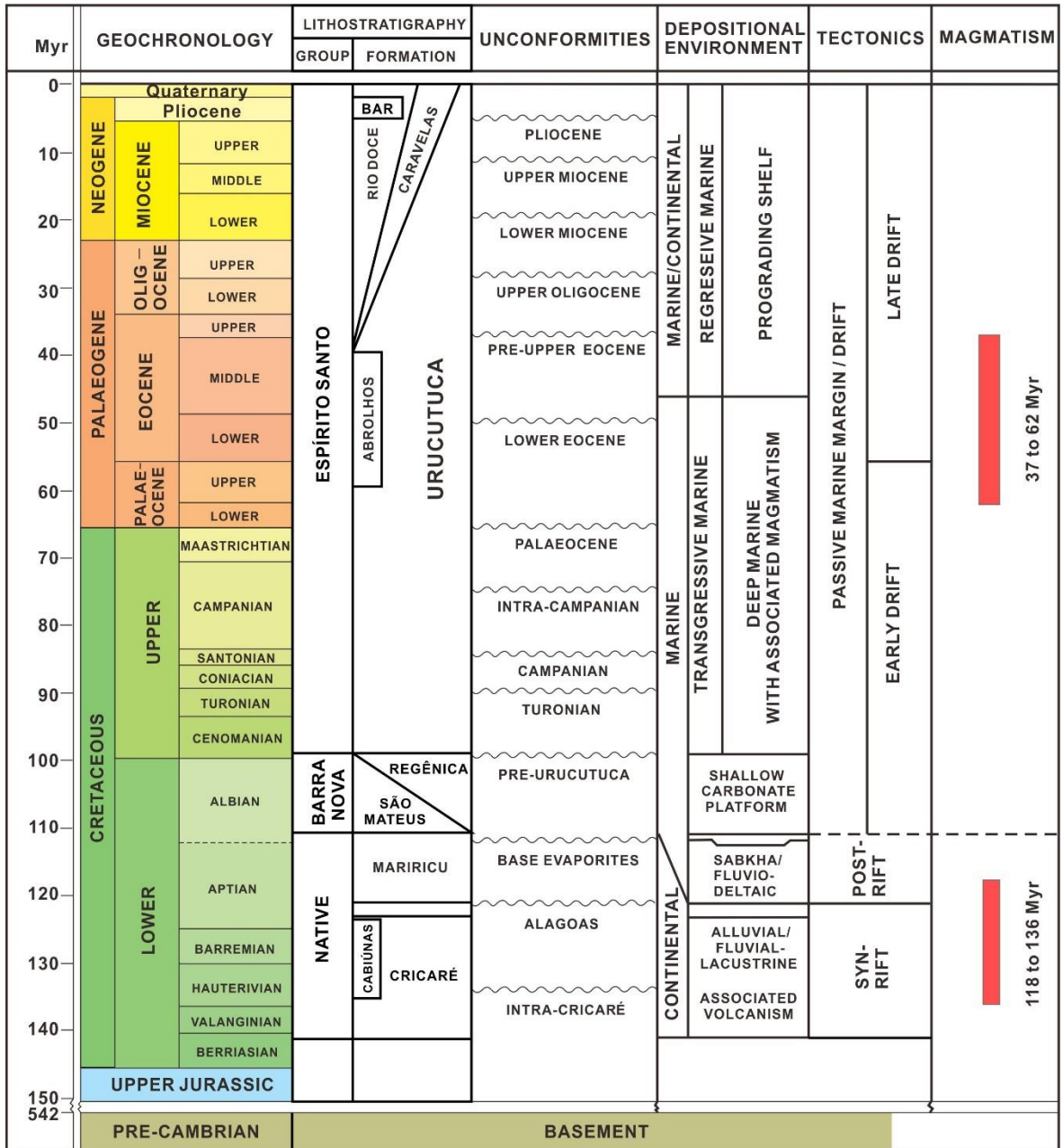
Figure 3.3. Stratigraphic column of the Espírito Santo Basin highlighting the main tectono-sedimentary stages and magmatic events in the basin (modified from França et al., 2007).

marine carbonates predominated at this stage (Ojeda, 1982) (Fig. 3.2). In the Espírito Santo Basin, the thick evaporite succession is named the Itaúnas Member, which belongs to the Mariricu Formation (França et al., 2007) (Fig. 3.3). The transitional stage is followed by a drift phase spanning from Late Aptian/Early Albian to the present day, and is characterised by the deposition of open marine strata (Ojeda, 1982; Chang et al., 1992) (Fig. 3.1). Strata deposited in this phase are divided into two megasequences: early-drift transgressive and late-drift regressive (Mohriak, 2003; Fiduk et al., 2004) (Fig. 3.3).

The transgressive megasequence consists of Albian carbonates and overlying muddy and sandy turbidites, and marks a general deepening-upwards trend towards the end of the Cretaceous (Davison, 1999; Fiduk et al., 2004; Alves et al., 2009). This megasequence started from the Eocene in the Espírito Santo Basin and is marked by the presence of calcareous marls (França et al., 2007). In the basin, the base of this megasequence comprises fan-delta clastics (São Mateus Member of the Barra Nova Formation) in the western proximal region, and shallow marine carbonates (Regência Member of the Barra Nova Formation) in distal regions of the basin (França et al., 2007) (Fig. 3.3). The carbonate platform is overlain by dark shales and turbidites (Urucutuca Formation) of Late Cretaceous age within the basin (França et al., 2007) (Fig. 3.3). Several submarine canyons were developed at this stage, e.g. the Regência and Fazenda Cedro Canyons, which are filled with turbidite and comprise important hydrocarbon reservoirs (e.g. Bruhn and Walker, 1997).

The transgressive megasequence is followed by the regressive megasequence, which started at the end of the Cretaceous and is related to the clastic progradation due to the uplift of the Serra do Mar and Serra da Mantiqueira ranges in southeast Brazil (Mohriak and Fainstein, 2012). The regressive megasequence marks the reactivation of rift structures and episodic magmatic activity (Demercian et al., 1993; Cobbold et al., 2001; Mohriak et al., 2008) (Fig. 3.3), and is associated with the development of the Abrolhos Bank to the north of the study area (Cordani, 1970). The development of the Abrolhos Bank changed local slope configuration by extending the continental shelf edge as far as 200 km eastwards (Fig. 3.1). The regressive megasequence is characterized by the deposition of recurrent MTDs (Omosanya and Alves 2013; Gamboa et al., 2010), together with turbiditic channels and lobes, which were sourced from the Abrolhos Bank and fluvial rivers (Bruhn and Walker, 1997; Davison, 1999; Alves et al., 2009; Gamboa and Alves, 2015).

3.2.2 Salt tectonics in the Espírito Santo Basin

In the Espírito Santo Basin, salt structures have been active since the Albian and play an important role in the stratigraphic architecture of the basin (Fiduk et al., 2004). Gravitational gliding and differential loading are two main reasons for salt movement in the basin (Demercian et al., 1993; Fiduk et al., 2004).

Seismic data show distinct salt deformation styles from west to east towards the lower continental slope and rise (Fiduk et al., 2004) (Fig. 3.4). Three domains are recognised based on the different types of salt structures across the basin (Fig. 3.4). In the proximal domain, the basin is characterised by salt rollers and rafts formed by extensional stresses (Demercian et al., 1993; Fiduk et al., 2004; Alves, 2012). In the transitional domain, salt diapirs predominate (Fiduk et al., 2004). In the distal domain, where compressional stress dominated, the basin is characterised by allochthonous salt canopies, tongues and overhangs (Fiduk et al., 2004; Mohriak et al., 2008) (Fig. 3.4).

3.2.3 Submarine channel systems in the Espírito Santo Basin

Submarine channels comprise the most important depositional features, and hydrocarbon reservoirs, in the Espírito Santo Basin (Fiduk et al., 2004). For example, Bruhn and Walker (1997) documented submarine channel complexes exposed near the mouth of the Rio Doce river (Fig. 3.1A). These channel complexes cut into underlying carbonates, evaporites and terrestrial sediments, and were filled with a thick succession of coarse-grained turbidites from Late Cretaceous to Middle Eocene. The Early Eocene coarse-grained turbidites within the channel complexes form the Lagoa Parda oil-field. An upwards trend of decreasing channel-element size and sediment grain size within the channel complexes is attributed to a reduction in sediment supply because of sea-level rise and decreasing fault activity (Bruhn and Walker, 1997). Multiple erosion and filling processes observed within the channel complexes are suggested to be controlled by variations in sediment supply, which in turn, are associated with sea level change, climate and tectonic events at the basin margin and source areas (Bruhn and Walker, 1997).
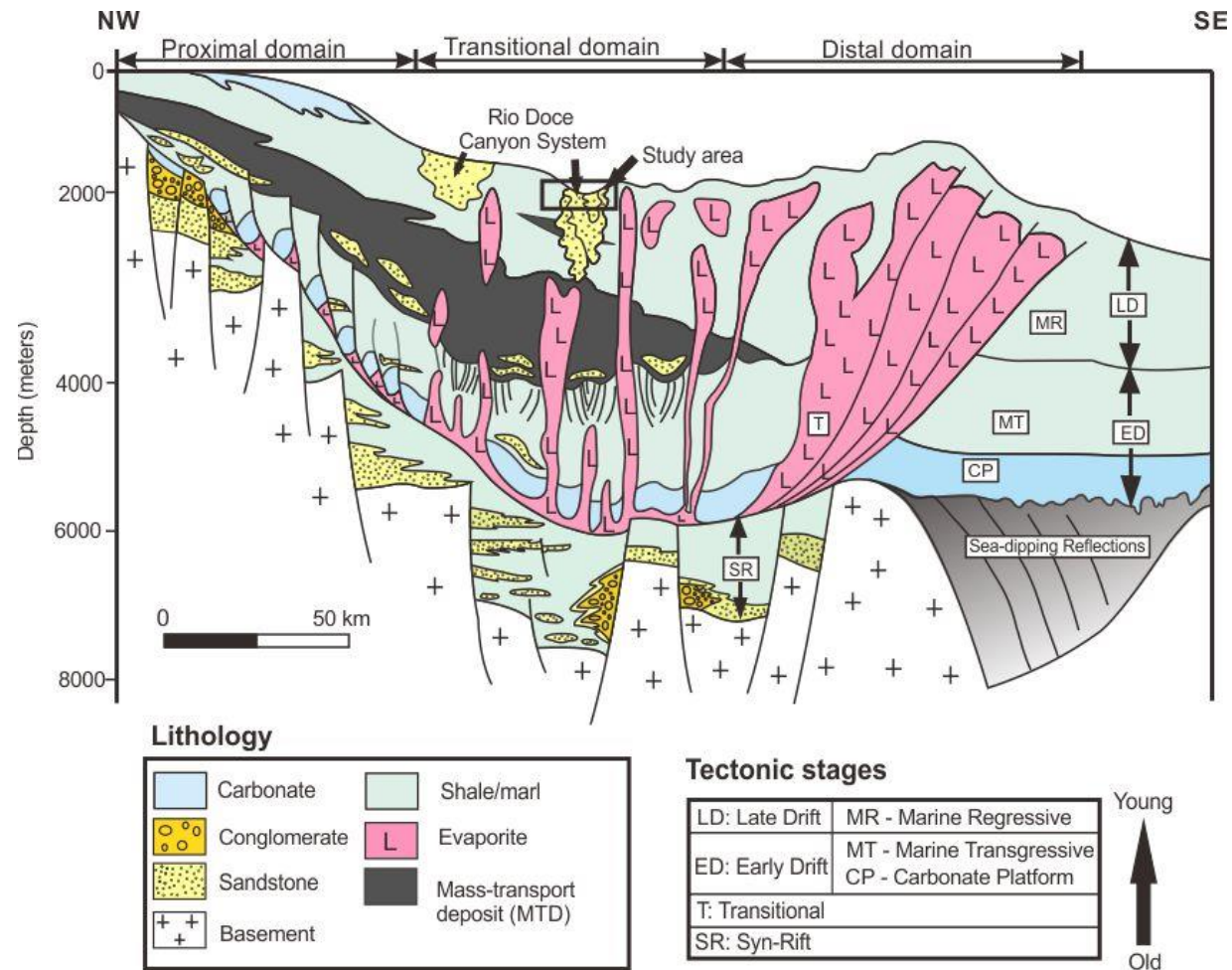
Figure 3.4. Simplified regional cross-section across the Espírito Santo Basin showing major depositional sequences and salt-tectonic domains (modified from Fiduk et al., 2004 and Gamboa et al., 2010). The location of the study area is indicated by the black box.

3.3 Geological setting of the study area

The study area is located in the northern Espírito Santo Basin and on the south of Abrolhos Bank (Fig. 3.1).

3.3.1 Seismic stratigraphy of study area

The stratigraphy in the study area is divided into four seismic units based on the interpretation of distinct seismic facies and unconformities (Baudon and Cartwright, 2008; Alves, 2009; Gamboa, 2011) (Fig. 3.5).

Unit 1 (Late Cretaceous-Palaeocene) shows discontinuous to continuous, low to moderate amplitude reflections (Fig. 3.5). Its top boundary is marked by a Lower-Eocene unconformity. This unit is characteristic by faults and folded strata because of underlying salt structures (Baudon and Cartwright, 2008; Alves, 2009). An Eocene channel system developed at the top of Unit 1 (Fig. 3.5). The evolution of this channel system is closely related to the development of fault systems on the flanks of growing diapirs (Alves et al., 2009). For example, a marked reduction of channel sinuosity during channel evolution is attributed to the cessation of faulting in salt withdrawal basin (Alves et al., 2009). In addition, these authors found that the activity of normal faults limited lateral channel migration and resulted in the vertical stacking of submarine channels (Alves et al., 2009).

Unit 2 (Eocene-Oligocene) shows moderate to high-amplitude seismic reflections. Several packages of discontinuous, chaotic reflections in this unit are interpreted as mass-transport deposits (MTDs) (Fig. 3.5). The high amplitude reflection in this unit may be related to volcanicalstic materials from the Abrolhos Bank (Gamboa, 2011).

Unit 3 (Miocene-Pliocene) is characterised by subparallel to parallel, low to moderate amplitude reflections (Fig. 3.5). V or U shaped erosional features in this unit (Figs. 3.5 A and B) are either circular to elliptical depressions or submarine channels (Gamboa, 2011). A Miocene channel system developed at the base of this unit. This channel system has a straight pathway and is located within a confined region imposed by salt diapirs (Gamboa et al., 2012). It has two tributaries upslope and a post-confluence channel downslope (Figs 3.5 B and C). The two tributaries merge at the same
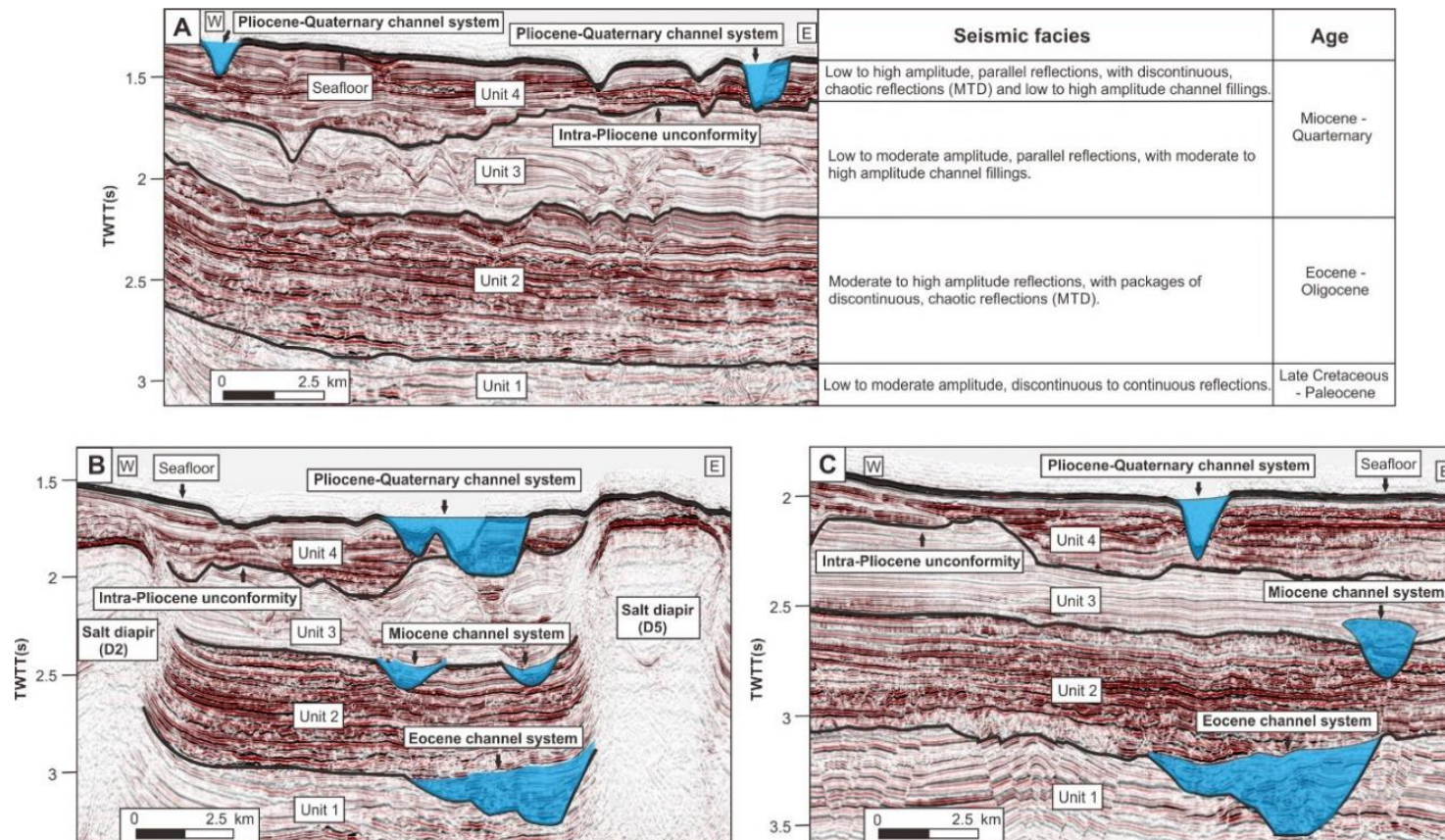
Figure 3.5. Seismic stratigraphy of study area and selected seismic sections highlighting three submarine channel systems in the study area. The location of the seismic sections is shown in Fig. 3.1B. Four seismic stratigraphic units are identified in the study area based on seismic facies. Three channel systems (Eocene, Miocene and Pliocene-Quaternary) are highlighted in blue on each seismic section. Some V or U shaped features in Unit 3 are circular to elliptical depressions (Gamboa and Alves, 2015).

elevation at the confluence point (Gamboa et al., 2012).

Unit 4 (Pliocene-Quaternary) shows parallel, low to high amplitude reflections, with discontinuous, chaotic reflections (MTDs) and low to high amplitude channel-fill deposits (Fig. 3.5). A Pliocene-Quaternary channel system developed in this unit (Fig. 3.5). Similar to the Miocene channel system, this channel system also consists of two tributaries and a post-confluence channel (Fig. 3.5), and the west tributary meets the east tributary with a steep drop at the confluence point (Gamboa et al., 2012).

3.3.2 Salt tectonics of study area

Two NW-SE trending salt ridges are observed and several salt diapirs are rooted on them (Gamboa and Alves, 2015) (Fig. 3.6). These two salt ridges delimited a NW-SE salt-withdrawal basin, within which a range of depositional elements (or genetic units) such as mass-transport deposits (MTDs), turbidite lobes, submarine canyons and channels are located (Gamboa and Alves, 2015). The distribution and geometry of these depositional elements are closely related to the location and movement of the salt diapirs (Baudon and Cartwright, 2008; Alves et al., 2009; Gamboa et al., 2012; Gamboa and Alves, 2015). For example, stacking patterns of submarine channels in the study area are affected by faulting activity associated with salt movement (Alves et al., 2009). In addition, the spacing of submarine channels varies with the degree of topographic confinement created by salt diapirs (Gamboa et al., 2012). It decreases from the unconfined region to topographically confined region on the continental slope (Gamboa et al., 2012).

Architectural elements such as mass-transport deposits (MTDs), turbidite lobes, submarine canyons and channels are observed within a salt-withdrawal basin delimited by salt diapirs D1 to D6 (Gamboa and Alves, 2015). These elements are strongly influenced by the relative location and movement of the salt diapirs (Baudon and Cartwright, 2008; Alves et al., 2009; Gamboa et al., 2012; Gamboa and Alves, 2015). Topographic confinement created by salt diapirs is reflected by changes in channel density, geometry and sinuosity (Alves et al., 2009; Gamboa et al., 2012). As an example, channel density decreases from the unconfined region to the topographically confined region (Gamboa et al., 2012).
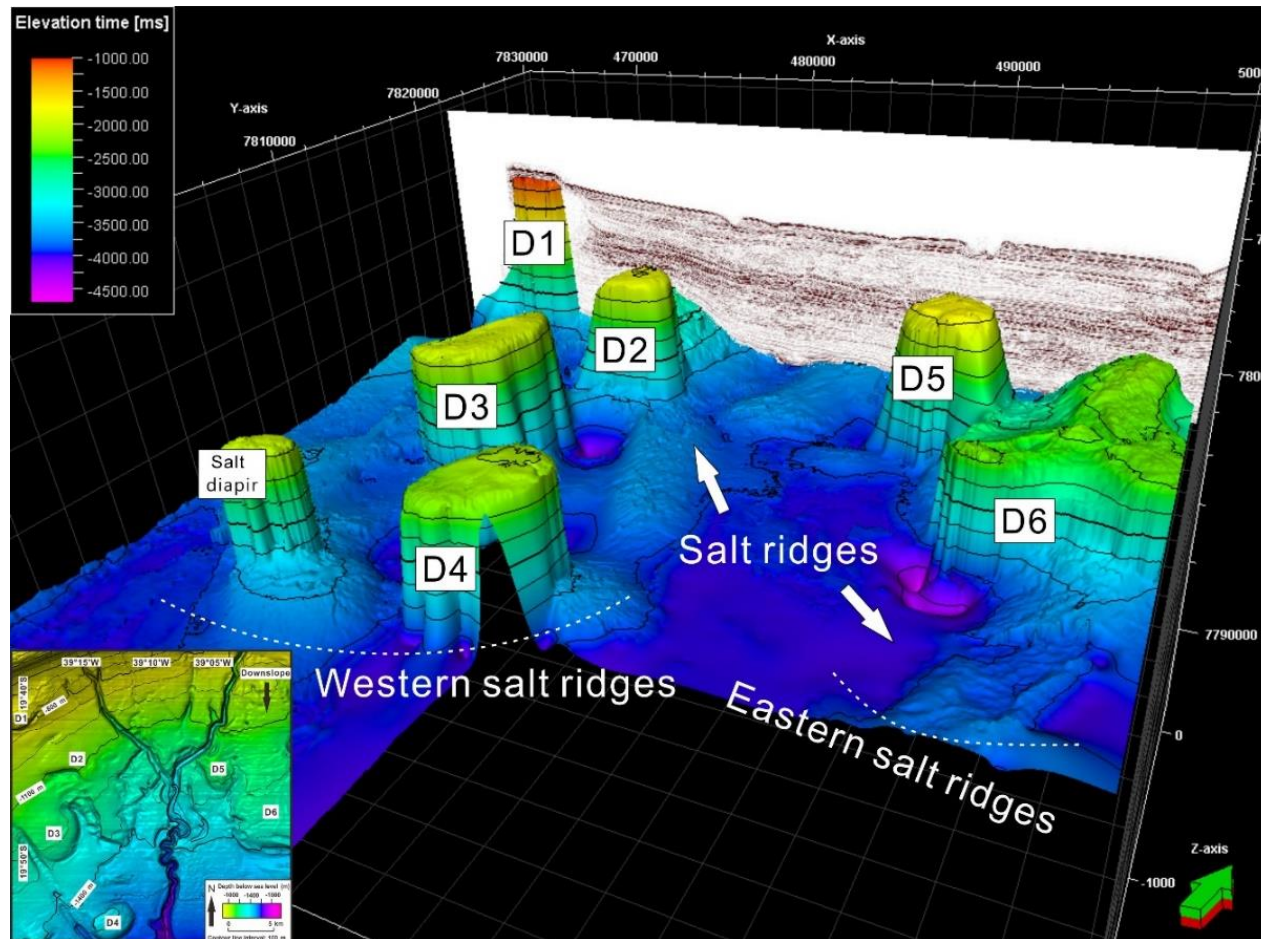
Figure 3.6. 3D morphology of salt structures in the study area. Several salt diapirs root in two NW-SE trending salt ridges (from Gamboa and Alves, 2015). The figure on the bottom left shows the seafloor expression of these salt diapirs. D1-D5 show the location of salt diapirs.

3.3.3 Seafloor morphology of study area

The study area is located on the southern flank of the Abrolhos Bank, a bathymetric feature that is associated with a unique slope configuration in the ESB (Fig. 3.1A). The presence of the Abrolhos Bank forces a shift in the orientation of the continental shelf, which changes from NE striking to the southwest to ENE striking in the northeastern part of the ESB. This change results in two different slope trends in the study area (Fig. 3.7). The western half of study area displays a decreasing slope from 8° in the northwest to 1° in the southeast, whereas the eastern part shows a gentler slope ranging from 1° to 2° (Figs. 3.7). The seafloor is also affected by growing salt diapirs, and in some areas, the slope angle decreases to nearly 0° (Fig. 3.7).

Three slope regions have been defined based on the degree of confinement imposed by salt diapirs deforming the seafloor (Gamboa et al., 2012) (Fig. 3.8). The pre-confluence slope (Zone 1) is relatively unconfined and shows a variety of erosional features such as gullies, channels, irregular depressions and headwalls of mass-wasting events (Fig. 3.8). The confluence region (Zone 2) presents a relatively higher topographic confinement when compared to Zone 1 due to the presence of salt diapirs D2, D3, D5 and D6. As a result, turbidity currents sourced from upslope are diverted by these salt diapirs, as shown by the shift in orientation of the two tributaries on the seafloor (Figs. 3.8). For example, the pathway of the east tributary changes from NNE-SSW in Zone 1 to NE-SW in Zone 2 due to the presence of salt diapir D5 (Fig. 3.8). A distinct confluence point for two Miocene tributaries has been observed in the same region (Gamboa et al., 2012), suggesting that the present-day slope configuration was established in the Miocene. Downslope from the post-confluence region (Zone 3), the seafloor becomes less confined after diapirs D2 and D5, and it is relatively smooth with fewer erosional features (Fig. 3.8).

3.3.4 Studied channel system

This thesis is working on the Pliocene-Quaternary channel system (Figs. 3.5 and 3.8). This channel system consists of a Quaternary channel system and some older channels (Fig. 3.9). The Quaternary channel system can be traced within entire seismic dataset, while older channels are
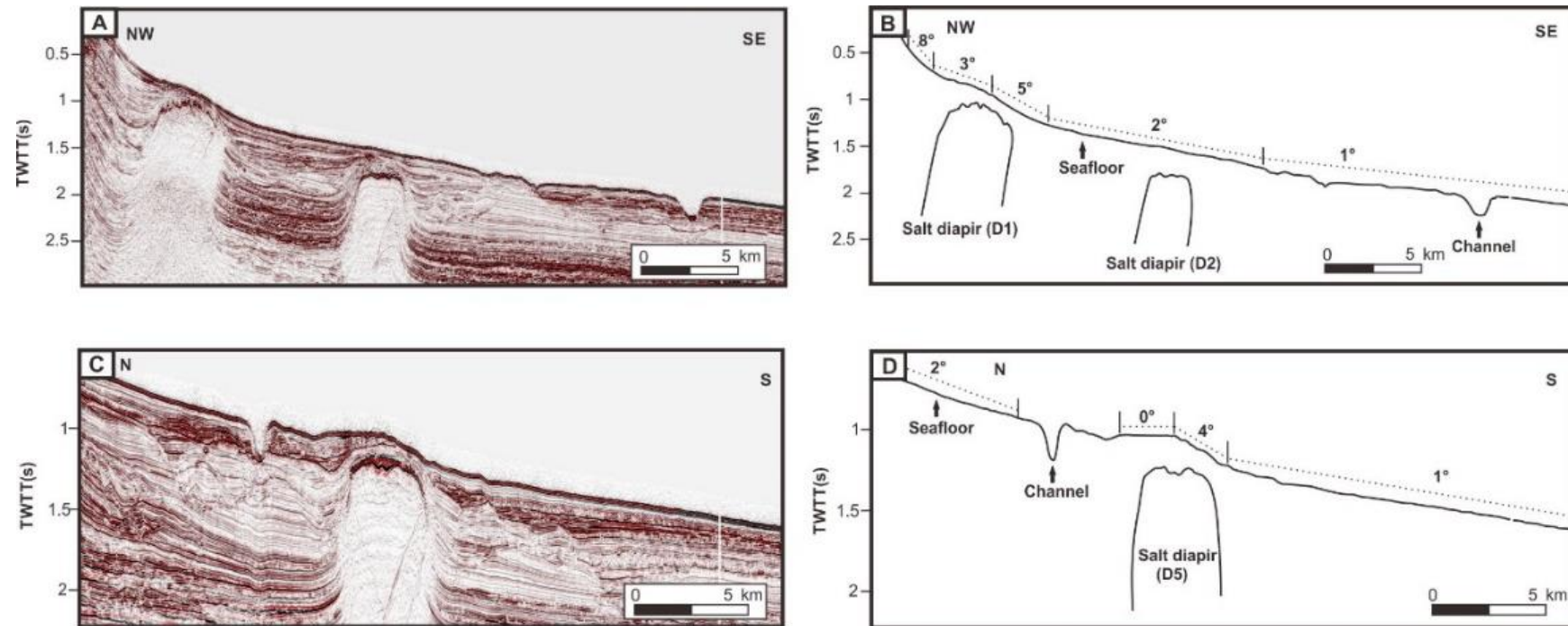
Figure 3.7. Selected seismic profiles illustrating different seafloor slope trends in the study area. The location of the seismic profiles is shown in Fig. 3.1B. A) Uninterpreted and B) interpreted seismic profile showing decreasing slope trend in a NW-SE direction. Salt diapir D1 decreases gradient upslope and increases gradient downslope. Salt diapir D2 has a minor influence on the slope. C) Uninterpreted and D) interpreted seismic profiles showing decreasing slope trends in a N-S direction. Salt diapir D5 induces a decrease in gradient upslope and an increase in gradient downslope.
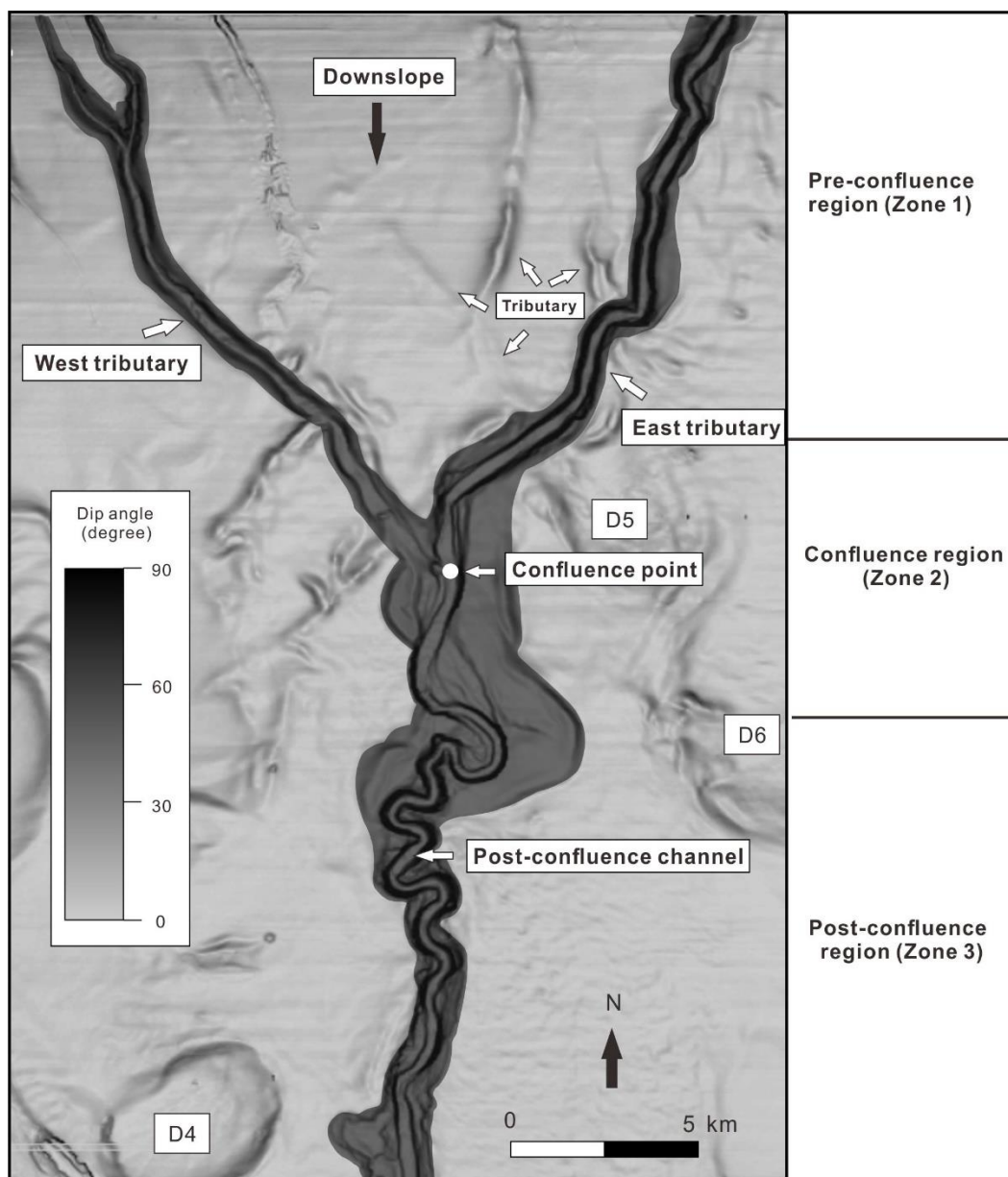
Figure 3.8. Dip map of the seafloor. The Pliocene-Quaternary channel system is shown in black area. This channel system has seafloor channels. These seafloor channels consist mainly of west and east tributaries upslope, and a post-confluence channel downslope. Other small tributaries connected to the east tributary are also observed on the seafloor. Both west and east tributaries change their orientation in the pre-confluence region, and were diverted into the confluence region due to the presence of salt diapirs. In the confluence and post-confluence regions, the general orientation of the channel changes to nearly N-S until the southern limit of the seismic volume is reached.
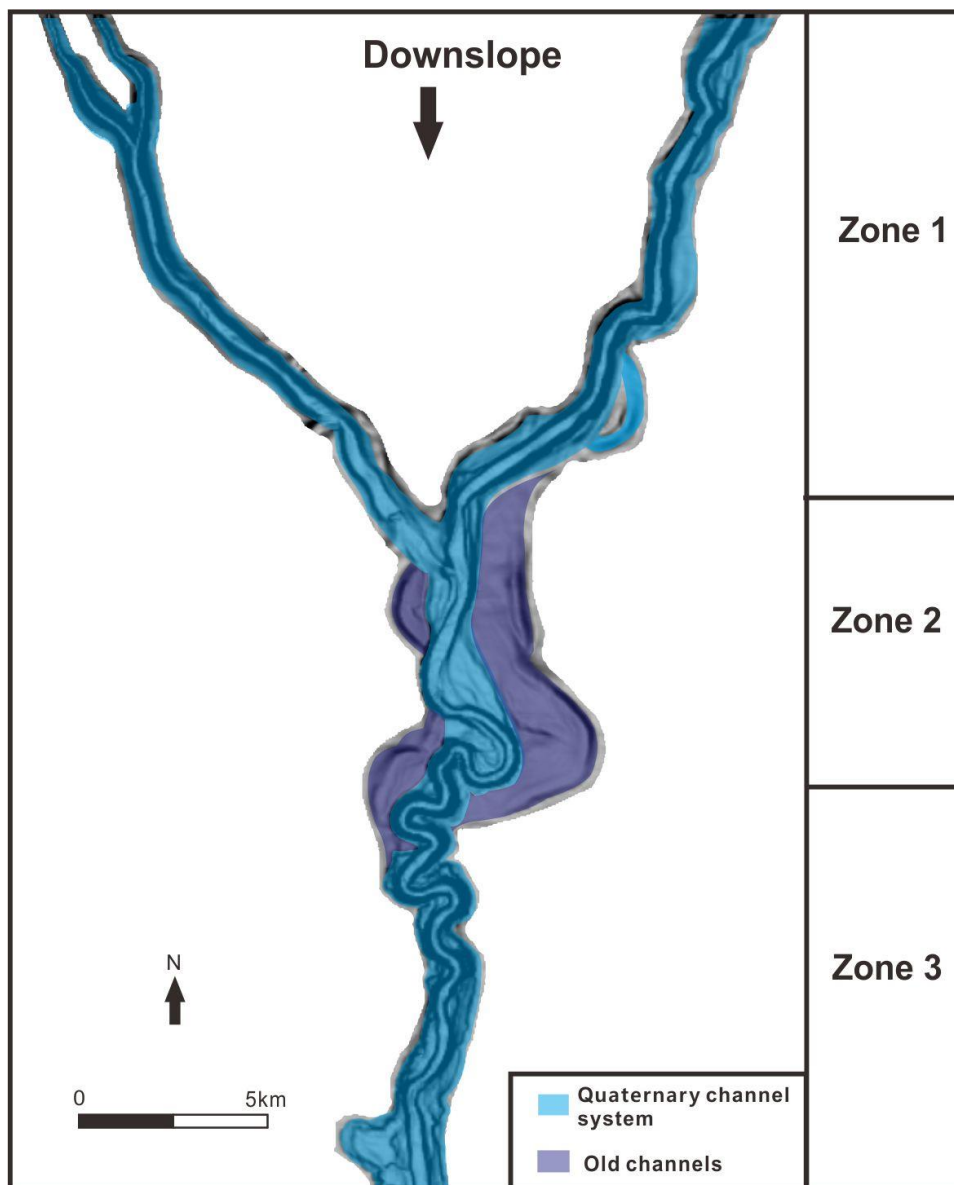
Figure 3.9. Dip map showing the Pliocene-Quaternary channel system comprises a Quaternary channel system that can be traced from Zone 1 to Zone 3 and older channels only preserved in Zone 2.

only observed in the confluence region (Fig. 3.9).

The Pliocene-Quaternary channel system is a partially filled channel system (Fig. 3.5). It has channels on the seafloor (Figs. 3.5 and 3.8). The seafloor channels comprise two upslope tributaries in Zone 1 and a post-confluence channel downslope in Zones 2 and 3 (Fig. 3.8). The continuity of sedimentary fill patterns between the east tributary and the post-confluence channel, as well as the continuity of the channel thalweg, indicate that these two channel segments constitute the main flow pathway at present (Gamboa et al., 2012). Other small tributaries connected to the east tributary are also observed on the seafloor (Fig. 3.8). Both west and east tributaries change their orientations due to diapirs (Fig. 3.8). The general orientation of the channel changes to nearly N-S until the southern boundary of the seismic volume is reached (Fig. 3.8).

Chapters 4 and 5 focus on the main flow pathway (east tributary and post-confluence channel) of the Quaternary channel system (Fig. 3.9). Chapter 6 is working on the Pliocene-Quaternary channel system (Fig. 3.9).

3.3.5 Possible sediment sources of seafloor channels in the study area

Rio Doce river is suggested to be one of sources for the submarine channels in the Espírito Santo Basin (Love et al., 2005). It has an annual suspended-sediment flux of 11×10^6 ton/year (Lima et al., 2005), and an annual average discharge of 900 m^3/s (Oliveira et al., 2012). Mud river water has been seen 40 km off the Rio Doce river after prolonged rains (Summerhayes et al., 1976). Therefore, hyperpycnal flows during river flood events may have delivered sediment from the river to the continental slope (Summerhayes et al., 1976). However, the distance between the mouth of Rio Doce river and the shelf edge is ~ 70 km (Fig. 2.1). Some studies show that sediments from rivers are limited to the vicinity of the river mouth and to the inner shelf (Albino et al., 2010). Thus, it is still unclear whether the sediments from the river can be transported for such a long distance to submarine channels on the continental slopes at present.

Dominguez et al. (1992) suggest that longshore drift plays a more important role in the transport of sediment to the continental slope than fluvial input. Longshore drift in the study area is controlled mainly by two types of waves (Dominguez et al., 1992) (Fig. 3.10): 1) north –
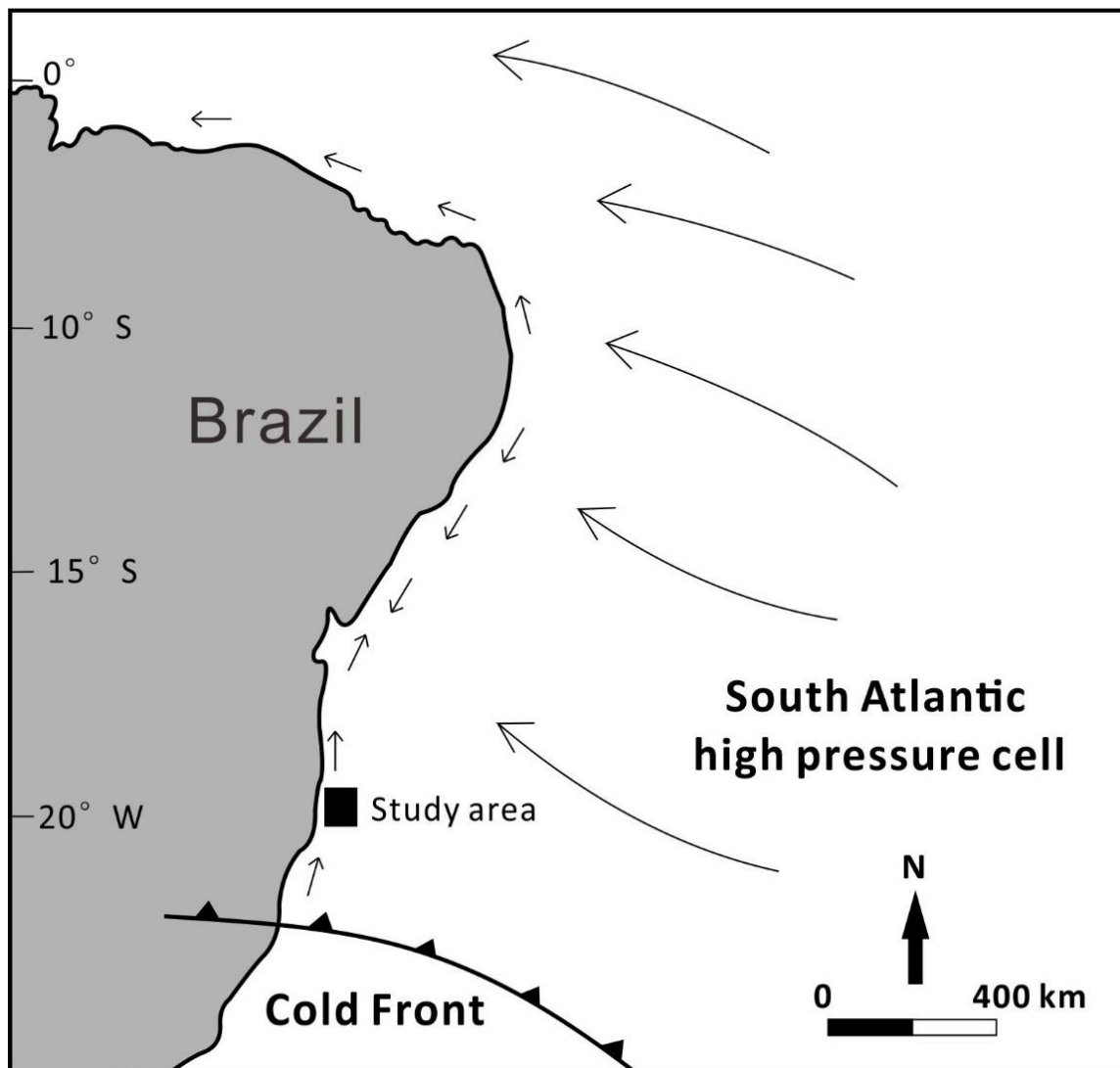
Figure 3.10. Schematic diagram showing major atmospheric circulation and associated longshore drifts along the coastline of Brazil at present (after Dominguez et al., 1992). The location of the study area is indicated by the black box. Seafloor channels in study area are affected by two types of waves related to South Atlantic high-pressure cell and cold front.

northeastern waves related to southern Atlantic high-pressure cell. 2) east – southeastern waves influenced by periodically advanced polar fronts during autumn and winter, which are less frequent than the southern Atlantic high-pressure cell. These two longshore drifts were recorded by the orientations of beach ridges at the Rio Doce strandplain (Martin and Suguio, 1992; Dominguez et al., 1992). In addition, seismic data shows valleys developed on the continental shelf (Bischoff and Lipski, 2008), and suggests that sediment transported by longshore drift may be intercepted by valleys and delivered to submarine channels on the continental slopes.

Chapter 4

Quantitative seismic geomorphology of Quaternary submarine channel system

4. Quantitative seismic geomorphology of Quaternary submarine channel system

4.1 Introduction

This Chapter focuses on the morphological characteristics of the Quaternary submarine channel system developed near the seafloor in the study area (Fig. 4.1A). It carries out morphological analyses of the channel system at both channel and valley (i.e. channel complex) scales. It also shows temporal variations in the sinuosity of channels within the channel system.

The formation of the studied channel system is similar to the 'channel complex', both of which were formed by vertical and lateral stacking of channels. However, the term 'channel complex' is not used here as it generally refers to filled stratigraphic element, while the studied channel system is partially filled. Instead, the term 'valley' is used to refer to the composite erosional surface formed by lateral channel migration in the study area. The terms used in this chapter are defined in Section 1.3 in Chapter 1.

4.2 Methods for quantitative analyses of the channel system

The mapping of the seafloor and channels followed a line-by-line interpretation combined with 3D auto-tracking. The quantitative analyses of the channel system followed the methods of Deptuck et al. (2007) and included channel and valley measurements (Fig. 4.1).

Channel measurements included the depth (i.e. depth below sea level) of the channel thalweg (i.e. the lowest point in channel) and channel bank, channel height (i.e. the distance between internal-levee crest or the top of erosional banks and channel thalweg), width of channel floor (i.e. the length of sub-horizontal to horizontal part of channel, generally less than 15°), width of channel (i.e. the distance between internal-levee crests or the top of channel erosional banks), aspect ratio (width/height) and cross-sectional area (CSA) (Figs. 4.1 and 4.2). These parameters were measured in equally spaced cross-sections that were oriented perpendicularly to the channel axis line. The channel CSA was measured at 1-km intervals and other parameters were measured at 125-m
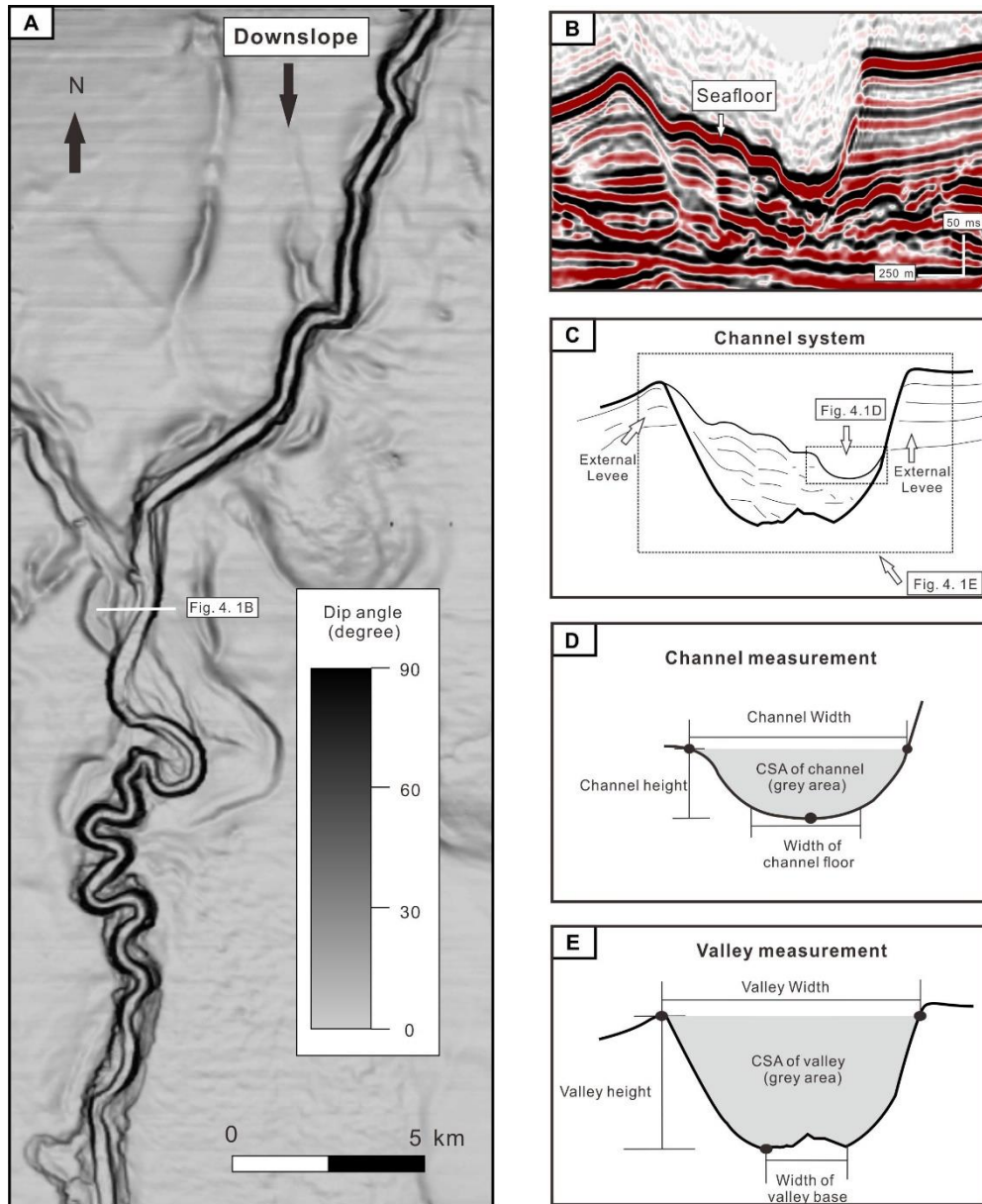
Figure 4.1. Measurements taken for the Quaternary channel system interpreted in this work. A) Dip map of seafloor showing the Quaternary channel system. B) and C) are uninterpreted and interpreted seismic sections of the channel system. D) Channel measurements were taken along the channel axis and included the depth of the channel bank and thalweg, the width of the channel floor (i.e. sub-horizontal to horizontal part of channel, generally less than 15°) and the channel, and the cross-sectional area (CSA) of the channel. Channel height is the distance between the depth of channel bank and the thalweg. E) Valley measurements were taken along the valley axis and included the depth of the valley wall and thalweg, the width of valley base (i.e. sub-horizontal to horizontal part of valley, generally less than 15°) and valley, and the cross-sectional area (CSA) of the valley. Valley height is the distance between the depth of valley wall and the thalweg.
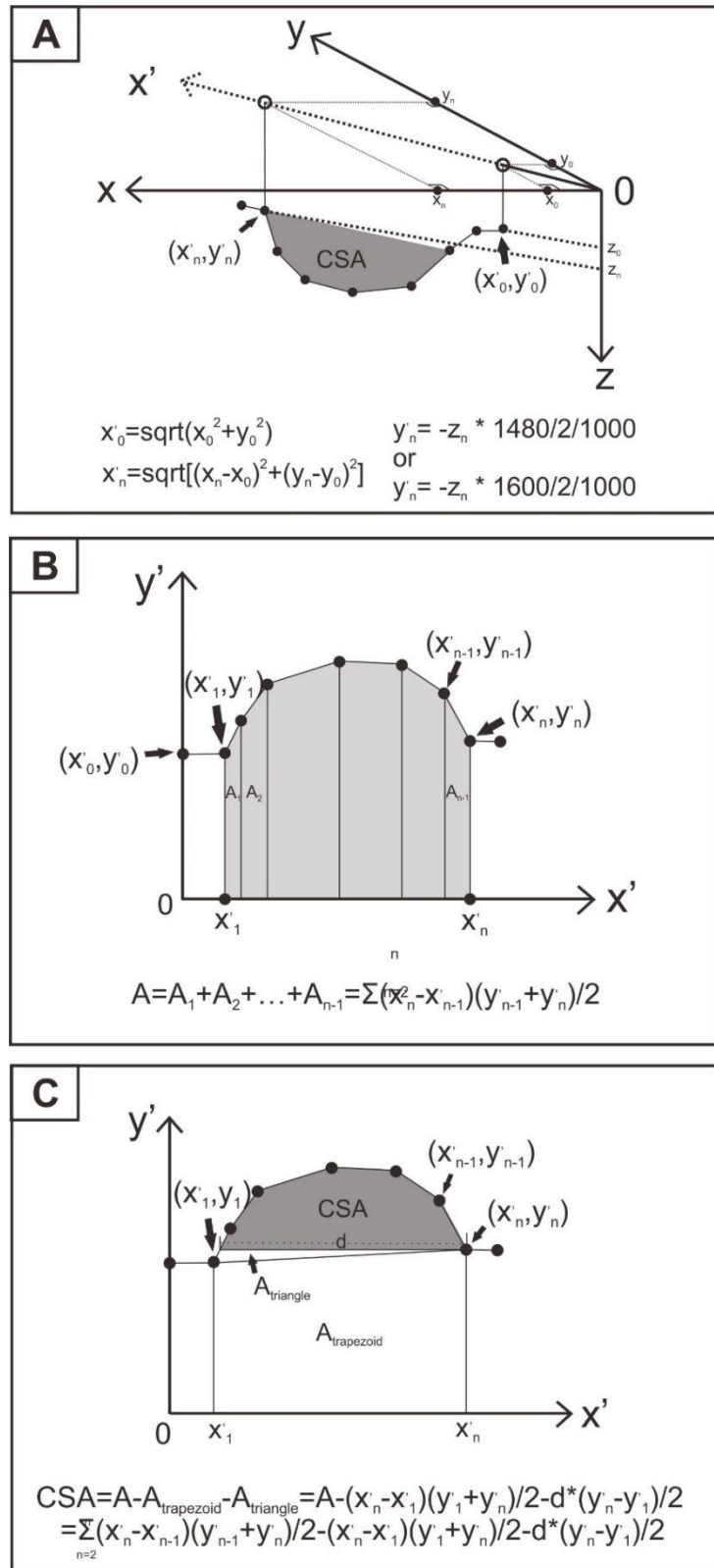
Figure 4.2. Measurement methods of cross-sectional area (CSA) of channel and valley. In this figure, $X_0, Y_0, Z_0, ...X_n, Y_n, Z_n$ represent the coordinates of mapped points in channels.

intervals. Channel gradient was calculated based on thalweg depth changes along the channel distance.

Valley measurements were conducted at cross-sections that are perpendicular to the valley axis. The parameters measured include the depth (i.e. depth below sea level) of the valley thalweg (i.e. the lowest point in valley) and valley wall, valley height (i.e. the distance between external-levee crest or the top of erosional banks and valley thalweg), width of valley base (i.e. the length of sub-horizontal to horizontal part of valley, generally less than 15°), width of valley ((i.e. the distance between external-levees crest or the top of erosional valley banks), the aspect ratio (width/height) and CSA of the valley (Fig. 4.1). The valley CSA was measured at 1-km intervals and other parameters were measured at 65 m intervals. The gradients of the valley thalweg (valley gradient) and the valley walls were calculated based on measurements of depth along the valley.

Channel mapping was completed through a line-by-line interpretation, and involved a combination of manual and autotracking. Multiple sinuous threads or bands in horizon slices can be used for reconstructing the evolution of submarine channels (e.g. Abreu et al., 2003; Kolla et al., 2007; Deptuck et al., 2007), but they are difficult to separate from each other as they vary with consecutive slides (i.e. upwards or downwards). Therefore, the combination of horizon slices and cross sections of channels are used for the reconstruction of channel pathways.

Channel sinuosity was calculated at intervals of 2.5 km along the channel axis, and was assigned to the middle points of the intervals. Depth profiles of the initial channel and of the seafloor channel (i.e. present channel) were measured along the valley at intervals of 125 m.

4.3 Spatial variations of dimensions of the Quaternary channel system

4.3.1 Quantitative channel analyses

The main pathway of the present channel is 42 km-long within the seismic dataset. It starts from a water depth of ~1000 m, down to ~1700 m at the southern edge of the seismic volume (Fig. 4.3). The channel shows marked variations in its dimension (Fig. 4.4 and Table 4.1). Five distinct Reaches (Reaches a to e) are recognised based on their morphological changes (Figs. 4.3 and 4.4,
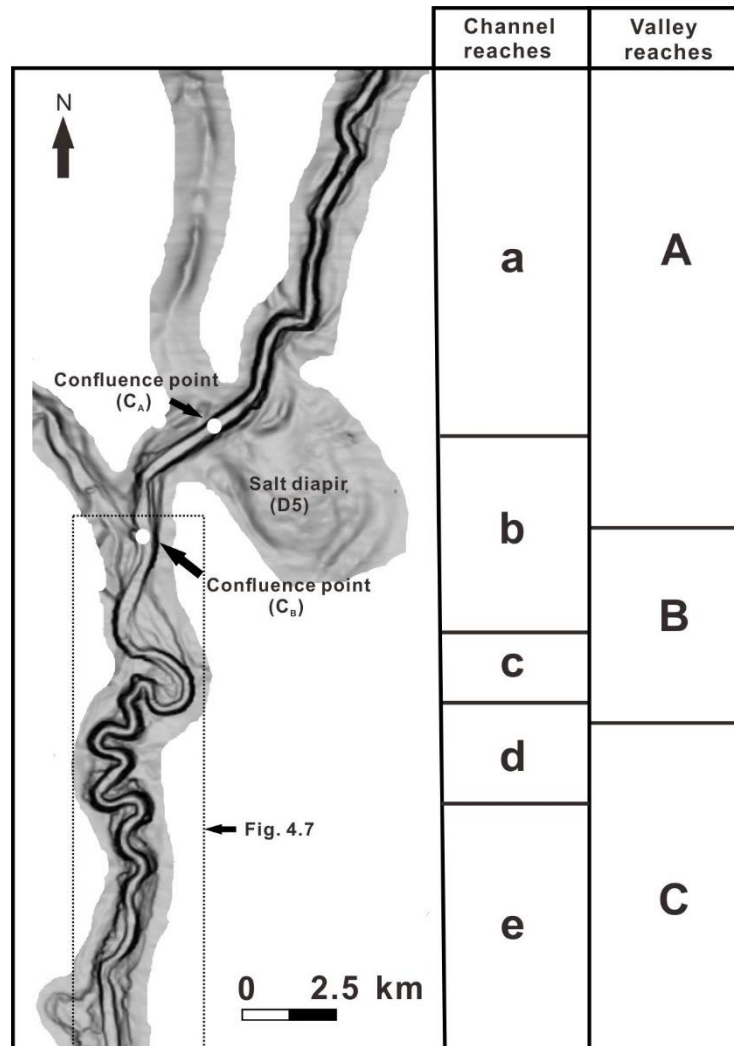
Figure 4.3. Dip map showing the main sediment pathway of the channel system. The pathway is divided into different reaches based on both channel (Reaches a to e) and valley dimensions (Reaches A to C).
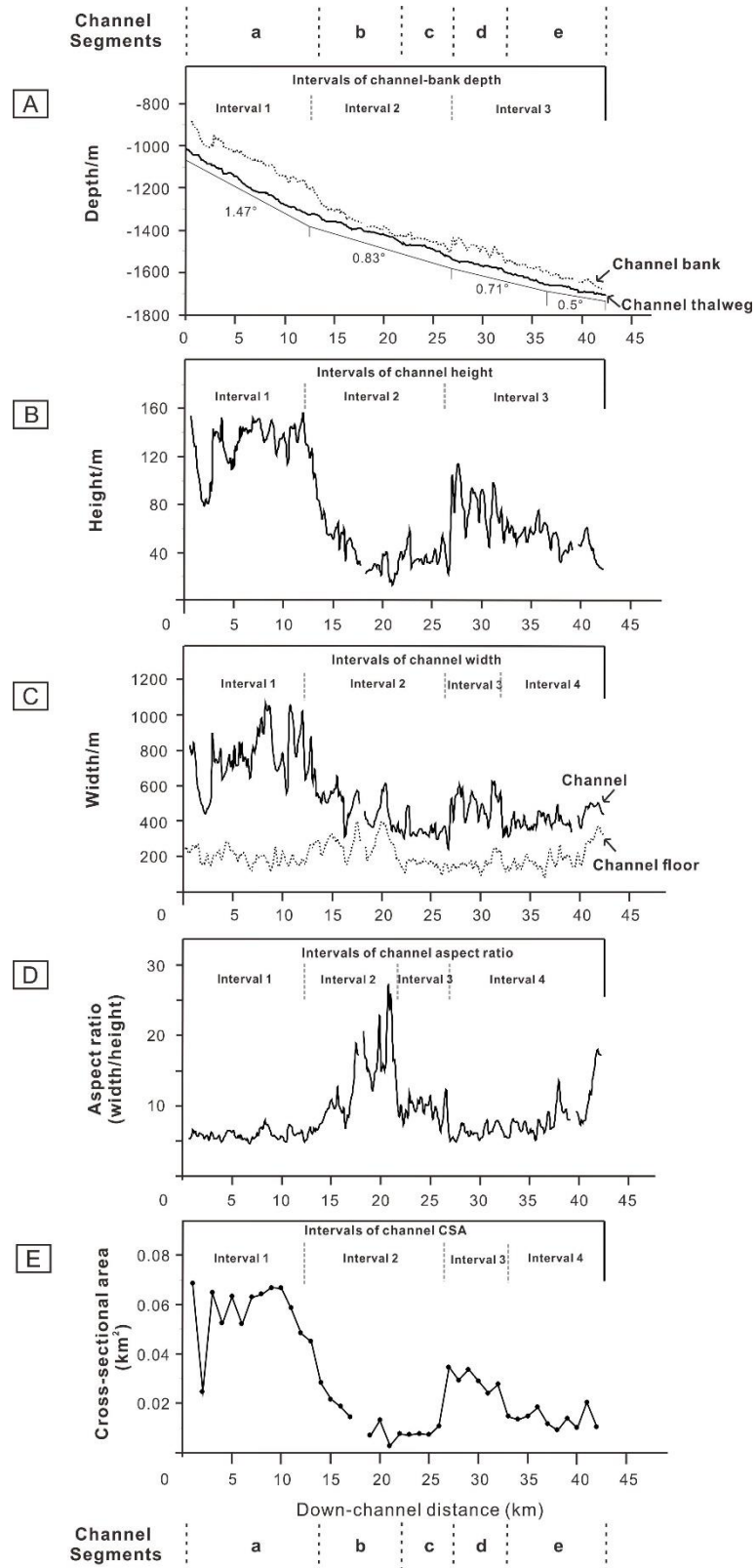
Figure 4.4. Quantitative analyses of the channel. A) Depth profile of the channel thalweg and channel bank. B) Channel height profile. C) Width of the channel floor and channel. D) Aspect ratio (width/height) of the channel. E) Cross-sectional area (CSA) of the channel.

Table 4.1. Summary of morphological data acquired along the channel.

	Downslope →				
Segments / Measurements	a (0-13 km)	b (13-22 km)	c (22-27 km)	d (27-32 km)	e (32-42 km)
Channel gradient/°	1.38	0.89	0.87	0.65	0.61
Channel height /m (ave.)	129	42	38	80	51
Width of channel floor /m (ave.)	201	277	165	166	197
Channel width /m (ave.)	759	483	345	497	412
Aspect Ratio (ave.)	6	13	9	6	9
CSA /km² (ave.)	0.057	0.015	0.008	0.03	0.014
Examples of channel cross section in each segment					
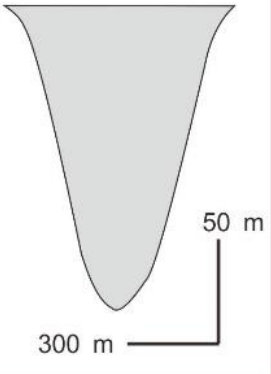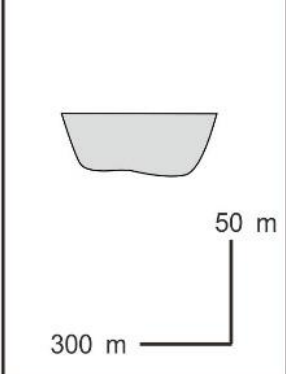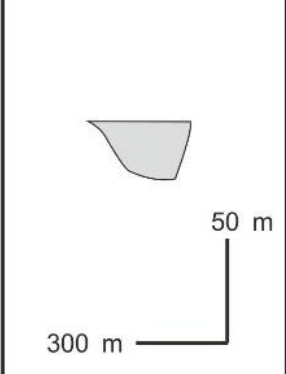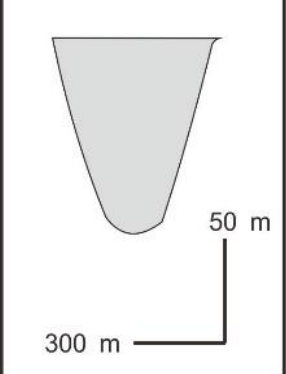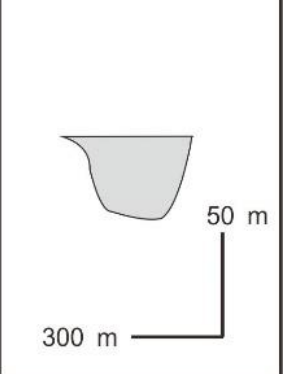
Table 4.1).

4.3.1.1 Depth profiles of channel thalweg and channel bank, and channel height profile

The depth profile of the channel thalweg shows an exponential trend and is divided into three intervals based on the observed variations in channel gradient (Fig. 4.4A). Channel gradient approaches 1.47° (25.7 m/km) in the first interval, where the steepest parts of the channel are recorded (Fig. 4.4A). Between 12 km and 27 km (interval 2), the channel shows a stepped profile and gradient decreases to 0.83° (14.5 m/km) due to the presence of salt diapir D5. In the remainder of the channel (interval 3), channel gradient decreases to 0.71° (12.4 m/km) between 27 and 37 m, and reaches its lowest value of 0.5° (8.7 m/km) in the last 8 km (Fig. 4.4A).

The depth profile of the channel bank shows marked changes (Fig. 4.4A), which correlate with variations in the channel height profile (Fig. 4.4B). There are three intervals observed in the depth profiles of the channel bank and channel height (Figs. 4.4A and B). The first interval (0-12 km) has the highest value of channel height, which ranges from 80 m to 156 m (Fig. 4.4B). In interval 2, between 12 and 27 km, the channel height decreases rapidly due to a decrease in the depth of the channel bank (Figs. 4.4A and B). The channel height reaches a minimum value of 13 m at 21 km, and then fluctuates between 22 m and 58 m for the remainder of interval 2 (Fig. 4.4 B). The third interval starts with a marked increase in channel height from 22 m to 100 m at 27 km, due to an abrupt increase in the depth of the channel bank, and is followed by a decreasing trend. The channel height decreases to 26 m at the southern edge of the seismic volume (Fig. 4.4B).

4.3.1.2 Width profiles of channel and channel floor

The channel-width profile in Fig. 4.3C displays four intervals. It fluctuates between 445 and 1060 m in the first 13 km within interval 1. In interval 2, the channel width decreases from 690 m to its lowest value of 240 m at 27 km. This decreasing trend is followed by an increase of the channel width between 27 km and 32 km (interval 3), where it ranges from 400 m to 610 m. In interval 4, the channel width decreases rapidly to 310 m at 32 km and then rises progressively. It increases to 440 m at the southern limit of the seismic volume (Fig. 4.4C).

The width of the channel floor varies from 80 to 400 m, showing an average value of 200 m,

and its profile can be divided in four intervals (Fig. 4.4C). For most of the channel length, channel-floor width shows small variations, but displays two increasing trends starting at 12 km in interval 2 and 36 km in interval 3 (Fig. 4.4C). These two trends relate to decreases in channel gradient at 12 km and 36 km (Figs. 4.4A and C).

4.3.1.3 Aspect ratio (width/height) and cross-sectional area (CSA) of channel

The aspect ratio of the channel ranges from 5 to 27 and four intervals are observed along the channel (Fig. 4.4D). It shows small changes in the first 13 km, with an average value of 6 in interval 1. The aspect ratio rises in interval 2, between 13 km and 21 km, and increases to a maximum of 27 at 21 km. The third interval starts with an abrupt drop at 21 km, where the aspect ratio decreases to 9 and then remains nearly constant. Between 27.5 and 36.5 km (interval 4), the aspect ratio displays an increasing trend towards the southern limit of the seismic volume, where the ratio increases up to 17 (Fig. 4.4D).

The CSA of the channel shows a similar trend to channel height and width (Figs. 4.4B, C and E). The CSA is ~0.06 km^2 in the first 10 km, except for an abrupt change at 2 km where the CSA decreases to 0.025 km^2 (Fig. 4.4E). Between 10 km and 25 km the CSA decreases by a factor of 22, from 0.067 km^2 at 10 km to a minimum value of 0.003 km^2 at 21 km. This significant reduction in CSA is followed by a nearly three-fold increase from 21 to 22 km, where it is 0.008 km^2 and remains constant for the next 3 km. The CSA shows a rapid increase from 25 km and an increase to 0.035 km^2 at 27 km. It then decreases gradually to 0.013 km^2 at 34 km, and varies between 0.009 km^2 and 0.02 km^2 for the remainder of the channel (Fig. 4.4E).

4.3.1.4 Bank slope angle of channel

The slope angle of the western channel bank ranges from 13° to 48° (Fig. 4.5A). There is no clear increasing or decreasing trend in western bank slope angles along the channel. Slope angles of eastern channel bank are higher than 20°, except at 20 m, where it shows the lowest value of 14°. Similar to the western bank, eastern bank also shows no clear patterns of variations in slope angles (Fig. 4.5B).
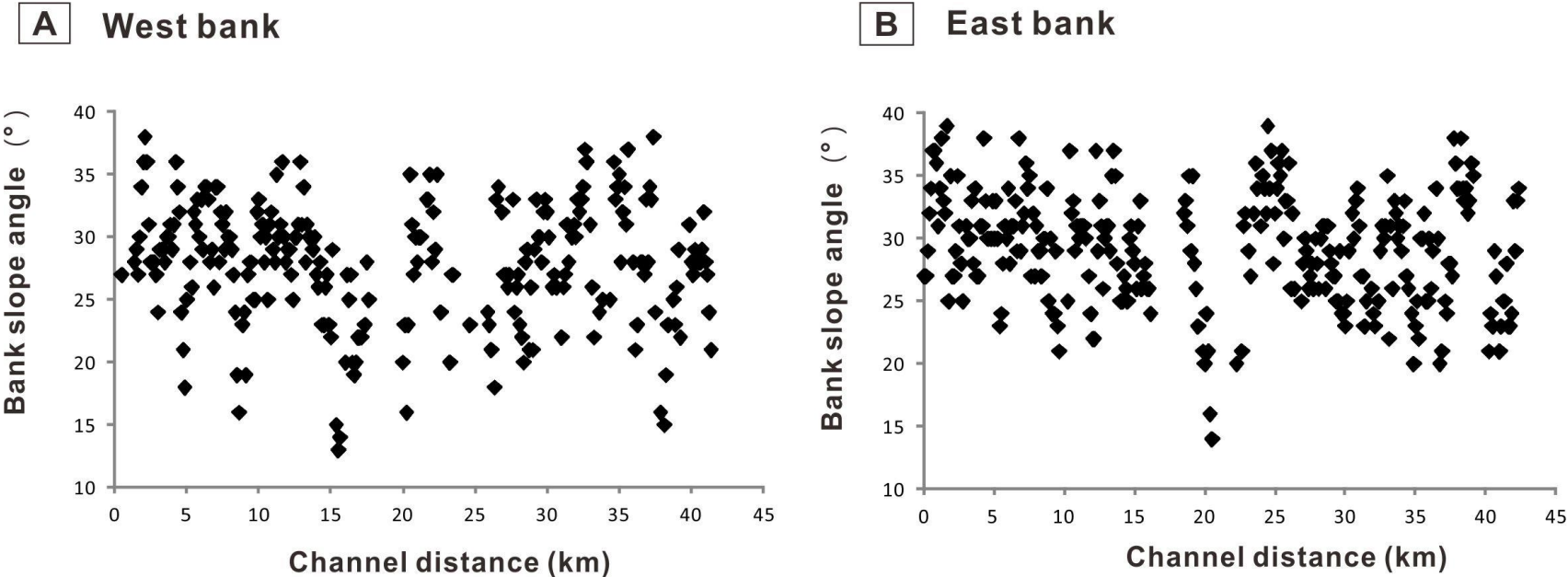
Figure 4.5. Variations in bank slope angles of channel western and eastern banks.

4.3.1.5 Variations in channel dimension

The channel displays significant morphological changes along the channel distance (Fig. 4.4 and Table 4.1). Five Reaches (Reaches a to e) are observed following variations in channel morphological parameters (Figs. 4.3 and 4.4, Table 4.1).

In the first 13 km of Reach a, the channel is steepest and has the largest cross-section, as shown by the highest value of channel gradient, height, width and CSA (Fig. 4.4 and Table 4.1).

In Reach b, between 13 km and 22 km, channel gradient decreases and is also accompanied by significant decreases of channel height, width and CSA (Fig. 4.4 and Table 4.1). For example, the channel width decreases more than 200 m and the CSA decreases by a factor of nearly 4 in this reach when compared to Reach a (Table 4.1). However, the width of the channel floor and the aspect ratio increase to their maximum value against a decreased channel size in Reach b (Figs. 4.4B-E and Table 4.1).

In Reach c (22-27 km), the channel size decreases to its lowest value, with a channel height of 38 m, a channel-floor width of 165 m, a channel width of 345 m and CSA of 0.008 km^2 (Table 4.1). The aspect ratio of the channel declines to 9 in this reach (Table 4.1).

In Reach d, abrupt increases in channel height and width are observed between 27 km and 32 km. These are accompanied by a nearly four-fold increase in the channel CSA when compared to Reach c (Figs. 4.4B, C and E, Table 4.1).

In Reach e (32-42 km) channel width, height and CSA decrease again with increasing aspect ratios (Figs. 4.4B-E and Table 4.1).

4.3.2 Quantitative valley analyses

The valley is divided into three reaches (Reaches A to C) based on the observed changes in valley dimension (Figs. 4.3 and 4.6, Table 4.2).

4.3.2.1 Depth profiles of valley thalweg and valley wall, and valley height profile

There are five intervals observed in the depth profile of the valley thalweg (Fig. 4.6A). The valley is steepest in the first 6 km, with a gradient of 1.88° (32.8 m/km). The valley gradient
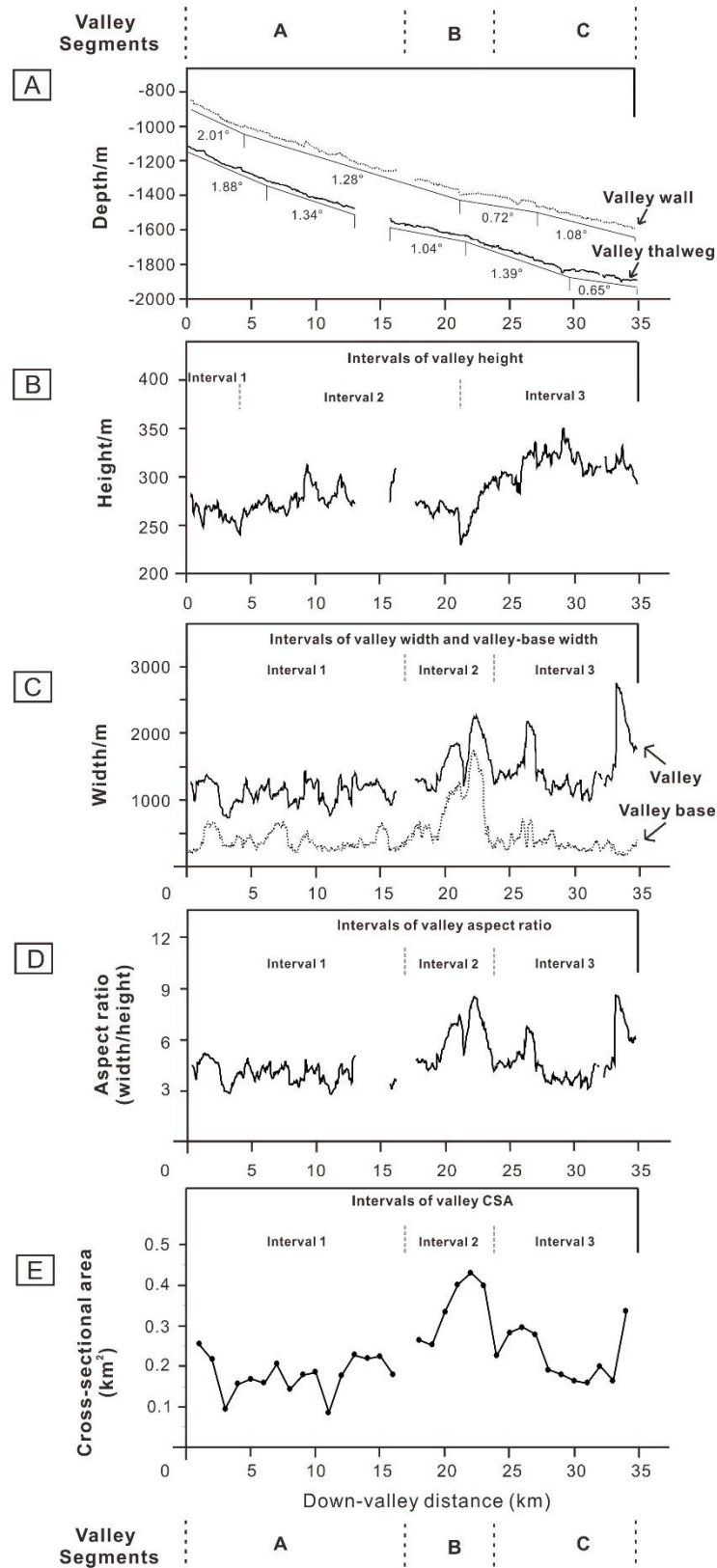
Figure 4.6. Quantitative analyses of the valley. A) Depth profile of the valley wall and thalweg. B) Valley height profile. C) Width of the valley base and valley. D) Aspect ratio (width/height) of the valley. E) Cross-sectional area (CSA) of the valley.

Table 4.2. Summary of morphological data acquired along the valley.

Measurements \ Segments	Downslope → A (0-17km)	B (17-24 km)	C (24-35 km)
Valley gradient/°	1.51	1.11	1
Valley height /m (ave.)	273	268	314
Width of valley base /m (ave.)	382	849	342
Valley width /m (ave.)	1117	1602	1495
Aspect Ratio (ave.)	4	6	5
CSA /km^2 (ave.)	0.181	0.348	0.226
Examples of valley cross section in each segment	100 m / 500 m	100 m / 500 m	100 m / 500 m
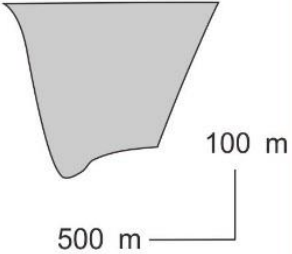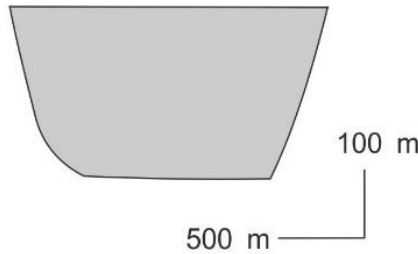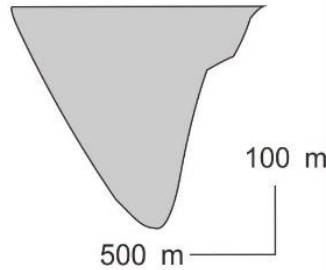
decreases to 1.34° (23.4 m/km) between 6 km and 13 km due to the presence of salt diapir D5. For the next 3 km, the valley thalweg is difficult to recognise because it presents similar seismic facies to an underlying MTD, both of which are composed of discontinuous, high-amplitude seismic reflections. Between 16 km and 22 km the valley gradient declines to 1.04° (18.2 m/km), and is then followed by an increase to 1.39° (24.3 m/km). In the remainder of the valley, the valley gradient decreases to its lowest value of 0.65° (11.3 m/km) between 30 m and 35 m (Fig. 4.6A).

The depth profile of the valley wall shows its steepest interval in the first 4 km, with a value of 2.01° (35.1 m/km) (Fig. 4.6A). This interval is followed by a decrease in valley wall gradient to 1.28° (22.3 m/km) between 4 and 21 km, and 0.72° (12.6 m/km) from 21 to 27 km. In the fourth interval, between 27 and 35 km, the valley wall gradient increases to 1.08° (18.9 m/km) (Fig. 4.6A).

The valley height is dependent on variations in both the depth of valley wall and valley thalweg (Figs. 4.6A and B). It ranges from 230 m to 350 m along the full length of the valley (Fig. 4.6B). In interval 1, the valley height decreases due to a rapid drop in valley wall depth (Figs. 4.6A and B). This trend is followed by an increase in valley height in the second interval (4-21 km), where it changes from 230 m to 310 m. The valley height decreases to its lowest value of 230 m at the end of interval 2. In interval 3, the valley height shows a marked increase. It increases to the highest value of 350 m at 29 km and is followed by a decrease in the remainder of the valley (Fig. 4.6B).

4.3.2.2 Width profiles of valley and valley base

The width profiles of the valley and the valley base share similar patterns. They both have relatively higher average values in interval 2 than those in intervals 1 and 3 (Fig. 4.6C).

The valley width ranges from 730 m to 2755 m (Fig. 4.6C). It fluctuates between 730 m and 1440 m in interval 1 (0-17 km). This fluctuation is followed by an increase to 2260 m between 17 m and 24 km in interval 2 (Fig. 4.6C). In interval 3 (24-35 km), valley width varies from 1000 m to 1500 m, with two maxima of 2190 m at 26.4 km and 2755 m at 33.25 km. The latter value of 2755 m represents where the valley width reaches its maximum (Fig. 4.6C).

The width of the valley base varies from 160 m to 700 m for most part of the valley. However, a rapid increase occurs between 19 km and 23 km, where the valley base can be up to 1740 m wide and an increase in valley width is also recorded (Fig. 4.6C).

4.3.2.3 Aspect ratio and cross-sectional area (CSA) of valley

The aspect ratio of the valley has a similar trend to the valley width (Figs. 4.6C and D), suggesting that valley width varies relatively more than the valley height. The aspect ratio ranges from 3 to 5 in the first 20 km. It is followed by an increase in interval 2 (20-24 km), where the aspect ratio rises up to 9. The aspect ratio decreases to 4 for the majority of interval 3 (24-35 m) but with two peak values, 7 at 26.5 m and 9 at 33.5 m, which are, induced by an increasing valley width (Fig. 4.6D).

The valley CSA also shares a similar pattern to valley width (Figs. 4.6C and E). The CSA is highest between 17 m and 23 m in interval 2, where it ranges from 0.25 km^2 to 0.43 km^2, whereas it varies between 0.087 and 0.337 km^2 in intervals 1 and 3 (Fig. 4.6E).

4.3.2.4 Variations in valley dimension

The valley is divided into three reaches based on the observed morphological variations (Figs. 4.3 and 4.6, Table 4.2). These reaches have similar aspect ratios but different valley CSAs (Table 4.2).

The valley is smallest in Reach A, showing the lowest average value of valley-base width of 380 m, valley width of 1120 m, valley height of 270 m and CSA of 0.18 km^2 (Table 4.2).

In Reach B, between 17 and 24 km, the width of the valley base and the valley record maximum average values of 850 m and 1600 m, respectively (Table 4.2). This is particularly observed when considering the width of the valley base, which increases more than two-fold from Reach A to Reach B (Table 4.2). Such an increase results in a relatively higher CSA value in Reach B (Table 4.2).

The size of the valley decreases in Reach C, as shown by the relatively lower values of the valley width and the CSA when compared to Reach B, despite the fact that the largest valley height is observed in Reach C (Table 4.2).

4.4 Variations in channel sinuosity within Quaternary submarine channel system

The following sections focus on the channel system downstream of confluence C_B, where the channel is more sinuous (Fig. 4.3). The studied channel system is divided into three reaches based on the variations in channel sinuosity (Fig. 4.7).

Channel reaches	Pathways of initial and present channel	Initial channel		Present channel	
		Pathway	Sinuosity	Pathway	Sinuosity
Reach I			1.11		1.72
Reach II			1.51		1.64
Reach III			1.05		1.06

Figure 4.7. Schematic diagram showing the spatial and temporal variations in the channel pathways. The location of this figure is shown in Fig. 4.3. Channel sinuosity increases from 1.11 to 1.17 in the Reach I. In contrast, there are small changes in channel sinuosity in the Reaches II and III.

4.4.1 Spatial and temporal changes of channel sinuosity

This study shows spatial and temporal changes in channel pathway and associated sinuosity (Fig. 4.7). The pathway of the initial channel has a highest sinuosity value of 1.51 in the Reach II (Fig. 4.7). It becomes less sinuous in the Reaches I and III, where channel sinuosity reduces to 1.11 and 1.05, respectively (Fig. 4.7).

The pathway of the present-day channel is much more sinuous in the Reach I and II, with sinuosity of 1.72 and 1.64, respectively (Fig. 4.7). Its sinuosity decreases to 1.06 in the Reach III (Fig. 4.7).

In addition, there are temporal changes of channel sinuosity during channel evolution (Fig. 4.7). In Reach I, channel sinuosity increases considerably from 1.11 for initial channel to 1.72 for present channel (Fig. 4.7). In contrast, channel sinuosity displays slight increases in Reaches II and III, 0.13 in Reach II and 0.01 in Reach III from the initial to the present channel (Fig. 4.7).

4.4.2 Depth profile of initial channel, present channel, and seafloor

The valley slope of the initial channel is 1° in Reach I. It increases to 1.44° in Reach II and is followed by a decrease in the Reach III, where the valley slope decreases to 0.61° (Fig. 4.8).

The valley-depth profile of present channel shows a similar trend to that of the initial channel (Fig. 4.8). It is highest (1.22°) in Reach II, and smaller in Reaches I and III, where the valley slopes are 0.96° and 0.57°, respectively (Fig. 4.8).

The seafloor slope on the west and east of the channels shows similar trends. It is 1.05° along the channel system without significant changes (Fig. 4.8).

4.4.3 The relationship between valley slope and channel sinuosity

The variations in valley slope of the initial channel are closely related to channel sinuosity. The channel is more sinuous in Reach II where valley slope is steeper, while the channel is less sinuous in Reaches I and III, where valley slope is lower (Fig. 4.9).

In addition, the valley slope of the present channel shows a positive relationship with channel
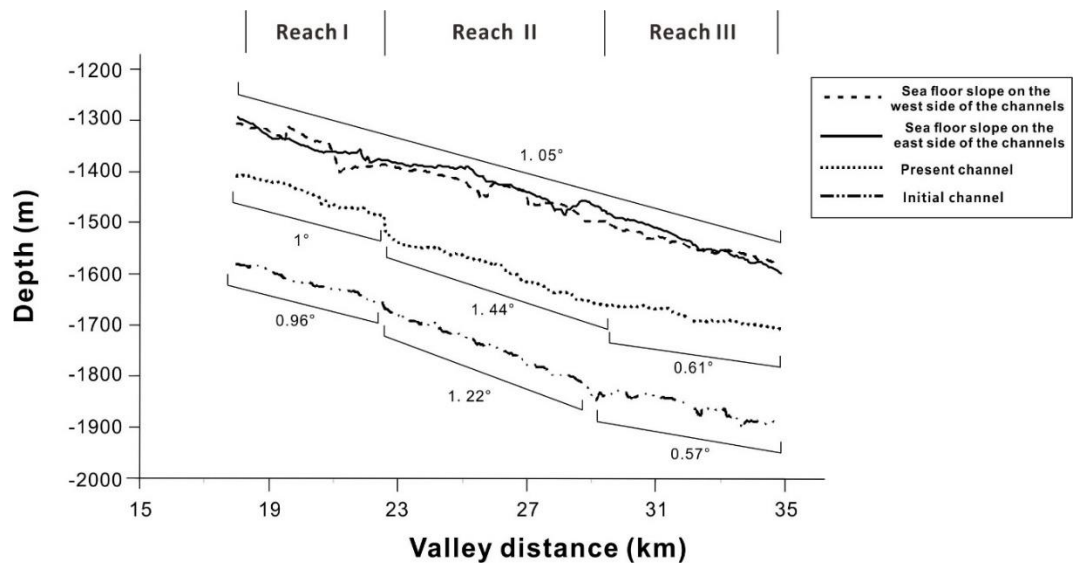
Figure 4.8. Thalweg-depth profiles of the initial and present channels within the Quaternary channel system. The valley slope of these two channels shows similar trends, with steeper slope in the middle reach and gentler slopes in the upper and lower reaches. Seafloor slope has no clear changes.
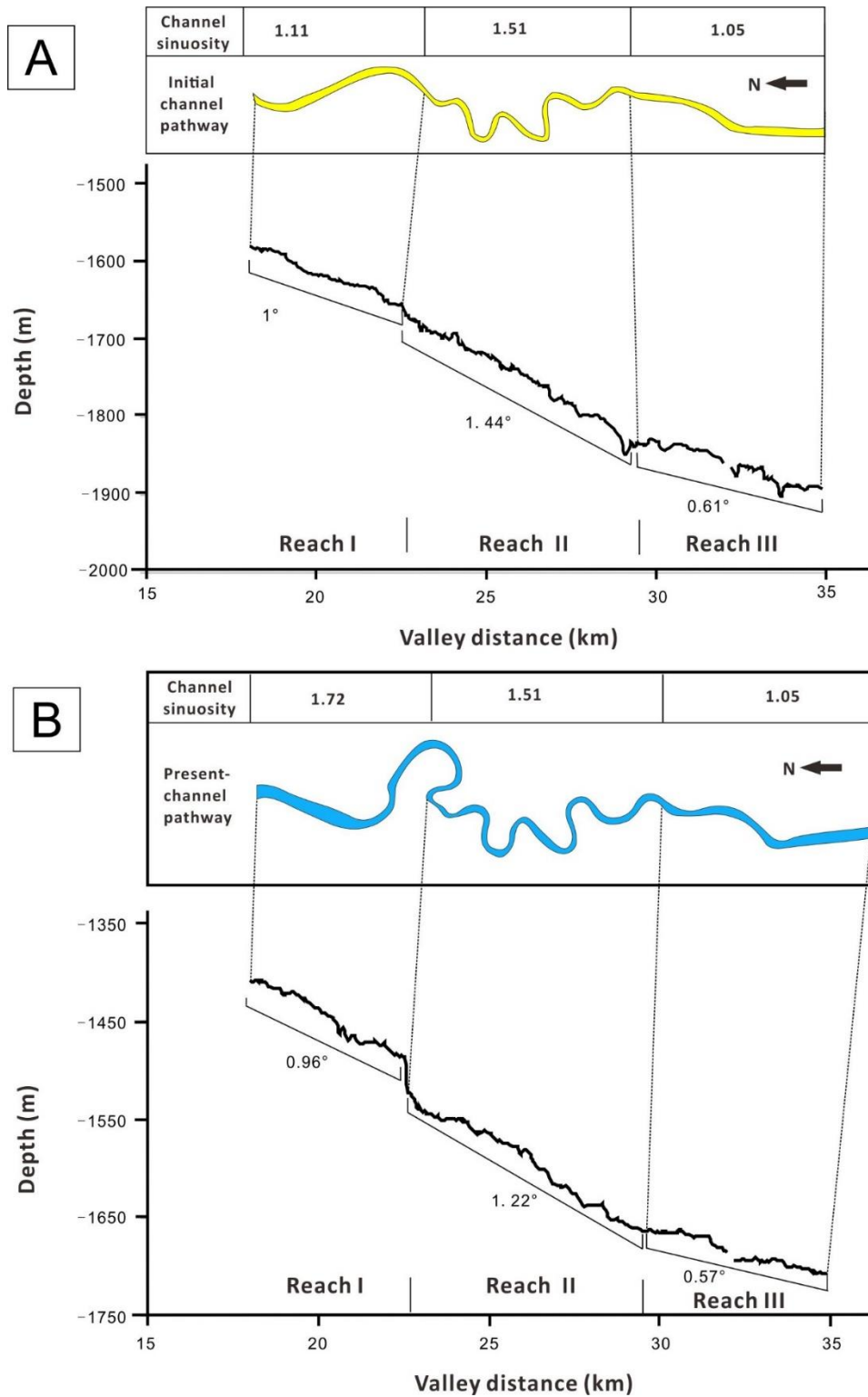
Figure 4.9. Schematic diagrams showing the relationship between valley slope and channel sinuosity. There is a positive relationship between the valley slope and channel sinuosity for the entire length of initial channel, and for the middle and lower reaches of the present channel.

sinuosity in Reaches II and III, but a negative relationship in Reach I (Fig. 4.9).

Chapter 5

Variations in sediment dispersal patterns within the Quaternary channel system

5. Variations in sediment dispersal patterns within the Quaternary channel system

5.1 Introduction

This chapter focuses on spatial variations in sediment dispersal patterns (i.e. sediment volumes and types) within the Quaternary submarine channel system.

5.2 Methods

The cross-sectional area of the valley (CSA_V) and valley-fill deposits (CSA_{VF}), and valley slope were measured at intervals of 1 km along the valley. A depositional ratio, defined as CSA_{VF}/CSA_V, is used here to quantify sediment dispersal patterns in the studied channel system. This ratio is the percentage of the area filled by sediments within the valley. It eliminates the influence of CSA_V on deposition, as flows may deposit more sediment when accommodation space is larger.

Lateral channel migration involves shifts in channel thalweg and banks. As the thalweg of the initial channel may have been eroded by subsequent gravity flows, its inner bank is usually preserved during lateral migration. The lateral displacement of channel banks is thus used to quantify lateral migration within the channel system (Fig. 5.1). The parameter L_M is the distance between the initial and present-day channel banks (Fig. 5.1). It indicates the magnitude of lateral migration and was obtained from the same cross-sections used to measure CSA_V.

5.3 Spatial variations in sediment volume and depositional ratio

Three reaches are divided based on variations in both sediment volume and types along the Quaternary channel system (Fig. 5.2).

In the upper reach, the sediment volume of the valley is 0.63 km^3 and is lower than other reaches (Fig. 5.2). The depositional ratio is here 54% on average (Fig. 5.3A). Valley aggradation
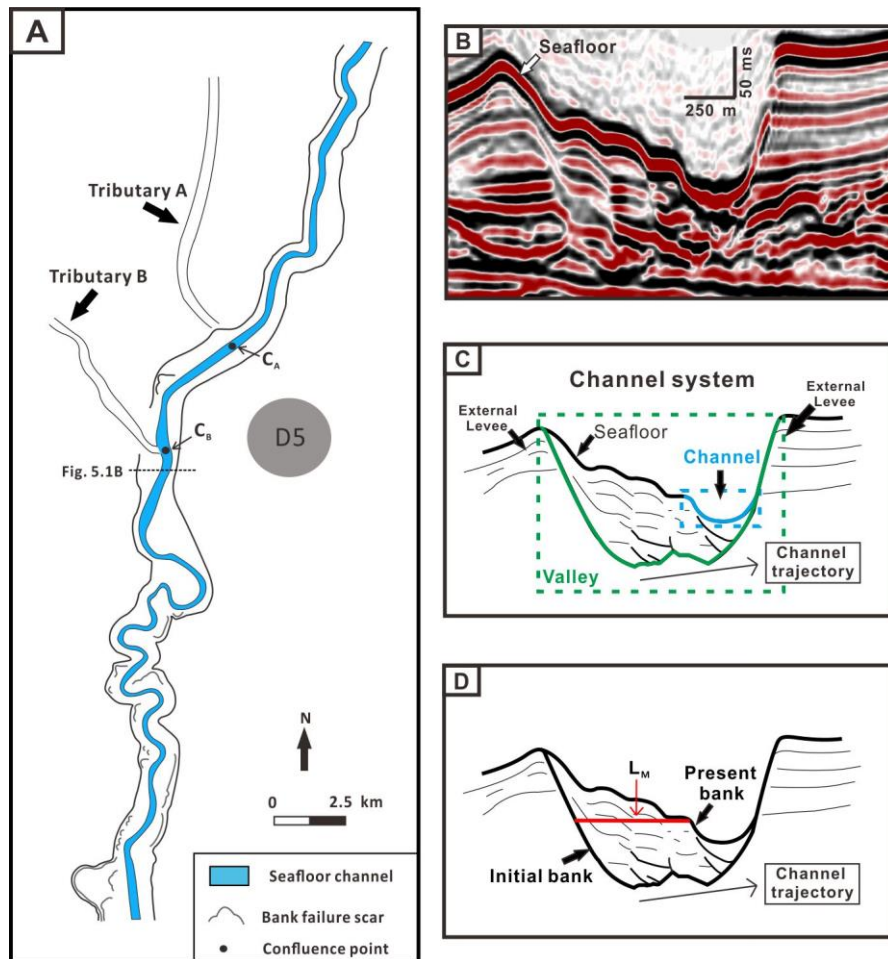
Figure 5.1. A) Schematic diagram shows the morphology of the Quaternary channel system. There are two major tributaries that contribute sediment to the main flow pathway. B) and C) Uninterpreted and interpreted seismic sections summarising the terminology used in this study. D) Schematic diagram showing the methods used to measure the magnitude of lateral channel migration (L_M).
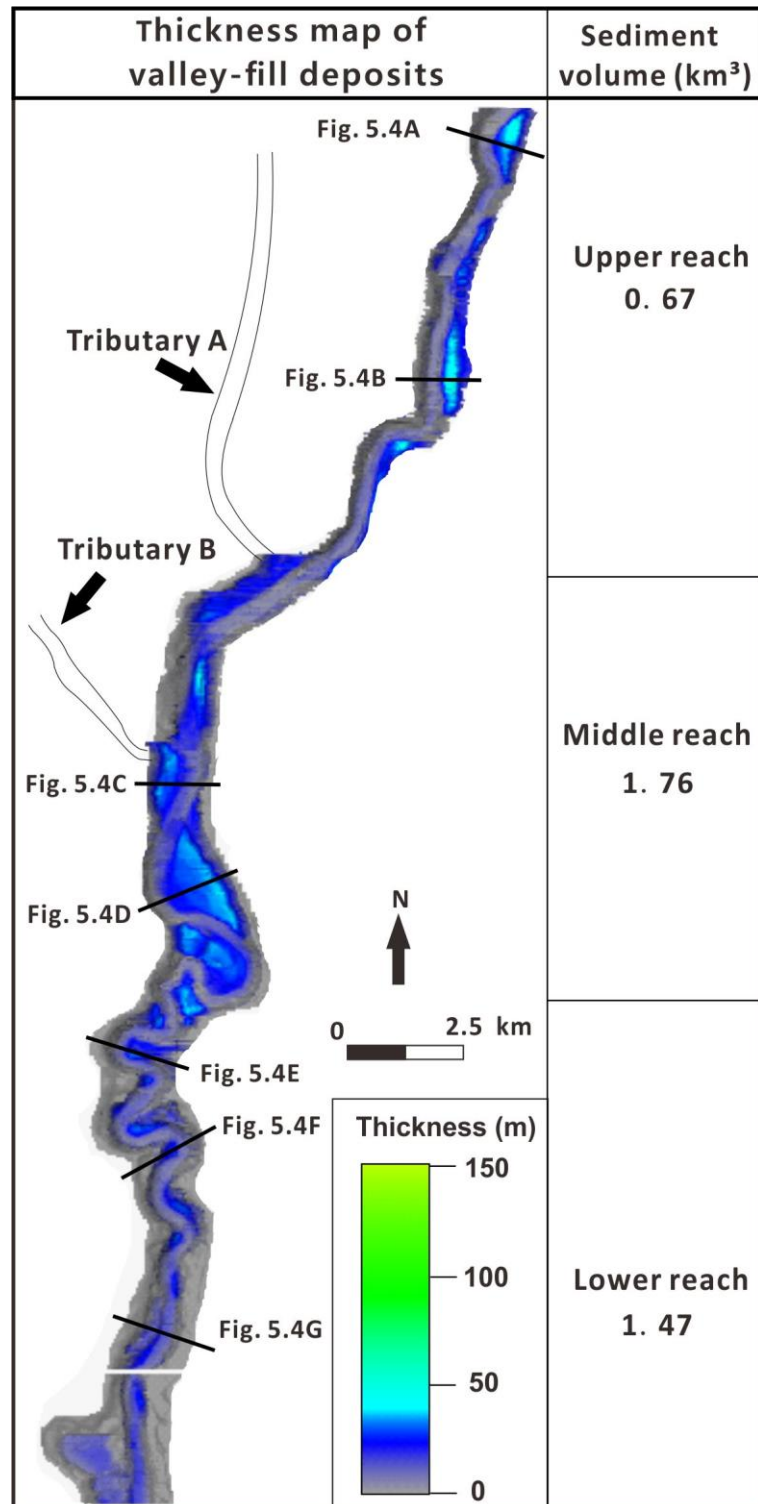
Figure 5.2. Thickness map of valley-filling deposits within the channel system. Sediment volume is higher in the middle reach than in the upper and lower reaches.
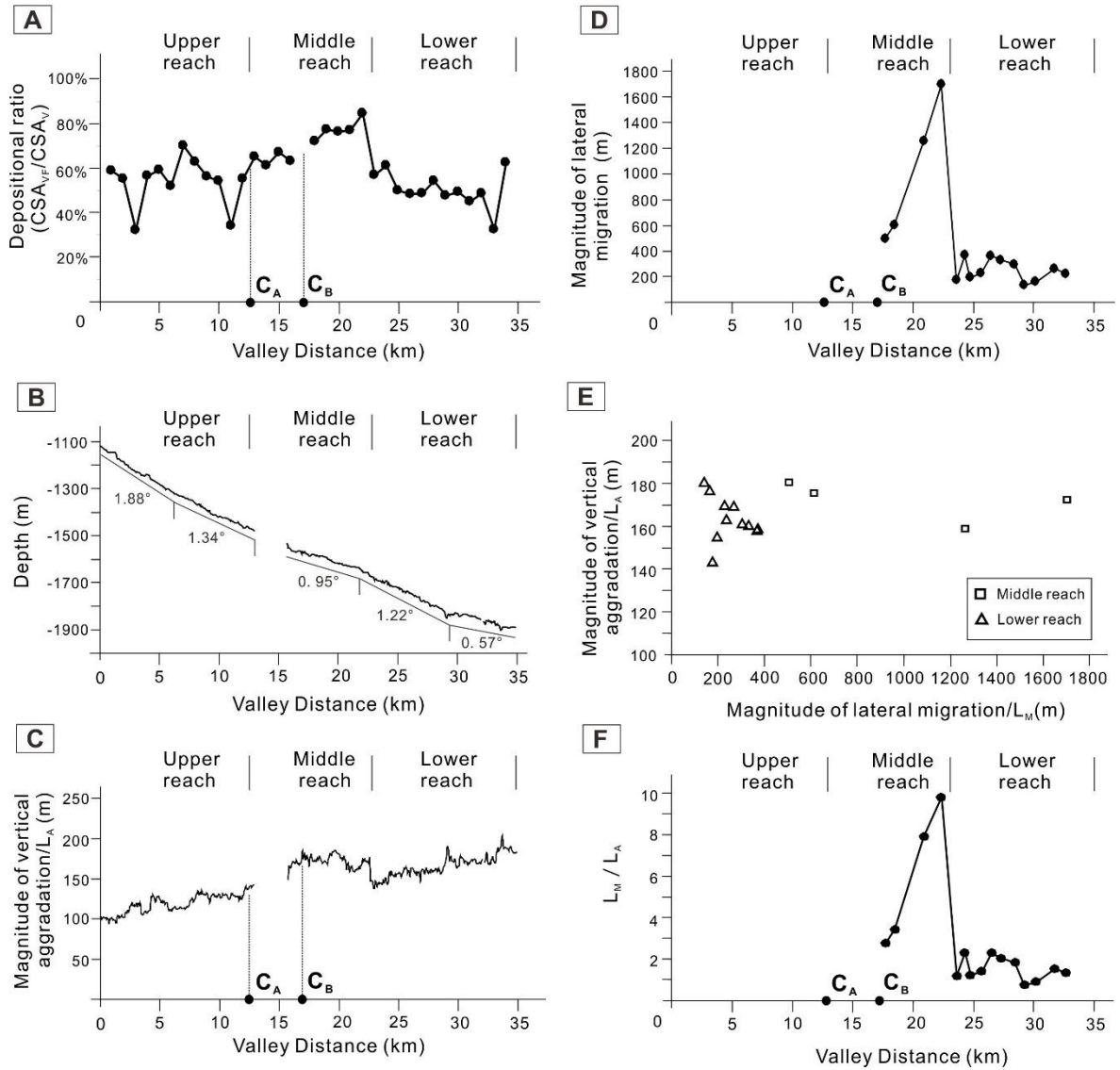
Figure 5.3. A) Depositional ratio along the channel system. B) Valley-depth profile. C) Magnitude of vertical aggradation (L_A) along the channel system. D) Magnitude of lateral migration (L_M) along the channel system. E) Relationship between L_A and L_M. F) L_M/L_A along the channel system.

is also lowest in this reach, which shows the steepest valley slope (Figs. 5.3 B and C).

In the middle reach, the channel system shows its largest depositional ratio (Fig. 5.3A), with an average value of 72%. Because the depositional ratio increases downstream of confluence points C_A and C_B (Fig. 5.3A), the observed increases in sediment amount are caused by enhanced sediment supply from Tributaries A and B.

In the middle reach, sediment volume within the valley is 1.74 km^3, increasing more than two-fold when compared to the upper reach (Fig. 5.2). The channel system here also shows its largest depositional ratio on the middle reach, with an average value of 72% and a maximum value of ~90% (Fig. 5.3A). These values correlate with the presence of Tributaries A and B. Sediment supply from tributaries led to the higher magnitude of lateral migration and vertical aggradation in this reach (Figs. 5.3C and D).

In the lower reach, the sediment volume decreases to 1.47 km^3 (Fig.5.2). The depositional ratio in this reach decreases 22% compared to the middle reach, showing an average value of 50% (Fig. 5.3A). These reductions in sediment volume and depositional ratio suggest that sediment sourced from upslope tributaries was not transported through long distances to fill the lower reach. As a result, L_M in this reach decreases to 60-270 m, much lower than L_M in the middle reach, where L_M can be more than 1000 m (Fig. 5.3D). Aggradation varies with valley slope in this reach (Fig. 5.3C). Between 23 km to 29 km, where the reach shows its steeper valley slope of 1.22° (Fig. 5.3B), valley aggradation ranges from 140 m to 160 m (Fig. 5.3C). From 29 km to the southern limit of dataset, valley aggradation changes between 160 m and 200 m due to a reduced valley slope of 0.57° (Figs. 5.3B and C).

5.4 Spatial variations in sediment types

Variations in sediment types of the Quaternary channel system are also described following three interpreted reaches (Fig. 5.2).

In the upper reach, the valley-fill deposits comprise slump deposits and overbank strata, as shown on seismic data by chaotic, transparent facies overlain by continuous, low- to high-amplitude reflections (Figs. 5.4A-B). Mass-transport deposits are mainly located in the upper reach. Slump
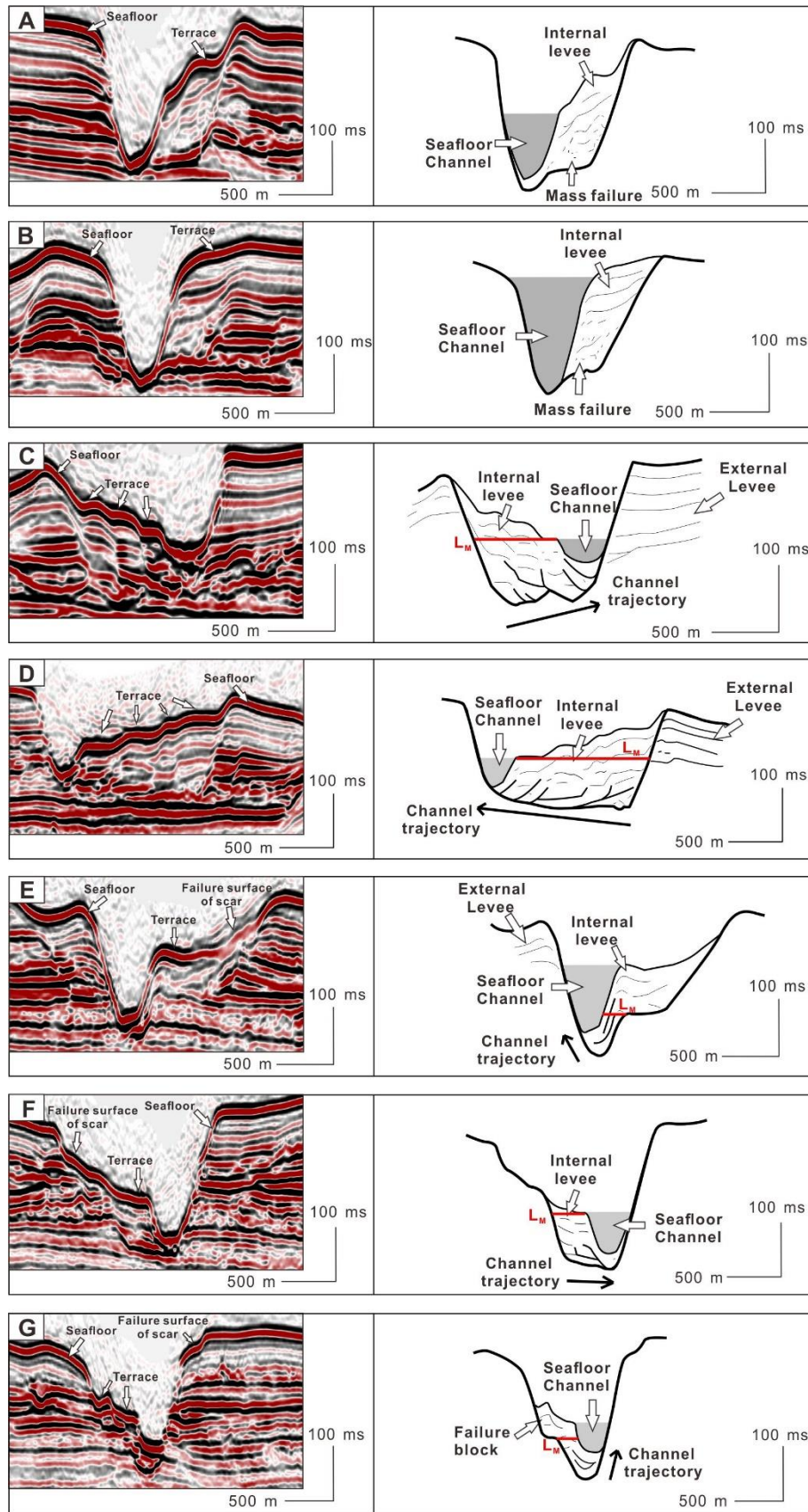
Figure 5.4. Selected seismic profiles from each of the reaches of the channel system.

deposits in this reach extend for 8 km along the channel system. Because it is unlikely that localized mass failure on channel banks is continuous for such a long distance, these deposits were likely sourced from the shelf edge.

In the middle and lower reaches, valley-fill deposits show similar seismic facies, which comprises discontinuous, higher amplitude reflections on the valley bases (Figs. 5.4C-G), and overlying sub-horizontal to horizontal, parallel, moderate- to high-amplitude reflections (Figs. 5.4C-D, F-G) and transparent to chaotic reflections at places (Fig. 5.4E).

In the study area, valley-fill architecture is similar to that of Benin's and Niger delta's submarine channel systems (Deptuck et al., 2003). Discontinuous, high-amplitude seismic reflections on the valley base are interpreted as basal lags (Figs.5.4C-G). Moderate- to high-amplitude reflections above basal lags (Figs. 5.4C-D, F-G) are difficult to identify as abandoned channel-fills or overbank deposits because these two deposits are similar to each other (Deptuck et al., 2003, 2007). Some wedge-shaped seismic reflections can, however, be interpreted as internal levees of the channel system (Figs. 5.4C and D).

Additionally, multiple channel-form erosional truncations are shown on the valley base in the middle and lower reaches (Figs. 5.4C-G). These erosional truncations are interpreted to represent the positions of previous channel banks (Figs. 5.4C-G). The shifts in the position of channel banks show the trajectory of lateral channel migration (Figs. 5.4C-G) and indicate discrete migration processes within the channel system. A similar discrete migration process has also been documented by previous studies (e.g. Deptuck et al., 2007; Kolla et al., 2007; Maier et al., 2012). This type of migration is a cut-and-fill process, which involves the infilling of channel before the channel shifts its position, with flows eroding the channel banks and generating remnant channel-fill deposits in inner banks (Deptuck et al., 2007; Kolla et al., 2007; Maier et al., 2012).

Inclined reflections, which indicate relative continuous migration somewhat similar to fluvial channels (Abreu et al., 2003; Kolla et al., 2007), are only seen at only one of the channel bends (Fig. 5.4E). They are dipping 24° toward the channel thalweg and were probably formed by continuous lateral migration. However, most of the bends in the lower reach are characterised by the presence of channel-form erosional truncations and the absence of inclined reflections (Figs. 5.4C-D, F-G). Subhorizontal to horizontal, moderate- to high-amplitude reflections within the valley (Figs. 5.4 C-

D, F) are interpreted as channel-fill deposits formed during the filling processes of discrete lateral migration. The presence of these reflections also supports the predominance of discrete migration processes within the channel system.

5.5 The relationship between lateral channel migration and other parameters

Lateral channel migration mainly occurred in the middle and lower reaches of the Quaternary channel system (Fig. 5.5). This section uses Reaches I, II and III to describe variation in the magnitude of lateral migration (L_M) along the channel system, similarly to Section 4.4 (Figs 4.7 and 5.5). Reach I is the middle reach in Fig. 5.2, Reaches II and III comprise the lower reach in Fig. 5.2.

L_M is positively correlated with CSA_{VF} in Reaches I and III (Fig. 5.6A), suggesting deposition during lateral migration is probably the main depositional process in these two reaches. However, there is no clear relationship between L_M and CSA_{VF} in Reach II (Fig. 5.6A), where numerous scars developed on the banks of the channel system (Fig. 5.5). These scars are formed by bank failures. The unclear relationship between L_M and CSA_{VF} in Reach II may relate to bank failures because some valley-fill deposits may have slumped into the channel.

L_M shows a positive relationship with CSA_V in Reach I (Fig. 5.6B). In this reach, the increase in valley size (i.e. CSA) is interpreted to result from cut bank erosion during lateral channel migration. Turbidity currents undercut the lower part of the valley and were followed by the collapse of overhanging blocks (i.e. cantilever failure), leading to the lateral widening of the valley, especially the valley base.

L_M does not appear to correlate with CSA_V in Reaches II and III (Fig. 5.6B), hinting at a different erosional mechanism, other than cut-bank erosion, contributing to the enlargement of the channel system in this reach. Such a mechanism comprised shallow-seated bank failure within the channel system, as evidenced by the large amounts of scars on its banks (Fig. 5.5).
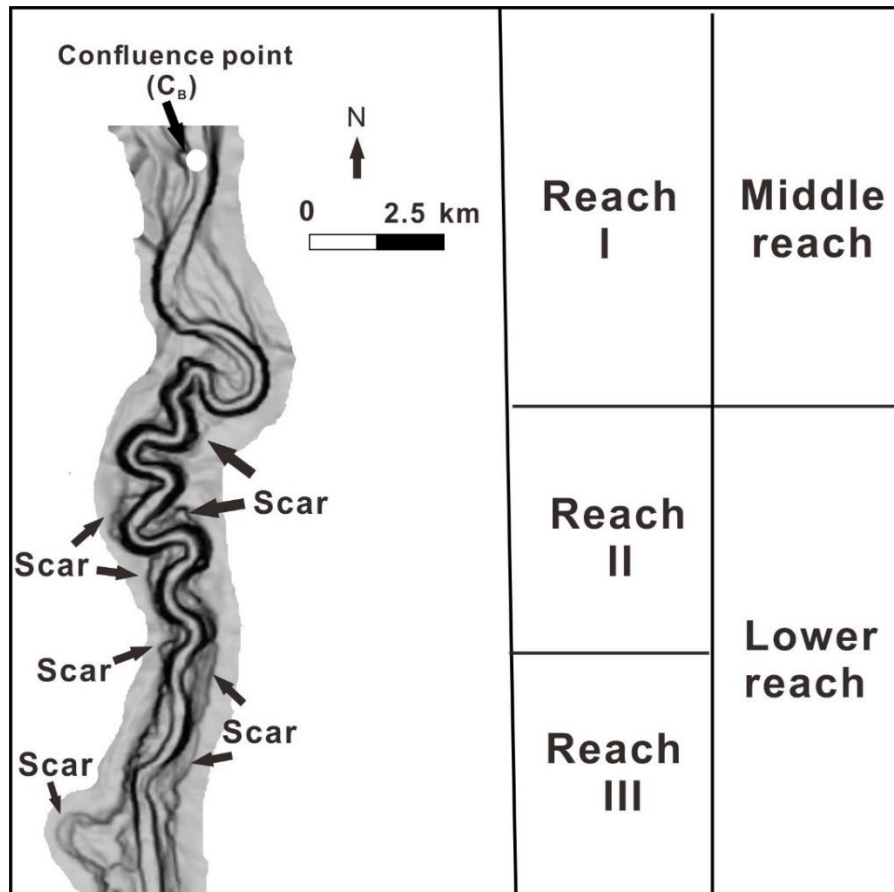
Figure 5.5. Dip map of the part of Quaternary channel system showing different reaches along the channel system. Various scars are present in the lower reach (Reaches II and III).
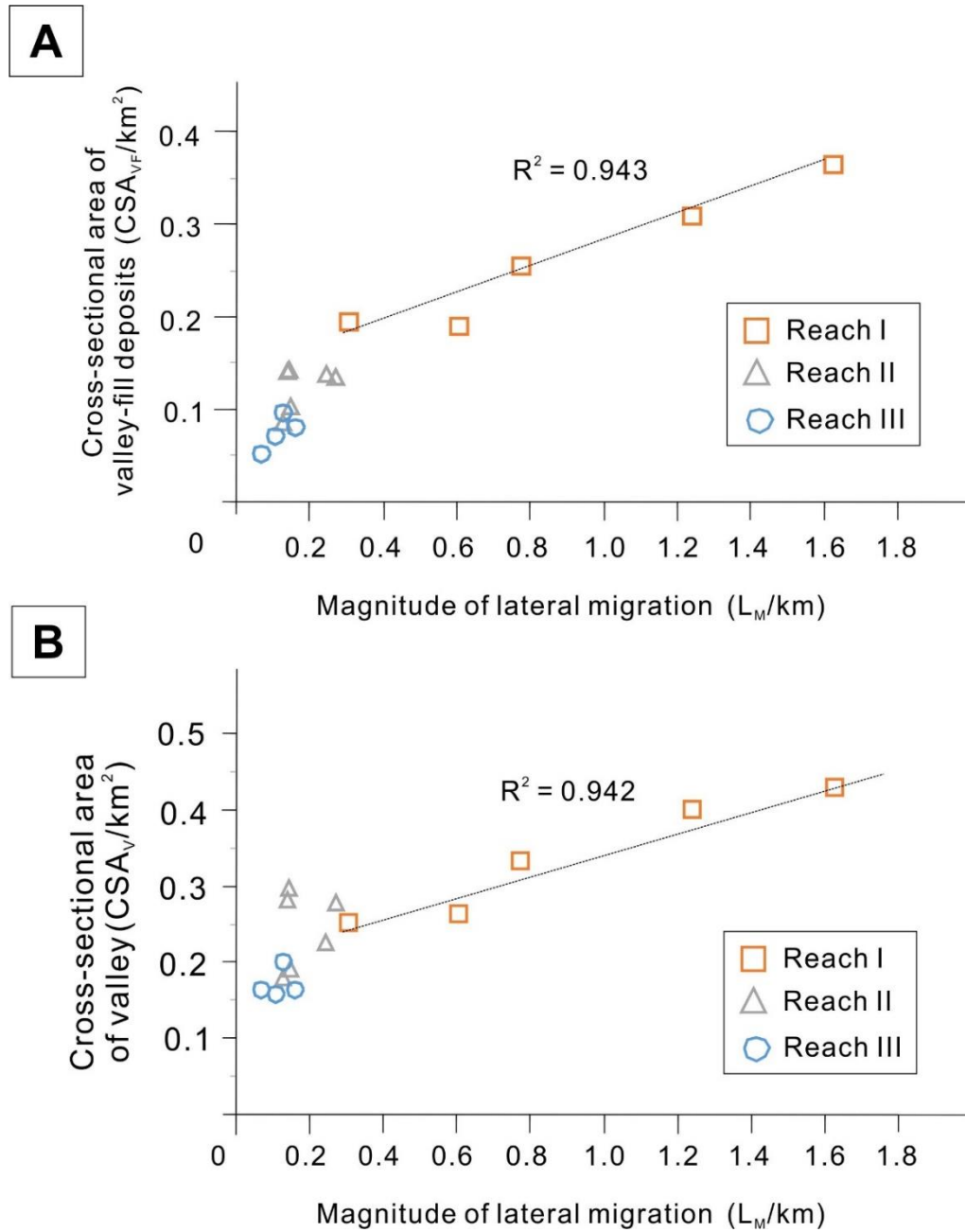
Figure 5.6. A) Magnitude of lateral migration (L_M) against Cross-sectional area of valley-fill deposits (CSA_{VF}). B) Magnitude of lateral migration (L_M) against Cross-sectional area of valley (CSA_V).

Chapter 6

Mass-wasting related features within the channel systems

6. Mass-wasting related features within the channel systems

6.1 Introduction

This chapter focuses on the erosional and depositional features related to mass-wasting events within the channel systems, including bank-failure scars on the banks of Quaternary channel system and mass-transport deposit within the Pliocene-Quaternary channel system.

6.2 Mass-failure events on the banks of the Quaternary channel system

A large number of arcuate-shaped scars are observed on the banks of the channel system, especially in Zone 3 (Fig. 6.1). Scars with different shapes, such as single scars with amphitheatre-shape headwalls and multiple scars with curved headwalls, are mainly located on the west bank of channel, regardless of being in the inner or outer banks of the channel (Fig. 6.1). Additionally, there are some elongate scars observed on the eastern bank of the channel system (Fig. 6.1).

These scars do not cross, or extend towards the channel floor and are located at upper part of channel bank, i.e. 70 m to 140 m above the modern channel thalweg (Fig. 6.2). The height of the scarps ranges from 30 m to 70 m. The headwall slope of scars ranges from 15° to 30°. The bottom of scar is nearly flat, varying in angle from 1° to 9° (Fig. 6.2).

Continuous seismic reflections beneath and adjacent to the scars indicate these scars are erosional features, which are bank failure surfaces left behind by mass blocks and slides that have collapsed into the channel (Fig. 6.2). The location of scars suggests that they were formed by shallow-seated bank failure (i.e. bank failure surface above channel floor), in contrast to deep-seated bank failures (i.e. bank failure surface cross or extend to channel floor) recognized in the Gulf of Mexico (Sawyer et al., 2013).

The presence of scars coincides spatially with the peak value in valley width at 26.5 km and 33 km (Fig. 6.3), indicating that the valley was widened through shallow-seated mass failures in Zone 3.
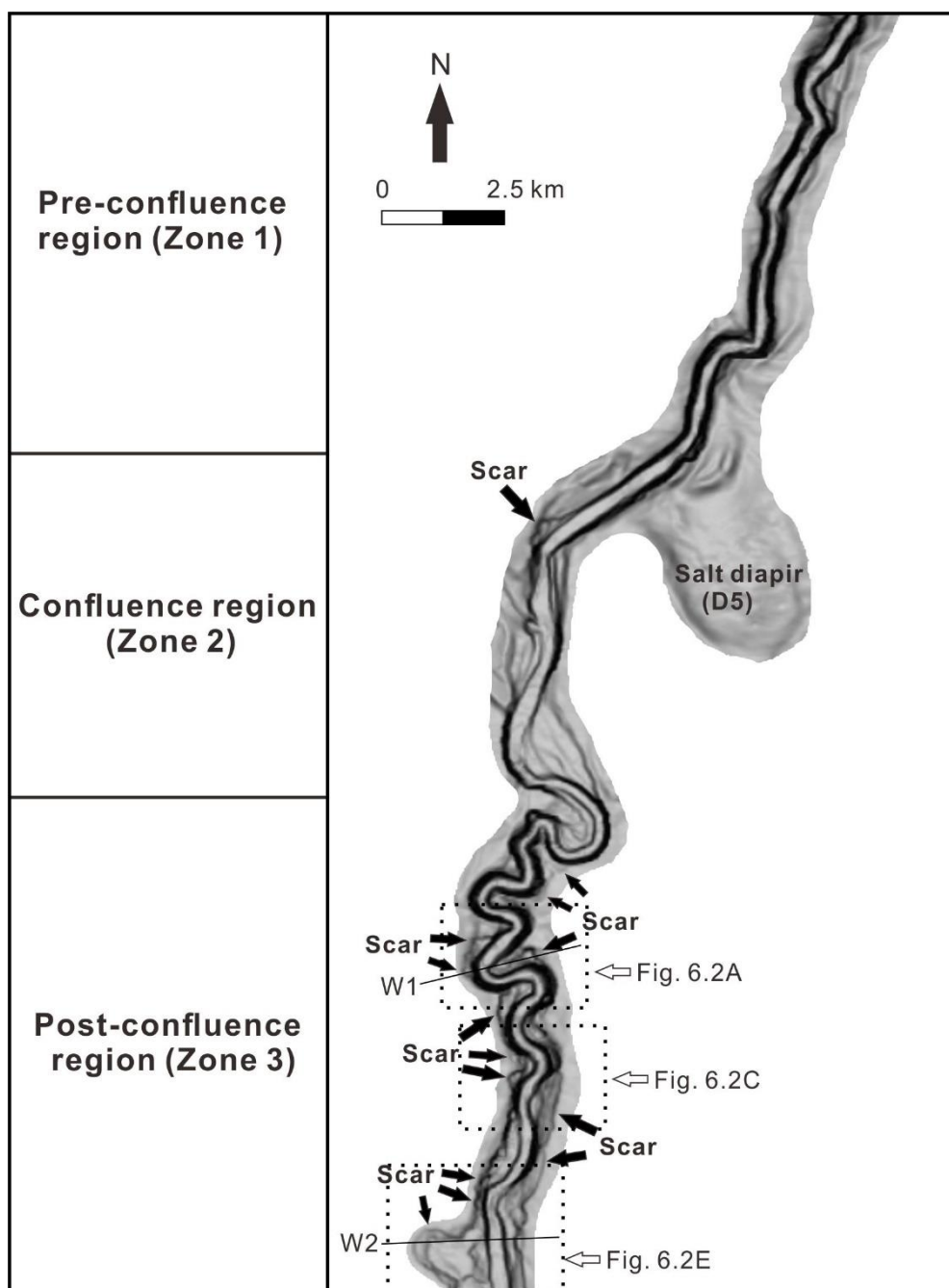
Figure 6.1. Dip map of the Quaternary channel system investigated in this thesis. Multiple scars are shown on the banks of the channel system in Zone 3.
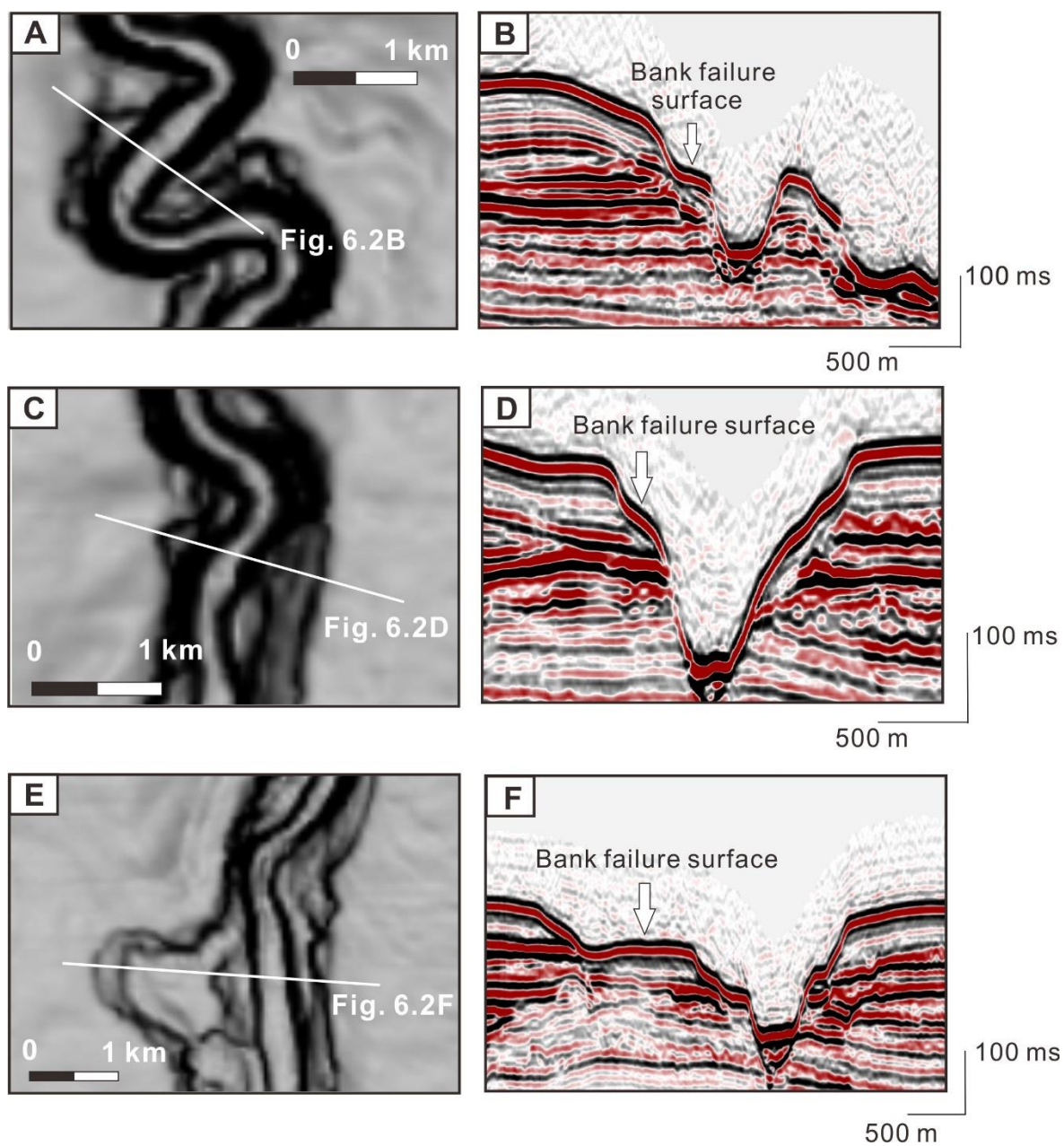
Figure 6.2. Dip maps and seismic sections showing bank failure scars within the Quaternary channel system. The location of dip maps is shown in Fig. 6.1.
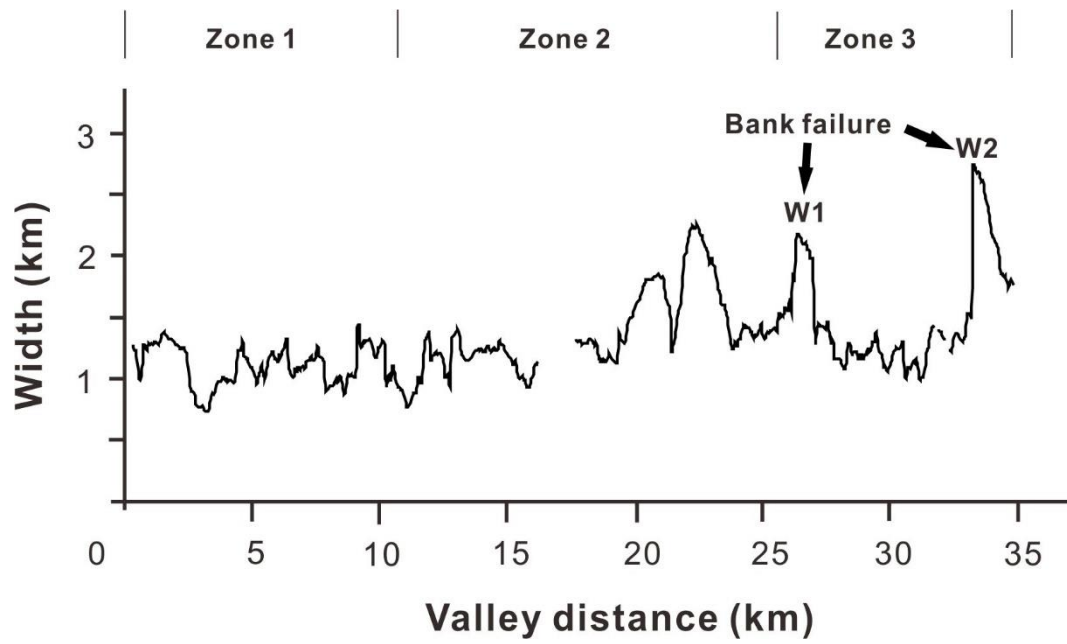
Figure 6.3. Width profile of the Quaternary channel system. It shows two peaks at 26.5 km and 33 km, both of which are associated with the occurrence of bank failure scars. The location of W1 and W2 are shown in Fig. 6.3.

6.3 Mass transport deposits (MTDs) and adjacent channel-fill deposits within the Pliocene-Quaternary submarine channels in the confluence region

6.3.1 Methods

The mapping of the Pliocene–Quaternary Rio Doce Channel System involved a combination of autotracking and manual line-by-line interpretation. Architectural elements in the channel system were imaged by selected seismic lines, combined with dip maps, root-mean-square (RMS) amplitude maps, thickness maps, and variance slices extracted from the interpreted seismic volume.

Quantitative analyses were conducted along the main pathway (east tributary and post-confluence channel) of the channel system (Figs. 6.4 and 6.5), with its width and height measured at 62.5 m intervals. The cross-sectional area (CSA) of the channel system was measured at 1 km intervals.

6.3.2 General morphology of the Pliocene–Quaternary Rio Doce Channel System

The Pliocene–Quaternary Rio Doce Channel System is a partly filled channel system. It is recognised as a sinuous channel on the seafloor (Fig. 6.5). The morphology of the channel system varies across the continental slope (Figs. 6.5 and 6.6).

Three main regions were established as a function of the topographic confinement imposed by salt diapirs (Gamboa et al., 2012) (Fig. 6.5). In the pre-confluence region of lower confinement, the channel system is composed of two tributaries (Fig. 6.5). The west tributary shows initially a NNW–SSE course on the upper slope, shifting to a NW–SE strike at a water depth of ~ 1100 m. The east tributary shows a change in strike from NNE–SSW to NE–SW at a water depth of ~ 1300 m, due to the presence of salt diapir D5 (Fig. 6.5). An abandoned channel segment is identified in this same region (Fig. 6.5). The channel system is ~ 1000 m wide, and more than 200 m high in the pre-confluence region (Figs. 6.6A and B). The cross-sectional area (CSA) of the channel system ranges from 0.087 km^2 to 0.256 km^2 (Fig. 6.6C).

In the confluence region, where gravity flows tend to be deflected off the salt diapirs due to
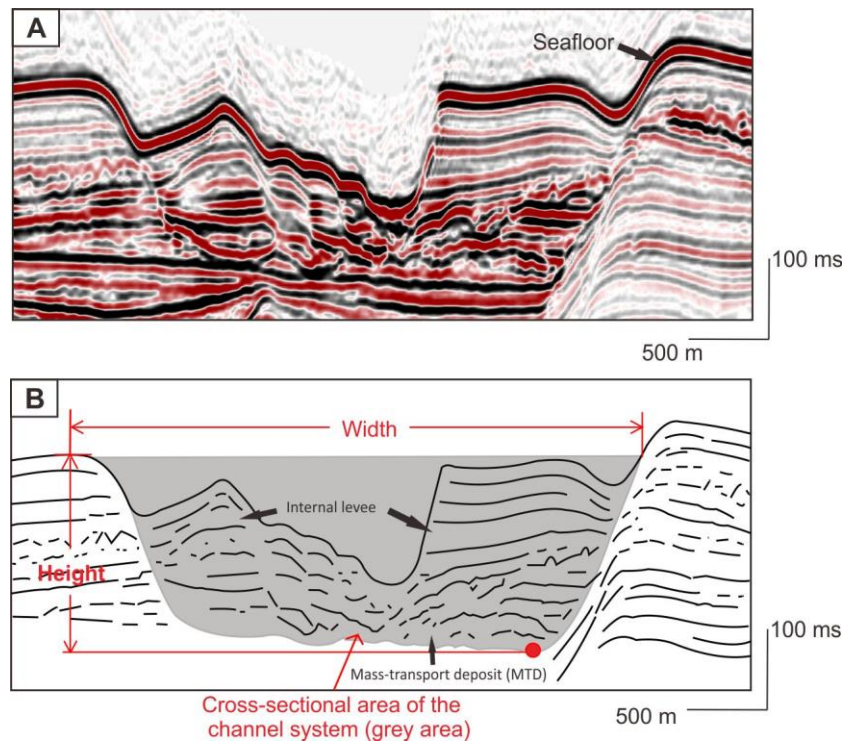
Figure 6.4. Schematic diagram showing the morphological parameters used in quantitative analyses of the Pliocene–Quaternary channel system, including the width, height, and cross-sectional area of the channel system. A) Uninterpreted cross section of the channel system. B) Interpreted cross section of the channel system with parameters used in quantitative analyses.
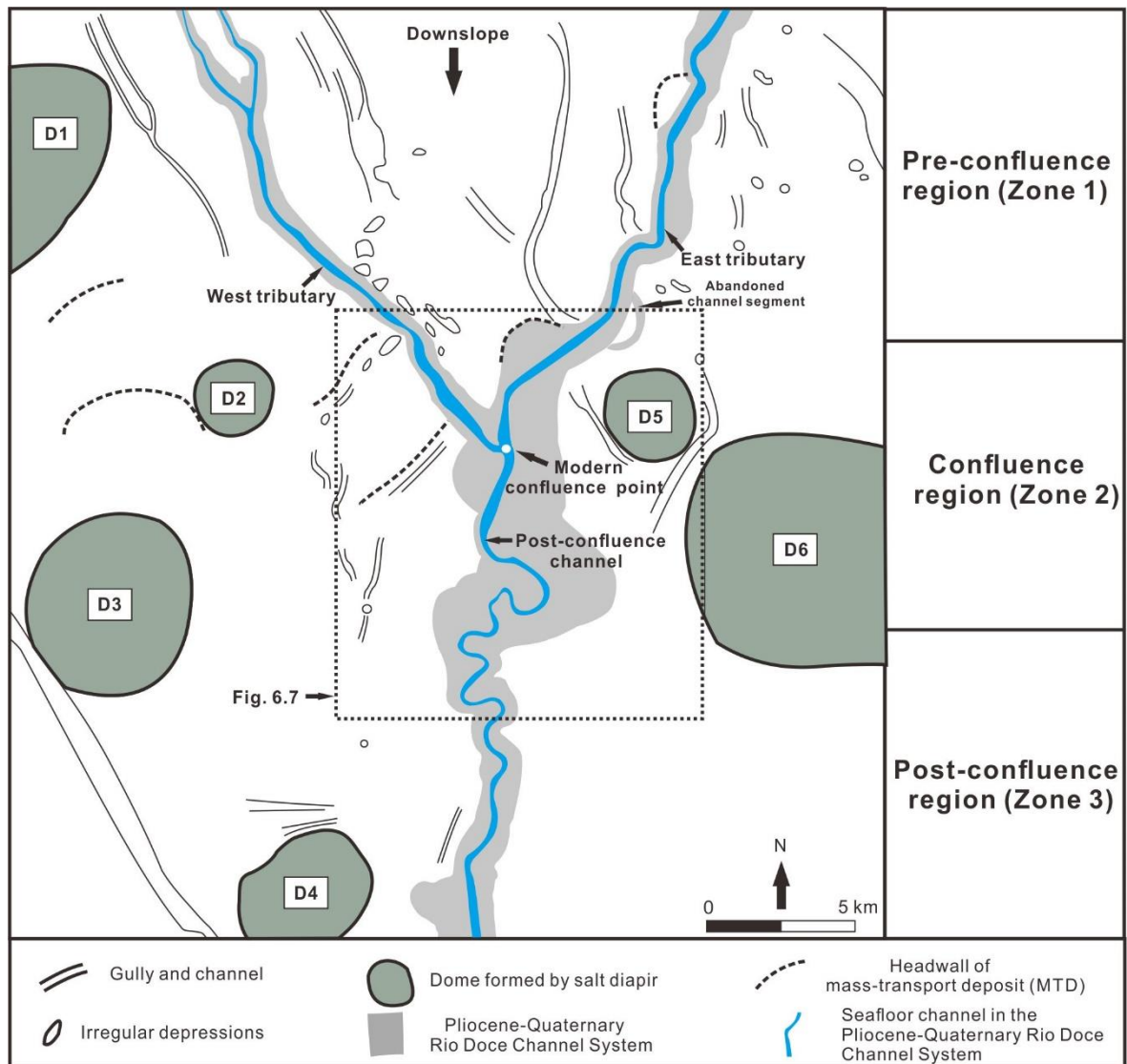
Figure 6.5. Schematic representation of seafloor geomorphologic features in the study area. The Pliocene–Quaternary channel system shows different morphology from Zone 1 to Zone 3. It is widest in Zone 2. The seafloor channels within the channel system comprise west and east tributaries upslope, and a post-confluence channel downslope.
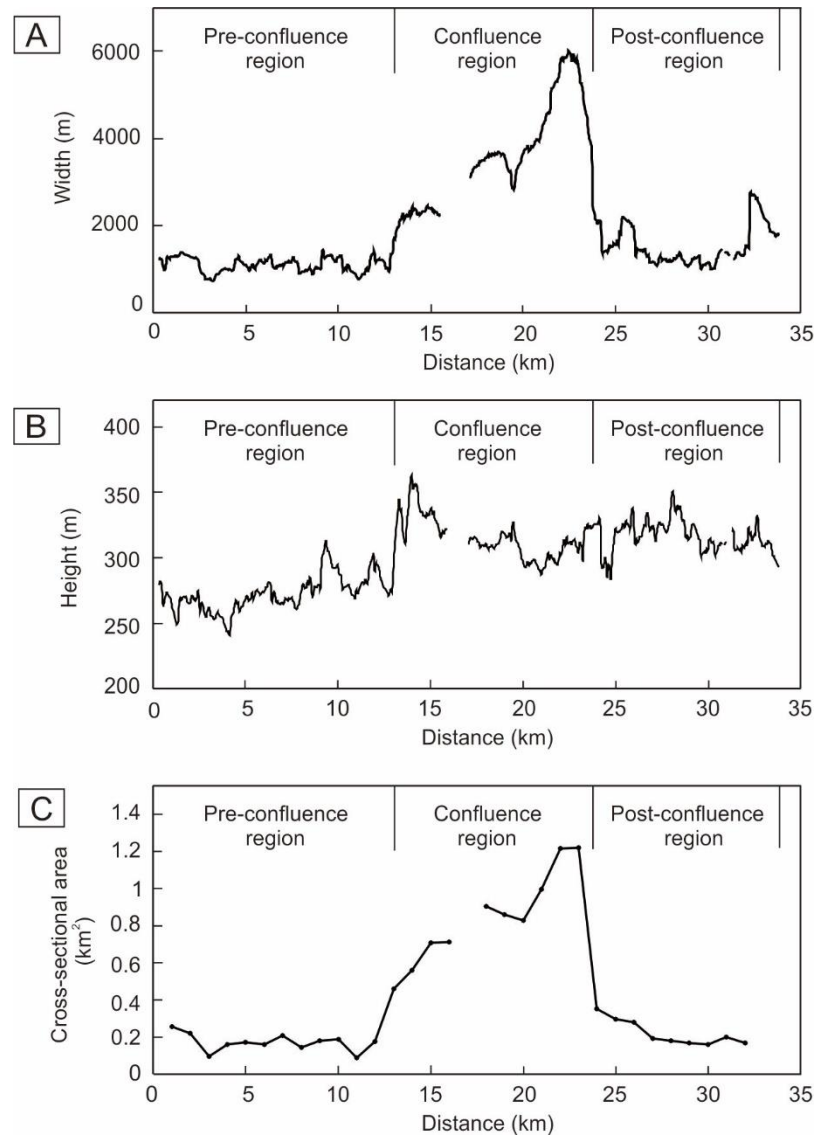
Figure 6.6. Quantitative analyses of the Pliocene–Quaternary channel system along the main pathway (East tributary and Post-confluence channel). The channel system is much larger in the confluence region than further upslope (i.e., pre-confluence region) and downslope (i.e., post-confluence region). A) Width profile of the channel system. B) Height profile of the channel system. C) Variations in the cross-sectional area (CSA) of the channel system.

the higher degree of confinement imposed by these structures, the general orientation of the channel system changes to nearly N–S and is maintained toward the southernmost part of the study area (Fig. 6.5). The width, height, and CSA of the channel system increase rapidly in the confluence region (Fig. 6.6). The width of the channel system increases from ~ 1 km to 6 km (Fig. 6.6A). Its height increases by ~ 50 m on average (Fig. 6.6B), and the CSA rises up to 1.2 km^2, which is 4 to 10 times larger than the CSA in other parts of the channel system (Fig. 6.6C).

In the post-confluence region, the width and CSA of the channel system decrease significantly, from 6 km to 1–2 km and from 1.2 km^2 to ~ 0.2 km^2, respectively (Figs. 6.6A and C). The height of the channel system shows small changes compared to the confluence region (Fig. 6.6B).

6.3.3 Architectural elements of the Pliocene-Quaternary channel system in the confluence region

The following sections focus on the Pliocene-Quaternary channel system in the confluence region, where the channel system shows largest width and CSA (Figs. 6.6A and C, Fig. 6.7).

In the confluence region, multiple erosional events are identified in the channel system (Fig. 6.8). Four main channel units, including three abandoned channels (Channels 1, 2a, and 2b), a channel complex (Channel 3), and an MTD are interpreted based on their seismic facies (Figs. 6.8 and 6.9).

6.3.3.1 Mass-Transport Deposit (MTD A)

This unit is chiefly composed of Seismic Facies 3 (Figs. 6.9C–H, K and L), and is interpreted as a locally sourced MTD, named MTD A. This deposit is located in a basal scar. The basal scar (or scar) in this study is defined as the erosional morphological feature within which MTD A was contained. The scar has a headwall, base, lateral margins and toe area, all of which are associated with the headwall, base, lateral margins, and toe of MTD A (Figs. 6.9E, F and 6.10A).

A continuous, negative-amplitude seismic reflection underlies the chaotic facies in MTD A. This reflection is interpreted as the basal surface of the scar (Figs. 6.9C–H, K and L). However, no clear kinematic indicators of mass wasting were identified on the basal surface (Fig. 6.10A). The top
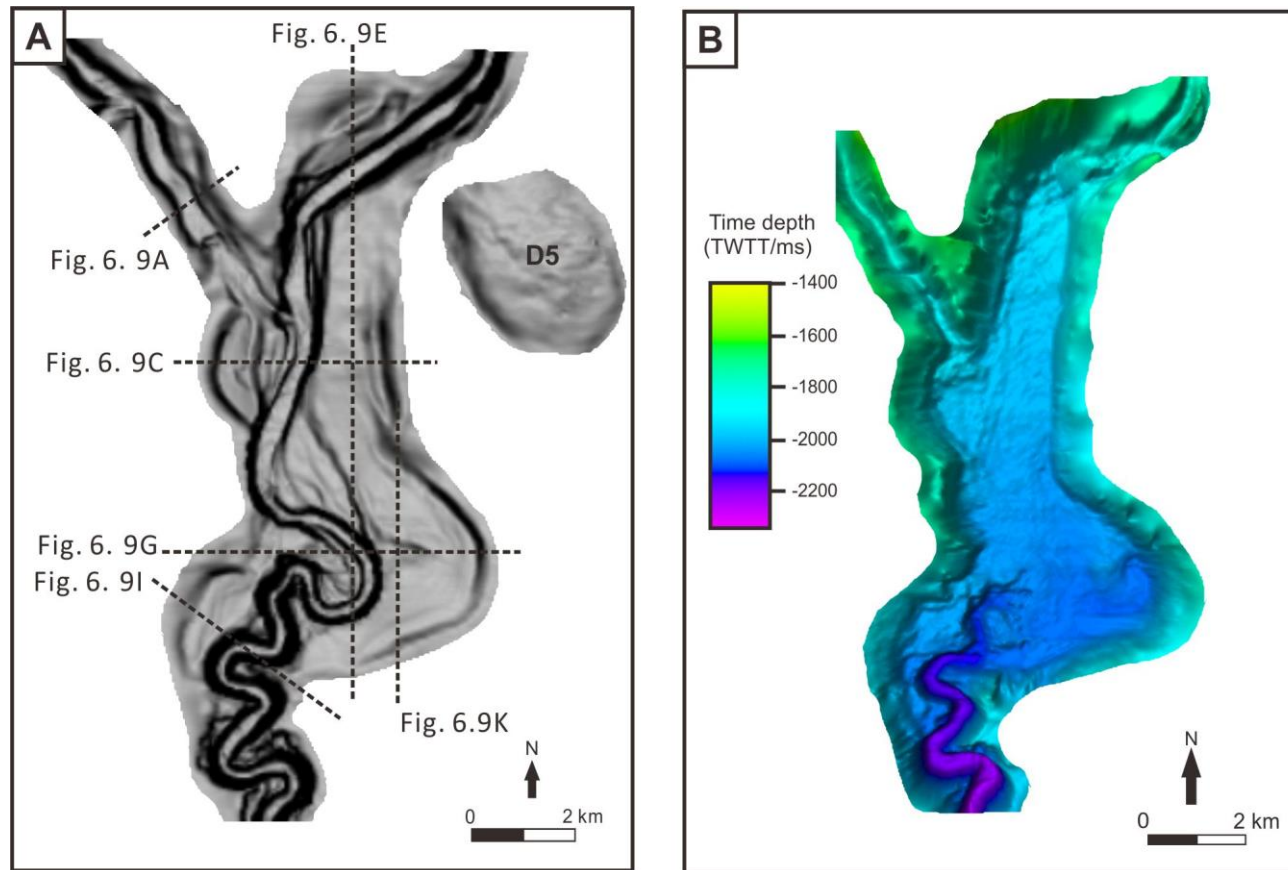
Figure 6.7. A) Dip map of the channel system in the confluence region. The location of cross sections in Figure 6.9 are shown in this figure. B) Basal erosional surface of the channel system in the confluence region. The base of the channel is much wider here than in both the pre- and post-confluence regions.
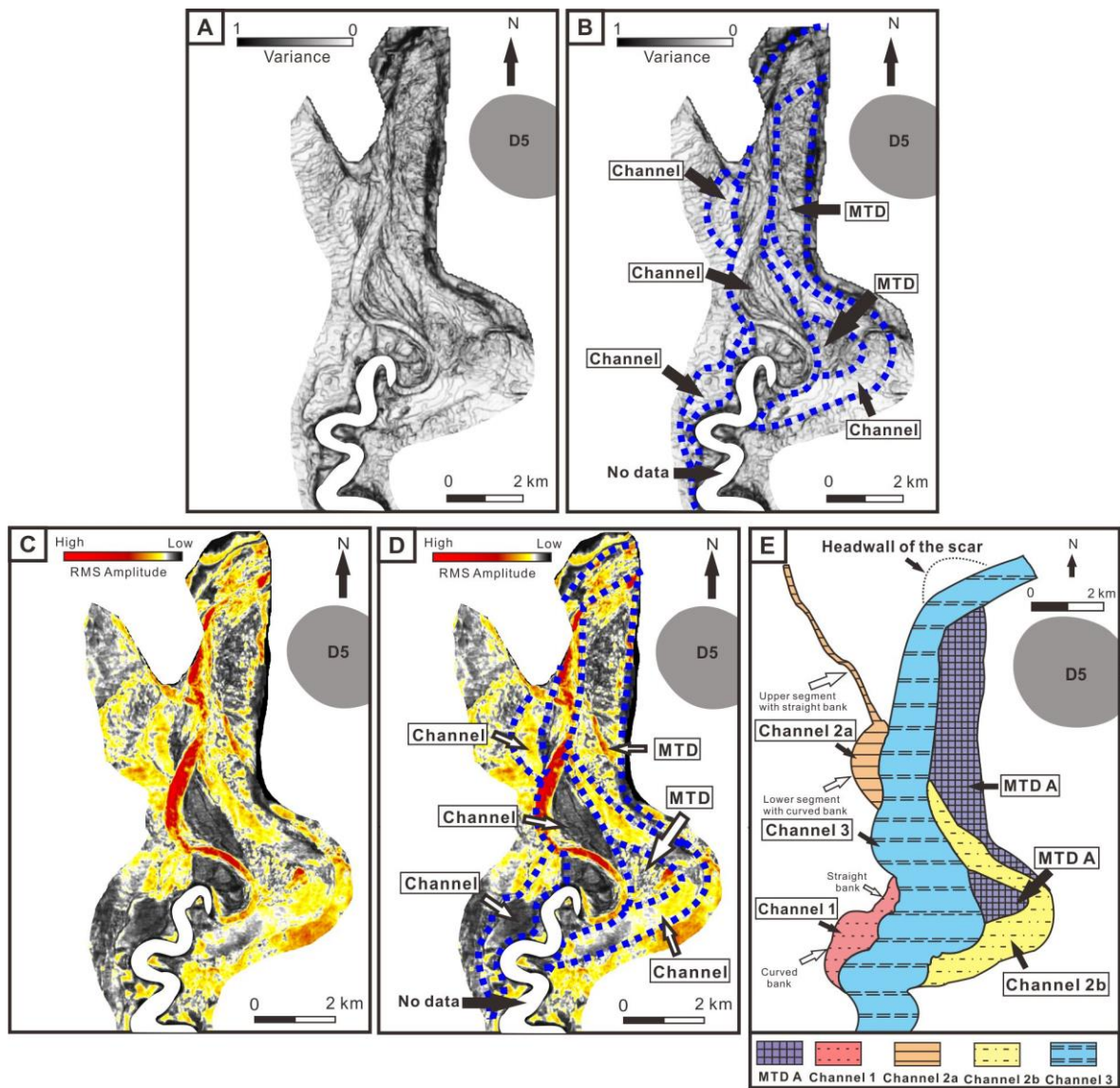
Figure 6.8. Architectural elements of the studied channel system in the confluence region. A, B) Uninterpreted and interpreted variance slices acquired 60 ms above Surface E, which is shown in Figure 4.9. They were extracted from a seismic volume flattened on Surface E. The dark irregular pattern represents chaotic MTDs, and the light colours represent channel-fill deposits. C, D) Uninterpreted and interpreted root-mean-square (RMS) amplitude maps acquired 65 ms above Surface E, which is shown in Figure 4.9. They are extracted from a flattened seismic volume based on Surface E. The irregular amplitude reflects the presence of chaotic MTDs. The RMS amplitude of channel-fill deposits ranges from low to high. E) Schematic diagram showing and naming architectural elements of the channel system in the confluence region, including three abandoned channels (Channels 1, 2a, and 2b), a channel complex (Channel 3), and MTD A. Channels 2a and 2b are interpreted as comprising a single channel.
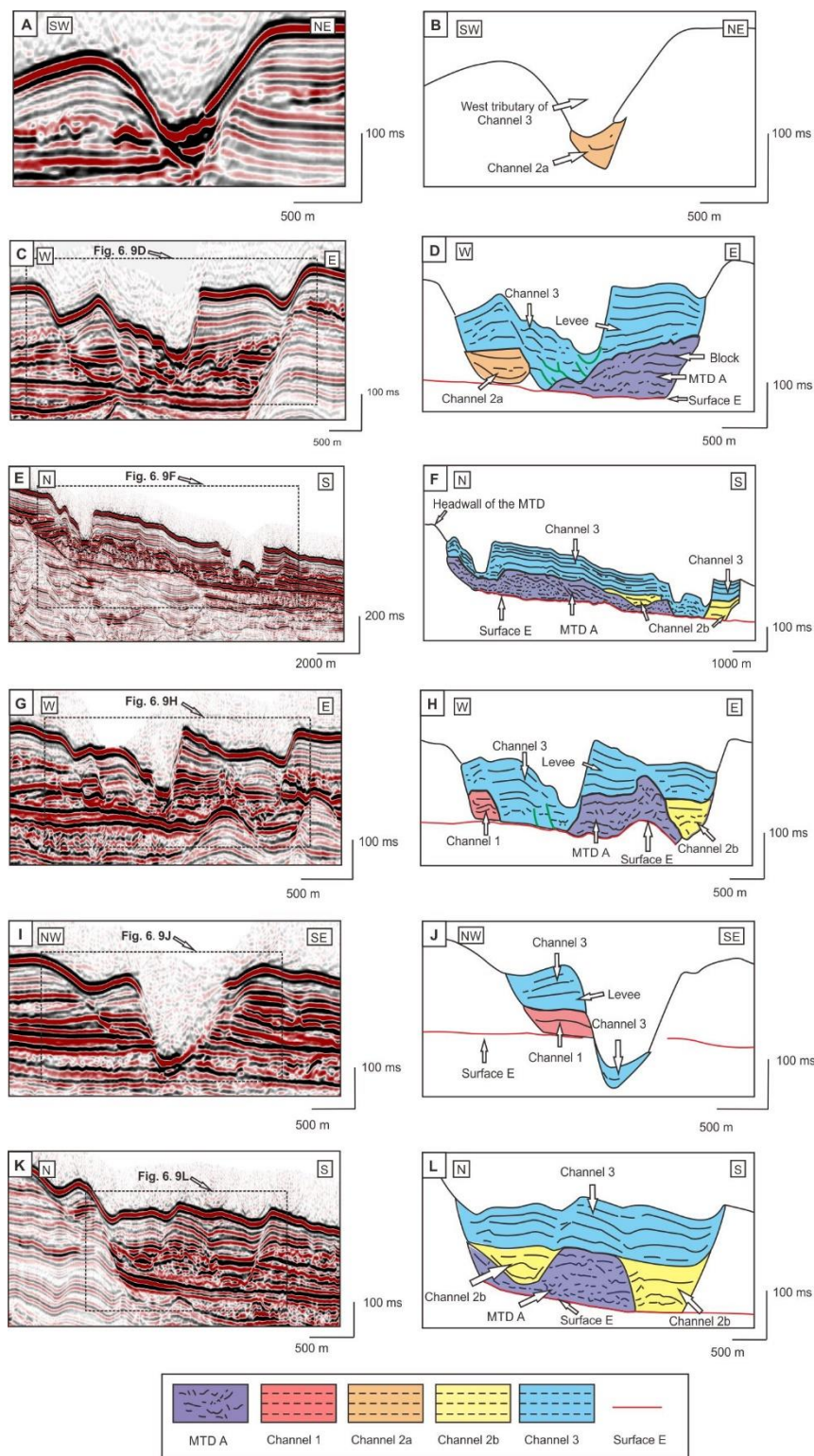
Figure 6.9. Selected seismic sections (left-hand side) and their corresponding interpretations (right-hand side) highlighting the key architectural elements of the channel system in the confluence region. The location of seismic sections is shown in Figure 6.7A.
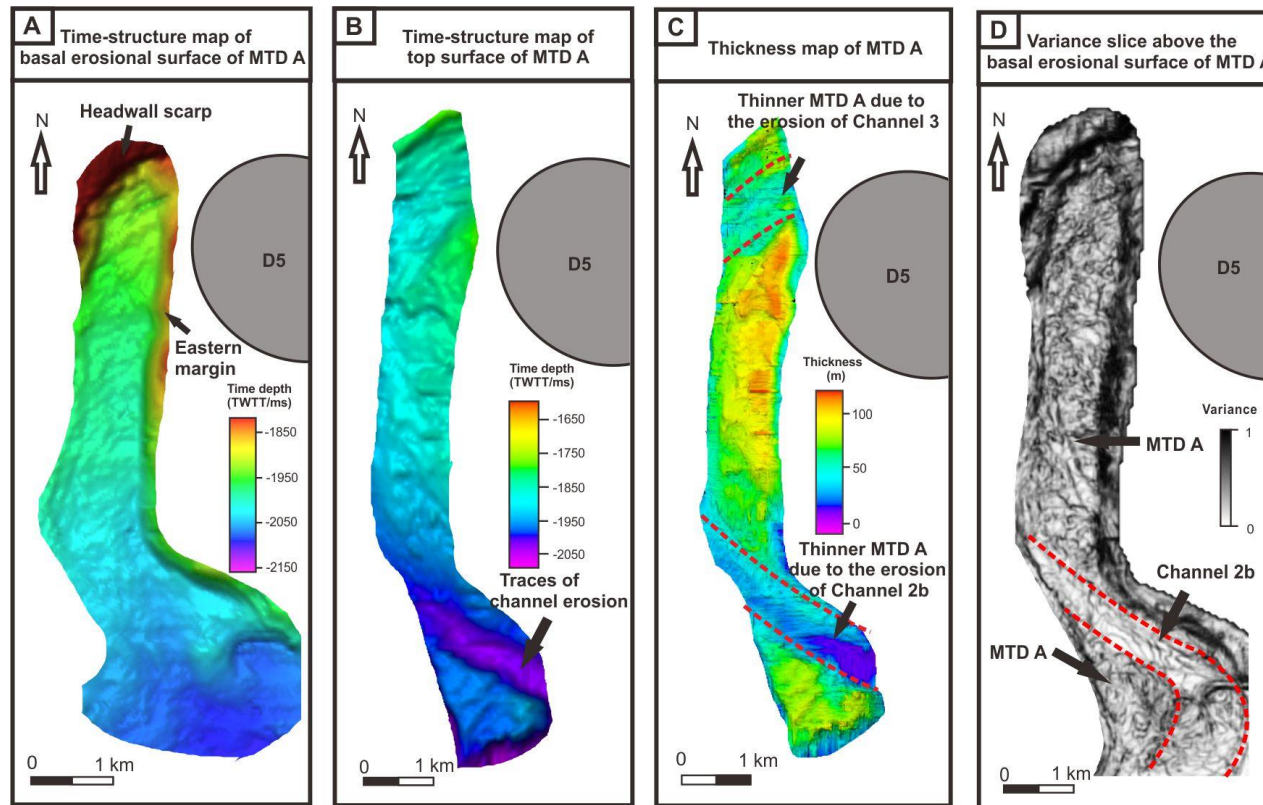
Figure 6.10. A) Time-structure map of the basal erosional surface of MTD A. B) Time-structure map of the top surface of MTD A. C) Thickness map of MTD A. The maximum thickness of MTD A is observed along its eastern margin, reaching ~120 m. The thickness of MTD A is much smaller where Channel 2b cuts through; it ranges from 8 to 40 m. D) Variance slice extracted 55 ms above the base of MTD A. The dark irregular pattern represents chaotic MTDs, and the light colours represent channel-fill deposits.

surface of MTD A is a hummocky surface and shows traces of channel erosion (Fig. 6.10B). A stratified block is recognised in the chaotic reflections of MTD A (Figs. 4.9C and D). The block is 1 km long and 80 m thick and covers an area of 0.6 km^2.

The thickness of MTD A ranges from 8 m to 120 m (Fig. 4.10C), which is lower than the height of scar margin of 160–240 m (Figs. 6.9C, D, G and H). Based on the extent of MTD A, we can conclude that the headwall of the scar is 3 km wide (Fig. 6.8E) and at least 260 m high (Figs. 6.9E and F). The length of the scar is at least 8 km along its longitudinal direction (Figs. 6.9E and F). The eastern margin of the scar is 160–240 m high, and its width is at least 1 km (Figs. 6.9C and D). The estimated original volume of the scar is 1.6 km^3. A scar of similar size has also been documented in Cambrian marine units in Canada, where the scar is at least 8 km long and 200 m high (Stewart et al., 1993).

Following the classification of Moscardelli and Wood (2008), MTD A is a detached MTD. Its formation is probably associated with salt deformation due to its spatial co-occurrence with salt diapir D5 (Fig. 6.8E). Moscardelli and Wood (2015) documented a relationship between the dimension of MTDs and their origins. They show that detached MTDs are smaller than shelf- and slope-attached MTDs (Moscardelli and Wood, 2015). The results of this work are consistent with the relationship observed by Moscardelli and Wood (2015), inasmuch as the area and length of MTD A plot into the area-length cluster of points for detached MTDs (fig. 3 of Moscardelli and Wood, 2015).

The presence of MTD A indicates a mass-wasting event that occurred in the confluence region, where the basal scar created by the mass-wasting event was later modified by subsequent channel erosion, as exemplified by the channel-fill deposits that overlie MTD A (Figs. 6.9C–H, K and L) and attribute maps for MTD A in Figure 6.10C and D.

MTD A was most likely frontally confined despite the fact that its frontal ramp is now eroded by Channel 2 (Figs. 6.9E and F). Because of topographic confinement at the toe region, MTD A was probably not transported downslope. This MTD is thus interpreted to have been formed by the mass-wasting event that created the scar, rather than being sourced from upslope regions.

The orientation of the eastern margin of MTD A indicates that mass-wasting deposits, chiefly transported to the south, were confined upslope by salt diapir D5 and formed wider lobes downslope (Figs. 6.8E, 6.9E, F, 6.10A and B).

The difference between the thickness of MTD A and scar-margin height suggests that part of MTD A has been removed downslope by turbidity currents. This removal is also supported by the thinner MTD A along the pathways of Channels 2b and 3 (Fig. 6.10C).

Additionally, significant erosion of MTD A by channels is revealed by the variance slice extracted above the basal surface of MTD A (Fig. 6.10D). This slice shows that channel deposits of lower variance cut through the higher-variance MTD A (Fig. 6.10D).

6.3.3.2 Submarine channels

Three abandoned channels (Channels 1, 2a, and 2b) and a channel complex (Channel 3) have been interpreted inside the channel system in the confluence region (Fig. 6.8E). These channels and channel complex comprise Seismic Facies 1 and 2 (Fig. 6.9).

Channel 1 is located on the western side of the channel system, being incised and overlain by Channel 3 (Figs. 6.8E and 6.9G–J). The height of Channel 1 is ~ 150 m with respect to its western bank. Its width increases from 550 up to 1200 m due to a sharp change from a straight to a curved bank (Fig. 6.8E) formed by localised bank failures.

Channel 2 is composed of two segments, identified as Channels 2a and 2b, which could have been connected as one single channel. Channel 2a occurs on the western side of the channel system and comprises an upper and a lower segment (Fig. 6.8E). The upper segment is relatively straight (Fig. 6.8E), and only shows its erosional base due to subsequent erosion by the west tributary of Channel 3 (Figs. 6.9A and B). The upper segment of Channel 2a is ~ 120 m high with a 100–200 m wide thalweg (Figs. 6.9A and B). The lower segment of Channel 2a is incised by Channel 3 to the east and shows a scalloped bank to the west (Fig. 6.8E). This segment is 150 m high and 800 m wide (Figs. 6.9C and D). The curved bank in this segment is interpreted to be a result of bank failure, which widened the base of the channel from 100 m to a maximum of 700 m (Figs. 6.9C and D).

Channel 2b is located on the eastern side of the channel system, being 1000 m wide and 150 m high (Figs. 6.8E, 6.9G, H, K and L). It incises MTD A in two parts and shows a relatively sinuous pathway, with sinuosity approaching 1.7 (Fig. 6.8E). Channel 2b is itself incised and overlain by Channel 3 (Figs. 6.8E, 6.9E–H, K and L).

Channel 3 is a channel complex marked by lateral channel migration, as revealed by abrupt

shifts in channel-forms erosional surfaces (Fig. 6.9C, D, G and H; fig 13 of Qin et al. 2016). Channel 3 has two tributaries and a post-confluence channel on the seafloor (Fig. 6.5). It is 1000–2000 m wide by 140–180 m high in the confluence region. This channel is traceable throughout the entire seismic volume and incises all the other erosional features, including Channels 1, 2 and MTD A (Fig. 6.8E). It also shows well-developed levees above both MTD A and sediment fills of other channels (Figs. 6.9C, D and G–J).

6.3.3.3 Surface E

Surface E is a high-amplitude, negative reflection that is interpreted throughout the study area (Figs. 6.9C–L and 6.11A). Part of Surface E was used as the basal erosional surface of MTD A (Figs. 6.9C–H, K and L). The thickness between Surface E and the basal erosional surfaces of channels (Channels 1 and 3, part of Channel 2) ranges from 0 to 10 ms (Fig. 6.11B).
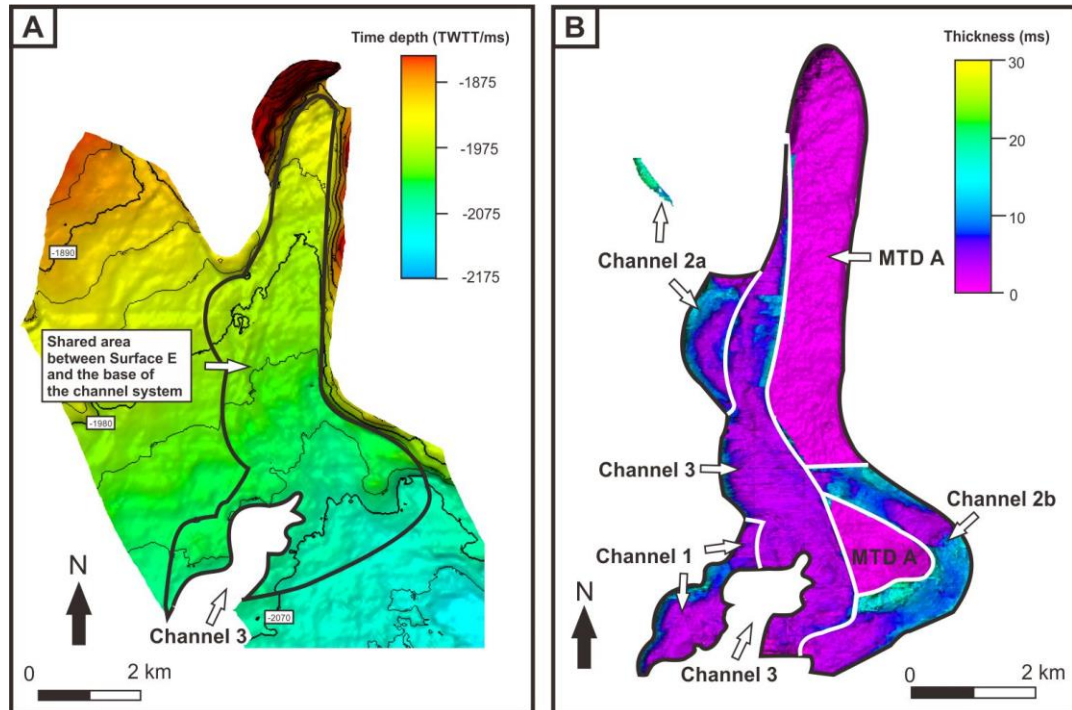
Figure 6.11. A) Time-structure map of Surface E. B) Thickness map between the basal erosional surfaces of erosional events (i.e., MTD A and channels) and Surface E. The thickness between the basal surface of MTD A and Surface E is 0 ms, whereas the thickness between the erosional surface of the channels and Surface E varies from 0 to 10 ms, suggesting the role of Surface E in delimiting the erosional surface of MTD A and adjacent channels.

Chapter 7

Discussion

7. Discussion

7.1 Possible causes for variations in the morphology of Quaternary channel system

7.1.1 Variations in channel and valley dimension

In terms of hierarchical scheme, the seafloor channel in this study is comparable to channel elements from the stratigraphic record (Fig. 7.1). They are all considered as basic architectural elements of a stratal hierarchical framework.

The valley is a higher-order architectural element when considering the hierarchical (channel) framework described in this work (Fig. 7.1). It is an integrated result of lateral migration and vertical stacking of channel elements through time, as shown by the shift of channel forms at the valley base (Figs. 5.4C-G). This observation is consistent with previous studies, which have shown that valley base is a diachronous surface or a composite erosional surface shaped by multiple erosional events (e.g. Deptuck et al., 2003; Sylvester et al., 2011; Kolla et al., 2012; Thomas and Bodin, 2013; Macauley and Hubbard, 2013; Bain and Hubbard, 2016; Di Celma et al., 2011).

7.1.1.1 Channel dimension

The channel dimension shows significant variations along the channel (Fig. 4.4 and Table 4.1). This is shown, for example, by the rapid decrease in channel CSA from Reach a to Reach c, which decreases by a factor of 7 (Table 4.1). Channel gradient is considered to be a major control on turbidity-current behaviour (e.g. Komar, 1969; Friedmann et al., 2000; Babonneau et al., 2002; McHargue et al., 2011; Wynn et al., 2012; Stevenson et al., 2013). Correlations between decreasing channel gradients and widened channel floors have been observed at 12 km and 36 km along the channel axis (Figs. 4.4A and C). These correlations are consistent with results from previous studies (Babonneau et al., 2002).

Apart from widened channel floors, decreases in channel gradient could also lead to reduced flow energy, sediment deposition, widened channels and decreased channel heights (e.g. Friedmann et al., 2000; Adeogba et al., 2005; Estrada et al., 2005). However, this is not strictly valid
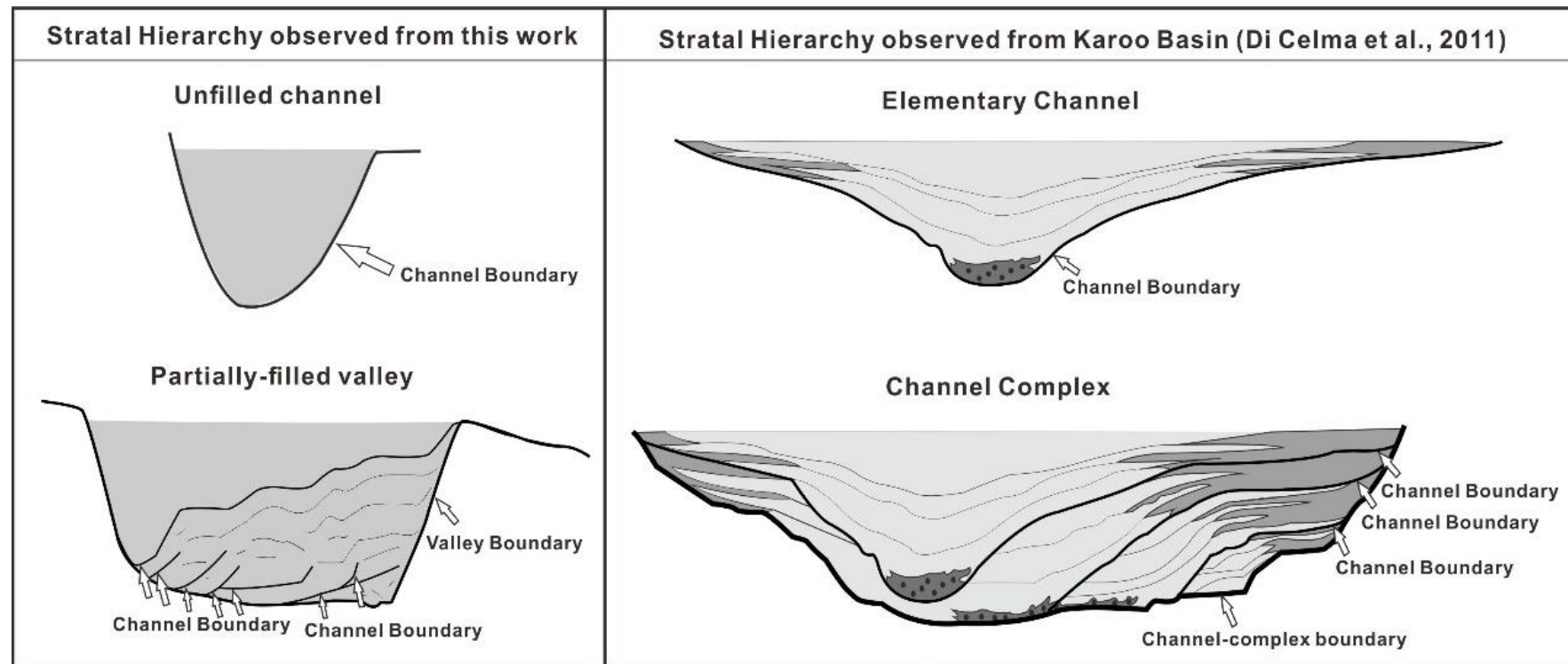
Figure 7.1. Comparison between the stratal hierarchy in this study and outcrop data from the Karoo Basin, South Africa (Di Celma et al., 2011). The channel corresponds to the elementary channel of the Karoo Basin, both of which are fundamental elements of hierarchy framework. The valley correlates with the channel complex in the Karoo Basin, both of which were formed by lateral migration and the vertical stacking of channel elements.

for the submarine channel investigated in this work. In our example, decreasing channel gradient from Reach a to Reaches b and c is accompanied by decreased channel width (Table 4.1). A similar relationship is also observed from Reach d to Reach e (Table 4.1). Additionally, increased channel height with decreased channel gradient from Reach c to Reach d also contradicts previous work. Therefore, channel gradient probably is not the main cause for the variations in channel size documented here.

Because the height of the leveed channel indicates the minimum thickness of turbidity-flows that forming internal levees, and can thus be used as an indicator of flow volume (Babonneau et al., 2002; Deptuck et al., 2003; Estrada et al., 2005), spatial variations in channel height along the channel length suggest that flows inside the channel were not the same in terms of their physical properties and erosional power. These variations may reveal spatial and temporal variations in flow volume. Such an observation agrees with the models proposed in McHargue et al. (2011), who suggest multiple waxing-waning cycles of turbidity currents at multiple scales.

Relationships between temporal changes in flow properties and channel size have been observed in the Niger delta, where a temporal decrease in channel size is correlated with a decrease in sediment supply (Jobe et al., 2015). Similar scenarios may also occur in the studied channel. The volume of turbidity currents flushed into the channel may have decreased through time, leading to smaller channels in Reaches b, c d, and e. Additionally, tributaries in the confluence region could have induced variations in channel size. Apart from the intersection of the west tributary with the main seafloor channel observed at the confluence point, two other tributary channels connecting to the east tributary are observed on the seafloor (Fig. 3.8). These tributaries may have provided low-volume, and less erosive flows to the main pathway. These flows tended to deposit in Reaches b and c, rather than transporting sediments downslope towards Reaches d and e, therefore generating small sized channels in Reaches b and c.

Despite the observed variations in channel size, the width of the channel floor shows relatively small changes (Fig. 4.4C and Table 4.1), suggesting it has been only slightly affected by variations in flow discharge.

7.1.1.2 Valley dimension

Valley dimension reveals spatial variations in erosional processes within the valley. It is difficult to identify the principal erosional mechanism in Reach A, but the morphology and architecture of the valley suggest spatial variations in erosional processes in both Reaches B and C.

In Reach B, the valley base is more than two times wider than in other reaches (Table 4.2). This difference is interpreted as resulting from cut bank erosion during multiple episodes of lateral channel migration (Fig. 7.2A), as shown by the channel forms at the valley base (Figs. 5.4C-G). Cantilever failure (i.e. a type of bank failure that occur when an overhanging block collapses due to undercutting erosion) is probably the main erosional processes in this reach. In Reach C, inner bank erosion in the form of shallow-seated mass failures (Figs. 5.4E-G) widened the upper part of the valley wall, and resulted in a stepped bank profile (Fig. 7.2B). Similar mass failures and associated scars have also been recorded in other submarine channels (e.g. Deptuck et al., 2007; Janocko et al., 2013), they contrast with deep-seated mass failures observed in the submarine channel system of the Gulf of Mexico (Sawyer et al., 2013). In addition, shallow-seated mass failures are mainly located in Reach C (Fig. 6.1), suggesting local factors predominantly control bank erosion in this area. A marked increase in valley height from Reach B and Reach C (Fig. 4.6B) reflects this process, as the increase may be associated with the occurrence of scars and associated mass wasting in Reach C.

Spatial variations in valley morphology suggest valley size (i.e. CSA) can change over a short distance (i.e. a few kilometres), as documented by the two-fold increase in valley CSA in Reach B, within just 7 km (Table 4.2). Such an increase in valley size can enhance the volume of channel-fill deposits and the reservoir potential of the valley, but the extent of valley enlargement is relatively small, increasing uncertainty when drilling. This observation is consistent with Mayall et al. (2005)'s finding that variations in stacking pattern of submarine channel systems can occur within a short distance.

7.1.1.3 Scale comparison with other submarine channel systems

This work shows a channel of 240-1060 m wide, and 13-156 m high (Figs. 4.4B and C). Channels hundreds of meters wide, tens of meters high have been documented, on seismic data in the Gulf
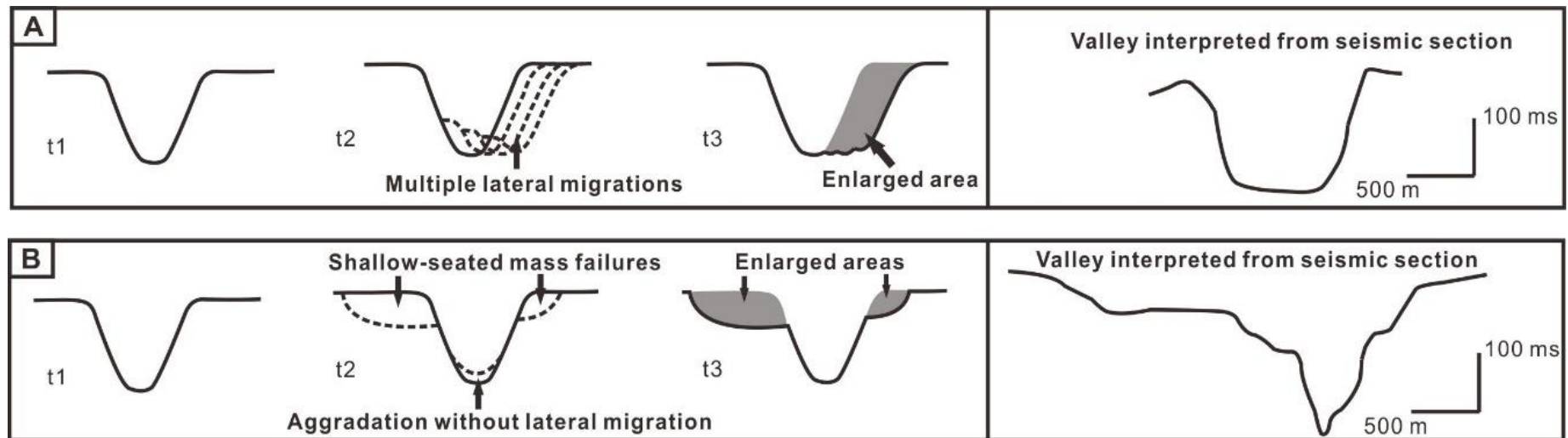
Figure 7.2. Schematic diagram showing the effects of different erosional processes on valley morphology. A) Cut bank erosion during lateral channel migration caused the retreat of the entire valley wall, leading to the widening of the valley, especially at the valley base. B) Shallow-seated mass failures only enlarged the uppermost half of the valley wall.

of Mexico (Sylvester et al., 2012) and Congo (Deptuck et al., 2007; Jobe et al., 2015), and on7.1 bathymetric data from offshore California (Normark, 1978; Maier et al., 2012). Similar channels have also been documented at outcrops (e.g. Mutti, 1977; Walker, 1985; Shanmugam and Moiola, 1988; Zelt and Rossen, 1995; Cronin, 1995; Clark and Pickering, 1996; Gardner et al., 2003; Brunt et al., 2013; Figueiredo et al., 2013; Di Celma et al., 2011; Moody et al., 2012; Bain and Hubbard, 2016). Furthermore, km-wide channels are recorded in the modern Amazon and Zaire fans (Pirmez and Flood, 1995; Babonneau et al., 2002). As submarine channels are products of turbidity currents, changes in their size probably reflect variations in flow properties (e.g. flow volume, grain-size distribution) (e.g. Komar, 1969; Babonneau et al., 2002; Pirmez and Imran, 2003; Sequeiros, 2012; Konsoer et al., 2013; Jobe et al., 2015). However, km-wide channels in the modern Amazon and Zaire fans probably reflect the width of channel complex (i.e. valley) rather than the width of channels, due to lower data resolution and misused terminology such as channels and canyons.

The valley in this work is 700-2800 m wide, 230-350 m high in this study (Figs. 4.6B and C). Similar valleys have been documented from both seismic (e.g. Wood and Mize-Spansky, 2009; Gamberi et al., 2013) and outcrop studies (e.g. Masalimova et al., 2016). However, valleys (or channel complexes) documented in the literature show marked variations in their height and width. For example, channel complexes less than 1000 m wide have been recorded at outcrop in North America (Pyles et al., 2010; Gardner et al., 2003), Italy (Thomas and Bodin, 2013) and Chile (Macauley and Hubbard, 2013). In contrast, valleys more than 3000 m wide have been recorded on seismic data (e.g. Samuel et al., 2003; Deptuck et al., 2007; Catterall et al., 2010; De Ruig and Hubbard, 2006; Kolla et al., 2012; Jolly et al., 2016), and at outcrops (e.g. Cronin et al., 2005b; Bain and Hubbard, 2016; Grecula et al., 2003). In the Indus fan, the valley can be up to 10 km wide (Deptuck et al., 2003). These marked variations may relate to the degree of lateral channel migration. This seems to be the case for the studied submarine channel, where the higher degree of lateral migration corresponds to the largest valley width and CSA in Reach B (Figs. 4.6C and D, Table 4.2). In contrast, the lower degree of lateral migration resulted in lower valley width and CSA (Figs. 4.6E-G, Table 4.2). Spatial correlations between channel Reaches b and c, and valley Reach B (Fig.4.3) suggests that increased degree of lateral channel migration in Reach B may be associated with local sediment input from tributaries. Apart from cut bank erosion during lateral channel migration, inner

bank erosion has also contributed to the widening of the valley, as reflected by the shallow-seated mass failures and associated scars observed in this study (Figs. 6.3).

The distinct channel and valley scale-relationships obtained from previous studies are also dependent on the data sources utilised and on the measurement methods applied (Kolla et al., 2001; Wood and Mize-Spansky, 2009; McHargue et al., 2011). Because of data resolution, seismic data seldom reveal small-scale channels, which may be only a single wavelength thick. Measurements performed on planform and cross-sections can make a difference to morphometric analyses (e.g. Wood and Mize-Spansky, 2009). Channel and valley width may be overestimated when outcrops are not perpendicular to the channel and valley axis, whereas they may be underestimated because muddy deposits at the top of channel fill tend to be eroded and poorly exposed (McHargue et al., 2011).

7.1.2 Relationship between sediment supply and channel sinuosity

In Reach I, where channel sinuosity shows a temporal increase from 1.11 to 1.72 (Fig. 4.7), the magnitude of lateral migration is the highest (Fig. 5.6), suggesting that variations in channel sinuosity are caused by lateral channel migration. This relationship is also supported by seismic data, which shows lateral migration resulted in the formation of channel bends (Figs. 5.4C and D), which led to an increase in channel sinuosity.

The magnitude of lateral channel migration (i.e., L_M) shows the highest value in Reach I, ranging from 300 m to 1600 m (Fig. 5.6A). This higher L_M is interpreted here to result from enhanced sediment supply from tributaries. Sediment from tributaries promoted lateral channel migration in the reach, leading to the formation of channel bend and temporal increases in channel sinuosity (Figs. 5.4C and D). During this process, valley size (CSA_V) was enlarged by cut-bank erosion associated with lateral channel migration and sediment from tributaries was stored in the inner bank, as evidenced by the positive relationship among L_M, CSA_{VF} and CSA_V (Fig. 5.6). These observations suggest that lateral channel migration is an important mechanism for accommodating enhanced sediment supply.

Increased channel sinuosity downstream of tributaries is also observed in the Amazon River

(Constantine et al., 2014). Enhanced sediment supply from tributaries results in point-bar growth, facilitating lateral erosion and channel migration (Constantine et al., 2014). In addition to tributaries, enhanced sediment supply can also be caused by floods (e.g. Nelson and Dubé, 2016) and earthquakes (e.g. Liu and Yang, 2015), both of which resulted in relative increases in the rates of lateral migration in rivers such as the Chehalis in the USA (Nelson and Dubé, 2016) and the Jianjiang in China (Liu and Yang, 2015).

However, in contrast to the continuous migration observed in fluvial rivers, a different migration process, punctuated migration, dominates the studied channel system (Figs. 5.4C-G), suggesting a different mechanism in submarine channels in response to increased sediment discharge. Because punctuated migration is a cut-and-fill process, we postulate that in submarine channels, enhanced sediment discharge leads to more frequent cut-and-fill processes, which in turn, result in larger scales of lateral migration, the formation of channel bends, and increased channel sinuosity.

Some researchers suggest that channel sinuosity can increase with time as channels become mature over time (e.g. Peakall et al., 2000; Deptuck et al., 2003; Gee et al., 2007; Babonneau et al., 2002, 2010; Maier et al., 2013). However, this channel maturity could also be affected by variations in sediment supply. For example, more sediment discharge in a shorter period, and less sediment discharge in a longer period, may result in similar frequency and magnitude of lateral channel migration, and similar variations in channel sinuosity. Therefore, it is difficult to determine which factor dominates without making use of robust age constraints.

7.1.3 Relationship between valley slope and channel sinuosity

Some authors suggest that submarine channels evolve from relative straight to more sinuous pathways, with sinuosity increases during this process (e.g. Gee et al., 2007; Maier et al. 2013). However, this study shows that sinuous channel can also form at the early incision stage of channel evolution due to the variations in valley slope.

This study shows a close relationship between valley slope and channel sinuosity (Fig. 4.9). The positive relationship is observed along the entire initial channel and in the middle and lower reaches

of the present channel (Fig. 4.9). This relationship shows that channel sinuosity increases with steeper valley slope, and decreases as valley slope becomes gentler (Fig. 4.9). The results in this work are consistent with observations from Amazon fan (Flood and Damuth, 1987; Pirmez and Flood, 1995), Boso canyon offshore Japan (Soh et al. 1990), southwest Mediterranean (Cronin et al., 1995), and Indonesia (Posmentier and Kolla, 2003). Flood and Damuth (1987) suggested that the adjustment of channels in response to an abrupt increase in valley slope occurs via an increase in channel sinuosity. This increase in sinuosity occurs in order to maintain a relatively constant channel slope, which is suitable to accommodate the volume of flow and sediment load that channels transport (Flood et al., 1987).

However, in West Africa, negative relationships between channel sinuosity and valley slope have also been documented by Ferry et al. (2005) and Gee et al. (2007). In addition, there are few correlations between canyon slope (i.e. valley slope) and channel sinuosity in the Tenryu and Kushiro Canyons offshore Japan (Soh and Tokuyama, 2002; Noda et al., 2008). The absence of positive relationship in these studies maybe because these channels are in a state of adjustment (i.e. out of equilibrium) rather than reaching their local equilibrium state (Pirmez and Flood, 1995; Ferry et al., 2005). It is difficult to determine whether channels are under non- equilibrium or equilibrium conditions based solely on quantitative analyses, as the morphological parameters usually obtained reflect a transient state of channels, rather than the processes of adjustment to equilibrium profiles. In the studied channel system, however, slight temporal changes occurred in channel sinuosity and valley depth profiles in the middle and lower reaches (Figs. 4.7 and 4.8), suggesting that the studied channel system is probably close to an equilibrium state in these two reaches. In addition, different measurement intervals may result in the absence of positive relationships between sinuosity and valley slope, as the measured intervals can be too large (or too small) to capture actual variations in channel sinuosity. Another alternative interpretation for the absence of such relationship is the existence of a threshold valley slope, above which channels would only increase vertical incision and follow a more direct course downslope, resulting in a rapid decrease in sinuosity (Clark et al., 1992; Gee et al., 2007).

7.1.4 Controlling factors of valley-slope variations in the study area

Valley-wall profiles for the channel system reflect seafloor slope, and display different trends from the valley-thalweg depth profile of the channel system (i.e. valley slope profile of the initial channel) (Fig. 4.8), suggesting the valley-thalweg slope is somewhat independent of the seafloor slope. Additionally, evidence for faults and folds beneath the studied channel system, channel avulsion events and meander cut-off, all of which can result in variations in valley slope, are not observed at the transition area between the reaches (Figs. 3.5 and 5.4).

Despite the lack of lithological data from cores, changes in substrate resistance beneath the channel system are probably key reasons behind variations in valley slope. Similar relationship between substrate resistance and valley slope have been documented in studies from fluvial channels. In fluvial channels, some researchers found that channels are steeper through resistant rocks and less steep through relatively weak rocks (e.g. Duvall et al., 2004; Goode and Wohl, 2010; Allen et al., 2013). Despite channel slope and valley slope are different concepts, they are both a function of flow incision depth within a certain interval, as channel slope is calculated along the channel axis and valley slope is calculated along the valley. Therefore, increasing channel slope due to enhanced incision suggests that the valley slope is also increasing during incision processes when substrate is relatively more resistant.

In the upper reach, the gentle slope observed here (1°) (Fig. 4.9B) resulted from less resistant sediments beneath the channel, because sediments in this reach have been reworked by several erosional events and became more erodible (Qin et al., 2017). In the middle reach, the channel probably incised into less erodible strata and resulted in a steep valley slope of 1.22°, together with higher channel sinuosity in this reach (Fig. 4.9B). Enhanced sinuosity with less erodible substrates has also been documented in a bedrock river in the Himalayan front (Allen et al., 2013). Allen et al. (2013) suggest that increased rock strength would promote lateral erosion and sinuosity growth. In the lower reach, the valley slope decreases to 0.57° (Fig. 4.9B), which could result from the presence of less resistant sediments.

Hansen et al. (2017) suggest that channel displays higher sinuosity when it carries and erodes into fine-grained sediment, while it shows lower sinuosity when it carries and erodes into coarse-

grained sediment. However, their study also does not show core data to validate substrate lithology. Therefore, the relationship between substrate and channel sinuosity needs to be investigated in more studies.

7.2 The influence of mass-wasting events on channel evolution

7.2.1 Bank failures in the Quaternary channel system

7.2.1.1 Formation mechanisms of shallow-seated mass failures

Bank height and bank slope angle are believed to be important factors controlling bank failure. Mass-wasting events occur if the bank height and angle exceed the critical shear strength of the bank materials (Thorne and Tovey, 1981; Simon et al., 2000). However, no apparent correlation between bank slope angles and the occurrence of mass failures can be established in the study area, in great part because there are no clear variations in bank slope angle along the channel axis (Fig. 4.5). The presence of failure scars in Zone 3 corresponds to a marked increase in the height of the channel system (Fig. 4.6B), suggesting bank height maybe is the factor that controls the occurrence of bank failures in the study area.

Sawyer et al. (2013) suggest that critical height (i.e. the threshold height above which bank failures occur) of channel banks could be achieved by rapid sediment loading from levees. For example, rapid levee deposition above channel banks is capable of generating high fluid pressures in near-seafloor strata, reducing effective stresses within the strata and promoting failure above a critical bank height (Sawyer et al., 2013). In this study, however, channel levees have not been observed on banks where failure scars developed (Figs. 5.4E-F), a character suggesting that sediment loading probably is not the main cause for shallow-seated bank failure. It is unlikely that levees deposited within scars and slumped in the channel. Because in that case, randomly distributed failure scars would indicate levee distribution without a clear pattern, which is unlikely to occur.

Another explanation for the occurrence of these scars is the presence of surge-type flow events, which may have triggered the failure of the inner bank of channels. Detailed studies of fluvial

channels show that mass failures occur mainly during and after extreme flow events, resulting in undercutting of bank toes, and imposing local variations of pore water pressure i.e., increasing the weight of bank material due to saturation and loss of confining pressure on the falling limb of the hydrograph (Simon et al., 2000; Osman and Throne, 1988). Surge-type flows (i.e. a type of flow with strong erosive power) might be one of reasons for the occurrence of mass-failure scars in the study area. However, as submarine settings have much higher bank moisture content than in sub-aerial settings, variations in the weight of bank material and pore water pressure are not significant as in fluvial channels.

7.2.1.2 The impact of bank failure on submarine channel systems

Bank failure is one of main processes for the widening of the studied channel system, especially in Zone 3, where numerous bank-failure scars are observed (Fig. 6.1). For example, two maxima in the width profile of the channel system, at 26.5 km and 33.5 km, correspond to the presence of failure scars on the banks of the channel system (Fig. 6.3). In addition to the width, bank failure also modified the morphology of channel systems in the study area. For example, shallow-seated bank failures enlarged the upper part of banks and resulted in stepped bank profiles on cross-sections of the studied channel system (Fig. 7.2). These terrace-like features constitute preferential places for subsequent deposition.

Furthermore, bank failure provides abrupt and discrete sediment pulses to channels downslope. These sediments can block channels, resulting in the shifts in channel position and the variation of channel sinuosity (Kolla et al., 2001). Failed bank material deposited at the bank toe may temporarily increase bank stability by buttressing the bank, protecting *in situ* bank material from erosion and entrainment by the flow (Simon et al., 2000). Therefore, bank-failure deposits produce plugs in channels and divert flows around the deposits. For example, a channel bend resulted from the block of mass-failure deposits is observed in Zone 1 (Fig. 7.3A). Slide and slump deposits, revealed by transparent and chaotic seismic facies, occur at the inner bend of the channel (Fig. 7.3B). These deposits diverted flows from upslope, leading to the formation of a channel bend.

In addition, channel-floor roughness is observed downstream the channel bend caused by
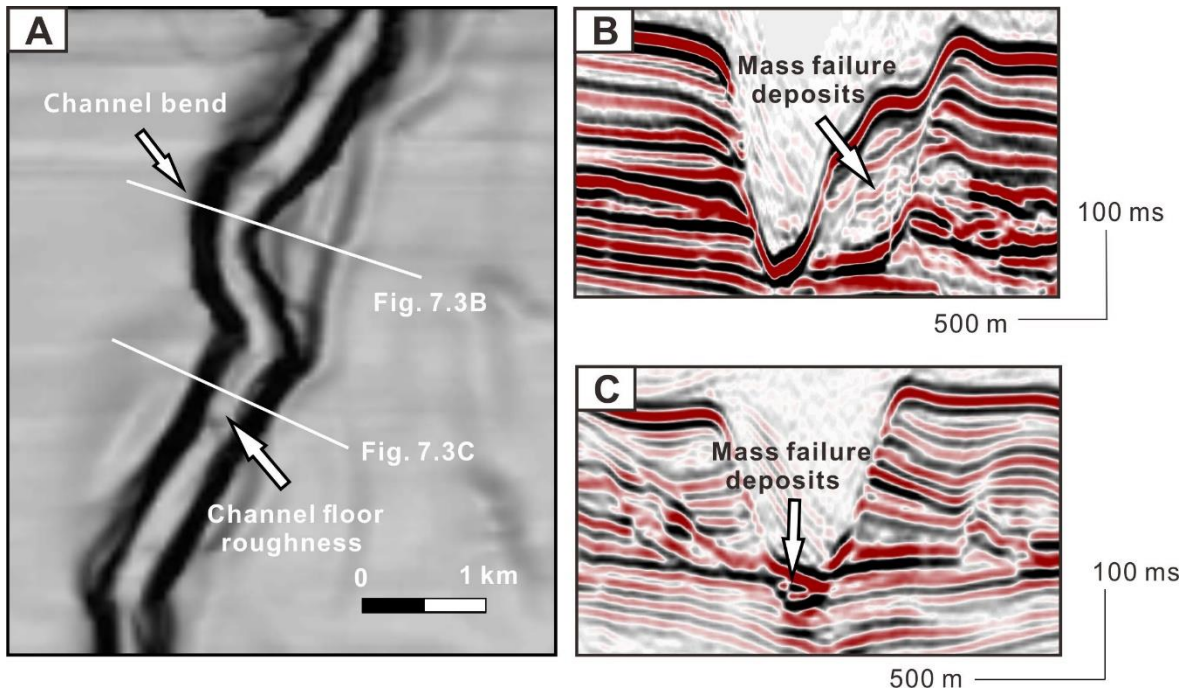
Figure 7.3. Dip map and seismic sections showing the effects of mass failure deposits on the channel. Mass failure deposits caused a formation of a channel bend, and the relative 'roughness' of the channel floor.

bank failure deposits (Fig. 7.3A), and was probably also caused by slide and slump deposits (Fig. 7.3C). Therefore, the abrupt in channel pathway documented here is interpreted as resulting from bank failure processes. Similar variations in channel pathways, caused by mass failures, have also been documented in previous studies (e.g. Droz and Bellaiche, 1985; Greene et al., 2002; Deptuck et al., 2003).

7.2.2 The influence of mass-transport deposits on the Pliocene-Quaternary channel system

7.2.2.1 Depletion zone of the basal scar and flow capture

Seismic data show that the enlargement of the channel system in the confluence region resulted mainly from the spatial co-occurrence of MTD A and Channels 1 and 2 (Fig. 6.8E). This character indicates that interactions between MTDs and turbidity currents occurred in the confluence region. Such interactions are suggested to have started with flow-capture processes.

Turbidity currents can be captured by depletion zones on the headwall domains of basal scars (Shultz et al., 2005; Kertznus, 2009; Kneller et al., 2016). Depletion zone is a relative bathymetric low that developed due to sediment evacuation and local extension (e.g. Lewis, 1971; Martinsen and Bakken, 1990; Frey Martinez et al., 2005; Bull et al., 2009). These same phenomena are exemplified in the Gulf of Mexico and the Nile Delta continental slope, where channels have been captured by the headwalls of basal scars or MTDs (Hackbarth and Shew, 1994; Winker and Booth, 2000; Loncke et al., 2009; Kertznus, 2009; Kneller et al., 2016).

In the study area, part of the depletion zone is presently filled by channel-fill deposits, but there is still a topographic low downslope of the headwall of the scar (Figs. 6.9E, F and 7.4A). Upslope from the headwall, a channel segment (Channel A) has been identified (Fig. 7.4A). The path of Channel A connects to the headwall of the scar (Fig. 7.4A), suggesting that turbidity currents are still captured by the scar at present. In addition, a set of NW–SE-trending grooves are observed upslope of the headwall (Fig. 7.4). These grooves can be tracked to a channel (Channel B) where bank failure occurred (Figs. 7.4A and B). Because submarine channels are flushed by turbidity currents, the grooves are thus believed to have been formed by sheet turbidity currents that breached the bank of Channel B. Despite the lack of temporal constraints for their genesis, the
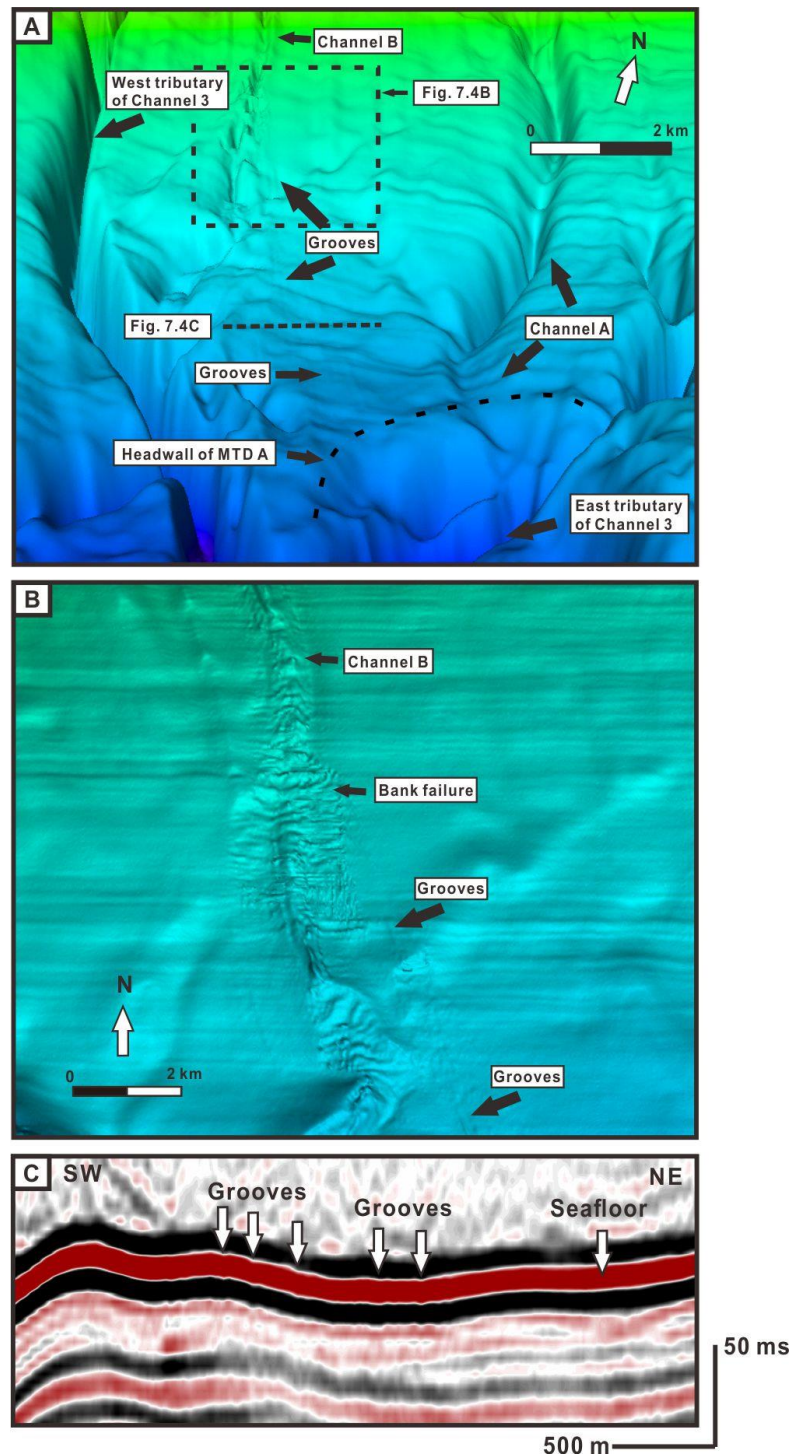
Figure 7.4. 3D view of seafloor morphology showing grooves upslope of the headwall of the scar. A) 2D view of seafloor morphology showing the grooves can be tracked to the bank of a channel (Channel B) where bank failures occurred. This character suggests that the grooves were formed by sheet turbidity currents that breached a channel bank. The location of this figure is shown in Fig. 7.4A. C) Seismic cross section showing a series of grooves on the seafloor. Its location is shown in Fig. 7.4A.

presence of grooves on the seafloor suggests that unconfined sheet flows may have been captured by the headwall of the basal scar.

Channels 1, 2, and 3 are interpreted to reflect different episodes of flow-capture processes (Fig. 7.5). After the basal scar was generated, it captured turbidity currents at its headwall (Figs. 7.5A and B) and these captured flows removed part of MTD A along the longitudinal direction (N–S) of the scar (Fig. 7.5B). Channel 1 was likely formed at this stage (Fig. 7.5B), because its bank orientation is similar to the longitudinal direction (N–S) of MTD A (Fig. 6.8E). Erosion along the longitudinal direction (N–S) of MTD A enlarged the depletion zone of the scar (Fig. 7.5B), and allowed flow capture at its west margin, as shown by the presence of Channel 2 (Fig. 7.5C). Channel 3 is believed to have been captured by the headwall of the scar, based on its position with respect to the scar (Fig. 7.5D).

Compared to shelf-edge scars recognised in the Gulf of Mexico (Winker and Booth 2000; Kneller et al. 2016) and the Nile Delta slope (Kertznus, 2009), which incise the shelf break and connect shelf-edge deltas with upper-slope depositional systems (Kneller et al., 2016), we present a case study of flow capture in a different slope setting. In this work, the basal scar is located in a confluence region confined by salt diapirs (Fig. 7.5A). Therefore, turbidity currents derived from source areas upslope tend to be deflected into the basal scar due to the presence of salt diapirs (Figs. 7.5A). Flow deflection caused by salt diapirs increases the probability of flow-capture processes, which might have been frequent throughout the evolution of the channel system. For example, adding to flow capture in the headwall region of the scar shown by the presence of Channels 1, 3, and A (Figs. 7.5B and D), this work exemplifies a flow-capture pattern that has not been documented in previous work. The relative positions of Channel 2 and adjacent basal scar (Figs. 6.8E and 7.5C) suggest that turbidity currents could also be captured by the lateral margins of scars. Such a capture process resulted mainly from flow deflection due to the presence of the confluence region created by the salt diapirs (Fig. 7.5A).

7.2.2.2 A mechanism for channel initiation

Flow confinement is an important process in channel initiation, and can be achieved by channel
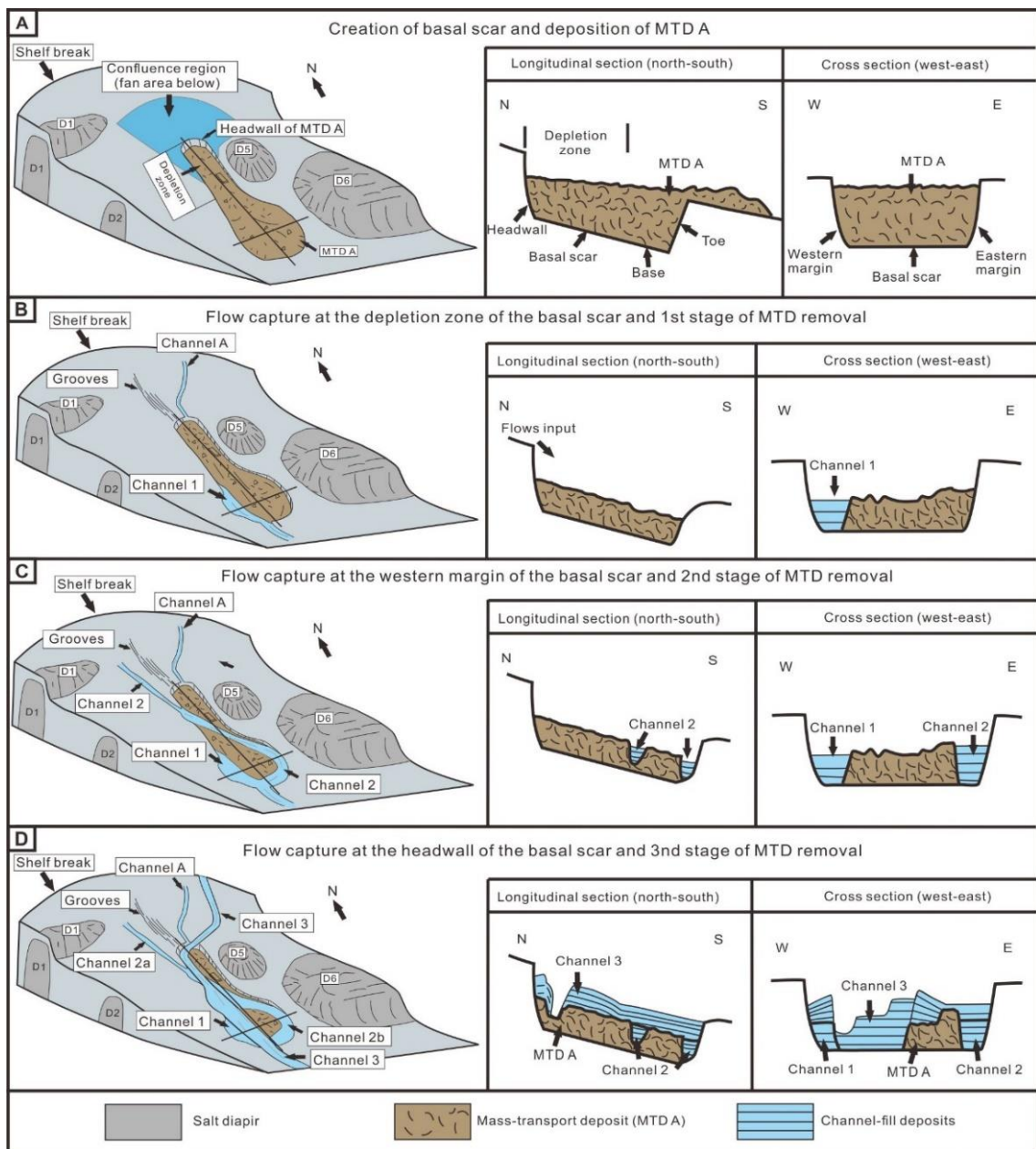
Figure 7.5. Schematic diagram summarising the evolution model of the channel system in the confluence region. D1 to D6 show the location of salt diapirs. A) Schematic diagram showing the occurrence of a mass-wasting process in a confluence region confined by salt diapirs. A basal scar was created and was filled with MTD A. B) Schematic diagram showing that turbidity currents were captured by the headwall of the scar; these flows removed the upper part of MTD A downslope. Channel 1 was formed at this stage. C) Schematic diagram showing the stage in which Channel 2 was captured by the western wall of the scar. Channel 2 used the eastern margin of the scar as its bank. D) Schematic diagram showing that Channel 3 was captured by the headwall of the scar. This channel incised the toe of the scar and extends downslope toward the continental rise.

incision and levee construction (e.g. Straub and Mohrig, 2009; Rowland et al., 2010; Weill et al., 2014; De Leeuw et al., 2016). In addition to these studies, we suggest that flow confinement and channelisation also result from flow-capture processes. On the seafloor, erosional grooves generated by unconfined flows are observed upslope of the scar (Fig. 7.4), indicating that sheet turbidity currents were funnelled into the scar. This process forced the unconfined sheet flows into a confined flow, thus enhancing flow channelization in the study area.

Large conduits have been suggested to be formed at the early stage of channel formation, with MTDs at their base (e.g. Samuel et al., 2003; Mayall et al., 2006; Macauley and Hubbard, 2013). As mass-wasting events can be precursors of submarine channels, some of these valleys may be created by mass-wasting events and filled by debris-flow deposits, and later modified by subsequent turbidity currents, which are able to erode MTDs on the continental slope and deposit channel-fill deposits in the scars (Fig. 7.5).

Previous studies applied sequence stratigraphic models to depositional sequence related to submarine settings (Vail et al. 1977; Mutti 1985, 1992; Posamentier et al. 1991; Posamentier, 2000; Posamentier and Kolla, 2003). For example, the depositional sequence of debris-flow deposits and overlying channel-fill deposits has been documented by previous studies (e.g. Jacobi, 1976; Jansen et al., 1987; Moore et al., 1989; Dam and Sønderholm, 1994; Piper, 1997; Beaubouf and Friedmann, 2000; Henrich, 2008; Fowler et al., 2004; Henrich et al., 2008; Bernhardt et al., 2012). This sequence maybe related to relative sea-level change (e.g. Dam and Sønderholm, 1994; Posamentier, 2000; Posamentier and Kolla, 2003). However, MTDs may occur at any stage of channel evolution, rather than only at the channel base (e.g. Cronin et al., 1998; Posamentier and Kolla, 2003), making it difficult to correlate the occurrence of MTDs and channel-fill deposits to relative sea-level change. In this study, it is difficult to confirm correlation between MTD and sea-level change due to the lack of dating results. Instead, MTD A here was probably triggered by salt movement due to close spatial association with salt diapir.

7.2.2.3 Interaction between MTDs and turbidity currents

7.2.2.3.1 Morphological changes in the basal scar

The basal scar is interpreted as having been widened on its western margin (Figs. 6.9C, D, G and H). The presence of curved banks in Channels 1 and 2a (Fig. 6.8E) highlights the role of localised mass failures in the widening of the scar.

These low thickness values suggest that Surface E played a key role in delimiting the erosional base of both the channels and MTD A. Surface E is probably a mechanically weak layer acting as a detachment surface, above which mass wasting tends to occur. However, the lithology of this surface is unknown due to the lack of well data in the study area.

The lateral continuity of Surface E indicates that most erosional processes occurred above this specific surface (Figs. 6.9C–L). Such an erosional pattern suggests that the interval between the deposition of MTD A and subsequent channel erosion may have been so short, that they preceded the consolidation of MTD A. Therefore, MTD A was weaker than the strata beneath Surface E, and, as a result, turbidity currents preferentially eroded less resistant MTD A above Surface E rather than incising downward into older deposits. This process resulted in a pronounced widening of the basal scar with small change in its height (Figs. 6.9C–H, K and L).

Differences in sediment strength within and outside of the scar also influence the pathways of channels. For instance, Channel 2b probably used the margin of the basal scar as its east bank (Fig. 6.8E), thus focusing erosion in areas where MTD A was present (Figs. 6.8E and 6.9E–H). A similar process occurred in the eastern Gulf of Mexico, where the east bank of the Einstein channel system was constrained by the eastern margin of a basal scar (fig. 11 of Kneller et al. 2016). Such a spatial association between the margins of channel systems and basal scars suggests that turbidity currents tend to erode less resistant MTDs within the scars rather than more resistant sediments forming the margins of the scars.

7.2.2.3.2 Replacement of strata in the basal scar, and reservoir implications

Along the course of Channel 2b, a large volume of MTD A was removed and replaced by sand-prone channel-fill deposits (Figs. 6.9E–H, K and L). As a result of such an erosion, the thickness of

MTD A ranges from 8 m to 40 m along Channel 2b, where is smallest, whereas the remainder of MTD A is 40 m to 120 m thick (Fig. 6.10C).

Additionally, the thickness variations in MTD A indicate that differential erosion occurred in this MTD, especially along the east margin of the scar and the pathway of Channel 2b (Fig. 6.10C). This erosional pattern may have resulted from variations in the properties of turbidity currents. The thicker MTD interval along the longitudinal direction (N–S) of the scar may have been affected by less erosive and less frequent flows captured by the headwall. Conversely, the thinner MTD interval along Channel 2b indicates more erosive and more frequent turbidity currents captured by the western margin of the scar.

Although MTDs are generally considered as poor reservoirs due to their low porosity and permeability (Posamentier and Kolla, 2003; Moscardelli et al., 2006), their associated depositional systems, especially submarine channels and lobes, are recognised as important hydrocarbon reservoirs in deep-water settings (Mayall et al., 2006; Armitage et al., 2009; Jackson and Johnson, 2009; Kneller et al., 2016). This work shows that the erosion and replacement of strata above basal scars increased reservoir potential by the continuous obliteration of pre-existing MTDs in scars. This process might have enhanced the lateral continuity of turbidites and limited compartmentalization of sandy reservoir intervals by MTDs (Mayall et al., 2006; Moscardelli et al., 2006).

7.3 The influence of salt diapirs on the dimension and architecture of submarine channels

In the study area, the seafloor was divided into three regions based on the degree of confinement imposed by salt diapirs (Figs. 3.8 and 6.5). There is the lack of evidences for faults and folds associated with salt structures adjacent to the studied channel system (Fig. 3.5). Therefore, the movement of salt diapirs and associated seafloor deformation are major factors controlling the dimension and architecture of submarine channel systems in the study area.

In the confluence region with the highest degree of confinement, local uplift associated with the growth of salt diapirs resulted in flank oversteepening, and the lowering of strength of sediment, in the vicinity of salt diapirs. As a result of salt movements, multiple mass-wasting events occurred

in this region, as shown by varied headwall scars on the seafloor (Figs. 3.8 and 6.5). Similar zones of instability surrounding active salt diapirs have also been documented in the Gulf of Mexico (Tripsanas et al. 2004) and the Nile deep-sea fan (Lonkce et al. 2009).

In the study area, turbidity currents were diverted into the confluence region due to the presence of local topographic highs created by salt diapirs, as evidenced by variations in pathways of channels and gullies (Fig. 6.5). Turbidity currents facilitate mass wasting on the banks of the channel system. As a consequence, a significantly widened channel system was formed in the confluence region, where the width can be increased by as much as 5 km when compared to other parts of the studied channel system (Fig. 6.6A).

Previous studies have documented width variations of channel systems in a confined region created by salt diapirs (Gamboa et al., 2012; Sylvester et al., 2012; Carter et al., 2016). However, the width variation recorded in previous studies is not as significant as the channel system in this work. For example, in the same region, but ~ 1.5 km below the modern seafloor, Gamboa et al. (2012) have shown that the width of a Miocene channel system only increases 1-2 km in the confluence region confined by diapirs studied here. In the Gulf of Mexico, the width of channel system increases less than 1 km when passing through a highly-confined region delimited by salt diapirs (Sylvester et al., 2012). These differences in width variations in distinct channel systems are probably associated with the relative movement of salt diapirs. Small increases in width may suggest that salt diapirs are relative stable at the exact time-period of channel development. In contrast, during the active stages of salt growth, bank failures tend to occur and lead to much widened channel systems (Fig. 6.6A).

Carter et al. (2016) proposed a different model to interpret width variations under salt-diapir confinement. They ascribed the widening of the channel system to the slowing down of the uplift of salt diapirs, and the narrowing of the channel system to the increased uplift rate of salt diapir (Carter et al., 2016). In their work, however, large slump scars are evident during the widening periods of channel system (Figs. 14E and F of Carter et al., 2016). These scars were possibly formed by bank failures triggered by the movement of salt diapirs, suggesting an increase, rather than the slowdown of salt movement interpreted by the latter authors.

In addition to channel-widening processes via mass wasting, the presence of salt diapirs

resulted in another type of widening process and associated changes of architectures within Quaternary Rio Doce Channel system. Salt diapirs (D1, D2, D5 and D6) divert turbidity currents from upslope areas and coalesce these flows into a specific region (i.e. confluence region), as shown by the changes of channel orientation and the presence of tributaries in the studied channel systems (Fig. 6.5). Sediments from these tributaries promoted lateral channel migration within the channel system, leading to the formation of bends and a widened channel system in the confluence area (Figs. 5.4C and D).

7.4 Variations in channel stacking patterns and its implications in channel evolution

Channel evolution, from initiation to abandonment, is a process of channel thalweg shifts that involves lateral and vertical movement. This study shows spatial variations in channel evolution and weak relationship between lateral migration and aggradation (Fig. 5.3E). In the middle reach, the ratio of lateral migration/vertical aggradation ranges from 3 to 10, higher than the ratio in the lower reach, where it varies from 1 to 2 (Fig. 5.3F). This observation is consistent with Kolla et al. (2001) findings that the influence of lateral migration vs. vertical aggradation varies from one channel to another and even along the length of a single channel or across a single sinuous loop.

Vertical aggradation appears to be related to tributaries and valley-slope variations in this work. It is larger where valley slope is lower and sediment input from tributaries is important (Figs. 5.3B and C). However, it is difficult to weight which factor is more important in aggradation amount along the channel system. In addition, the trigger for transition from early channel incision to vertical aggradation is also unknow in this work. This transition is ascribed to variations in flow properties within submarine channels in previous studies (e.g. Kneller et al., 2003; McHargue et al., 2011), though the controls on such variations is no yet unravelled.

Lateral movement is another key element of channel evolution (e.g. Mutti and Normark, 1987; Clark and Pickering, 1996; Deptuck et al., 2003; Sylvester et al., 2011; Jobe et al., 2016). This work shows that enhanced sediment supply can promote lateral channel migration. Increased sediment discharge in this work is interpreted to result from tributaries based on increased sediment volume

downstream of confluence points, but it could also result from tectonic activity and climate change that affected source areas on the land and continental shelves (Kneller, 2003; Kolla, 2007; McHargue et al., 2011; Hodgson et al., 2011; Jobe et al., 2015).

Sediment supply caused by tectonic deformation and climate change could result in enhanced lateral migration occurring at any stage of channel evolution. In this case, perhaps leading to the unclear patterns of lateral migration, which may have occurred at any stage of channel evolution (e.g. Samuel et al., 2003; Deptuck et al., 2007; Janocko et al., 2013; Jobe et al., 2015). For example, lateral migration with degradation (Jobe et al. 2015) and little aggradation (Sameul et al., 2003; Janocko et al., 2013) at the early stage of channel evolution may be caused by erosive flows, which have higher discharge and calibre (i.e. grain size).

7.5 Limitations of this research

In this study, there is a lack of accurate age constraints on the current stratigraphic framework of the basin, which was constructed based on variations in seismic facies and regional unconformities in the Espírito Santo Basin (França et al., 2007). Therefore, the ages of channel initiation and main stages of channel evolution are difficult to know due to a lack of chronostratigraphic dates for the interpreted depositional elements. This makes the relationship between sea level change and channel evolution hard to evaluate in the study area, and thus requires the future collection of sediment core data to assess this relationship.

In addition, well data would have provided stratigraphic information necessary to develop time-depth conversion within the seismic data. It could also have provided lithological and age constraints on channels, and allowed evaluation of sediment transport processes and associated flows properties within the channels, as well as the reservoir potential of channel systems.

The seismic dataset used in this work is limited to the continental slope of Espírito Santo Basin, making it difficult to assess the sediment sources of channel systems and the role of the Rio Doce river in submarine-channel evolution. Therefore, the extension of the dataset to the continental shelf would help elucidate 1) whether Rio Doce river delta connects to submarine channels in the

study area, 2) the relationship between shelf-margin architecture and submarine-channel evolution, and 3) sediment dispersal patterns from continental shelf to slope in the Espírito Santo Basin.

7.6 Future work

Bank erosion is an important process in submarine-channel evolution. Numerous bank failure scars are observed in this study and in other submarine channels around the world, but there are few studies of bank erosion processes in submarine channels compared to fluvial channels (e.g. Sawyer et al., 2013; Mitchell et al., 2014). Therefore, more numerical modelling and experimental studies of bank erosion are needed to better understand channel enlargement and turbidity-flow properties.

Apart from the studied channel system, there are two other submarine channel systems in the study area: a Miocene channel system and an Eocene channel system. These two channel systems have been studied in previous work (Alves et al, 2009; Gamboa et al., 2012; Gamboa and Alves, 2015), but more detailed studies are needed for these channel systems. For example, these three channel systems show different morphology and architectures. Comparison between these channel systems helps to reconstruct the paleogeography of the study area and their sediment sources.

Several MTDs are observed in the study area. Their distribution and morphology seems to be associated with the development of submarine channels. This thesis provides a case study of interaction between MTDs and channels, but further studies are needed to understand how the internal structures and heterogeneous nature of MTDs affect turbidity currents. Lithological information from wells, outcrop, or flume-tank models, will be beneficial to these studies.

Salt tectonics plays a key role in the evolution of depositional systems in the study area, such as submarine channels, MTDs, and lobes. For example, submarine channels are sensitive to changes in the seafloor deformation caused by salt structures. They respond to the deformation through various ways such as slope profile and sinuosity. Therefore, a detailed reconstruction of salt movements is crucial to further understanding the spatial and temporal distribution of multiple depositional elements in the study area.

Chapter 8

Conclusions

8. Conclusions

In this thesis, a 3D seismic volume from offshore Espírito Santo (SE Brazil) was used to analyse a submarine channel system developed on the modern sea floor. The studied channel systems in this thesis show distinct spatial variations in morphology, architecture, and evolutionary history along their pathways. These variations suggest the impacts of local factors (e.g. mass-wasting events, tributaries, substrate and salt tectonics) on the submarine-channel evolution. The main conclusions are as follows:

8.1 Quantitative analyses of Quaternary channel system

This work carried out a quantitative morphological analysis of a Quaternary Channel System in terms of its hierarchical framework.

•   On channel scale at a fundamental hierarchical level, five reaches (Reaches a to e) are identified based on the marked variations in morphologic parameters. For example, the cross-sectional area of the channel decreases by a factor of 7 from Reach t a to Reach c at the maximum, and is then followed by a nearly four-fold increase from Reach c to Reach d. The observed variations are related to spatial and temporal changes of flow volume within the channel.

•   On valley scale of a higher-order hierarchical level, three Reaches (Reaches A to C) are recognised according to the morphological changes of the valley, with similar aspect ratios but marked variations in dimension along the valley distance. The variations of valley dimension were controlled by two distinct erosional processes. Cut bank erosion during lateral channel migration results in the widening of the valley, especially the valley base. Another form of bank failure process, shallow-seated mass failure, only enlarged the upper part of the valley wall, resulting in stepped profiles of valley cross section.

•   The scales of channel and valley in this study are comparable to examples observed on other

continental slopes. Scale comparisons of valleys between the study area and in other parts of the world show significant variations in valley size. These variations suggest an important role of local factors in the development of submarine channel systems.

8.2 The role of mass-wasting events on channel evolution

This work used 3D seismic data to document how mass wasting influenced the geometry and distribution of subsequent submarine channels, as well as the replacement of MTDs by channel-fill deposits. In summary:

• In a confluence region confined by salt diapirs, the Pliocene–Quaternary Rio Doce Channel System is wider and larger than other parts of channel system. An MTD, three abandoned channels, and a channel complex are identified in the channel system in the confluence region confined by salt diapirs. In this confluence region, the cross-sectional area (CSA) of the channel system can be up to 1.2 km^2, i.e. 4 to 10 times larger than in other parts of the study area. These morphological and architectural features are interpreted to result from the interaction between mass-wasting deposits and subsequent turbidity currents.

• After a basal scar was generated by a mass-wasting event, it was used as a preferential pathway for subsequent turbidity currents, which were captured by the headwall and lateral margins of the scar.

• The morphology of the scar was modified by subsequent turbidity currents. The scar was greatly widened, with a small change in height, because of differences in sediment strength within and outside of the scar. In other words, the presence of softer MTDs hindered the downward incision of turbidity currents which, instead, widened the scar laterally. This process resulted in a much wider channel system than expected in the confluence region.

• Basal scars formed by mass-wasting events can provide flow confinement and facilitate flow

channelisation, which are key processes for submarine-channel initiation.

•   This work shows that the replacement of MTDs by channel-fill deposits was achieved through multiple cut-and-fill episodes associated with turbidity currents captured by the scar. The replacement has profound implications for reservoir volumes and net-to-gross ratios in channel systems. An MTD with poor reservoir quality was replaced by channel-fill deposits of higher reservoir potential. Such a replacement and associated reservoir potential relate to the properties of turbidity currents, such as their erosive ability and frequency. The more erosive and frequent flows are captured by the basal scar, the larger is the accommodation space created for subsequent sand-prone turbidites.

8.3 Stacking patterns and evolution of Quaternary channel system

Spatial and temporal variations in channel sinuosity are documented using 3D seismic data within the Quaternary submarine channel system. This work shows that a sinuous channel formed at early incision stage of channel evolution, and evolved through lateral channel migration. The channel system displays spatial variation in evolutionary history and was mainly affected by local factors such as tributaries and substrate lithology.

•   In the upper reach downstream of tributaries, the channel system shows marked temporal variations in channel sinuosity, which increases from 1.11 to 1.57. This increase in channel sinuosity resulted from higher magnitude of lateral channel migration, which in turn was caused by enhanced sediment supply from tributaries. The enhancement in sediment discharge led to more frequent and increased magnitude of lateral migration in the upper reach. Lateral channel migration is a main mechanism of channels response to enhanced sediment supply. The resulting enhancement in sediment discharge led to more frequent cut-and-fill processes. These, in turn, resulted in more frequent (and larger) scales of lateral migration in the submarine channel.

•   A positive relationship between valley slope and channel sinuosity is observed in the study area. The adjustment of channel in response to substrate erodibility may occur via variations in valley slope and channel sinuosity. Spatial variation in channel sinuosity is interpreted to reflect substrate

erodibility beneath the channel system. The channel has higher sinuosity when encountering resistant substrate, and shows lower sinuosity when the substrate is more erodible.

• The results presented here highlight lateral channel migration as an important mechanism linking external factors (e.g., sediment supply) to the morphology and architecture of submarine channel systems. The results show that submarine channels accommodate additional sediment supply through erosion and deposition during lateral migration, as shown by the enlarged valley size and larger sediment volumes downslope of tributaries. This work offers insights on sediment dispersal patterns and stratigraphic evolution on the continental slopes. It provides an analogue not only for studying submarine channels, but also for fluvial channels in sub-aerial settings.

References

Abdurrokhim and Ito, M., 2013. The role of slump scars in slope channel initiation: A case study from the Miocene Jatiluhur Formation in the Bogor Trough, West Java. Journal of Asian Earth Sciences, 73, 68-86.

Abreu, V., Sullivan, M., Pirmez, C., and Mohrig, D., 2003. Lateral accretion packages (LAPs): an important reservoir element in deep water sinuous channels. Marine and Petroleum Geology, 20, 631-648.

Adeogba, A.A., McHargue, T.R., and Graham, S.A., 2005. Transient fan architecture and depositional controls from near-surface 3-D seismic data, Niger Delta continental slope. American Association of Petroleum Geologists, Bulletin, 89, 627-643.

Albino, J., and Suguio, K., 2010. Sedimentation processes and beach morphodynamics active at the Doce River mouth, Espírito Santo State, Brazil. Anais da Academia Brasileira de Ciências, 82, 1031-1044.

Allen, G. H., Barnes, J.B., Pavelsky, T.M., and Kirby, E., 2013. Lithologic and tectonic controls on bedrock channel form at the northwest Himalayan front. Journal of Geophysical Research: Earth Surface, 118, 1806–1825, doi:10.1002/jgrf.20113.

Alves, T.M., 2010. 3D Seismic examples of differential compaction in mass-transport deposits and their effect on post-failure strata. Marine Geology, 271, 212-224.

Alves, T.M., 2012. Scale-relationships and geometry of normal faults reactivated during gravitational gliding of Albian rafts (Espírito Santo Basin, SE Brazil). Earth and Planetary Science Letters, 331-332, 80-96.

Alves, T.M., Cartwright, J. and Davies, R.J., 2009. Faulting of salt-withdrawal basins during early halokinesis: Effects on the Paleogene Rio Doce Canyon system (Espirito Stanto Basin, Brazil). American Association of Petroleum Geologists, Bulletin, 93, 617-652.

Amante, C., and Eakins, B.W., 2009. ETOPO1 1 Arc-Minute Global Relief Model: Procedures, Data Sources and Analysis. NOAA Technical Memorandum NESDIS NGDC-24. National Geophysical Data Center, NOAA. doi:10.7289/V5C8276M.

Amir, A., 1992. Channel-levee systems on the Indus deep-sea fan. Ph. D thesis, University of Wales, 230pp.

Antobreh, A.A., and Krastel, S., 2006. Morphology, seismic characteristics and development of Cap Timiris Canyon, offshore Mauritania: a newly discovered canyon preserved off a major arid climatic region. Marine and Petroleum Geology, 23, 37-59.

Armitage, D.A., McHargue, T., Fildani, A., and Graham, S.A., 2012. Postavulsion channel evolution: Niger Delta continental slope. American Association of Petroleum Geologists, Bulletin, 96, 823–843.

Armitage, D.A., Romans, B.W., Covault, J.A., and Graham, S.A., 2009. The influence of mass transport deposit surface topography on the evolution of turbidite architecture: the Sierra Contreras, Tres Pasos Formation (Cretaceous), southern Chile. Journal of Sedimentary Research, 79, 287-301.

Arnott, R. W. C., 2007. Stratal architecture and origin of lateral accretion deposits (LADs) and conterminuous inner-bank levee deposits in a base-of-slope sinuous channel, lower Isaac Formation (Neoproterozoic), East-Central British Columbia, Canada. Marine and Petroleum

Geology, 24, 515-528.

Arzola, R.G., Wynn, R.B., Lastras, G., Masson, D.G. and Weaver, P.P.E., 2008. Sedimentary features and processes in the Nazaré and Setúbal submarine canyons, west Iberian margin. Marine Geology, 250, 64-88.

Babonneau, N., Savoye, B., Cremer, M. and Bez, M., 2010. Sedimentary architecture in meanders of a submarine channel: detailed study of the Present Congo turbidite channel (Zaiango project). Journal of Sedimentary Research, 80, 852-866.

Babonneau, N., Savoye, B., Cremer, M., and Bez, M., 2004. Multiple terraces within the deep incised Zaire Valley (ZaiAngo Project): are they confined levees? Geological Society London Special Publications, 222, 91-114.

Babonneau, N., Savoye, B., Cremer, M., and Klein, B., 2002. Morphology and architecture of the present canyon and channel system of the Zaire deep-sea fan. Marine and Petroleum Geology, 19, 445-467.

Bacon, M., Simm, R., and Redshaw, T., 2003. 3-D seismic interpretation. Cambridge University Press, 209 pp.

Bain, H.A., and Hubbard, S.M., 2016, Stratigraphic evolution of a long-lived submarine channel system in the late Cretaceous Nanaimo Group, British Columbia, Canada. Sedimentary Geology, 337, 113-132.

Bastos, C., Quaresma, V., Marangoni, M., D'Agostini, D., Bourguignon, S., Cetto, P., Silva, A., Filho, G., Moura, R., and Collins, M., 2015. Shelf morphology as an indicator of sedimentary regimes: A synthesis from a mixed siliciclastic–carbonate shelf on the eastern Brazilian margin. Journal of South American Earth Sciences, 63, 125-136.

Baudon, C., and Cartwright, J., 2008. The kinematics of reactivation of normal faults using high resolution throw mapping. Journal of Structural Geology, 30, 1072-1084.

Beaubouef, R.T., Rossen, C., Zelt, F.B., Sullivan, M.D., Mohrig, D.C., and Jennette, D.C., 1999. Deepwater sandstones of the Brushy Canyon Formation, west Texas, Field Guide, American Association of Petroleum Geologists, Bulletin, Hedberg Field Research Conference, April 15-20, 48 pp.

Beauboeuf, R.T., and Friedmann, S.J., 2000, High-resolution seismic/sequence stratigraphic framework for the evolution of Pleistocene intra slope basins, Western Gulf of Mexico: depositional models and reservoir analogs, in Weimer, P., Slatt, R.M., Coleman, J., Rosen, N.C., Nelson, H., Bouma, A.H., Styzen, M.J., and Lawrence, D.T., eds., Deep-Water Reservoirs of the World: Gulf Coast Society of the Society of Economic Paleontologists and Mineralogists Foundation, 20th Annual Research Conference, p. 40–60.

Beaubouef, R.T., 2004. Deep-water leveed-channel complexes of the Cerro Toro Formation, Upper Cretaceous, southern Chile. American Association of Petroleum Geologists, Bulletin, 88, 1471–1500.

Bernhardt, A., Stright, L., and Lowe, D.R., 2012, Channelized debris-flow deposits and their impact on turbidity currents: the Puchkirchen axial channel belt in the Austrian Molasse Basin. Sedimentology, 59, 2042–2070.

Bernhardt, A., Hebbeln, D., Regenberg, M, Lückge, A., and Strecker, M., 2016. Shelfal sediment transport by an undercurrent forces turbidity-current activity during high sea level along the Chile continental margin. Geology, 44, 295-298.

Bischoff, A., and Lipsky, M., 2008. Estilos arquiteturais de turbiditos na Bacia do Espírito Santo. III

Simpósio Brasileiro da SBGf, Belém, Brazil.

Bouma, A. H., 1962. Sedimentology of some Flysch deposits: a graphic approach to facies interpretation. Elsevier, Amsterdam, 168 pp.

Bouma, A., Coleman, J.M., DSDP Leg 96 Shipboard Scientists, 1985. Mississippi Fan: Leg 96 Program and Principal Results. Submarine Fans and Related Turbidite System, 247-252.

Bowen, A.J., Normark, W.R. and Piper, D.J.W., 1984. Modelling of turbidity currents on Navy Submarine Fan, California continental Borderland. Sedimentology, 31, 169-185.

Brown, A.R., 2004. Interpretation of Three-Dimensional Seismic Data, AAPG Memoir, 42. American Association of Petroleum Geologists.

Bruhn, C.H.L., and Walker, R.G., 1997, Internal architecture and sedimentary evolution of coarse-grained, turbidite channel-levee complexes, early Eocene Regência canyon, Espírito Santo Basin, Brazil. Sedimentology, 44, 17-46.

Brunt, R., Di Celma, C., Hodgson, D., Flint, S., Kavanagh, J., and Van der Merwe, W., 2013. Driving a channel through a levee when the levee is high: an outcrop example of submarine down-dip entrenchment. Marine and Petroleum Geology, 41, 134-145.

Buffington, E.C., 1952. Submarine 'natural levees'. Journal of Geology, 60, 473–479.

Bull, S., Cartwright, J., and Huuse, M., 2009, A review of kinematic indicators from mass-transport complexes using 3D seismic data. Marine and Petroleum Geology, 26, 1132-1151.

Campion, K.M., Sprague, A.R., Mohrig, D., Lovell, R.W., Drzewiecki, P.A., Sullivan, M.D., Ardill, J.A., Jensen, G.N., and Sickafoose, D.K., 2000. Outcrop expression of confined channel complexes. In: Weimer, P., Slatt, R.M., Coleman, J., Rosen, N.C., Nelson, H., Bouma, A.H., Styzen, M.J., Lawrence, D.T. (Eds.), Deepwater Reservoirs of the World. Gulf Coast Section SEPM 20th Bob F. Perkins Research Conference, pp. 127-150.

Carter, 1998, The nature and evolution of deep-sea channel systems. Basin Research, 1, 41-54.

Carter, R.C., Gani, M.R., Roesler, T., and Sarwar, A.K.M., 2016. Submarine channel evolution linked to rising salt domes, Gulf of Mexico, USA, Sedimentary Geology, 342, 237-253.

Catterall, V., Redfern, J., Gawthorpe, R., Hansen, D. and Thomas M., 2010. Architectural style and quantification of a submarine channel–levee system located in a structurally complex area: offshore Nile delta. Journal of Sedimentary Research, 80, 991-1017.

Chang, H.K., Kowsmann, R.O., Figueiredo, A.M., and Bender, A.A., 1992. Tectonics and stratigraphy of the East Brazil Rift system—an overview. Tectonophysics, 213, 97-138.

Chiang, C.S. and Yu, H.S., 2006. Morphotectonics and incision of the Kaoping submarine canyon, SW Taiwan orogenic wedge. Geomorphology, 80, 199-213.

Chiang, C.S., Yu, H.S., Noda, A., Tuzino, T. and Su, C.C., 2012. Avulsion of the Fangliao submarine canyon off southwestern Taiwan as revealed by morphological analysis and numerical simulation. Geomorphology, 177-178, 26-37.

Chough, S. and Hesse, R., 1976. Submarine meandering thalweg and turbidity currents flowing for 4000 km in the Northwest Atlantic Mid-Ocean Channel, Labrador Sea. Geology, 20, 633-636.

Clark, I.R., and Cartwright, J.A., 2009. Interactions between submarine channel systems and deformation in deep-water fold belts: examples from the Levant Basin, Eastern Mediterranean Sea. Marine and Petroleum Geology, 26, 1465-1482.

Clark, I.R., and Cartwright, J.A., 2011. Key controls on submarine channel development in structurally active settings. Marine and Petroleum Geology, 28, 1333-1349.

Clark, J.D. and Pickering, K.T., 1996. Architectural elements and growth patterns of submarine

channels; application to hydrocarbon exploration. American Association of Petroleum Geologists, Bulletin, 80, 194-221.

Clark, J.D., Kenyon, N.H., and Pickering, K.T., 1992. Quantitative analysis of the geometry of submarine channels: implications for the classification of submarine fans. Geology, 20, 633-636.

Clift, P., Gaedicke, C., Edwards, R., Lee, J.I., Hildebrand, P., Amjad, S., White, R.S. and Schlüter, H., 2002. The stratigraphic evolution of the Indus fan and the history of sedimentation in the Arabian Sea. Marine Geophysical Researches 223–245.

Cobbold, P.R., Meisling, K.E., and Mount, V.S., 2001. Reactivation of an obliquely rifted margin, Campos and Santos basins, southeastern Brazil. American Association of Petroleum Geologists, Bulletin, 85, 1925-1944.

Constantine, J., A., Dunne, T., Ahmed, J., Legleiter, C., and Lazarus, E.D., 2014. Sediment supply as a driver of river meandering and floodplain evolution in the Amazon Basin. Nature Geoscience, 7, 899–903.

Conway, K.W., Barrie, J.V., Picard, K., and Bornhold, B.D., 2012. Submarine channel evolution: active channels in fjords, British Columbia, Canada. Geo-Marine Letters 32, 301–312.

Cordani, U.G., 1970. Idade do vulcanismo no Oceano Atlântico Sul. Boletim do Instituto de Geociências e Astronomia da Universidade de São Paulo, 1, 9-76.

Corella, J.P., Loizeau, J.L., Kremer, K., Hilbe, M., Gerard, J., Le Dantec, N., Stark, N., González-Quijano, M., and Giradclos, S., 2016. The role of mass-transport deposits and turbidites in shaping modern lacustrine deepwater channels. Marine and Petroleum Geology, 77, 515-525.

Covault, J.A., Fildani, A., Romans, B.W. and McHargue, T., 2011. The natural range of submarine canyon-and-channel longitudinal profiles. Geosphere, 7, 313-332.

Covault, J.A., Kostic, S., Paull, C.K., Ryan, H.F., and Fildani, A., 2014. Submarine channel initiation, filling and maintenance from sea-floor geomorphology and morphodynamic modelling of cyclic steps. Sedimentology, 61, 1031–1054.

Covault, J.A., Kostic, S., Paull, C.K., Sylvester, Z., and Fildani, A., 2016. Cyclic steps and related supercritical bedforms: building blocks of deep-water depositional systems, western North America. Marine Geology, in press.

Cronin, B.T. Akhmetzhanov, A.M., Mazzini, A., Akhmanov, G., Ivanov, M. and Kenyon, N., 2005a. Morphology, evolution and fill: Implications for sand and mud distribution in filling deep-water canyons and slope channel complexes. Sedimentary Geology, 179, 71-97.

Cronin, B.T., 1994. Channel-fill architecture in deep-water sequences: variability, quantification and applications. Unpublished Ph.D. thesis, University of Wales, 332pp.

Cronin, B.T., 1995. Structurally-controlled deep sea channel courses: examples from the Miocene of southeast Spain and the Alboran Sea, southwest Mediterranean. Geological Society of London Special Publication, 94, 115-135.

Cronin, B.T., Çelik, H., Hurst, A., and Türkmen, I., 2005b. Mud prone entrenched deep-water slope channel complexes from the Eocene of eastern Turkey. In: Hodgson, D.M., Flint, S.S. (Eds.), Submarine Slope Systems: Processes and Products. Geological Society, London, Special Publication, vol. 244, pp. 155–180.

Cronin, B.T., Hurst, A., Çelik, H., and Türkmen, I., 2000. Superb exposure of a channel levee and overbank complex in an ancient deep-water slope environment. Sedimentary Geology, 132, 205–216.

Cronin, B.T., Kenyon, N.H., Woodside, J., den Bezemer, T., van der Wal, A., Millington, J., Ivanov, M.K., and Limonov, A., 1995. The Almeria Canyon: a meandering channel system on an active margin, Alboran and Sea, western Mediterranean. In: Pickering, K.T., Hiscott, R.N., Kenyon, N.H., Lucchi, F.R., Smith, R.D.A. (Eds.), Atlas of Deepwater Environments: Architectural Styles in Turbidite Systems. Chapman & Hall, London, pp. 84–88.

Cronin, B.T., Owen, D., Hartley, A.J. and Kneller, B., 1998. Slumps, debris flows and sandy deep-water channel systems: implications for the application of sequence stratigraphy to deep-water clastic sediments. Journal of the Geological Society of London, 155, 429–432.

Cross, N.E., Cunningham, A., Cook, R.J., Taha, A., Esmaie, E., and El Swidan, N., 2009. Three-dimensional seismic geomorphology of a deep-water slope-channel system: the Sequoia field, offshore west Nile delta, Egypt. American Association of Petroleum Geologists, Bulletin, 93, 1063-1086.

Curray, J.R., Emmel, F.J. and Moore, D.G., 2003. The Bengal Fan: morphology, geometry, stratigraphy, history and processes. Marine and Petroleum Geology 19, 1191–1223.

Daly R.A., 1936. Origin of submarine canyons. American Journal of Science, 31, 401-420.

Damuth, J.E., Embley, R.W., 1981. Mass-transport processes on the Amazon Cone: western equatorial Atlantic. American Association of Petroleum Geologists, Bulletin, 65, 629-643.

Damuth, J. E., Kowsmann, R. O., Flood, R. D., Belderson, R. H., and Gorini, M. A., 1983. Age relationships of distributary channels on Amazon deep-sea fan: Implications for fan growth pattern. Geology, 11, 470–473.

Damuth, J.E. and Kumar, N., 1975. Amazon Cone: morphology, sediments, age, and growth pattern. Geological Society of America Bulletin, 86, 863-878.

Davison, I., 1999. Tectonics and hydrocarbon distribution along the Brazilian South Atlantic margin. In: N.R. Cameron, R.H. Bate and V.S. Clure (Eds.), The oil and gas habitats of the South Atlantic. Geological Society London Special Publications. 153, 133-151.

De Leeuw, J., Eggenhuisen, J.T., and Cartigny, M.J.B., 2016. Morphodynamics of submarine channel inception revealed by new experimental approach. Nature communication, 7, 1-7.

De Ruig, M.J., and Hubbard, S.M., 2006. Seismic facies and reservoir characteristics of a deep-marine channel belt in the Molasse foreland basin, Puchkirchen Formation, Austria. American Association of Petroleum Geologists, Bulletin, 90, 735-752.

Demercian, S., Szatmari, P., and Cobbold, P.R., 1993. Style and pattern of salt diapirs due to thin-skinned gravitational gliding, Campos and Santos basins, offshore Brazil: Tectonophysics, 228, 393-433.

Deptuck, M.E., Steffens, G.S., Barton, M. and Pirmez, C., 2003. Architecture and evolution of upper fan channel-belts on the Niger Delta slope and in the Arabian Sea. Marine and Petroleum Geology, 20, 649-676.

Deptuck, M.E., Sylvester, Z., Pirmez, C., and O'Byrne, C., 2007. Migration-aggradation history and 3-D seismic geomorphology of submarine channels in the Pleistocene Benin-major Canyon, western Niger Delta slope. Marine and Petroleum Geology, 24, 406-433.

Dietz, R.S., 1953. Possible deep-sea turbidity-current channels in the Indian Ocean. Geological Society of America Bulletin, 64, 375-378.

Di Celma, C.N., Brunt, R.L., Hodgson, D.M., Flint, S.S., and Kavanagh, J.P., 2011. Spatial and temporal evolution of a Permian submarine slope channel-levee system, Karoo Basin, South Africa. Journal of Sedimentary Research, 81, 579-599.

Dill, R.F., Dietz, R.S. and Stewart, H.B. Jr., 1954. Deep-sea channels and delta of the Monterey submarine canyon. Geological Society of America Bulletin, 65, 191–194.

Dominguez, J.M.L., Bittencourt, A.C.S.P., and Martin, L., 1992. Controls on Quaternary coastal evolution of the east-northeastern coast of Brazil: roles of sea-level history, trade winds and climate. Sedimentary Geology, 80, 213-232.

Droz, L. and Bellaiche, G., 1985. Rhone deep-sea fan: morphostructure and growth pattern. American Association of Petroleum Geologists, Bulletin, 69, 460-479.

Dugan, B., and Sheahan, T. C., 2012. Offshore sediment overpressures of passive margins: mechanism, measurement, and models. Review of Geophysics, 50, RG3001, doi:10.1029/2011RG000379.

Duvall, A., Kirby, E., and Burbank, D., 2004. Tectonic and lithologic controls on bedrock channel profiles and processes in coastal California. Journal Geophysical Research, 109, F03002, doi:10.1029/2003JF000086.

Dykstra, M., and Kneller, B.C., 2009. Lateral accretion in a deep-marine channel complex: implications for channelized flow processes in turbidity currents. Sedimentology, 56, 1411-1432.

Eggenhuisen, J.T., McCaffrey, W.D., Haughton, P.D.W., Butler, R.W.H., Moore, I., Jarvie, A., and Hakes, W.G., 2010. Reconstructing large-scale remobilisation of deep-water deposits and its impact on sand-body architecture from cored wells: the Lower Cretaceous Britannia Sandstone Formation, UK North Sea. Marine and Petroleum Geology, 27, 1595–1615.

Elliott, T., 2000. Depositional architecture of a sand-rich, channelized turbidite system: the Upper Carboniferous Ross Sandstone Formation, western Ireland. In: Weimer, P., et al. (Eds.) Turbidite Reservoirs of the World. 20th Annual Gulf Coast Section SEPM Proceedings, pp. 342–373.

Embley, R.W., 1980. The role of mass-transport in the distribution and character of deep-ocean sediments with special reference to the North Atlantic. Marine Geology, 38, 23–50.

Emmel, F.J., and Curray, J.R., 1985. Bengal Fan, Indian Ocean. In: Bouma, A.H., Normark, W.R., Barnes, N.E. (Eds.), Submarine Fans and Related Turbidite Systems, Springer. New York, pp. 107-I 12.

Ericson, D.B., Ewing, M., Heezen, B.C., 1952. Turbidity currents and sediments in North Atlantic. American Association of Petroleum Geologists, Bulletin, 36, 489–511.

Ericson, D.B., Ewing, M., Wollin, G., and Heezen, B., 1961. Atlantic deep-sea sediment cores. Geological Society of America Bulletin, 72, 193–286.

Estrada, F., Ercilla, G., and Alonso, B., 2005. Quantitative study of a Magdalena submarine channel (Caribbean Sea): implications for sedimentary dynamics. Marine and Petroleum Geology, 22, 623-635.

Ewing, M., Heezen, B. C., Ericson, D. B., Northrop, J., and Dorman, J., 1953, Exploration of the Northwest Atlantic Mid-Ocean Canyon. Geological Society of America Bulletin, 64, 865–868.

Estrella, G., Mello, M.R., Gaglianone, P.C., Azevedo, R.L.M., Tsubone, K., Rossetti, E., Concha, J., and Brüning, I.M.R.A., 1984. The Espírito Santo Basin, Brazil: source rock characterization and petroleum habitat. In: Demaison, G. and Murris, R. J. (Eds), Petroleum Geochemistry and Basin Evaluation. AAPG Memoir 35, 253-271.

Ferry, J.N., Mulder, T., Parize, O., and Raillard, S., 2005. Concept of equilibrium profile in deep-water turbidite system: effects of local physiographic changes on the nature of sedimentary process and the geometries of deposits. In: D.M. Hodgson and S.S. Flint (Eds.), Submarine Slope System. Geological Society of London, Special Publications, 244, 181-193.

Fiduk, J.C., Brush, E.R., Anderson, L.E., Gibbs, P.B., Rowan, M.G., 2004. Salt deformation, magmatism, and hydrocarbon prospectivity in the Espirito Santo Basin, offshore Brazil. In: Post, P.J., et al. (Eds.), Salt-sediment Interactions and Hydrocarbon Prospectivity: Concepts, Applications, and Case Studies for the 21st Century. GCSSEPM 24th Annual Research Conference, pp. 370-392.

Field, M.E., Gardner, J.V., and Prior, D.B., 1999. Geometry and significance of stacked gullies on the northern California slope. Marine Geology, 154, 271–286.

Figueiredo, J.J.P., Hodgson, D.M., Flint, S.S., and Kavanagh, J.P., 2013. Architecture of a channel complex formed and filled during long-term degradation and entrenchment on the upper submarine slope, Unit F, Fort Brown Fm., SW Karoo Basin, South Africa. Marine and Petroleum Geology, 41, 104–116.

Fildani, A., Normark, W.R., Kostic, S., and Parker, G., 2006. Channel formation by flow stripping: large-scale scour features along the Monterey East Channel and their relation to sediment waves. Sedimentology, 53, 1265–1287.

Flood, R.D., and Damuth, J.E., 1987. Quantitative characteristics of sinuous distributary channels on the Amazon deep-sea fan. Geological Society of America Bulletin, 98, 728-738.

Flood, R.D., Hiscott, R.N., and Aksu, A., 2009. Morphology and evolution of an anastomosed channel network where saline underflow enters the Black Sea. Sedimentology, 56, 807-839.

Fowler, J.N., Guritno, E., Sherwood, P., Smith, M.J., Algar, S., Busono, I., Goffey, G. & Strong, A., 2004. Depositional architectures of Recent deepwater deposits in the Kutei Basin, East Kalimantan. In: 3D Seismic Technology: Application to the Exploration of Sedimentary Basins (Ed. by Davies, R.J., Cartwright, J., Stewart, S.A., Underhill, J.R., and Lappin, M), Geological Society, London, Memoirs, 29, 25-33.

França, R.L., Del Rey, A.C., Tagliari, C.V., Brandão, J.R., and De Rossi Fontanelli, P., 2007. Bacia do Espírito Santo. Boletim de Geociencias da Petrobras, 15, 501-509.

Frey Martinez, J., Cartwright, J., and Hall, B., 2005. 3D seismic interpretation of slump complexes: examples from the continental margin of Israel. Basin Research, 17, 83–108.

Friedmann, S.J., Beaubouef, R.T., Pirmez, C., and Jennette, D.C., 2000. The effects of gradient changes on deep-water depositional systems: an integrated approach. In: American Association of Petroleum Geologists, 2000 Annual Meeting, Extended Abstracts, New Orleans, U.S, p. 51.

Gamberi, F., Rovere, M., Dykstra, M., Kane, I.A., and Kneller, B.C., 2013. Integrating modern seafloor and outcrop data in the analysis of slope channel architecture and fill. Marine and Petroleum Geology, 41, 83-103.

Gamboa, D., Alves, T., Cartwright, J., and Terrinha, P., 2010. MTD distribution on a 'passive' continental margin: the Espírito Santo Basin (SE Brazil) during the Palaeogene. Marine and Petroleum Geology, 27, 1311-1324.

Gamboa, D., 2011. An integrated seismic-scale analysis of reservoir compartmentalisation on continental margins: the Espirito Santo Basin, SE Brazil. PhD thesis, Cardiff University, 453pp.

Gamboa, D., Alves, T.M., and Cartwright, J., 2012. A submarine channel confluence classification for topographically confined slopes. Marine and Petroleum Geology, 35, 176-189.

Gamboa, D., and Alves, T.M., 2015. Spatial and dimensional relationships of submarine slope architectural elements: A seismic-scale analysis from the Espírito Santo Basin (SE Brazil). Marine and Petroleum Geology, 64, 43-57.

Garcia, M. and Parker, G., 1989. Experiments on Hydraulic Jumps in Turbidity Currents Near a

Canyon-Fan Transition. Science, 245, 393-396.

Gardner, M.H., and Borer, J.M., 2000. Submarine channel architecture along a slope to basin profile, Brushy Canyon Formation, West Texas. In: Bouma, A.H., Stone, C.G. (Eds.), Fine-grained Turbidite Systems. Memoir 72-American Association of Petroleum Geologists and Special Publication 68-SEPM, pp. 195-214.

Gardner, M.H., Borer, J.M., Melik, J.J., Mavilla, N., Dechesne, M., and Wagerle, R.D., 2003. Stratigraphic process-response model for submarine channels and related features from studies of Permian Brushy Canyon outcrops, West Texas. Marine and Petroleum Geology, 20, 757-788.

Garrison, L.E., Kenyon, N.H. and Bouma, A.H., 1982. Channel systems and lobe construction in the Mississippi Fan. Geo-Marine Letters, 2, 32-39.

Gaudin, M., Mulder, T., Cirac, P, Berne, S. and Imbert, P., 2006. Past and present sedimentary activity in the Capbreton Canyon, southern Bay of Biscay. Geo-Marine Letter, 26, 331-345.

Gee, M.J.R. and Gawthorpe, R.L., 2006. Submarine channels controlled by salt tectonics: Examples from 3D seismic data offshore Angola. Marine and Petroleum Geology, 23, 443-458.

Gee, M.J.R., Gawthorpe, R.L., Bakke, K. and Friedmann, S.J., 2007. Seismic Geomorphology and Evolution of Submarine Channels from the Angolan Continental Margin. Journal of Sedimentary Research, 77, 433-446.

Georgiopoulou, A., and Cartwright, J.A., 2013. A critical test of the concept of submarine equilibrium profile. Marine and Petroleum Geology, 41, 35-47.

Goode, J.R., and Wohl, E.E., 2010. Substrate controls on the longitudinal profile of bedrock channels: implications for reach-scale roughness. Journal of Geophysical Research, 115, F03018, doi.org/10.1029/2008JF001188.

Graham, S.A., and Bachman, S.B., 1983, Structural controls on submarine-fan geometry and internal architecture: Upper La Jolla fan system, offshore southern California. American Association of Petroleum Geologists Bulletin, 67, 83–96.

Grecula, M., Flint, S.S., Wickens, H.D., and Johnson, S.D., 2003. Upward-thickening patterns and lateral continuity of Permian sand-rich turbidite channel fills, Laingsburge Karoo, South Africa. Sedimentology, 50, 831-853.

Greene, H. G., Maher, N.M. and Paull, C.K., 2002. Physiography of the Monterey Bay National Marine Sanctuary and implications about continental margin development. Marine Geology, 181, 55-82.

Hackbarth, C.J., and Shew, R.D., 1994, Morphology and stratigraphy of a mid Pleistocene turbidite leveed channel from seismic, core, and log data, in Bouma, A.H., Weimer, P., and Perkins, B., eds., Submarine Fans and Turbidite Systems: SEPM, Gulf Coast Section, 15th Annual Research Conference, p. 127–133.

Hagen, R.A., Bergersen, D.D., Moberly, R., and Coulbourn, W.T., 1994. Morphology of a large meandering submarine canyon system on the Peru-Chile forearc. Marine Geology, 119, 7-37.

Hampton, M.A., Lee, H.J. and Locat, J., 1996. Submarine landslides, Review of Geophysics, 34, 33–59.

Hansen, L., Janocko, M., Kane, I., and Kneller, B., 2017. Submarine channel evolution, terrace development, and preservation of intra-channel thin-bedded turbidites: Mahin and Avon channels, offshore Nigeria. Marine Geology, 383, 146-167.

Hansen, L., L'Heureux, J.S., Sauvin, G., Polom, G., Lecomte, I., Vaneste, M., Longva, O. and Krawczyk,

C., 2013. The effect of mass-wasting on the stratigraphic architecture of a fjord-valley fill: correlation of onshore, shear wave seismics and marine seismic data at Trondheim, Norway. Sedimentary Geology, 289, 1–18.

Hansen, L.A.S., Callow, R.H.T., Kane, I.A., Gamberi, F., Rovere, M., Cronin, B.T., and Kneller, B.C., 2015. Genesis and character of thin-bedded turbidites associated with submarine channels. Marine and Petroleum Geology, 67, 852-879.

Hart, B. S., 2000. 3-D Seismic Interpretation: A Primer for Geologists. SEPM Short Course Notes, 48, p. 123.

Hart, B.S., 2011. An Introduction to Seismic Interpretation. American Association of Petroleum Geologists, p.224.

Heezen, B.C., and Ewing, M., 1952. Turbidity currents and submarine slumps, and the 1929 Grand Banks earthquake. American Journal of Science, 250, 849–873.

Heezen, B. C., Menzies, R. J., Schneider, E. D., Ewing, W. M., and Granelli, N. C., 1964. Congo submarine canyon. American Association of Petroleum Geologists Bulletin, 48, 1126–1149.

Heiniö, P. and Davies, R.J., 2007. Knickpoint migration in submarine channels in response to fold growth, western Niger Delta. Marine and Petroleum Geology, 24, 434-449.

Heiniö, P., and Davies, R.J., 2009. Trails of depressions and sediment waves along submarine channels on the continental margin of Espírito Santo Basin, Brazil. Geological Society of America Bulletin, 121. 698–711.

Henrich, R., Hanebuth, T., Krastel, S., et al., 2008. Architecture and sediment dynamics of the Mauritania Slide Complex. Marine and Petroleum Geology 25, 17–33.

Hess, R. and Rakofsky, A., 1992. Deep-sea channel/submarine-Yazoo system of the Labrador Sea: a new deep-water facies model. American Association of Petroleum Geologists, Bulletin,76, 680-707.

Hodgson, D.M., DiCelma, C.N., Brunt, R.L., and Flint, S.S., 2011. Submarine slope degradation, aggradation and the stratigraphic evolution of channel-levee systems. Journal of the Geological Society of London, 168, 625-628.

Hubbard, S.M., Covault, J.A., Fildani, A., and Romans, B.R., 2014. Sediment transfer and deposition in slope channels: deciphering the record of enigmatic deep-sea processes from outcrop. Geological Society of America Bulletin, 126, 857-871.

Hubbard, S.M., De Ruig, M.J., and Graham, S.A., 2009. Confined channel-levee complex development in an elongate depocenter: deep-water Tertiary strata of the Austrian Molasse Basin. Marine and Petroleum Geology, 26, 85-112.

Hubbard, S.M., Romans, B.W., and Graham, S.A., 2008. Deep-water foreland basin deposits of the Cerro Toro Formation, Magallanes basin, Chile: architectural elements of a sinuous basin axial channel belt. Sedimentology, 55, 1333-1359.

Hübscher, C., Spieβ, V., Breitzke, M. and Weber, M.E., 1997. The youngest channel-levee system of the Bengal Fan: results from digital sediment echosounder data. Marine Geology, 141, 125-145.

Hull, E., 1912. Monograph on the sub-oceanic physiography of the North Atlantic Ocean. Edward Stanford, London, pp. 41.

Huyghe, P., Foata, M., Deville, E., Mascle, G. and Caramba Working Group. 2004, Channel profiles through the active thrust front of the southern Barbados prism. Geology, 32, 429-432.

Imran, J., Parker, G., and Pirmez, C., 1999. A nonlinear model of flow in meandering submarine and subaerial channels. Journal of Fluid Mechanics, 400, 295-331.

Jackson, C.A.L. and Johnson, H.D., 2009. Sustained turbidity currents and their interaction with debrite-related topography; Labuan Island, offshore NW Borneo, Malaysia. Sedimentary Geology, 219, 77-96.

Jacobi, R. E., 1976. Sediment slides on the northwestern continental margin of Africa. Marine Geology, 22, 157-173.

Janocko, M., Nemec, W., Henriksen, S., and Warchoł, M., 2013. The diversity of deep-water sinuous channel belts and slope valley-fill complexes. Marine and Petroleum Geology, 41, 7-34.

Jansen, E., Befring, S., Bugge, T., Eidvin, T., Holtedahl, H. and Sejrup, H.P., 1987. Large submarine slides on the Norwegian continental margin: Sediments transport and timing. Marine Geology, 78, 77-107.

Joanne, C., Collot, J.-Y., Lamarche, G. and Migeon, S., 2010. Continental slope reconstruction after a giant mass failure, the example of the Matakaoa margin, New Zealand. Marine Geology, 268, 67–84.

Jobe, Z.R., Howes, N.C., and Auchter, N., 2016. Comparing submarine and fluvial channel kinematics: Implications for stratigraphic architecture. Geology, 44, 931-934.

Jobe, Z.R., Lowe, D.R. and Uchytil, S.J., 2011. Two fundamentally different types of submarine canyons along the continental margin of Equatorial Guinea. Marine and Petroleum Geology, 28, 843-860.

Jobe, Z.R., Sylevster, Z., Parker, A.O., Howes, N., Slowey, N. and Pirmez, C., 2015. Rapid adjustment of submarine channel architecture to changes in sediment supply. Journal of Sedimentary Research, 85, 729-753.

Jolly, B.A., Lonergan, L., and Whittaker, A.C., 2016. Growth history of fault-related folds and interaction with seabed channels in the toe-thrust region of the deep-water Niger delta. Marine and Petroleum Geology, 70, 58-76.

Kane, I. A., Catterall, V., McCaffrey, W. D., and Martinsen, O. J., 2010. Submarine channel response to intra-basinal tectonics. American Association of Petroleum Geologists, Bulletin, 94, 189–219.

Kane, I. and Hodgson, D., 2011. Sedimentological criteria to differentiate submarine channel levee subenvironments: exhumed examples from the Rosario Fm. (Upper cretaceous) of Baja California, Mexico, and the Fort Brown Fm. (Permian), Karoo Basin, S. Africa. Marine and Petroleum Geology, 28, 807-823.

Kane, I.A., McCaffrey, W.D. and Peakall, J., 2008. Controls on sinuosity evolution within submarine channels. Geology, 36, 287-290.

Kane, I.A., McGee, D.T. and Jobe, Z.R., 2012. Halokinetic effects on submarine channel equilibrium profiles and implications for facies architecture: conceptual model illustrated with a case study from Magnolia Field, Gulf of Mexico, Geological Society, London, Special Publications, 363, 289-302.

Kastens, K.A. and Shor, A.N., 1985. Depositional processes of a meandering channel on Mississippi Fan. American Association of Petroleum Geologists, Bulletin, 69, 190-202

Kastens, K.A. and Shor, A.N., 1986b. Evolution of a channel meander on the Mississippi Deep-sea Fan. Marine Geology, 71, 165-175.

Kenyon, N.H., A.H. Stride, A.H. and Belderson, R.H., 1975. Plan views of active faults and other features on the lower Nile cone. Geological Society of America Bulletin, 86, 1733–1739.

Kertznus, V., 2009. Stratigraphic Development of Delta-Fed Slope Systems: Offshore Ebro and Nile

Deltas: University of Aberdeen, Ph.D. thesis, 298 p.

Khripounoff, A., Vangriesheim, A., Babonneau, N., Crassous, P., Denniellou, B. and Savoye, B., 2003. Direct observation of intense turbidity activity in the Zaire submarine valley at 4000m water depth. Marine Geology, 194,151–158.

Klaucke, I., Hesse, R., and Ryan, W.B.F., 1997. Flow parameters of turbidity currents in a low-sinuosity giant deep-sea channel. Sedimentology, 44, 1093-1102.

Kneller, B. and McCaffrey, W., 1999. Depositional effects of flow nonuniformity and stratification within turbidity currents approaching a bounding slope: deflection, reflection, and facies variations: Journal of Sedimentary Research, 69, 980–991.

Kneller, B., 2003. The influence of flow parameters on turbidite slope channel architecture. Marine and Petroleum Geology, 20, 901-910.

Kneller, B., Dykstra, M., Fairweather, L., and Milana, J.P., 2016. Mass-transport and slope accommodation: Implications for turbidite sandstone reservoirs. American Association of Petroleum Geologists, Bulletin, 100, 213-235.

Knoppers, B., Ekau, W., and Figueiredo, A.G., 1999. The coast and shelf of east and northeast Brazil and material transport. Geo-Marine Letters, 19, 171-178.

Kolla, V. and Coumes, F., 1987. Morphology, internal structure, seismic stratigraphy, and sedimentation of Indus Fan. American Association of Petroleum Geologists, Bulletin, 650–677.

Kolla, V., 2007. A review of sinuous channel avulsion patterns in some major deep-sea fans and factors controlling them. Marine and Petroleum Geology, 24, 450-469.

Kolla, V., Bandyopadhyay, A., Gupta, P., Mukherjee, B., and Ramana, D.V., 2012. Morphology and internal structure of a recent upper Bengal Fan-Valley Complex. In: Prather, B.E., Deptuck, M.E., Mohrig, D., Van Hoorn, B., Wynn, R.B. (Eds.), Application of the Principles Seismic Geomorphology to Continental Slope and Base-of-slope Systems: Case Studies from Seafloor and Near-seafloor, vol. 99, pp. 347-369. SEPM Special Publication No.

Kolla, V., Bourges, P., Urrity, J.M., and Safa, P., 2001. Evolution of deep-water tertiary sinuous channels offshore, Angola (West Africa) and implications to reservoir architecture. American Association of Petroleum Geologists, Bulletin, 85, 1373-1405.

Kolla, V., Posamentier, H.W., and Wood, L.J., 2007. Deep-water and fluvial sinuous channels: characteristics, similarities and dissimilarities, and modes of formation. Marine and Petroleum Geology, 24, 388-405.

Komar, P.D., 1969. The channelized flow of turbidity currents with application to Monterey Deep-Sea Channel. Geological Society of America Bulletin, 78, 4544-4558.

Komar, P.D., 1971. Hydraulic jumps in turbidity currents. Geological Society of America Bulletin, 82, 1477–1488.

Komar, P.D., 1973. Continuity of turbidity current flow and systematic variations in deep-sea channel morphology. Geological Society of America Bulletin, 84, 3329–3338.

Konsoer, K., Zinger, J., and Parker, G., 2013. Bankfull hydraulic geometry of submarine channels created by turbidity currents: relations between bankfull channel characteristics and formative flow discharge. Journal of Geophysical Research: Earth Surface, 118, 216-228.

Kostic, S., and Parker G., 2006. The response of turbidity currents to a canyon–fan transition: internal hydraulic jumps and depositional signatures. Journal of Hydraulic Research, 44, 631-653.

Kuenen, P.H., 1937. Experiments in connection with Daly's hypothesis on the formation of submarine canyons. Leidsche geologische mededelingen, 8, 327-335.

Kuenen, P.H., and Carozzi, A., 1953. Turbidity currents and sliding in geosynclinal basins of the Alps. The Jounal of Geology, 61, 363-373.

Kuenen, P.H., and Migliorini, C.L., 1950. Turbidity currents as a cause of graded bedding. Journal of Geology, 58, 91-127.

Laughton, A.S., 1960. An interplain deep-sea channel system. Deep-Sea Research, 7, 75-88.

Lewis, K.B., 1971. Slumping on a continental slope inclined at 1°–4°. Sedimentology, 16, 97–110.

Lien, T., Walker, R.G., and Martinsen, O.J., 2003. Turbidites in the Upper carboniferous Ross Formation, western Ireland: reconstruction of a channel and spillover system. Sedimentology, 50, 113-148.

Lima, J.E.F.W., Lopes, W.T.A., De Carvalho, N.O., Vieira, M.R., and Da Silva, E.M., 2005. Suspended sediment fluxes in the large river basins of Brazil, in: Walling, D.E., Horowitz, A.J., eds., Sediment Budgets 1, Proceedings of the Foz do Iguacu Symposium, April 2005, IAHS Publication, vol. 291, IAHS Press, Wallingford, UK (2005), p. 355–363.

Liu, F. and Yang, S. H., 2014. The effect of the Wenchuan earthquake on the fluvial morphology in the Longmen Shan, eastern Tibetan Plateau: Discussion and speculation. Quaternary International, 371, 280-289.

Loncke, L., Gaullier, V., Droz, L., Ducassou, E., Migeon, S. and Mascle, J., 2009, Multi-scale slope instabilities along the Nile deep-sea fan, Egyptian margin: A general overview. Marine and Petroleum Geology, 26, 633–646.

Love, F., Brush. E., Fiduk, J. C., Gibbs, P., Brink-Larsen, S., and Farrow, G., 2005. Northern Espírito Santo basin canyon models ancient sand transport. Offshore, 74-78.

Lucente, C.C. and Pini, G.A., 2008. Basin-wide mass-wasting complexes as markers of the Oligo-Miocene foredeep-accretionary wedge evolution in the Northern Apennines, Italy. Basin Research, 20, 49–71.

Macauley, R.V. and Hubbard, S.M., 2013. Slope channel sedimentary processes and stratigraphic stacking, Cretaceous Tres Pasos Formation slope system, Chilean Patagonia. Marine and Petroleum Geology, 41, 146–162.

Maier, K., Fildani, A., Paull, C., McHargue, T., Graham, S., and Caress, D., 2013. Deep-sea channel evolution and stratigraphic architecture from inception to abandonment from high-resolution Autonomous Underwater Vehicle surveys offshore central California. Sedimentology, 60, 935-960.

Maier, K.L., Fildani, A., McHargue, T.R., Paull, C.K., Graham, S.A., Caress, D.W., 2012. Punctuated deep-water channel migration: high-resolution subsurface data from the Lucia Chica channel system, offshore California, USA. Journal of Sedimentary Research 82, 1–8.

Martin, L., and Suguio, K., 1992. Variation of coastal dynamics during the last 7000 years recorded in beach-ridge plains associated with river mouths: example from the central Brazilian coast. Palaeogeography, Palaeoclimatology, Palaeoecology, 99, 119-140.

Martinsen, O.J. and Bakken, B., 1990. Extensional and compressional zones in slumps and slides in the Namurian of County Clare, Ireland. Geological Society of London, Journal, 147, 153–164.

Mas, V., Mulder, T., Dennielou, B., Schmidt, S., Khripounoff, A. and Savoye, B., 2010. Multiscale spatio-temporal variability of sedimentary deposits in the Var turbidite system (North-Western Mediterranean Sea). Marine Geology, 275, 37-52.

Masalimova, L., Lowe, D.R., McHargue, T. and Derksen, R., 2015. Interplay between an axial channel belt, slope gullies and overbank deposition in the Puchkirchen Formation in the Molasse Basin,

Austria. Sedimentology, 62, 1717-1748.

Masalimova, L.U., Lowe, D.R., Sharman, G.R., King, P.R., and Arnot, M.J., 2016. Outcrop characterization of a submarine channel-lobe complex: the lower mount messenger formation, Taranaki basin, New Zealand. Marine and Petroleum Geology, 71, 360-390.

Mascle, J., Zitter, T., Bellaiche, G., Droz, L., Gaullier, V. and Loncke, L., 2001. The Nile deep sea fan: preliminary results from a swath bathymetry survey. Marine and Petroleum Geology, 18, 471-477.

Masson, D. G., Huvenne, V. A. I., Stigter, H. C., Arzola, R. G. and LeBas, T. P., 2011. Sedimentary processes in the middle Nazare´ Canyon. Deep – Sea Research II, 58, 2369-2387.

Mayall, M., and Stewart, I., 2000. The architecture of turbidite slope channels. In: Weimer, P., Slatt, R.M., Coleman, J.L., Rosen, N., Nelson, C.H., Bouma, A.H., Styzen, M., Lawrence, D.T (Eds.), Global Deep-water Reservoirs: Gulf Coast Section SEPM Foundation 20th Annual Bob F Perkins Research Conference, pp. 578-586.

Mayall, M., Jones, E. and Casey, M., 2006. Turbidite channel reservoirs-Key elements in facies prediction and effective development. Marine and Petroleum Geology, 23, 821-841.

Mayall, M., Lonergan, L., Bowman, A., James, S., Mills, K., Primmer, T., Pope, D., Rogers, L. and Skeene, R., 2010. The response of turbidite slope channels to growth-induced seabed topography. American Association of Petroleum Geologists, Bulletin, 94, 1011-1030.

McAdoo, B.G., Pratson, L.F. and Orange, D.L., 2000. Submarine landslide geomorphology, U.S. continental slope. Marine Geology, 169, 103-136.

McHargue, T. R. and Webb, J. E., 1986. Internal geometry, seismic facies, and petroleum potential of canyons and inner fan channels of the Indus Submarine Fan. American Association of Petroleum Geologists, Bulletin, 70, 161-180.

McHargue, T., Pyrez, M.J., Sullivan, M.D., Clark, J.D., Fildani, A., Romans, B.W., Covault, J.A., Levy, M., Posamentier, H.W. and Drinkwater, N.J., 2011. Architecture of turbidite channel systems on the continental slope: patterns and predictions. Marine and Petroleum Geology, 28, 728–743.

Meiburg, E., and Kneller, B., 2010. Turbidity currents and their deposits. Annual Review of Fluid Mechanics, 42, 135-156.

Menard, H.W., 1964. Marine geology of the Pacific. McGraw-Hill Book, New York, 271pp.

Menard, H. W., 1955. Deep-sea channels, topography, and sedimentation. American Association of Petroleum Geologists, Bulletin, 39, 236-255.

Micallef, A, and Mountjoy, J.J., 2011. A topographic signature of a hydrodynamic origin for submarine gullies. Geology, 39: 115-118.

Mitchell, N.C., 2006. Morphologies of knickpoints in submarine canyons. Geological Society of America Bulletin, 118, 589-605.

Mitchell, N.C., 2014. Bedrock erosion by sedimentary flows in submarine canyons. Geosphere, 10, 892-904.

Mitchum, R.M., Vail, J.R., and Thompson, S., 1977. The depositional sequence as a basic unit for stratigraphic analysis. American Association Geological Bulletin, Memory, 26, 53 – 62.

Mohriak, W.U., 2003. Bacias sedimentares da margem continental Brasileira. In: Bizzi, L.A., Schobbenhaus, C., Vidotti, R.M., Goncalves, J.H. (Eds.), Geologia, Tectonica e Recursos Minerais do Brasil. CPRM, Brasilia, pp. 87-165.

Mohriak, W.U., 2005. Interpretaçao geologica e geofísica da Bacia do Espírito Santo e da regiao de Abrolhos: Petrogra fia, dataçao radiom etrica e visualizaçao sísmica das rochas vulcanicas:

Boletim de Geociências da Petrobrás, 14, 133-142.

Mohriak, W.U., and Fainstein, R., 2012. Phanerozoic regional geology of the eastern Brazilian margin, in Roberts D.G., e.d., Regional Geology and Tectonics: Phanerozoic Passive Margins, Section 1, p. 222–282.

Mohriak, W.U., Nemcok, M., and Enciso, G., 2008, South Atlantic divergent margin evolution: rift-border uplift and salt tectonics in the basins of Southeastern Brazil, in Pankhurst, R.J., Trouw, R.A.J., Brito Neves, B.B., De Wit, M.J., eds., West Gondwana Pre-Cenozoic Correlations across the South Atlantic Region, Geological Society of London, Special Publication 294, p. 365-398.

Moody, J.D., Pyles, D.R., Clark, J., and Bouroullec, R., 2012. Quantitative outcrop characterization of an analog to weakly confined submarine channel systems: Morillo 1 member, Ainsa Basin, Spain. American Association of Petroleum Geologists, Bulletin, 96, 1813-1841.

Moore, J. G., Clague, D. A., Holcom, R. T., Lipman, P. W., Normark, W. R, and Torresan, M. E., 1989. Prodigious Submarine Landslides on the Hawaiian Ridge. Journal of Geophysical Research, 94, 17,465-17,484.

Morgan, R., 2004. Structural controls on the positioning of submarine channels on the lower slopes of the Niger Delta. In: Davies, R.J., Cartwright, J.A., Stewart, S.A., Lappin, M., Underhill, J.R. (Eds.), 3D Seismic Technology: Application to the Exploration of Sedimentary Basins. Geological Society, London, Memoirs, vol. 29, pp. 45-51.

Moscardelli, L. and Wood, L., 2008. New classification system for mass transport complexes in offshore Trinidad. Basin Research, 20, 73-98.

Moscardelli, L. and Wood, L., 2015. Morphometry of mass-transport deposits as a predictive tool. Geological Society of America, Bulletin, 128, 47-30.

Moscardelli, L., Wood, L. and Mann, P., 2006. Mass-transport complexes and associated processes in the offshore area of Trinidad and Venezuela. American Association of Petroleum Geologists, Bulletin, 90, 1059-1088.

Mulder, T., Zaragosi, S., Garlan, T., Mavel, J., Cremer, M., Sottolichio, A., Senechal, N. and Schmidt, S., 2012. Present deep-submarine canyons activity in the Bay of Biscay (NE Atlantic). Marine Geology, 295 – 298, 113-127.

Mutti, E., and Ricci Lucchi, F., 1975. Turbidite facies and facies associations. In: Mutti, E., Parea, G.C., Ricci-Lucchi, F., Sa, G.R.I.M., Zanaucchi, G., Chibaudoand, G., Iraccarion, S. (Eds.), Examples of Turbidite Facies and Facies Associations from Selected Formations of the Northern Apennines IX International Congress on Sedimentologists, Nice, Field Trip A-l1, pp. 21– 36.

Mutti, E, 1977. Distinctive thin-bedded turbidite facies and related depositional environments in the Eocene Hecho Group (South-central Pyrenees, Spain. Sedimentology, 24, 107-131.

Mutti, E., and Normark, W. R., 1987. Comparing examples of modern and ancient turbidite systems: problems and concepts. In J. R. Leggett, and G. G. Zuffa, Marine clastic sedimentology: concepts and case studies, London, Graham and Trotman, pp, 1–38.

Mutti, E., and Normark, W.R., 1991. An integrated approach to the study of turbidite systems, in Weimer, P., and Link, M.H., eds., Seismic Facies and Sedimentary Processes of Submarine Fans and Turbidite Systems: New York, Springer-Verlag, p.75–106.

Nakajima, T., Peakall, J., McCaffrey, W.D., Paton, D.A., and Thompson, P.J.P., 2009. Outer-bank bars: a new intra-channel architectural element within sinuous submarine slope channels. Journal of Sedimentary Research, 79, 872–886.

Nakajima, T., Satoh, M., and Okamura, Y., 1998, Channel–levee complexes, terminal deep-sea fan

and sediment wave fields associated with the Toyama Deep-Sea Channel system in the Japan Sea. Marine Geology, 147, 25–41.

Nardin, T.R., Hein, F.J., Gorsline, D.S., and Edwards, B.D., 1979. A review of mass movement processes, sediment and acoustic characteristics, and contrasts in slope and base-of-slope systems versus canyon–fan–basin floor systems, in Doyle, L.J., and Pilkey, O.H., eds., Geology of Continental Slopes: Society of Economic Paleontologists and Mineralogists, Special Publication 27, p. 61–73

Natland, M. L., and Kuenen, Ph H., 1951. Sedimentary history of the Ventura Basin, California, and the action of turbidity currents. In Hough, J.L., Turbidity currents and the transportation of coarse sediments to deep water (pp. 76-107). Society of Economic Paleontologists and Mineralogists Special Publication, Vol. 2.

Nelson, A., and Dubé, K., 2016. Channel response to an extreme flood and sediment pulse in a mixed bedrock and gravel-bed river. Earth Surface Processes and Landforms, 41, 178-195.

Noda, A., TuZino, T., Furukawa, R., Joshima, M., and Uchida, J.I., 2008. Physiographical and sedimentological characteristics of submarine canyons developed upon an active forearc slope: The Kushiro Submarine Canyon, northern Japan. Geological Society of America Bulletin, 120, 750–767.

Normandeau, A., Lajeunesse, P., St-Onge, G., Bourgault, D., Drouin, S.S.O., Senneville, S., and Bélanger, S., 2014. Morphodynamics in sediment-starved inner-shelf submarine canyons (Lower St. Lawrence Estuary, Eastern Canada). Marine Geology, 357, 243–255.

Normark, W.R., and Piper, D.J.W., 1991. Initiation processes and flow evolution of turbidity currents: implications for the depositional record: in Osborne, R.H., ed., From Shoreline to Abyss, SEPM, Special Publication 46, p. 207–230.

Normark, W.R. and Piper, D.J., 1969. Deep-Sea Fan –Valley, past and present. Geological Society of America Bulletin, 80, 1859-1866.

Normark, W.R., 1973. Fan valley, channels, and depositional lobes on modern submarine fans: characters for recognition of sandy turbidite environments. American Association of Petroleum Geologists, Bulletin, 62, 912-931.

Normark, W.R., Piper, D.J., Posamentier, H., Pirmez, C., and Migeon, S., 2002. Variability in form and growth of sediment waves on turbidite channel levees. Marine Geology, 192, 23–58.

Normark, W.R., Piper, D.J., Romans, B.W., Covault, J.A., Dartnell, P., and Sliter, R.W., 2009. Submarine canyon and fan systems of the California continental borderland. Geological Society of America Special Paper, 454, 141–168.

Normark, W.R., Posamentier, H. and Mutti, E., 1993. Turbidite systems: State of the art and future directions. Reviews of Geophysics, 31, 91-116.

Ojeda, H.A.O., 1982. Structural framework, stratigraphy, and evolution of Brazilian marginal basins: American Association of Petroleum Geologists, Bulletin, 66, 732-749.

Olafiranye, K., Jackson, C.A.-L., and Hodgson, D.M., 2013. The role of tectonics and mass-transport complex emplacement on upper slope stratigraphic evolution: a 3D seismic case study from offshore Angola. Marine and Petroleum Geology, 44, 196-216.

Oliveira, E.N.D., Knoppers, B.A., Lorenzzetti, J.A., Medeiros, P.R.P., Carneiro, M.E., and Souza, W.F.L.D., 2012. A satellite view of riverine turbidity plumes on the NE–E Brazilian coastal zone. Brazilian Journal of Oceanography, 60, 283–298.

Oluboyo, A.P., Gawthorpe, R.L., Bakke, K. and Jacobsen, F.H., 2013. Salt tectonic controls on deep-

water turbidite depositional systems:Miocene, southwestern Lower Congo Basin, offshore Angola. Basin Research, 26, 1-24.

Omosanya, K.O. and Alves, T.M., 2013. A 3-dimensional seismic method to assess the provenance of Mass-Transport Deposits (MTDs) on salt-rich continental slopes (Espírito Santo Basin, SE Brazil): Marine and Petroleum Geology, 44, 223-239.

Ortiz-Karpf, A., Hodgson, D.M. and McCaffrey, W.D., 2015. The role of mass-transport complexes in controlling channel avulsion and the subsequent sediment dispersal patterns on an active margin: The Magdalena Fan, offshore Colombia. Marine and Petroleum Geology, 64, 58-75.

Osman, A. M., and Thorne, C.R., 1988. Riverbank stability analysis. I: Theory. Journal of Hydraulic engineering, 114, 134-150.

Peakall, J., Amos, K.J., Keevil, G.M., Bradbury, P.W. and Gupta, S., 2007. Flow processes and sedimentation in submarine channel bends. Marine and Petroleum Geology, 24, 470-486.

Peakall, J., and Sumner, E.J., 2015. Submarine channel flow processes and deposits: A process-product perspective. Geomorphology, 244, 95-120.

Peakall, J., Kane, I.A., Masson, D.G., Keevil, G., McCaffrey, W.D., and Corney, R., 2012. Global (latitudinal) variation in submarine channel sinuosity. Geology, 40, 11-14.

Peakall, J., McCaffrey, W.D. and Kneller, B.C., 2000. A process model for the evolution, morphology, and architecture of sinuous submarine channels. Journal of Sedimentary Research, 70, 434–448.

Phleger, F.B., 1951. Displaced foraminifera faunas. Society of Economic Paleontologists and Mineralogists Special Publication, no. 2, p. 66-75.

Pickering, K.T., 1982, Middle-fan deposits from the late Precambrian kongsfjord formation submarine fan, Northeast Finnmark, Northern Norway. Sedimentary Geology, 33, 79–110.

Pickering, K.T., Stow, D.A.V., Watson, M.P. and Hiscott, R.N., 1986. Deep-water facies, processes and models: a review and classification scheme for modern and ancient sediments. Earth Science Review, 23, 75-174.

Pickering, K.T., and Corregidor, J., 2005, Mass-transport complexes and tectonic control on confined basin-floor submarine fans, Middle Eocene, south Spanish Pyrenees, in Hodgson, D.M., and Flint, S.S., eds., Submarine Slope Systems: Processes and Products: Geological Society of London, Special Publication 244, 51-74.

Piper, D.J.W., 1970. A Silurian deep sea fan deposit in western Ireland and its bearing on the nature of turbidity currents. Journal of Geology, 78, 509-522.

Piper, D.J.W. and Normark, W.R., 1983. Turbidite depositional patterns and flow characteristics, Navy submarine fan, California Borderland. Sedimentology, 30, 681–694.

Piper, D.J.W. and Normark, W.R., 2009. Processes That Initiate Turbidity Currents and Their Influence on Turbidites: A Marine Geology Perspective. Journal of Sedimentary Research, 79, 347-362

Piper., D.J.W., Hiscott, R.N. and Normark, W.R., 1999. Outcrop-scale acoustic facies analysis and latest Quaternary development of Hueneme and Dume submarine fans, offshore California. Sedimentology, 46, 47-78.

Pirmez, C., and Flood, R. D., 1995. Morphology and structure of Amazon Channel. In R. D. Flood, D. J. W. Piper, A. Klaus, et al. (Eds.), Proceedings of the Ocean Drilling Program, Initial Reports, Vol. 155, College Station, TX (Ocean Drilling Program), 23-45.

Pirmez, C., and Imran, J., 2003. Reconstruction of turbidity currents in Amazon channel. Marine and Petroleum Geology, 20, 823-849.

Pirmez, C., Beaubouef, R.T., Friedmann, S.J. and Mohrig, D.C., 2000. Equilibrium profile and baselevel in submarine channels: examples from Late Pleistocene systems and implications for the architecture of deepwater reservoirs, Deepwater Reservoirs of the World, GCSSEPM Foundation 20th Annual Research Conference, pp. 782–805.

Posamentier, H.W., Erksine, R.D., and Mitchum, R.M., Jr., 1991, Models for submarine fan deposition within a sequence stratigraphic framework, in Welmer, B., and Link, M.H., eds., Seismic facies and sedimentary processes of submarine fans and turbidite systems: New York, Springer Verlag, p. 127–136.

Posamentier, H., 2003. Depositional elements associated with a basin floor channel-levee system: case study from the Gulf of Mexico. Marine and Petroleum Geology, 20, 677-690.

Posamentier, H.W. and Kolla, V., 2003. Seismic Geomorphology and Stratigraphy of Depositional Elements in Deep-Water Settings. Journal of Sedimentary Research, 73, 367-388.

Pyles, D.R., Jennette, D.C., Tomasso, M., Beaubouef, R.T., and Rossen, C., 2010. Concepts learned from a 3D outcrop of a sinuous slope channel complex: Beacon Channel complex, Brushy Canyon Formation, West Texas, U.S.A. Journal of Sedimentary Research, 80, 67-96.

Pyles, D.R., Tomasso, M. and Jennette, D.C., 2012. Flow processes and sedimentation associated with erosion and filling of sinuous submarine channels. Geology, 40, 143-146.

Qin, Y., Alves, T.M., Constantine, J. and Gamboa, D., 2016. Quantitative seismic geomorphology of a submarine channel system in SE Brazil (Espírito Santo Basin): Scale comparison with other submarine channel systems. Marine and Petroleum Geology, 78, 455-473.

Qin, Y., Alves, T.M., Constantine, J. and Gamboa, D., 2016. The role of mass wasting in the progressive development of submarine channels (Espírito Santo Basin). Journal of Sedimentary Research, 87, 500-516.

Reimchen, A.P., Hubbard, S.M., Stright, L., and Romans, B.W., 2016. Using sea-floor morphometrics to constrain stratigraphic models of sinuous submarine channel systems. Marine and Petroleum Geology, 77, 92–115.

Richards, M., Bowman, M. and Reading, H., 1998. Submarine-fan system i: characterization and stratigraphic predication. Marine and Petroleum Geology, 15, 689-717.

Roberts, M.T. and Compani, B., 1996. Miocene example of a meandering submarine channel-levee system from 3-D seismic reflection data, Gulf of Mexico Basin. in Pacht, J.A., Sheriff, R.E., and Perkins, B.F., eds., Stratigraphic Analysis Utilizing Advanced Geophysical, Wireline and Borehole Technology for Petroleum Exploration and Production, SEPM, Gulf Coast Section, 17th Annual Research Conference, p. 241–254.

Rowland, J.C., Hilley, G.E. and Fildani, A., 2010. A test of initiation of submarine leveed channels by deposition alone. Journal of Sedimentary Research, 80, 710-727.

Samuel, A., Kneller, B., Raslan, S., Sharp, A. and Parsons, C., 2003. Prolific deep-marine slope channels of the Nile Delta, Egypt. American Association of Petroleum Geologists Bulletin, 87, 541–560.

Sawyer, D.E., Flemings, P.B. and Nikolinakou, M., 2013. Continuous deep-seated slope failure recycles sediments and limits levee height in submarine channels. Geology, 42, 15-18.

Schumm, S.A., and Khan, H.R., 1972. Experimental study of channel patterns. Geological Society of America Bulletin, 83, 1755-1770.

Sequeiros, O.A., 2012. Estimating turbidity current conditions from channel morphology: a Froude number approach: J. Geophys. Res. 117, C04003. http://dx.doi.org/10.1029/2011JC007201.

Shanmugam, G. and Moiola, R.J., 1988. Submarine fans: characteristics, models, classification, and reservoir potential. Earth Science Review, 23, 383-428.

Shanmugam, G., 2008. The constructive functions of tropical cyclones and tsunamis on deep-water sand deposition during sea level highstand: Implications for petroleum exploration. American Association of Petroleum Geologists Bulletin, 92, 443-471.

Shepard, F. P., 1951. Transportation of sand into deep water, Society of Economic Paleontologists and Mineralogists Special Publication, no. 2, 53–65.

Shepard, F. P., and Emery, K. O., 1941, Submarine topography off the California coast. Geological Society of America Special Papers, no. 31, pp. 171.

Shepard, F.P., 1936. The underlying causes of submarine canyons. National Academic Sciences of National Research Council Publication, 22, 496-502.

Shultz, M.R., Fildani, A., Cope, T.D. and Graham, S.A., 2005, Deposition and stratigraphic architecture of an outcropping ancient slope system: Tres Pasos Formation, Magallanes Basin, southern Chile, in Hodgson, D.M., and Flint, S.S., eds., Submarine Slope Systems: Processes and Products: Geological Society of London, Special Publication 244, p. 27–50.

Simon, A., Curini, A., Darby, S.E., and Langendoen, E.J., 2000. Bank and near-bank processes in an incised channel. Geomorphology, 35, 193-217.

Skene, K.I., Piper, D.J.W., and Hill, P.S., 2002. Quantitative analysis of variations in depositional sequence thickness from submarine channel levees. Sedimentology, 49, 1411-1430.

Snedden, J.W., 2013. Channel-body basal scours: Observations from 3D seismic and importance for subsurface reservoir connectivity. Marine and Petroleum Geology, 39, 150-163.

Soh, W., and Tokuyama, H., 2002. Rejuvenation of submarine canyon associated with ridge subduction, Tenryu Canyon, off Tokai, central Japan. Marine Geology, 187, 203–220.

Soh, W., Tokuyama, H., Fujioka, K., Kato, S., and Taira, A., 1990. Morphology and development of a deep-sea meandering canyon (Boso Vanyon) on an active plate margin, Sagami Trough, Japan. Marine Geology 91, 227-241.

Spencer, J.W., 1903. Submarine valleys off the American coast and in the North Atlantic. Geological Society of America Bulletin, 14, 207-226.

Sprague, A.R., Sullivan, M.D., Campion, K.M., Jensen, G.N., Goulding, D.K., Sickafoose, D.K., and Jennette, D.C., 2002. The physical stratigraphy of deep-water strata: a hierarchical approach to the analysis of genetically related elements for improved reservoir prediction. In: American Association of Petroleum Geologists Annual Meeting Abstracts, Houston, Texas, pp. 10-13.

Sprague, A.R.G., Garfield, T.R., Goulding, F.J., Beaubouef, R.T., Sullivan, M.D., Rossen, C., Campion, K.M., Sickafoose, D.K., Abreu, V., Schellpeper, M.E., Jensen, G.N., Jennette, D.C., Pirmez, C., Dixon, B.T., Ying, D., Ardill, J., Mohrig, D.C., Porter, M.L., Farrell, M.E., and Mellere, D., 2005. Integrated slope channel depositional models: the key to successful prediction of reservoir presence and quality in offshore West Africa. In: CIPM, Cuarto E-exitep 2005, February 20-23, 2005, Veracruz, Mexico, pp. 1-13.

Stelting, C.E. and DSDP Leg 96 shipboard scientists, 1985, Migratory characteristics of a mid-fan meander belt, Mississippi Fan, in Bouma, A.H., Normark, W.R., and Barnes, N.E., eds., Submarine Fans and Related Turbidite Systems: New York, Springer-Verlag, p. 283–290.

Stevenson, C.J., Talling, P.J., Wynn, R.B., Masson, D.G., Hunt, J.E., Frenz, M., Akhmetzhanhov, A., and Cronin, B.T., 2013. The flows that left no trace: very large volume turbidity currents that bypassed sediment through submarine channels without eroding the seafloor. Marine and

Petroleum Geology, 41, 186-205.

Stewart, W.D., Dixon, O.A. and Rust, B.R., 1993. Middle Cambrian carbonate-platform collapse, southeastern Canadian Rocky Mountains. Geology, 21, 687–690.

Straub, K.M. and Mohrig, D., 2009, Constructional canyons built by sheet-like turbidity currents: observations from offshore Brunei Darussalam: Journal of Sedimentary Research, 79, 24–39.

Stright, L., Bernhardt, A. and Boucher, A., 2013. DFTopoSim: modeling topographically-controlled deposition of subseismic scale sandstone packages within a mass transport dominated deep-water channel belt. Mathematical Geosciences, 45, 277–296.

Summerhayes, C.P., De Melo, U., and Barretto, H.T., 1976. The influence of upwelling on suspended matter and shelf sediments off southeastern Brazil. Journal of Sedimentary Petrology, 46, 819-828.

Surpless, K.D., Ward, R.B., and Graham, S.A., 2009. Evolution and stratigraphic architecture of marine slope gully complexes: Monterey Formation (Miocene), Gaviota Beach, California. Marine and Petroleum Geology, 26, 269–288.

Sylvester, Z. and Covault, J.A., 2016. Development of cutoff-related knickpoints during early evolution of submarine channels. Geology 44, 835–838.

Sylvester, Z., Deptuck, M.E., Prather, B.E., Pirmez, C. and O'Byrne, C., 2012. Seismic stratigraphy of a shelf-edge delta and linked submarine channels in the North-Eastern Gulf of Mexico, in Prather, B.E., Deptuck, M.E., Mohrig, D., van Hoorn, B., and Wynn, R., eds., Application of the Principles of Seismic Geomorphology to Continental-Slope and Base-of-Slope Systems: Case Studies from Seafloor and Near-Seafloor Analogues: SEPM, Special Publication 99, p. 31–59.

Sylvester, Z., Pirmez, C., and Cantelli, A., 2011. A model of submarine channel-levee evolution based on channel trajectories: implications for stratigraphic architecture. Marine and Petroleum Geology, 28, 716-727.

Thomas, M., and Bodin, S., 2013. Architecture and evolution of the Finale channel system, the Numidian Flysch formation of Sicily: insights from a hierarchical approach. Marine and Petroleum Geology, 41, 163-185.

Thorne, C.R., and Tovey, N.K. 1981. Stability of composite river banks. Earth surface processes and landforms, 6, 469-484.

Tolstoy, I., 1951. Submarine topography in the North Atlantic. Geological Society of America Bulletin, 62, 441-450.

Tripsanas, E.K., Bryant, W.R. and Phaneuf, B.A., 2004. Slope-instability processes caused by salt movements in a complex deep-water environment, Bryant Canyon area, northwest Gulf of Mexico. American Association of Petroleum Geologists Bulletin, 88, 801-823.

Turner, O.C., 2015, Depositional Framework and Controls on Coeval Deep-Water Slope Channel and Slope Fan Systems in the Eocene Juncal formation, Southern California: Colorado School of Mines, Ph.D. thesis, 129 p.

Van Andel, T.H. and Komar P.D., 1969. Ponded sediments of the Mid-Atlantic Ridge between 22° and 23° North Latitude. Geological Society of America Bulletin, 80, 1163-1190.

Vangriesheim, A., Khripounoff, A. and Crassous, P., 2009. Turbidity events observed in situ along the Congo submarine channel. Deep – Sea Research II, 56, 2208-2222.

Veatch, A. C., and Smith, P. A., 1939. Atlantic submarine valleys of the United States and the Congo submarine Valley. Geological Society of America Special Papers, no. 7, pp. 101.

Vigorito, M., Murru, M., and Simone, L., 2006. Architectural patterns in a multistorey mixed

carbonate-siliciclastic submarine channel, Porto Torres Basin, Miocene, Sardinia, Italy. Sedimentary Geology, 186, 213-236.

Walker, R.G., 1975. Nested Submarine-Fan Channels in the Capistrano Formation, San Clemente, California. Geological Society of America Bulletin, 86, 915-924.

Weill, P., Lajeunesse, E. and Devauchelle, O., 2014. Experimental investigation on self-channelized erosive gravity currents. Journal of Sedimentary Research, 84, 487–498.

Weimer, P., 1991, Seismic facies, characteristics and variations in channel evolution, Mississippi Fan (Plio–Pleistocene), Gulf of Mexico, in Weimer, P., and Link, M.H., eds., Seismic Facies and Sedimentary Processes of Submarine Fans and Turbidite Systems: New York, Springer-Verlag, p. 323–347.

Wells, M.G. and Cossu, R. 2013. The possible role of Coriolis forces in structuring large-scale sinuous patterns in submarine channel/levee systems. Philosophical Transactions of the Royal Society A, 371, 20120366.

Winker, C.D. and Booth, J.R., 2000, Sedimentary dynamics of the salt-dominated continental slope, Gulf of Mexico: Integration of observations from the seafloor, near surface and deep subsurface, in Weimer, P., Slatt, R.M., Coleman, J., Rosen, N.C., Nelson, H., Bouma, A.H., Styzen, M.J., and Lawrence, D.T., eds., Deep-Water Reservoirs of the World: SEPM, Gulf Coast Section, 20th Annual Research Conference, p. 1059–1086.

Wonham, J.B., Jayr, S., Mougamba, R., and Chuilon, P., 2000. 3D sedimentary evolution of a canyon fill (lower Miocene-age) from the Mandorove Formation, offshore Gabon. In: Stow, V.D.A., Mayall, M. (Eds.), Deep-water Sedimentary Systems: New Models for the 21st Century. Pergamon, Oxford, pp. 175-197.

Wood, L.J., and Mize-Spansky, K.L., 2009. Quantitative seismic geomorphology of a Quaternary leveed-channel system, offshore eastern Trinidad and Tobago, northeastern South America. American Association of Petroleum Geologists, Bulletin, 93, 101-125.

Wynn, R.B., Cronin, B.T., and Peakall, J., 2007. Sinuous deep-water channels: genesis, geometry and architecture. Marine and Petroleum Geology, 24, 341-387.

Wynn, R.B., Piper, D.J.W. and Gee, M.J.R., 2002. Generation and migration of coarse-grained sediment waves in turbidity current channels and channel–lobe transition zones. Marine Geology, 192, 59-78.

Wynn, R.B., Talling, P.J., Masson, D.G., Le Bas, T.P., Cronin, B.T., and Stevenson, C.J., 2012. The Influence of Subtle Gradient Changes on Deep-water Gravity Flows: a Case Study from the Moroccan Turbidite System, SEPM Special Publication, vol. 99, pp. 371-383.

Xu, J. P., Noble, M.A., Eittreim, S.L., Rosenfeld, L.K., Schwing, F.B. and Pilskaln, C.H., 2002, Distribution and transport of suspended particulate matter in Monterey Canyon, California, Marine Geology, 181, 215– 234.

Xu, J.P., Noble, M.A. and Rosenfeld, L.K., 2004. In-situ measurements of velocity structure within turbidity currents. Geophysical Research Letters, 31 (L09311).

Zelt, F. B., and Rossen, C., 1995, Geometry and continuity of deep-water sandstones and siltstones, Brushy Canyon Formation (Permian), Delaware Mountains, Texas, in K. T. Pickering, R. N. Hiscott, N. H. Kenyon, F. Ricci Lucchi, and R. D. A. Smith, eds., Atlas of deep water environments: architectural style in turbidite systems: London, Chapman and Hall, p. 167–183.

Zhong, G., Cartigny, M.J., Kuang, Z., Wang, L., 2015. Cyclic steps along the South Taiwan Shoal and West Penghu submarine canyons on the northeastern continental slope of the South China Sea.

Geological Society of America Bulletin, 127, 804–824.

Zucker, E., Gvirtzman, Z., Steinberg, J., and Enzel, Y., 2017. Diversion and morphology of submarine channels in response to regional slopes and localized salt tectonics, Levant Basin. Marine and Petroleum Geology, 81, 98-111.

Appendix

Appendix 1. Supplementary materials for Chapter 4

Table A1.1. Summary of channel morphological data for the Quaternary channel system. Morphological parameters include the depth of channel thalweg and banks, channel height, the width of channel floor and channel, width/height, and cross-sectional area of channel (CSA).

Channel distance /km	Channel-thalweg depth/m	Channel-bank depth/m	Channel height/m	Channel - floor width/m	Channel Width/m	Width/height	CSA/km²
0	-1010.84			230			
0.125	-1018.98			242			
0.25	-1021.94			254			
0.375	-1027.12			237			
0.5	-1030.08			219			
0.625	-1038.22	-884.3	153.92	225	830	5.39	
0.75	-1044.88	-897.62	147.26	233	792	5.38	
0.875	-1042.66	-906.5	136.16	260	782	5.74	
1	-1041.92	-913.16	128.76	252	843	6.55	0.068655
1.125	-1043.4	-914.64	128.76	253	790	6.14	
1.25	-1041.92	-930.18	111.74	248	706	6.32	
1.375	-1052.28	-947.94	104.34	269	606	5.81	
1.5	-1063.38	-962	101.38	267	571	5.63	
1.625	-1067.08	-976.8	90.28	207	545	6.04	
1.75	-1072.26	-989.38	82.88	156	503	6.07	
1.875	-1076.7	-995.3	81.4	162	486	5.97	
2	-1080.4	-1001.22	79.18	158	464	5.86	0.024731
2.125	-1084.84	-1000.48	84.36	166	445	5.28	
2.25	-1085.58	-1003.44	82.14	186	445	5.42	
2.375	-1086.32	-1005.66	80.66	222	471	5.84	
2.5	-1086.32	-1002.7	83.62	180	475	5.68	
2.625	-1092.98	-994.56	98.42	154	494	5.02	
2.75	-1092.98	-1001.22	91.76	154	531	5.79	
2.875	-1094.46	-951.64	142.82	180	887	6.21	
3	-1100.38	-962.74	137.64	207	809	5.88	0.064847
3.125	-1106.3	-966.44	139.86	201	737	5.27	
3.25	-1106.3	-965.7	140.6	204	751	5.34	
3.375	-1111.48	-972.36	139.12	214	734	5.28	
3.5	-1110	-975.32	134.68	235	728	5.41	
3.625	-1111.48	-978.28	133.2	233	767	5.76	
3.75	-1132.94	-979.76	153.18	184	809	5.28	
3.875	-1135.16	-1006.4	128.76	187	633	4.92	
4	-1132.2	-1006.4	125.8	213	647	5.14	0.052429

Channel distance /km	Channel-thalweg depth/m	Channel-bank depth/m	Channel height/m	Channel - floor width/m	Channel Width/m	Width/height	CSA/km²
4.125	-1132.2	-1010.1	122.1	240	661	5.41	
4.25	-1130.72	-1012.32	118.4	277	681	5.75	
4.375	-1129.24	-1014.54	114.7	280	698	6.09	
4.5	-1129.98	-1015.28	114.7	281	740	6.45	
4.625	-1132.2	-1013.8	118.4	258	774	6.54	
4.75	-1135.9	-1027.12	108.78	230	709	6.52	
4.875	-1144.04	-1025.64	118.4	230	738	6.23	
5	-1143.3	-1031.56	111.74	228	701	6.27	0.063326
5.125	-1146.26	-1017.5	128.76	215	832	6.46	
5.25	-1153.66	-1028.6	125.06	219	718	5.74	
5.375	-1161.8	-1030.08	131.72	176	712	5.41	
5.5	-1165.5	-1033.04	132.46	179	721	5.44	
5.625	-1172.16	-1026.38	145.78	209	847	5.81	
5.75	-1178.08	-1040.44	137.64	201	752	5.46	
5.875	-1181.78	-1037.48	144.3	218	839	5.81	
6	-1187.7	-1046.36	141.34	224	741	5.24	0.052198
6.125	-1191.4	-1047.84	143.56	216	758	5.28	
6.25	-1196.58	-1053.76	142.82	194	756	5.29	
6.375	-1200.28	-1061.16	139.12	177	703	5.05	
6.5	-1201.02	-1059.68	141.34	156	750	5.31	
6.625	-1206.2	-1064.12	142.08	143	678	4.77	
6.75	-1209.9	-1069.3	140.6	123	647	4.60	
6.875	-1213.6	-1061.16	152.44	122	765	5.02	
7	-1215.08	-1067.08	148	164	821	5.55	0.062935
7.125	-1218.04	-1068.56	149.48	170	792	5.30	
7.25	-1218.78	-1070.04	148.74	170	805	5.41	
7.375	-1223.22	-1072.26	150.96	208	859	5.69	
7.5	-1223.96	-1072.26	151.7	198	923	6.08	
7.625	-1223.22	-1073	150.22	195	876	5.83	
7.75	-1223.22	-1079.66	143.56	202	957	6.67	
7.875	-1222.48	-1082.62	139.86	205	977	6.99	
8	-1221	-1089.28	131.72	201	895	6.79	0.064277
8.125	-1226.92	-1092.98	133.94	205	907	6.77	
8.25	-1228.4	-1093.72	134.68	201	1061	7.88	
8.375	-1232.84	-1095.2	137.64	173	1027	7.46	
8.5	-1232.84	-1091.5	141.34	176	1026	7.26	
8.625	-1235.06	-1089.28	145.78	148	1052	7.22	
8.75	-1240.24	-1090.02	150.22	116	1017	6.77	
8.875	-1243.2	-1095.2	148	140	914	6.18	
9	-1251.34	-1107.78	143.56	151	823	5.73	0.066789

Channel distance /km	Channel- thalweg depth/m	Channel- bank depth/m	Channel height/m	Channel - floor width/m	Channel Width/m	Width/height	CSA/km²
9.125	-1254.3	-1123.32	130.98	201	741	5.66	
9.25	-1255.04	-1133.68	121.36	254	705	5.81	
9.375	-1263.18	-1138.12	125.06	212	689	5.51	
9.5	-1268.36	-1138.12	130.24	145	687	5.27	
9.625	-1272.06	-1137.38	134.68	151	703	5.22	
9.75	-1274.28	-1139.6	134.68	169	718	5.33	
9.875	-1277.24	-1141.82	135.42	195	761	5.62	
10	-1279.46	-1140.34	139.12	232	785	5.64	0.066701
10.125	-1281.68	-1148.48	133.2	211	718	5.39	
10.25	-1284.64	-1155.14	129.5	180	649	5.01	
10.375	-1287.6	-1173.64	113.96	169	556	4.88	
10.5	-1289.08	-1170.68	118.4	149	595	5.03	
10.625	-1292.04	-1148.48	143.56	152	1001	6.97	
10.75	-1289.82	-1144.78	145.04	171	1059	7.30	
10.875	-1289.82	-1146.26	143.56	198	1023	7.13	
11	-1292.04	-1148.48	143.56	215	1001	6.97	0.058692
11.125	-1300.18	-1153.66	146.52	184	899	6.14	
11.25	-1303.14	-1165.5	137.64	177	790	5.74	
11.375	-1303.88	-1172.16	131.72	157	765	5.81	
11.5	-1303.14	-1166.24	136.9	161	819	5.98	
11.625	-1308.32	-1165.5	142.82	153	870	6.09	
11.75	-1314.24	-1166.98	147.26	168	894	6.07	
11.875	-1314.98	-1163.28	151.7	167	930	6.13	
12	-1315.72	-1159.58	156.14	189	1021	6.54	0.048390
12.125	-1319.42	-1178.08	141.34	176	839	5.94	
12.25	-1325.34	-1195.1	130.24	156	634	4.87	
12.375	-1328.3	-1198.06	130.24	180	658	5.05	
12.5	-1328.3	-1201.02	127.28	219	667	5.24	
12.625	-1323.86	-1204.72	119.14	229	709	5.95	
12.75	-1322.38	-1201.02	121.36	263	787	6.48	
12.875	-1324.6	-1198.06	126.54	256	876	6.92	
13	-1324.6	-1221.74	102.86	252	625	6.08	0.045085
13.125	-1328.3	-1222.48	105.82	274	659	6.23	
13.25	-1329.04	-1227.66	101.38	282	689	6.80	
13.375	-1332	-1246.9	85.1	280	545	6.40	
13.5	-1337.18	-1253.56	83.62	283	561	6.71	
13.625	-1345.32	-1263.92	81.4	290	536	6.58	
13.75	-1349.76	-1275.02	74.74	263	534	7.14	
13.875	-1352.72	-1284.64	68.08	205	503	7.39	

Channel distance /km	Channel- thalweg depth/m	Channel- bank depth/m	Channel height/m	Channel - floor width/m	Channel Width/m	Width/height	CSA/km²
14	-1355.68	-1283.9	71.78	221	540	7.52	0.028279
14.125	-1357.9	-1284.64	73.26	228	564	7.70	
14.25	-1359.38	-1296.48	62.9	258	525	8.35	
14.375	-1357.9	-1301.66	56.24	272	509	9.05	
14.5	-1357.16	-1302.4	54.76	286	503	9.19	
14.625	-1357.16	-1302.4	54.76	303	525	9.59	
14.75	-1357.16	-1301.66	55.5	310	536	9.66	
14.875	-1359.38	-1305.36	54.02	328	567	10.50	
15	-1357.9	-1306.84	51.06	319	556	10.89	0.021701
15.125	-1360.12	-1305.36	54.76	302	564	10.30	
15.25	-1361.6	-1300.92	60.68	308	584	9.62	
15.375	-1363.82	-1303.14	60.68	284	586	9.66	
15.5	-1362.34	-1297.96	64.38	294	656	10.19	
15.625	-1364.56	-1321.64	42.92	284	545	12.70	
15.75	-1365.3	-1309.8	55.5	267	561	10.11	
15.875	-1371.22	-1314.24	56.98	256	549	9.63	
16	-1373.44	-1317.94	55.5	250	512	9.23	0.018763
16.125	-1375.66	-1315.72	59.94	250	538	8.98	
16.25	-1380.84	-1348.28	32.56	182	314	9.64	
16.375	-1387.5	-1339.4	48.1	161	329	6.84	
16.5	-1388.98	-1338.66	50.32	158	389	7.73	
16.625	-1391.2	-1340.14	51.06	191	443	8.68	
16.75	-1396.38	-1344.58	51.8	205	432	8.34	
16.875	-1395.64	-1348.28	47.36	222	459	9.69	
17	-1395.64	-1351.98	43.66	257	485	11.11	0.014469
17.125	-1395.64	-1352.72	42.92	278	510	11.88	
17.25	-1395.64	-1354.2	41.44	307	544	13.13	
17.375	-1391.94	-1358.64	33.3	382	555	16.67	
17.5	-1389.72	-1359.38	30.34	397	571	18.82	
17.625	-1391.94	-1359.38	32.56	368	565	17.35	
17.75	-1393.42	-1364.56	28.86	320	499	17.29	
17.875	-1400.08			277			
18	-1404.52						
18.125	-1404.52						
18.25	-1404.52		22.2		458	20.63	
18.375	-1408.22	-1383.8	24.42	253	414	16.95	
18.5	-1407.48	-1383.06	24.42	179	409	16.75	
18.625	-1409.7	-1383.8	25.9	196	388	14.98	

Channel distance /km	Channel- thalweg depth/m	Channel- bank depth/m	Channel height/m	Channel - floor width/m	Channel Width/m	Width/height	CSA/km²
18.75	-1408.22	-1383.06	25.16	206	382	15.18	
18.875	-1409.7	-1383.8	25.9	210	374	14.44	
19	-1409.7	-1382.32	27.38	226	367	13.40	0.007038
19.125	-1413.4	-1383.06	30.34	246	368	12.13	
19.25	-1414.14	-1383.8	30.34	252	398	13.12	
19.375	-1416.36	-1388.24	28.12	295	410	14.58	
19.5	-1418.58	-1388.98	29.6	326	442	14.93	
19.625	-1422.28	-1393.42	28.86	334	456	15.80	
19.75	-1421.54	-1397.12	24.42	350	471	19.29	
19.875	-1419.32	-1397.86	21.46	388	487	22.69	
20	-1420.06	-1381.58	38.48	395	577	14.99	0.013178
20.125	-1423.76	-1386.76	37	387	575	15.54	
20.25	-1425.98	-1388.24	37.74	383	598	15.85	
20.375	-1428.94	-1388.24	40.7	376	611	15.01	
20.5	-1428.94	-1393.42	35.52	354	577	16.24	
20.625	-1434.86	-1414.88	19.98	321	455	22.77	
20.75	-1434.12	-1418.58	15.54	310	425	27.35	
20.875	-1434.86	-1417.84	17.02	283	403	23.68	
21	-1438.56	-1425.24	13.32	273	345	25.90	0.002867
21.125	-1441.52	-1424.5	17.02	270	377	22.15	
21.25	-1443.74	-1421.54	22.2	262	366	16.49	
21.375	-1447.44	-1425.98	21.46	227	356	16.59	
21.5	-1452.62	-1428.94	23.68	192	340	14.36	
21.625	-1457.8	-1423.02	34.78	189	386	11.10	
21.75	-1461.46	-1423.72	37.74	171	340	9.01	
21.875	-1467.07	-1426.37	40.7	158	346	8.50	
22	-1462.12	-1427.34	34.78	139	353	10.15	0.007674
22.125	-1468.38	-1432.12	36.26	131	331	9.13	
22.25	-1470.68	-1429.24	41.44	122	304	7.34	
22.375	-1471.67	-1428.75	42.92	111	347	8.08	
22.5	-1471.34	-1420.28	51.06	166	474	9.28	
22.625	-1468.71	-1414.69	54.02	174	488	9.03	
22.75	-1470.02	-1411.56	58.46	180	482	8.24	
22.875	-1471.01	-1443.63	27.38	171	319	11.65	
23	-1471.67	-1441.33	30.34	182	317	10.45	0.007220
23.125	-1471.01	-1439.19	31.82	187	339	10.65	
23.25	-1470.02	-1436.72	33.3	175	334	10.03	
23.375	-1471.34	-1437.3	34.04	177	322	9.46	

Channel distance /km	Channel- thalweg depth/m	Channel- bank depth/m	Channel height/m	Channel - floor width/m	Channel Width/m	Width/height	CSA/km²
23.5	-1472.98	-1438.2	34.78	160	317	9.11	
23.625	-1472.33	-1437.55	34.78	162	330	9.49	
23.75	-1471.99	-1438.69	33.3	167	354	10.63	
23.875	-1473.99	-1439.21	34.78	156	357	10.26	
24	-1470.35	-1438.53	31.82	173	358	11.25	0.007761
24.125	-1472.33	-1441.99	30.34	171	334	11.01	
24.25	-1477.93	-1442.41	35.52	189	333	9.38	
24.375	-1481.89	-1444.15	37.74	175	337	8.93	
24.5	-1483.54	-1451.72	31.82	173	326	10.25	
24.625	-1484.52	-1452.7	31.82	163	321	10.09	
24.75	-1486.5	-1455.42	31.08	162	313	10.07	
24.875	-1488.47	-1455.91	32.56	170	342	10.50	
25	-1489.47	-1456.91	32.56	173	376	11.55	0.007362
25.125	-1494.4	-1457.4	37	167	337	9.11	
25.25	-1498.69	-1456.51	42.18	150	341	8.08	
25.375	-1498.03	-1455.85	42.18	142	385	9.13	
25.5	-1499.02	-1468.68	30.34	156	300	9.89	
25.625	-1500.34	-1468.52	31.82	145	297	9.33	
25.75	-1505.94	-1468.94	37	134	313	8.46	
25.875	-1509.66	-1467.48	42.18	127	337	7.99	
26	-1515.57	-1461.55	54.02	96	343	6.35	0.010927
26.125	-1521.51	-1471.19	50.32	108	354	7.03	
26.25	-1520.52	-1474.64	45.88	151	368	8.02	
26.375	-1521.18	-1483.44	37.74	160	371	9.83	
26.5	-1521.45	-1494.07	27.38	153	325	11.87	
26.625	-1524.61	-1502.41	22.2	152	271	12.21	
26.75	-1533.74	-1503.4	30.34	116	243	8.01	
26.875	-1538.32	-1468.02	70.3	124	403	5.73	
27	-1541.12	-1436.78	104.34	124	525	5.03	0.034732
27.125	-1543.57	-1451.81	91.76	155	489	5.33	
27.25	-1546.4	-1473.14	73.26	152	404	5.51	
27.375	-1545.68	-1446.52	99.16	145	527	5.31	
27.5	-1548.86	-1438.6	110.26	130	550	4.99	
27.625	-1552.36	-1438.4	113.96	144	552	4.84	
27.75	-1548.86	-1440.82	108.04	140	592	5.48	
27.875	-1548.15	-1447.51	100.64	144	601	5.97	
28	-1548.15	-1465.27	82.88	166	534	6.44	0.029391
28.125	-1549.2	-1471.5	77.7	160	586	7.54	
28.25	-1548.07	-1474.07	74	160	538	7.27	

Channel distance /km	Channel-thalweg depth/m	Channel-bank depth/m	Channel height/m	Channel - floor width/m	Channel Width/m	Width/height	CSA/km²
28.375	-1548.5	-1495.22	53.28	160	394	7.39	
28.5	-1551.57	-1489.41	62.16	146	396	6.37	
28.625	-1552.45	-1481.41	71.04	156	436	6.14	
28.75	-1552.88	-1476.66	76.22	161	483	6.34	
28.875	-1555.55	-1467.49	88.06	169	499	5.67	
29	-1558.71	-1464.73	93.98	176	548	5.83	0.033722
29.125	-1561.51	-1471.97	89.54	145	567	6.33	
29.25	-1563.29	-1473.01	90.28	131	539	5.97	
29.375	-1561.51	-1474.19	87.32	161	525	6.01	
29.5	-1562.21	-1477.11	85.1	174	524	6.16	
29.625	-1567.06	-1487.88	79.18	140	483	6.10	
29.75	-1568.37	-1503.25	65.12	147	396	6.08	
29.875	-1570.56	-1483.24	87.32	109	450	5.15	
30	-1572.32	-1479.82	92.5	95	482	5.21	
30.125	-1571.19	-1479.43	91.76	124	500	5.45	0.02910
30.25	-1569.79	-1483.21	86.58	126	480	5.54	
30.375	-1569.51	-1499.21	70.3	159	442	6.29	
30.5	-1571.19	-1511.25	59.94	180	442	7.37	
30.625	-1572.87	-1519.59	53.28	153	409	7.68	
30.75	-1573.99	-1528.85	45.14	163	360	7.98	
30.875	-1576.81	-1509.47	67.34	159	409	6.07	
31	-1577.66	-1504.4	73.26	164	450	6.14	0.024123
31.125	-1576.53	-1478.85	97.68	200	621	6.36	
31.25	-1575.97	-1480.51	95.46	240	610	6.39	
31.375	-1577.38	-1486.36	91.02	245	623	6.84	
31.5	-1584.68	-1511.42	73.26	250	539	7.36	
31.625	-1579.06	-1508.76	70.3	223	545	7.75	
31.75	-1579.62	-1515.24	64.38	226	504	7.83	
31.875	-1582.44	-1513.62	68.82	232	534	7.76	
32	-1590.03	-1513.81	76.22	234	561	7.36	0.027661
32.125	-1597.33	-1538.87	58.46	168	403	6.89	
32.25	-1601.26	-1553.9	47.36	150	314	6.63	
32.375	-1601.85	-1544.13	57.72	140	357	6.19	
32.5	-1603.95	-1544.01	59.94	112	333	5.56	
32.625	-1605	-1538.4	66.6	142	376	5.65	
32.75	-1605.7	-1548.72	56.98	140	313	5.49	
32.875	-1608.53	-1550.81	57.72	120	316	5.47	
33	-1612.39	-1550.23	62.16	136	347	5.58	0.014750

Channel distance /km	Channel-thalweg depth/m	Channel-bank depth/m	Channel height/m	Channel - floor width/m	Channel Width/m	Width/height	CSA/km²
33.125	-1610.28	-1551.08	59.2	152	405	6.84	
33.25	-1609.24	-1557.44	51.8	165	415	8.01	
33.375	-1612.04	-1555.8	56.24	188	454	8.07	
33.5	-1614.49	-1567.87	46.62	160	361	7.74	
33.625	-1615.92	-1564.12	51.8	124	397	7.66	
33.75	-1616.61	-1564.07	52.54	147	408	7.77	
33.875	-1615.92	-1561.9	54.02	160	404	7.48	
34	-1617.66	-1562.16	55.5	134	363	6.54	0.013473
34.125	-1622.23	-1564.51	57.72	130	367	6.36	
34.25	-1623.1	-1563.9	59.2	163	383	6.47	
34.375	-1624.86	-1564.18	60.68	172	435	7.17	
34.5	-1624.86	-1576.02	48.84	199	378	7.74	
34.625	-1626.16	-1577.32	48.84	216	378	7.74	
34.75	-1634.08	-1580.8	53.28	192	352	6.61	
34.875	-1637.18	-1577.24	59.94	178	361	6.02	
35	-1636.27	-1578.55	57.72	175	351	6.08	0.014916
35.125	-1637.61	-1581.37	56.24	177	375	6.67	
35.25	-1638.05	-1582.55	55.5	162	350	6.31	
35.375	-1636.71	-1578.25	58.46	154	381	6.52	
35.5	-1643.75	-1577.15	66.6	166	380	5.71	
35.625	-1646.37	-1573.85	72.52	147	367	5.06	
35.75	-1650.78	-1576.04	74.74	131	454	6.07	
35.875	-1651.66	-1594.68	56.98	134	458	8.04	
36	-1652.1	-1595.12	56.98	146	452	7.93	0.018403
36.125	-1653.85	-1594.65	59.2	139	425	7.18	
36.25	-1657.36	-1593.72	63.64	114	444	6.98	
36.375	-1658.7	-1593.58	65.12	80	444	6.82	
36.5	-1659.58	-1595.94	63.64	104	393	6.18	
36.625	-1658.7	-1597.28	61.42	150	407	6.63	
36.75	-1660.89	-1605.39	55.5	178	437	7.87	
36.875	-1663.08	-1615.72	47.36	223	431	9.10	
37	-1661.59	-1618.67	42.92	239	386	8.99	0.011801
37.125	-1663.96	-1609.94	54.02	200	364	6.74	
37.25	-1662.64	-1606.4	56.24	175	386	6.86	
37.375	-1663.96	-1607.72	56.24	166	390	6.93	
37.5	-1663.96	-1606.98	56.98	144	400	7.02	
37.625	-1664.39	-1611.85	52.54	156	467	8.89	
37.75	-1663.08	-1615.72	47.36	178	491	10.37	
37.875	-1662.64	-1630.08	32.56	240	404	12.41	
38	-1662.64	-1630.82	31.82	265	430	13.51	0.009087

Channel distance /km	Channel-thalweg depth/m	Channel-bank depth/m	Channel height/m	Channel - floor width/m	Channel Width/m	Width/height	CSA/km²
38.125	-1666.15	-1628.41	37.74	189	416	11.02	
38.25	-1667.89	-1628.67	39.22	186	385	9.82	
38.375	-1668.33	-1626.89	41.44	200	380	9.17	
38.5	-1668.8	-1626.62	42.18	187	381	9.03	
38.625	-1667.89	-1627.93	39.96	208	377	9.43	
38.75	-1670.72	-1630.02	40.7	204	386	9.48	
38.875	-1676.35	-1628.99	47.36	206	377	7.96	
39	-1678.11	-1629.27	48.84	195	391	8.01	0.013915
39.125	-1679.5	-1637.32	42.18	169	339	8.04	
39.25	-1681.61			140			
39.375	-1683.36						
39.5	-1683.66			144			
39.625	-1692.14			181			
39.75	-1692.61	-1645.99	46.62	220	431	9.24	
39.875	-1692.61	-1646.73	45.88	206	414	9.02	
40	-1693.66	-1648.52	45.14	161	370	8.20	0.010074
40.125	-1692.96	-1643.38	49.58	151	363	7.32	
40.25	-1690.86	-1640.54	50.32	172	400	7.95	
40.375	-1694.36	-1636.64	57.72	204	435	7.54	
40.5	-1694.71	-1635.51	59.2	234	464	7.84	
40.625	-1695.07	-1634.39	60.68	274	481	7.93	
40.75	-1693.66	-1637.42	56.24	282	485	8.62	
40.875	-1692.61	-1645.25	47.36	286	472	9.97	
41	-1694.36	-1648.48	45.88	276	500	10.90	0.020439
41.125	-1695.41	-1653.97	41.44	299	498	12.02	
41.25	-1700.69	-1657.77	42.92	290	496	11.56	
41.375	-1699.99	-1664.47	35.52	300	485	13.65	
41.5	-1699.64	-1666.34	33.3	318	482	14.47	
41.625	-1700.34	-1670	30.34	340	487	16.05	
41.75	-1701.74	-1672.88	28.86	366	497	17.22	
41.875	-1703.46	-1675.34	28.12	368	504	17.92	
42	-1705.62	-1678.24	27.38	364	477	17.42	0.010453
42.125	-1705.97	-1679.33	26.64	334	461	17.30	
42.25	-1706.67	-1680.77	25.9	328	445	17.18	
42.375	-1707.73			325	440		

Table A1.2. Summary of valley morphological data for the Quaternary channel system. Morphological parameters include the depth of valley thalweg and banks, valley height, the width of valley floor and channel, width/height, and cross-sectional area of valley (CSA).

Valley distance /km	Valley-thalweg depth/m	Valley-bank depth/m	Valley height/m	Valley-floor width/m	Valley Width/m	Width/height	CSA/km²
0	-1113.6			252			
0.0625	-1117.6			242			
0.125	-1117.6			207			
0.1875	-1120			241			
0.25	-1124			208			
0.3125	-1127.2	-848.04	279.16	233	1274	4.56	
0.375	-1129.6	-849.52	280.08	210	1235	4.41	
0.4375	-1129.6	-848.04	281.56	221	1232	4.38	
0.5	-1132.8	-856.92	275.88	256	1126	4.08	
0.5625	-1133.6	-870.98	262.62	271	1001	3.81	
0.625	-1139.2	-873.94	265.26	224	984	3.71	
0.6875	-1141.6	-871.72	269.88	247	1085	4.02	
0.75	-1142.4	-869.5	272.9	263	1278	4.68	
0.8125	-1143.2	-870.98	272.22	254	1271	4.67	
0.875	-1143.2	-873.2	270	262	1237	4.58	
0.9375	-1144	-874.68	269.32	265	1295	4.81	
1	-1143.2	-876.9	266.3	278	1284	4.82	0.255802
1.0625	-1141.6	-879.86	261.74	317	1288	4.92	
1.125	-1142.4	-884.3	258.1	378	1284	4.97	
1.1875	-1141.6	-887.26	254.34	332	1304	5.13	
1.25	-1141.6	-890.22	251.38	409	1307	5.20	
1.3125	-1142.4	-893.92	248.48	525	1279	5.15	
1.375	-1147.2	-896.14	251.06	613	1301	5.18	
1.4375	-1161.6	-897.62	263.98	595	1343	5.09	
1.5	-1168.8	-899.84	268.96	620	1377	5.12	
1.5625	-1168.8	-901.32	267.48	672	1377	5.15	
1.625	-1171.2	-902.06	269.14	678	1365	5.07	
1.6875	-1173.6	-903.54	270.06	636	1349	5.00	
1.75	-1176	-906.5	269.5	592	1327	4.92	
1.8125	-1180	-910.2	269.8	614	1321	4.90	
1.875	-1180.8	-914.64	266.16	640	1313	4.93	
1.9375	-1181.6	-916.86	264.74	649	1299	4.91	
2	-1184	-919.08	264.92	662	1282	4.84	0.218449

Valley distance /km	Valley-thalweg depth/m	Valley-bank depth/m	Valley height/m	Valley-floor width/m	Valley Width/m	Width/height	CSA/km²
2.0625	-1188	-921.3	266.7	660	1274	4.78	
2.125	-1193.6	-922.78	270.82	662	1268	4.68	
2.1875	-1194.4	-925	269.4	606	1246	4.63	
2.25	-1195.2	-927.96	267.24	568	1257	4.70	
2.3125	-1197.6	-928.7	268.9	542	1261	4.69	
2.375	-1198.4	-930.18	268.22	585	1219	4.54	
2.4375	-1205.6	-930.92	274.68	560	1215	4.42	
2.5	-1208	-938.32	269.68	504	1082	4.01	
2.5625	-1210.4	-952.38	258.02	418	940	3.64	
2.625	-1213.6	-948.68	264.92	439	900	3.40	
2.6875	-1217.6	-952.38	265.22	446	892	3.36	
2.75	-1217.6	-956.08	261.52	306	861	3.29	
2.8125	-1219.2	-962.74	256.46	318	776	3.03	
2.875	-1220	-965.7	254.3	324	765	3.01	
2.9375	-1223.2	-965.7	257.5	311	772	3.00	
3	-1225.6	-964.96	260.64	323	772	2.96	0.096539
3.0625	-1227.2	-965.7	261.5	297	778	2.98	
3.125	-1226.4	-970.88	255.52	297	743	2.91	
3.1875	-1228.8	-973.84	254.96	310	734	2.88	
3.25	-1229.6	-975.32	254.28	308	732	2.88	
3.3125	-1229.6	-976.8	252.8	291	758	3.00	
3.375	-1232	-979.02	252.98	327	856	3.38	
3.4375	-1235.2	-979.76	255.44	311	885	3.46	
3.5	-1240.8	-982.72	258.08	356	879	3.41	
3.5625	-1240.8	-984.2	256.6	299	910	3.55	
3.625	-1240	-984.94	255.06	323	950	3.72	
3.6875	-1241.6	-987.16	254.44	364	977	3.84	
3.75	-1243.2	-988.64	254.56	389	979	3.85	
3.8125	-1242.4	-990.12	252.28	436	998	3.96	
3.875	-1240	-991.6	248.4	455	1015	4.09	
3.9375	-1239.2	-992.34	246.86	446	994	4.03	
4	-1238.4	-994.56	243.84	450	1001	4.11	0.157693
4.0625	-1240	-996.78	243.22	445	983	4.04	
4.125	-1240.8	-999.74	241.06	449	995	4.13	
4.1875	-1242.4	-1001.96	240.44	416	984	4.09	
4.25	-1256.8	-1002.7	254.1	322	966	3.80	
4.3125	-1259.2	-1002.7	256.5	271	977	3.81	

Valley distance /km	Valley-thalweg depth/m	Valley-bank depth/m	Valley height/m	Valley-floor width/m	Valley Width/m	Width/height	CSA/km²
4.375	-1259.2	-1001.22	257.98	414	1055	4.09	
4.4375	-1262.4	-998.26	264.14	349	1216	4.60	
4.5	-1263.2	-996.04	267.16	371	1237	4.63	
4.5625	-1266.4	-1001.96	264.44	380	1229	4.65	
4.625	-1265.6	-1000.48	265.12	411	1312	4.95	
4.6875	-1268.8	-1010.1	258.7	436	1184	4.58	
4.75	-1271.2	-1010.84	260.36	421	1170	4.49	
4.8125	-1272.8	-1010.84	261.96	432	1160	4.43	
4.875	-1274.4	-1011.58	262.82	478	1121	4.27	
4.9375	-1276.8	-1010.84	265.96	464	1093	4.11	
5	-1277.6	-1010.1	267.5	405	1086	4.06	0.170393
5.0625	-1280.8	-1010.84	269.96	397	1057	3.92	
5.125	-1282.4	-1012.32	270.08	340	1020	3.78	
5.1875	-1284.8	-1018.24	266.56	358	957	3.59	
5.25	-1286.4	-1018.24	268.16	309	1029	3.84	
5.3125	-1288	-1019.72	268.28	318	1055	3.93	
5.375	-1292	-1018.98	273.02	248	1123	4.11	
5.4375	-1293.6	-1025.64	267.96	275	1030	3.84	
5.5	-1296.8	-1027.12	269.68	348	1004	3.72	
5.5625	-1300.8	-1027.12	273.68	345	1071	3.91	
5.625	-1300	-1024.9	275.1	331	1137	4.13	
5.6875	-1300	-1026.38	273.62	363	1179	4.31	
5.75	-1300	-1027.12	272.88	354	1208	4.43	
5.8125	-1300	-1028.6	271.4	352	1217	4.48	
5.875	-1302.4	-1030.82	271.58	348	1175	4.33	
5.9375	-1304.8	-1030.82	273.98	343	1161	4.24	
6	-1307.2	-1033.78	273.42	350	1132	4.14	0.160301
6.0625	-1311.2	-1036.74	274.46	438	1204	4.39	
6.125	-1314.4	-1037.48	276.92	409	1181	4.26	
6.1875	-1316	-1038.22	277.78	442	1226	4.41	
6.25	-1319.2	-1038.22	280.98	447	1259	4.48	
6.3125	-1319.2	-1038.22	280.98	514	1310	4.66	
6.375	-1319.2	-1039.7	279.5	505	1324	4.74	
6.4375	-1320	-1053.76	266.24	527	1079	4.05	
6.5	-1324	-1053.02	270.98	505	1046	3.86	
6.5625	-1328	-1054.5	273.5	522	1025	3.75	
6.625	-1328	-1057.46	270.54	554	1017	3.76	

Valley distance /km	Valley-thalweg depth/m	Valley-bank depth/m	Valley height/m	Valley-floor width/m	Valley Width/m	Width/height	CSA/km²
6.6875	-1328.8	-1063.38	265.42	559	1079	4.07	
6.75	-1329.6	-1062.64	266.96	574	1054	3.95	
6.8125	-1331.2	-1066.34	264.86	646	1097	4.14	
6.875	-1331.2	-1067.08	264.12	633	1074	4.07	
6.9375	-1332	-1067.08	264.92	635	1097	4.14	
7	-1332.8	-1067.08	265.72	649	1108	4.17	0.207305
7.0625	-1333.6	-1069.3	264.3	645	1081	4.09	
7.125	-1336.8	-1070.04	266.76	620	1143	4.28	
7.1875	-1339.2	-1070.78	268.42	629	1155	4.30	
7.25	-1339.2	-1071.52	267.68	594	1152	4.30	
7.3125	-1338.4	-1071.52	266.88	589	1184	4.44	
7.375	-1340	-1071.52	268.48	616	1155	4.30	
7.4375	-1341.6	-1073.74	267.86	692	1148	4.29	
7.5	-1344	-1074.48	269.52	647	1206	4.47	
7.5625	-1345.6	-1078.18	267.42	600	1270	4.75	
7.625	-1345.6	-1079.66	265.94	583	1192	4.48	
7.6875	-1345.6	-1084.1	261.5	603	1172	4.48	
7.75	-1347.2	-1087.06	260.14	489	1169	4.49	
7.8125	-1347.2	-1086.32	260.88	336	1135	4.35	
7.875	-1350.4	-1087.06	263.34	287	900	3.42	
7.9375	-1353.6	-1087.8	265.8	289	903	3.40	
8	-1356.8	-1085.58	271.22	269	923	3.40	0.144674
8.0625	-1361.6	-1085.58	276.02	271	942	3.41	
8.125	-1366.4	-1087.06	279.34	332	947	3.39	
8.1875	-1366.4	-1088.54	277.86	239	950	3.42	
8.25	-1364	-1087.8	276.2	239	988	3.58	
8.3125	-1364.8	-1087.8	277	232	961	3.47	
8.375	-1369.6	-1087.06	282.54	250	980	3.47	
8.4375	-1368	-1090.02	277.98	205	1028	3.70	
8.5	-1376.8	-1092.24	284.56	222	990	3.48	
8.5625	-1373.6	-1095.2	278.4	211	917	3.29	
8.625	-1374.4	-1105.56	268.84	289	876	3.26	
8.6875	-1377.6	-1104.82	272.78	331	962	3.53	
8.75	-1382.4	-1104.82	277.58	327	1037	3.74	
8.8125	-1383.2	-1106.3	276.9	371	1020	3.68	
8.875	-1384.8	-1107.78	277.02	423	1034	3.73	
8.9375	-1388	-1109.26	278.74	397	1023	3.67	

Valley distance /km	Valley-thalweg depth/m	Valley-bank depth/m	Valley height/m	Valley-floor width/m	Valley Width/m	Width/height	CSA/km²
9	-1390.4	-1111.48	278.92	475	1012	3.63	0.180376
9.0625	-1390.4	-1115.18	275.22	456	1009	3.67	
9.125	-1392.8	-1097.42	295.38	434	1424	4.82	
9.1875	-1390.4	-1088.54	301.86	462	1439	4.77	
9.25	-1396	-1092.24	303.76	481	1255	4.13	
9.3125	-1402.4	-1092.98	309.42	538	1272	4.11	
9.375	-1406.4	-1093.72	312.68	427	1309	4.19	
9.4375	-1408	-1103.34	304.66	381	1306	4.29	
9.5	-1410.4	-1105.56	304.84	349	1313	4.31	
9.5625	-1410.4	-1107.78	302.62	387	1315	4.35	
9.625	-1408.8	-1111.48	297.32	399	1330	4.47	
9.6875	-1409.6	-1115.18	294.42	400	1264	4.29	
9.75	-1410.4	-1118.88	291.52	360	1217	4.17	
9.8125	-1413.6	-1121.84	291.76	342	1177	4.03	
9.875	-1415.2	-1123.32	291.88	324	1175	4.03	
9.9375	-1417.6	-1124.8	292.8	302	1259	4.30	
10	-1419.2	-1124.8	294.4	304	1261	4.28	0.186444
10.0625	-1415.2	-1127.02	288.18	254	1281	4.45	
10.125	-1416	-1129.24	286.76	303	1310	4.57	
10.1875	-1419.2	-1132.94	286.26	298	1275	4.45	
10.25	-1421.6	-1146.26	275.34	296	937	3.40	
10.3125	-1421.6	-1145.52	276.08	302	997	3.61	
10.375	-1420.8	-1144.04	276.76	328	1037	3.75	
10.4375	-1420.8	-1143.3	277.5	226	981	3.54	
10.5	-1420.8	-1142.56	278.24	287	1103	3.96	
10.5625	-1422.4	-1143.3	279.1	280	1074	3.85	
10.625	-1424.8	-1147	277.8	289	1006	3.62	
10.6875	-1425.6	-1150.7	274.9	300	939	3.42	
10.75	-1426.4	-1155.14	271.26	273	934	3.44	
10.8125	-1428	-1156.62	271.38	255	916	3.38	
10.875	-1430.4	-1159.58	270.82	238	908	3.35	
10.9375	-1431.2	-1162.54	268.66	255	874	3.25	
11	-1436.8	-1161.8	275	220	834	3.03	0.087341
11.0625	-1434.4	-1161.8	272.6	251	770	2.82	
11.125	-1436.8	-1163.28	273.52	246	775	2.83	
11.1875	-1438.4	-1162.54	275.86	295	806	2.92	
11.25	-1441.6	-1161.8	279.8	269	849	3.03	

Valley distance /km	Valley-thalweg depth/m	Valley-bank depth/m	Valley height/m	Valley-floor width/m	Valley Width/m	Width/height	CSA/km²
11.3125	-1442.4	-1161.8	280.6	271	877	3.13	
11.375	-1442.4	-1161.8	280.6	255	883	3.15	
11.4375	-1442.4	-1162.54	279.86	238	891	3.18	
11.5	-1444.8	-1161.8	283	255	1017	3.59	
11.5625	-1444.8	-1164.02	280.78	255	961	3.42	
11.625	-1440.8	-1161.06	279.74	267	970	3.47	
11.6875	-1447.2	-1157.36	289.84	300	1097	3.78	
11.75	-1449.6	-1154.4	295.2	275	1284	4.35	
11.8125	-1451.2	-1154.4	296.8	250	1326	4.47	
11.875	-1452	-1152.92	299.08	239	1348	4.51	
11.9375	-1456.8	-1153.66	303.14	244	1395	4.60	
12	-1458.4	-1169.2	289.2	247	1152	3.98	0.177246
12.0625	-1464	-1169.2	294.8	364	1185	4.02	
12.125	-1464	-1169.94	294.06	278	1201	4.08	
12.1875	-1464	-1170.68	293.32	272	1219	4.16	
12.25	-1463.2	-1172.16	291.04	311	1201	4.13	
12.3125	-1459.2	-1175.12	284.08	317	1206	4.25	
12.375	-1460	-1178.08	281.92	342	1210	4.29	
12.4375	-1462.4	-1183.26	279.14	371	1188	4.26	
12.5	-1464	-1186.96	277.04	322	1137	4.10	
12.5625	-1467.2	-1191.4	275.8	299	1017	3.69	
12.625	-1467.2	-1192.88	274.32	295	1034	3.77	
12.6875	-1468.8	-1195.84	272.96	342	1008	3.69	
12.75	-1470.4	-1199.54	270.86	292	941	3.47	
12.8125	-1472	-1198.06	273.94	342	1306	4.77	
12.875	-1475.2	-1199.54	275.66	317	1353	4.91	
12.9375	-1476	-1202.5	273.5	267	1364	4.99	
13	-1477.6	-1205.46	272.14	325	1382	5.08	0.229496
13.0625		-1207.68		297	1402		
13.125		-1209.9		295	1342		
13.1875		-1215.82		269	1223		
13.25		-1216.56		328	1188		
13.3125		-1217.3		392	1163		
13.375		-1217.3		425	1157		
13.4375		-1217.3		433	1155		
13.5		-1217.3		400	1155		
13.5625		-1217.3		392	1160		

Valley distance /km	Valley-thalweg depth/m	Valley-bank depth/m	Valley height/m	Valley-floor width/m	Valley Width/m	Width/height	CSA/km²
13.625		-1218.78		342	1201		
13.6875		-1219.52		305	1224		
13.75		-1220.26		283	1232		
13.8125		-1221.74		344	1235		
13.875		-1223.96		319	1249		
13.9375		-1225.44		325	1232		
14		-1227.66		330	1249		0.220536
14.0625		-1229.14		325	1224		
14.125		-1231.36		325	1226		
14.1875		-1236.54		358	1265		
14.25		-1239.5		342	1265		
14.3125		-1240.98		347	1238		
14.375		-1241.72		375	1224		
14.4375		-1242.46		353	1246		
14.5		-1243.2		367	1257		
14.5625		-1243.2		353	1229		
14.625		-1240.24		417	1249		
14.6875		-1238.02		528	1317		
14.75		-1240.24		511	1285		
14.8125		-1241.72		573	1282		
14.875		-1243.94		612	1243		
14.9375		-1246.16		603	1226		
15		-1249.12		614	1212		0.225427
15.0625		-1252.08		645	1192		
15.125		-1255.04		651	1162		
15.1875		-1257.26		575	1130		
15.25		-1255.78		559	1116		
15.3125		-1257.26		548	1157		
15.375		-1258		587	1054		
15.4375		-1257.26		536	1015		
15.5		-1256.52		483	999		
15.5625		-1256.52		475	1020		
15.625		-1255.78		245	1000		
15.6875		-1255.78		282	988		
15.75	-1530.4	-1256.52	273.88	228	941	3.44	
15.8125	-1549.6	-1257.26	292.34	257	936	3.20	
15.875	-1551.2	-1255.78	295.42	261	934	3.16	

Valley distance /km	Valley-thalweg depth/m	Valley-bank depth/m	Valley height/m	Valley-floor width/m	Valley Width/m	Width/height	CSA/km²
15.9375	-1552	-1257.26	294.74	261	1003	3.40	
16	-1553.6	-1257.26	296.34	295	1014	3.42	0.179847
16.0625	-1558.4	-1254.3	304.1	282	1119	3.68	
16.125	-1562.4	-1254.3	308.1	224	1114	3.62	
16.1875	-1563.2	-1255.04	308.16	297	1144	3.71	
16.25	-1564			293			
16.3125	-1564.8			288			
16.375	-1566.4			237			
16.4375	-1568			286			
16.5	-1564.8			322			
16.5625	-1564.8			287			
16.625	-1564			364			
16.6875	-1563.2			375			
16.75	-1564			326			
16.8125	-1563.2			292			
16.875	-1564.8			391			
16.9375	-1575.2			335			
17	-1567.2			391			
17.0625	-1569.6			408			
17.125	-1572.8			461			
17.1875	-1566.4			403			
17.25	-1570.4			408			
17.3125	-1575.2			395			
17.375	-1576.8			405			
17.4375	-1577.6			501			
17.5	-1579.2			514			
17.5625	-1584			445			
17.625	-1585.6			596			
17.6875	-1584.8	-1309.8	275	595	1321	4.80	
17.75	-1580.8	-1308.32	272.48	632	1308	4.80	
17.8125	-1577.6	-1306.84	270.76	623	1319	4.87	
17.875	-1577.6	-1306.1	271.5	567	1301	4.79	
17.9375	-1579.2	-1306.1	273.1	565	1279	4.68	
18	-1580	-1306.1	273.9	685	1295	4.73	0.265506
18.0625	-1580.8	-1306.1	274.7	618	1295	4.71	
18.125	-1582.4	-1306.84	275.56	436	1295	4.70	
18.1875	-1583.2	-1308.32	274.88	454	1322	4.81	

Valley distance /km	Valley-thalweg depth/m	Valley-bank depth/m	Valley height/m	Valley-floor width/m	Valley Width/m	Width/height	CSA/km²
18.25	-1582.4	-1309.8	272.6	435	1322	4.85	
18.3125	-1584	-1310.54	273.46	564	1315	4.81	
18.375	-1587.2	-1312.76	274.44	605	1288	4.69	
18.4375	-1584	-1315.72	268.28	605	1270	4.73	
18.5	-1584.8	-1315.72	269.08	612	1286	4.78	
18.5625	-1585.6	-1314.98	270.62	574	1185	4.38	
18.625	-1583.2	-1313.5	269.7	565	1160	4.30	
18.6875	-1585.6	-1315.72	269.88	630	1135	4.21	
18.75	-1587.2	-1318.68	268.52	603	1160	4.32	
18.8125	-1587.2	-1322.38	264.82	539	1140	4.30	
18.875	-1588	-1325.34	262.66	511	1143	4.35	
18.9375	-1590.4	-1327.56	262.84	446	1165	4.43	
19	-1591.2	-1332	259.2	377	1207	4.66	0.253179
19.0625	-1591.2	-1333.48	257.72	359	1168	4.53	
19.125	-1596.8	-1334.96	261.84	454	1148	4.38	
19.1875	-1599.2	-1335.7	263.5	440	1140	4.33	
19.25	-1600	-1334.96	265.04	445	1129	4.26	
19.3125	-1601.6	-1335.7	265.9	471	1132	4.26	
19.375	-1601.6	-1334.22	267.38	389	1375	5.14	
19.4375	-1606.4	-1337.92	268.48	411	1328	4.95	
19.5	-1608.8	-1344.58	264.22	567	1315	4.98	
19.5625	-1610.4	-1335.7	274.7	551	1295	4.71	
19.625	-1612	-1336.44	275.56	611	1310	4.75	
19.6875	-1613.6	-1338.66	274.94	707	1401	5.10	
19.75	-1614.4	-1340.14	274.26	787	1477	5.39	
19.8125	-1615.2	-1342.36	272.84	810	1497	5.49	
19.875	-1616.8	-1344.58	272.22	772	1498	5.50	
19.9375	-1616.8	-1346.8	270	829	1543	5.71	
20	-1616.8	-1348.28	268.52	896	1599	5.95	0.335191
20.0625	-1617.6	-1349.02	268.58	881	1631	6.07	
20.125	-1616	-1349.76	266.24	1016	1634	6.14	
20.1875	-1617.6	-1351.24	266.36	1043	1648	6.19	
20.25	-1618.4	-1352.72	265.68	972	1696	6.38	
20.3125	-1617.6	-1354.2	263.4	1129	1760	6.68	
20.375	-1622.4	-1356.42	265.98	1084	1776	6.68	
20.4375	-1624	-1358.64	265.36	1081	1809	6.82	
20.5	-1623.2	-1359.38	263.82	1146	1818	6.89	

Valley distance /km	Valley-thalweg depth/m	Valley-bank depth/m	Valley height/m	Valley-floor width/m	Valley Width/m	Width/height	CSA/km²
20.5625	-1624.8	-1360.12	264.68	1122	1812	6.85	
20.625	-1624.8	-1361.6	263.2	1086	1815	6.90	
20.6875	-1624	-1362.34	261.66	1105	1815	6.94	
20.75	-1626.4	-1361.6	264.8	1167	1839	6.94	
20.8125	-1628	-1360.86	267.14	1201	1842	6.90	
20.875	-1628	-1360.86	267.14	1142	1846	6.91	
20.9375	-1628.8	-1360.86	267.94	1225	1858	6.93	
21	-1629.6	-1363.08	266.52	1193	1824	6.84	0.401831
21.0625	-1630.4	-1374.92	255.48	1271	1836	7.19	
21.125	-1631.2	-1388.98	242.22	1254	1818	7.51	
21.1875	-1630.4	-1400.08	230.32	1181	1679	7.29	
21.25	-1631.2	-1400.08	231.12	1032	1644	7.11	
21.3125	-1631.2	-1395.64	235.56	1014	1605	6.81	
21.375	-1632	-1392.68	239.32	1009	1568	6.55	
21.4375	-1632	-1391.2	240.8	1023	1222	5.07	
21.5	-1633.6	-1394.16	239.44	1044	1288	5.38	
21.5625	-1634.4	-1394.16	240.24	1055	1332	5.54	
21.625	-1632.8	-1393.42	239.38	1079	1440	6.02	
21.6875	-1635.2	-1391.2	244	1143	1536	6.30	
21.75	-1635.2	-1392.68	242.52	1143	1582	6.52	
21.8125	-1640.8	-1391.2	249.6	1280	1674	6.71	
21.875	-1640.8	-1391.94	248.86	1445	1838	7.39	
21.9375	-1644	-1392.68	251.32	1500	1995	7.94	
22	-1650.4	-1391.2	259.2	1603	2036	7.85	0.431202
22.0625	-1649.6	-1391.2	258.4	1695	2127	8.23	
22.125	-1654.4	-1390.46	263.94	1723	2175	8.24	
22.1875	-1655.2	-1389.72	265.48	1738	2231	8.40	
22.25	-1655.2	-1391.2	264	1659	2253	8.53	
22.3125	-1655.2	-1391.94	263.26	1703	2229	8.47	
22.375	-1656	-1390.46	265.54	1665	2236	8.42	
22.4375	-1656	-1388.24	267.76	1656	2260	8.44	
22.5	-1654.4	-1387.5	266.9	1576	2222	8.33	
22.5625	-1663.2	-1387.5	275.7	1511	2176	7.89	
22.625	-1668.8	-1387.5	281.3	1424	2170	7.71	
22.6875	-1669.6	-1388.24	281.36	1422	2110	7.50	
22.75	-1674.4	-1388.98	285.42	1469	2079	7.28	
22.8125	-1675.2	-1390.46	284.74	1392	2062	7.24	

Valley distance /km	Valley-thalweg depth/m	Valley-bank depth/m	Valley height/m	Valley-floor width/m	Valley Width/m	Width/height	CSA/km²
22.875	-1674.4	-1391.2	283.2	1397	2009	7.09	
22.9375	-1676.8	-1391.94	284.86	1258	1943	6.82	
23	-1677.6	-1392.68	284.92	767	1989	6.98	0.399908
23.0625	-1688.8	-1394.16	294.64	747	1933	6.56	
23.125	-1683.2	-1394.16	289.04	501	1919	6.64	
23.1875	-1684	-1394.9	289.1	471	1830	6.33	
23.25	-1688	-1397.12	290.88	526	1736	5.97	
23.3125	-1688	-1399.34	288.66	609	1705	5.91	
23.375	-1692	-1398.6	293.4	358	1613	5.50	
23.4375	-1691.2	-1398.6	292.6	395	1607	5.49	
23.5	-1691.2	-1397.86	293.34	381	1602	5.46	
23.5625	-1692.8	-1397.12	295.68	388	1543	5.22	
23.625	-1694.4	-1397.86	296.54	276	1502	5.07	
23.6875	-1699.2	-1398.6	300.6	269	1380	4.59	
23.75	-1693.6	-1397.86	295.74	306	1286	4.35	
23.8125	-1696.8	-1399.34	297.46	326	1248	4.20	
23.875	-1700	-1400.08	299.92	272	1262	4.21	
23.9375	-1699.2	-1402.3	296.9	383	1303	4.39	
24	-1693.6	-1402.3	291.3	391	1265	4.34	0.226424
24.0625	-1692.8	-1403.78	289.02	429	1331	4.61	
24.125	-1693.6	-1406	287.6	404	1328	4.62	
24.1875	-1706.4	-1406.74	299.66	359	1394	4.65	
24.25	-1707.2	-1406.74	300.46	389	1439	4.79	
24.3125	-1705.6	-1407.48	298.12	407	1415	4.75	
24.375	-1712.8	-1407.48	305.32	417	1429	4.68	
24.4375	-1712	-1408.96	303.04	374	1415	4.67	
24.5	-1713.6	-1409.7	303.9	365	1394	4.59	
24.5625	-1715.2	-1410.44	304.76	289	1380	4.53	
24.625	-1716	-1411.18	304.82	275	1338	4.39	
24.6875	-1717.6	-1412.66	304.94	244	1364	4.47	
24.75	-1716	-1414.14	301.86	247	1346	4.46	
24.8125	-1717.6	-1414.88	302.72	277	1356	4.48	
24.875	-1716.8	-1415.62	301.18	265	1394	4.63	
24.9375	-1718.4	-1416.36	302.04	263	1450	4.80	
25	-1720	-1417.1	302.9	316	1345	4.44	0.283733
25.0625	-1720.8	-1417.84	302.96	452	1325	4.37	
25.125	-1724.8	-1422.28	302.52	504	1334	4.41	

Valley distance /km	Valley-thalweg depth/m	Valley-bank depth/m	Valley height/m	Valley-floor width/m	Valley Width/m	Width/height	CSA/km²
25.1875	-1721.6	-1428.2	293.4	468	1380	4.70	
25.25	-1725.6	-1432.64	292.96	410	1370	4.68	
25.3125	-1727.2	-1435.6	291.6	349	1390	4.77	
25.375	-1730.4	-1437.82	292.58	354	1398	4.78	
25.4375	-1737.6	-1437.82	299.78	395	1422	4.74	
25.5	-1735.2	-1441.52	293.68	412	1415	4.82	
25.5625	-1737.6	-1453.36	284.24	414	1383	4.87	
25.625	-1738.4	-1444.48	293.92	441	1543	5.25	
25.6875	-1740	-1448.18	291.82	420	1502	5.15	
25.75	-1733.6	-1450.4	283.2	416	1519	5.36	
25.8125	-1737.6	-1442.26	295.34	492	1519	5.14	
25.875	-1737.6	-1429.68	307.92	539	1585	5.15	
25.9375	-1738.4	-1425.98	312.42	678	1561	5.00	
26	-1744	-1422.28	321.72	714	1561	4.85	0.297392
26.0625	-1744	-1424.5	319.5	682	1658	5.19	
26.125	-1745.6	-1426.72	318.88	589	1550	4.86	
26.1875	-1746.4	-1426.72	319.68	465	1863	5.83	
26.25	-1748.8	-1428.94	319.86	356	1791	5.60	
26.3125	-1751.2	-1429.68	321.52	284	2142	6.66	
26.375	-1753.6	-1429.68	323.92	394	2187	6.75	
26.4375	-1756	-1430.42	325.58	630	2166	6.65	
26.5	-1754.4	-1431.9	322.5	622	2148	6.66	
26.5625	-1759.2	-1431.16	328.04	666	2107	6.42	
26.625	-1758.4	-1432.64	325.76	702	2100	6.45	
26.6875	-1760	-1434.86	325.14	696	2117	6.51	
26.75	-1760	-1436.34	323.66	527	2058	6.36	
26.8125	-1758.4	-1437.08	321.32	369	2058	6.40	
26.875	-1772.8	-1438.56	334.24	282	1982	5.93	
26.9375	-1776.8	-1439.3	337.5	366	1982	5.87	
27	-1778.4	-1449.66	328.74	369	1721	5.24	0.279469
27.0625	-1777.6	-1467.42	310.18	359	1286	4.15	
27.125	-1776	-1461.5	314.5	345	1415	4.50	
27.1875	-1774.4	-1462.98	311.42	399	1453	4.67	
27.25	-1777.6	-1465.94	311.66	401	1432	4.59	
27.3125	-1782.4	-1466.68	315.72	373	1429	4.53	
27.375	-1780.8	-1465.2	315.6	403	1436	4.55	
27.4375	-1782.4	-1465.94	316.46	383	1411	4.46	

Valley distance /km	Valley-thalweg depth/m	Valley-bank depth/m	Valley height/m	Valley-floor width/m	Valley Width/m	Width/height	CSA/km²
27.5	-1781.6	-1460.02	321.58	329	1443	4.49	
27.5625	-1784.8	-1460.02	324.78	329	1467	4.52	
27.625	-1787.2	-1462.98	324.22	432	1345	4.15	
27.6875	-1795.2	-1462.24	332.96	400	1283	3.85	
27.75	-1798.4	-1464.46	333.94	409	1318	3.95	
27.8125	-1796.8	-1471.86	324.94	332	1161	3.57	
27.875	-1796	-1475.56	320.44	399	1161	3.62	
27.9375	-1797.6	-1474.08	323.52	389	1161	3.59	
28	-1796.8	-1474.82	321.98	426	1165	3.62	0.192257
28.0625	-1798.4	-1474.08	324.32	490	1147	3.54	
28.125	-1799.2	-1482.22	316.98	462	1109	3.50	
28.1875	-1796.8	-1484.44	312.36	529	1081	3.46	
28.25	-1796	-1474.08	321.92	558	1105	3.43	
28.3125	-1799.2	-1474.82	324.38	520	1220	3.76	
28.375	-1801.6	-1474.82	326.78	537	1297	3.97	
28.4375	-1801.6	-1477.04	324.56	448	1265	3.90	
28.5	-1804.8	-1480	324.8	427	1192	3.67	
28.5625	-1808	-1482.96	325.04	328	1227	3.77	
28.625	-1809.6	-1486.66	322.94	293	1220	3.78	
28.6875	-1812	-1491.84	320.16	299	1220	3.81	
28.75	-1815.2	-1496.28	318.92	310	1164	3.65	
28.8125	-1818.4	-1498.5	319.9	267	1193	3.73	
28.875	-1822.4	-1498.5	323.9	309	1200	3.70	
28.9375	-1824.8	-1498.5	326.3	340	1164	3.57	
29	-1836.8	-1497.76	339.04	337	1199	3.54	0.180781
29.0625	-1847.2	-1497.76	349.44	325	1195	3.42	
29.125	-1848	-1497.76	350.24	288	1252	3.57	
29.1875	-1840.8	-1499.24	341.56	293	1224	3.58	
29.25	-1832	-1497.76	334.24	270	1241	3.71	
29.3125	-1836	-1498.5	337.5	261	1304	3.86	
29.375	-1838.4	-1498.5	339.9	306	1307	3.85	
29.4375	-1833.6	-1497.02	336.58	306	1384	4.11	
29.5	-1834.4	-1495.54	338.86	357	1310	3.87	
29.5625	-1835.2	-1502.94	332.26	302	1227	3.69	
29.625	-1834.4	-1506.64	327.76	331	1213	3.70	
29.6875	-1836.8	-1508.12	328.68	296	1171	3.56	
29.75	-1832.8	-1510.34	322.46	289	1091	3.38	

Valley distance /km	Valley-thalweg depth/m	Valley-bank depth/m	Valley height/m	Valley-floor width/m	Valley Width/m	Width/height	CSA/km²
29.8125	-1828	-1513.3	314.7	288	1102	3.50	
29.875	-1828	-1510.34	317.66	293	1060	3.34	
29.9375	-1828.8	-1515.52	313.28	320	1095	3.50	
30	-1830.4	-1516.26	314.14	274	1119	3.56	0.165813
30.0625	-1831.2	-1515.52	315.68	326	1150	3.64	
30.125	-1840	-1515.52	324.48	272	1227	3.78	
30.1875	-1841.6	-1516.26	325.34	282	1230	3.78	
30.25	-1842.4	-1517	325.4	262	1258	3.87	
30.3125	-1840.8	-1518.48	322.32	253	1241	3.85	
30.375	-1840	-1519.22	320.78	266	1258	3.92	
30.4375	-1837.6	-1519.96	317.64	234	1286	4.05	
30.5	-1834.4	-1519.96	314.44	239	1300	4.13	
30.5625	-1834.4	-1521.44	312.96	239	1008	3.22	
30.625	-1834.4	-1533.28	301.12	278	998	3.31	
30.6875	-1834.4	-1532.54	301.86	274	1095	3.63	
30.75	-1834.4	-1531.06	303.34	253	1091	3.60	
30.8125	-1836.8	-1531.8	305	271	1088	3.57	
30.875	-1836	-1532.54	303.46	232	1140	3.76	
30.9375	-1839.2	-1532.54	306.66	225	1130	3.68	
31	-1840.8	-1535.5	305.3	225	1161	3.80	0.159526
31.0625	-1841.6	-1528.84	312.76	263	1130	3.61	
31.125	-1843.2	-1528.84	314.36	235	998	3.17	
31.1875	-1840.8	-1529.58	311.22	237	998	3.21	
31.25	-1842.4	-1531.06	311.34	270	1015	3.26	
31.3125	-1842.4	-1531.06	311.34	243	1025	3.29	
31.375	-1843.2	-1541.42	301.78	251	1119	3.71	
31.4375	-1842.4	-1539.94	302.46	293	1234	4.08	
31.5	-1843.2	-1538.46	304.74	320	1262	4.14	
31.5625	-1845.6	-1536.98	308.62	344	1370	4.44	
31.625	-1847.2	-1537.72	309.48	386	1418	4.58	
31.6875	-1848.8	-1537.72	311.08	345	1432	4.60	
31.75	-1850.4	-1540.68	309.72	394	1415	4.57	
31.8125	-1850.4			353			
31.875	-1852	-1542.9	309.1	339	1408	4.56	
31.9375	-1856	-1545.12	310.88	310	1382	4.45	
32	-1859.2	-1547.34	311.86	222	1382	4.43	0.200760
32.0625		-1548.08			1342		

Valley distance /km	Valley-thalweg depth/m	Valley-bank depth/m	Valley height/m	Valley-floor width/m	Valley Width/m	Width/height	CSA/km²
32.125		-1550.3			1312		
32.1875	-1863.2			282			
32.25	-1866.4			256			
32.3125	-1874.4	-1554.74	319.66	293	1234	3.86	
32.375	-1876	-1555.48	320.52	314	1227	3.83	
32.4375	-1861.6	-1555.48	306.12	317	1272	4.16	
32.5	-1861.6	-1556.22	305.38	338	1351	4.42	
32.5625	-1861.6	-1555.48	306.12	399	1373	4.49	
32.625	-1864	-1556.96	307.04	399	1377	4.48	
32.6875	-1862.4	-1556.96	305.44	346	1349	4.42	
32.75	-1865.6	-1559.18	306.42	362	1328	4.33	
32.8125	-1864	-1559.92	304.08	350	1299	4.27	
32.875	-1868.8	-1559.92	308.88	241	1329	4.30	
32.9375	-1866.4	-1559.18	307.22	246	1344	4.37	
33	-1865.6	-1556.96	308.64	329	1527	4.95	0.165804
33.0625	-1865.6	-1554.74	310.86	303	1539	4.95	
33.125	-1864	-1555.48	308.52	274	1533	4.97	
33.1875	-1878.4	-1556.22	322.18	210	1488	4.62	
33.25	-1876.8	-1559.18	317.62	186	2755	8.67	
33.3125	-1880.8	-1562.14	318.66	188	2729	8.56	
33.375	-1876.8	-1563.62	313.18	161	2681	8.56	
33.4375	-1880	-1565.84	314.16	224	2699	8.59	
33.5	-1882.4	-1565.1	317.3	202	2684	8.46	
33.5625	-1884.8	-1568.06	316.74	194	2613	8.25	
33.625	-1898.4	-1568.06	330.34	183	2640	7.99	
33.6875	-1901.6	-1569.54	332.06	164	2537	7.64	
33.75	-1890.4	-1572.5	317.9	219	2471	7.77	
33.8125	-1887.2	-1573.24	313.96	177	2406	7.66	
33.875	-1888.8	-1576.94	311.86	161	2336	7.49	
33.9375	-1887.2	-1578.42	308.78	183	2233	7.23	
34	-1888	-1579.16	308.84	177	2173	7.04	0.336700
34.0625	-1888	-1579.9	308.1	180	2146	6.97	
34.125	-1888	-1577.68	310.32	181	2119	6.83	
34.1875	-1887.2	-1577.68	309.52	235	2090	6.75	
34.25	-1890.4	-1577.68	312.72	246	2038	6.52	
34.3125	-1892	-1580.64	311.36	232	1869	6.00	
34.375	-1892.8	-1582.12	310.68	255	1855	5.97	

Valley distance /km	Valley-thalweg depth/m	Valley-bank depth/m	Valley height/m	Valley-floor width/m	Valley Width/m	Width/height	CSA/km²
34.4375	-1892	-1583.6	308.4	257	1835	5.95	
34.5	-1888.8	-1587.3	301.5	301	1846	6.12	
34.5625	-1888.8	-1588.04	300.76	335	1804	6.00	
34.625	-1888	-1589.52	298.48	309	1742	5.84	
34.6875	-1888	-1591	297	329	1794	6.04	
34.75	-1888.8	-1593.96	294.84	315	1811	6.14	
34.8125	-1889.6	-1596.92	292.68	389	1770	6.05	
34.875	-1891.2			405			

Table A1.3. Channel bank angle of the Quaternary channel system.

Channel distance/km	West bank angle/°	East bank angle/°
0		27
0.125		27
0.25		29
0.375		32
0.5	27	34
0.625		37
0.75		37
0.875		36
1		31
1.125		34
1.25		38
1.375	28	33
1.5	29	32
1.625	27	39
1.75	30	25
1.875	34	35
2	36	27
2.125	38	27
2.25	36	29
2.375	31	35
2.5	28	31
2.625	28	28
2.75	28	25
2.875	27	
3	24	31
3.125	29	30
3.25	29	30
3.375	29	33
3.5	28	28
3.625	30	34
3.75	30	27
3.875	31	27
4	29	31
4.125	31	31
4.25	36	38
4.375	34	33
4.5	32	30
4.625	24	30
4.75	21	30
4.875	18	33

Channel distance/km	West bank angle/°	East bank angle/°
5	25	30
5.125		33
5.25	28	30
5.375	26	23
5.5	32	24
5.625	31	28
5.75	33	31
5.875	30	30
6	33	34
6.125	29	28
6.25	34	31
6.375	34	31
6.5	33	33
6.625	28	29
6.75	29	38
6.875	26	29
7	34	31
7.125	34	32
7.25	28	36
7.375	32	34
7.5	31	35
7.625	29	27
7.75	32	32
7.875	30	27
8	30	31
8.125	29	29
8.25	27	29
8.375	24	27
8.5	19	30
8.625	16	30
8.75		34
8.875	23	25
9	24	30
9.125	19	24
9.25	27	24
9.375	28	29
9.5	28	23
9.625	25	21
9.75	25	
9.875	32	
10	33	
10.125	30	

Channel distance/km	West bank angle/°	East bank angle/°
10.25	31	25
10.375	28	37
10.5	30	32
10.625	25	33
10.75	31	29
10.875	32	31
11	29	30
11.125	28	31
11.25	35	31
11.375	30	31
11.5	31	30
11.625	36	
11.75	30	27
11.875	28	24
12	29	22
12.125	29	22
12.25	27	37
12.375	25	29
12.5	30	33
12.625	30	31
12.75	31	26
12.875	36	30
13	31	31
13.125	34	31
13.25	28	29
13.375	31	35
13.5	30	37
13.625	30	35
13.75	29	28
13.875	30	
14	27	25
14.125	26	25
14.25	28	27
14.375	23	26
14.5	23	25
14.625	26	30
14.75	27	31
14.875	23	29
15	22	28
15.125	29	26
15.25		31
15.375	15	33

Channel distance/km	West bank angle/°	East bank angle/°
15.5	13	26
15.625	14	27
15.75		28
15.875		26
16	20	26
16.125	27	24
16.25	25	
16.375	27	
16.5	20	
16.625	19	
16.75	20	
16.875	22	
17	22	
17.125	22	
17.25		
17.375	23	
17.5	28	
17.625	25	
17.75		
17.875		
18		
18.125		
18.25		
18.375		
18.5		32
18.625		33
18.75		31
18.875		35
19		29
19.125		35
19.25		28
19.375		26
19.5		23
19.625		
19.75		
19.875		21
20	20	20
20.125	23	24
20.25	16	21
20.375	23	16
20.5	35	14
20.625	31	

Channel distance/km	West bank angle/°	East bank angle/°
20.75	27	
20.875	30	
21	28	
21.125	30	
21.25	30	
21.375		
21.5		
21.625	33	
21.75	33	
21.875	35	
22	28	
22.125	32	
22.25	29	20
22.375	35	
22.5		
22.625	24	21
22.75		31
22.875		32
23		
23.125		29
23.25	20	27
23.375	27	
23.5	27	32
23.625		36
23.75		34
23.875		
24		31
24.125		35
24.25		34
24.375		32
24.5		39
24.625	23	34
24.75		37
24.875		28
25		32
25.125		34
25.25		36
25.375		35
25.5		37
25.625		30
25.75		33
25.875	24	33

Channel distance/km	West bank angle/°	East bank angle/°
26	23	36
26.125	21	26
26.25		32
26.375	18	26
26.5	33	
26.625	34	
26.75		
26.875	32	25
27	27	28
27.125	27	30
27.25	26	29
27.375	27	26
27.5		27
27.625	33	28
27.75	24	26
27.875	26	30
28	27	28
28.125	23	26
28.25	22	30
28.375	20	31
28.5	28	31
28.625	29	26
28.75	21	31
28.875	26	29
29	21	28
29.125	29	27
29.25	33	27
29.375	30	25
29.5	30	25
29.625	28	29
29.75	32	24
29.875	33	24
30	32	23
30.125	30	25
30.25		29
30.375	26	
30.5	27	32
30.625	26	30
30.75		33
30.875		34
31	22	31
31.125	26	27

Channel distance/km	West bank angle/°	East bank angle/°
31.25	27	27
31.375	31	23
31.5	28	25
31.625		
31.75	30	
31.875	31	26
32	30	24
32.125	33	23
32.25	32	
32.375	33	25
32.5	34	29
32.625	37	31
32.75	36	30
32.875		31
33	31	35
33.125	26	22
33.25	22	31
33.375		26
33.5		33
33.625	24	32
33.75		30
33.875	25	31
34		29
34.125		31
34.25		33
34.375	25	27
34.5		26
34.625	36	
34.75	33	24
34.875	34	20
35	35	23
35.125	28	25
35.25	32	22
35.375	34	30
35.5	31	30
35.625	37	32
35.75		25
35.875		25
36	28	30
36.125	21	26
36.25	23	29
36.375		

Channel distance/km	West bank angle/°	East bank angle/°
36.5	28	34
36.625	28	30
36.75	27	20
36.875	33	21
37	28	
37.125	34	25
37.25	33	24
37.375	38	28
37.5	24	28
37.625		27
37.75		38
37.875	16	36
38		34
38.125	15	34
38.25	19	38
38.375	23	34
38.5		33
38.625		34
38.75	25	32
38.875	23	33
39	26	36
39.125	29	35
39.25	22	
39.375		
39.5		
39.625		
39.75		
39.875	31	
40	28	
40.125	27	
40.25	29	21
40.375	28	24
40.5	28	23
40.625	28	29
40.75	29	27
40.875	32	
41	28	21
41.125	27	23
41.25	24	25
41.375	21	25
41.5		28

Channel distance/km	West bank angle/°	East bank angle/°
41.625		23
41.75		23
41.875		24
42		33
42.125		29
42.25		33
42.375		34

Table A1.4. Summary of morphological data for the Quaternary channel system. Morphological parameters include the thalweg depths of initial and present channels.

Valley distance/km	Thalweg depth of initial channel/m	Thalweg depth of present channel/m
18	-1580	-1407.48
18.0625	-1580.8	-1408.96
18.125	-1582.4	-1408.22
18.1875	-1583.2	-1406.74
18.25	-1582.4	-1408.96
18.3125	-1584	-1406.74
18.375	-1587.2	-1408.96
18.4375	-1584	-1408.22
18.5	-1584.8	-1411.18
18.5625	-1585.6	-1413.4
18.625	-1583.2	-1413.4
18.6875	-1585.6	-1414.88
18.75	-1587.2	-1415.62
18.8125	-1587.2	-1414.88
18.875	-1588	-1416.36
18.9375	-1590.4	-1419.32
19	-1591.2	-1422.28
19.0625	-1591.2	-1420.8
19.125	-1596.8	-1420.8
19.1875	-1599.2	-1420.06
19.25	-1600	-1418.58
19.3125	-1601.6	-1420.8
19.375	-1601.6	-1422.28
19.4375	-1606.4	-1422.28
19.5	-1608.8	-1424.5
19.5625	-1610.4	-1426.72
19.625	-1612	-1425.98
19.6875	-1613.6	-1428.2
19.75	-1614.4	-1430.42
19.8125	-1615.2	-1432.64
19.875	-1616.8	-1434.12
19.9375	-1616.8	-1434.86
20	-1616.8	-1435.6
20.0625	-1617.6	-1437.82
20.125	-1616	-1440.04
20.1875	-1617.6	-1440.78
20.25	-1618.4	-1443
20.3125	-1617.6	-1443.74

Valley distance/km	Thalweg depth of initial channel/m	Thalweg depth of present channel/m
20.375	-1622.4	-1444.48
20.4375	-1624	-1445.96
20.5	-1623.2	-1449.66
20.5625	-1624.8	-1451.14
20.625	-1624.8	-1462.98
20.6875	-1624	-1457.8
20.75	-1626.4	-1456.32
20.8125	-1628	-1461.5
20.875	-1628	-1468.9
20.9375	-1628.8	-1466.68
21	-1629.6	-1464.46
21.0625	-1630.4	-1464.46
21.125	-1631.2	-1468.16
21.1875	-1630.4	-1470.38
21.25	-1631.2	-1471.86
21.3125	-1631.2	-1472.6
21.375	-1632	-1470.38
21.4375	-1632	-1470.38
21.5	-1633.6	-1470.38
21.5625	-1634.4	-1471.12
21.625	-1632.8	-1470.38
21.6875	-1635.2	-1469.64
21.75	-1635.2	-1472.6
21.8125	-1640.8	-1474.08
21.875	-1640.8	-1474.08
21.9375	-1644	-1471.12
22	-1650.4	-1475.56
22.0625	-1649.6	-1477.78
22.125	-1654.4	-1479.26
22.1875	-1655.2	-1482.22
22.25	-1655.2	-1482.96
22.3125	-1655.2	-1482.22
22.375	-1656	-1485.18
22.4375	-1656	-1484.44
22.5	-1654.4	-1485.18
22.5625	-1663.2	-1486.66
22.625	-1668.8	-1521.44
22.6875	-1669.6	-1522.18
22.75	-1674.4	-1525.88
22.8125	-1675.2	-1528.1
22.875	-1674.4	-1534.02
22.9375	-1676.8	-1538.46

Valley distance/km	Thalweg depth of initial channel/m	Thalweg depth of present channel/m
23	-1677.6	-1537.72
23.0625	-1688.8	-1541.42
23.125	-1683.2	-1540.68
23.1875	-1684	-1543.64
23.25	-1688	-1542.9
23.3125	-1688	-1543.64
23.375	-1692	-1545.86
23.4375	-1691.2	-1546.6
23.5	-1691.2	-1545.86
23.5625	-1692.8	-1548.82
23.625	-1694.4	-1551.04
23.6875	-1699.2	-1549.56
23.75	-1693.6	-1548.82
23.8125	-1696.8	-1548.08
23.875	-1700	-1548.08
23.9375	-1699.2	-1548.08
24	-1693.6	-1548.82
24.0625	-1692.8	-1549.56
24.125	-1693.6	-1548.08
24.1875	-1706.4	-1550.3
24.25	-1707.2	-1548.08
24.3125	-1705.6	-1552.52
24.375	-1712.8	-1552.52
24.4375	-1712	-1556.22
24.5	-1713.6	-1558.44
24.5625	-1715.2	-1561.4
24.625	-1716	-1562.88
24.6875	-1717.6	-1562.14
24.75	-1716	-1562.88
24.8125	-1717.6	-1561.4
24.875	-1716.8	-1560.66
24.9375	-1718.4	-1561.4
25	-1720	-1562.88
25.0625	-1720.8	-1562.88
25.125	-1724.8	-1567.32
25.1875	-1721.6	-1568.8
25.25	-1725.6	-1571.76
25.3125	-1727.2	-1570.28
25.375	-1730.4	-1571.76
25.4375	-1737.6	-1573.98
25.5	-1735.2	-1573.24
25.5625	-1737.6	-1573.24

Valley distance/km	Thalweg depth of initial channel/m	Thalweg depth of present channel/m
25.625	-1738.4	-1574.72
25.6875	-1740	-1576.2
25.75	-1733.6	-1576.2
25.8125	-1737.6	-1576.94
25.875	-1737.6	-1577.68
25.9375	-1738.4	-1585.08
26	-1744	-1582.12
26.0625	-1744	-1579.9
26.125	-1745.6	-1582.12
26.1875	-1746.4	-1582.86
26.25	-1748.8	-1588.78
26.3125	-1751.2	-1591.74
26.375	-1753.6	-1596.18
26.4375	-1756	-1597.66
26.5	-1754.4	-1599.88
26.5625	-1759.2	-1600.62
26.625	-1758.4	-1600.62
26.6875	-1760	-1601.36
26.75	-1760	-1603.58
26.8125	-1758.4	-1611.72
26.875	-1772.8	-1614.68
26.9375	-1776.8	-1614.68
27	-1778.4	-1616.16
27.0625	-1777.6	-1616.16
27.125	-1776	-1618.38
27.1875	-1774.4	-1617.64
27.25	-1777.6	-1616.9
27.3125	-1782.4	-1618.38
27.375	-1780.8	-1620.6
27.4375	-1782.4	-1624.3
27.5	-1781.6	-1624.3
27.5625	-1784.8	-1625.04
27.625	-1787.2	-1628.74
27.6875	-1795.2	-1633.18
27.75	-1798.4	-1636.88
27.8125	-1796.8	-1637.62
27.875	-1796	-1636.88
27.9375	-1797.6	-1636.88
28	-1796.8	-1636.14
28.0625	-1798.4	-1636.14
28.125	-1799.2	-1636.14
28.1875	-1796.8	-1636.14

Valley distance/km	Thalweg depth of initial channel/m	Thalweg depth of present channel/m
28.25	-1796	-1636.88
28.3125	-1799.2	-1635.4
28.375	-1801.6	-1639.84
28.4375	-1801.6	-1642.06
28.5	-1804.8	-1647.98
28.5625	-1808	-1651.68
28.625	-1809.6	-1651.68
28.6875	-1812	-1650.94
28.75	-1815.2	-1650.2
28.8125	-1818.4	-1652.42
28.875	-1822.4	-1653.16
28.9375	-1824.8	-1653.16
29	-1836.8	-1656.12
29.0625	-1847.2	-1656.86
29.125	-1848	-1658.34
29.1875	-1840.8	-1659.82
29.25	-1832	-1659.08
29.3125	-1836	-1659.82
29.375	-1838.4	-1659.82
29.4375	-1833.6	-1661.3
29.5	-1834.4	-1662.78
29.5625	-1835.2	-1663.52
29.625	-1834.4	-1663.52
29.6875	-1836.8	-1661.3
29.75	-1832.8	-1661.3
29.8125	-1828	-1663.52
29.875	-1828	-1664.26
29.9375	-1828.8	-1663.52
30	-1830.4	-1664.26
30.0625	-1831.2	-1664.26
30.125	-1840	-1662.78
30.1875	-1841.6	-1665
30.25	-1842.4	-1665
30.3125	-1840.8	-1664.26
30.375	-1840	-1665
30.4375	-1837.6	-1665
30.5	-1834.4	-1664.26
30.5625	-1834.4	-1662.04
30.625	-1834.4	-1662.78
30.6875	-1834.4	-1662.78
30.75	-1834.4	-1666.48
30.8125	-1836.8	-1666.48

Valley distance/km	Thalweg depth of initial channel/m	Thalweg depth of present channel/m
30.875	-1836	-1667.22
30.9375	-1839.2	-1668.7
31	-1840.8	-1669.44
31.0625	-1841.6	-1667.96
31.125	-1843.2	-1668.7
31.1875	-1840.8	-1667.96
31.25	-1842.4	-1667.96
31.3125	-1842.4	-1667.96
31.375	-1843.2	-1667.96
31.4375	-1842.4	-1668.7
31.5	-1843.2	-1673.88
31.5625	-1845.6	-1676.1
31.625	-1847.2	-1677.58
31.6875	-1848.8	-1679.06
31.75	-1850.4	-1679.06
31.8125	-1850.4	-1680.54
31.875	-1852	-1682.76
31.9375	-1856	-1683.5
32	-1859.2	-1684.24
32.0625		
32.125		
32.1875	-1863.2	-1693.12
32.25	-1866.4	-1693.12
32.3125	-1874.4	-1693.86
32.375	-1876	-1692.38
32.4375	-1861.6	-1690.9
32.5	-1861.6	-1693.12
32.5625	-1861.6	-1693.12
32.625	-1864	-1693.86
32.6875	-1862.4	-1693.86
32.75	-1865.6	-1690.9
32.8125	-1864	-1689.42
32.875	-1868.8	-1690.9
32.9375	-1866.4	-1693.86
33	-1865.6	-1693.86
33.0625	-1865.6	-1695.34
33.125	-1864	-1693.12
33.1875	-1878.4	-1694.6
33.25	-1876.8	-1692.38
33.3125	-1880.8	-1691.64
33.375	-1876.8	-1691.64
33.4375	-1880	-1692.38

Valley distance/km	Thalweg depth of initial channel/m	Thalweg depth of present channel/m
33.5	-1882.4	-1693.86
33.5625	-1884.8	-1693.86
33.625	-1898.4	-1695.34
33.6875	-1901.6	-1697.56
33.75	-1890.4	-1699.04
33.8125	-1887.2	-1699.04
33.875	-1888.8	-1699.04
33.9375	-1887.2	-1698.3
34	-1888	-1699.04
34.0625	-1888	-1699.78
34.125	-1888	-1699.78
34.1875	-1887.2	-1701.26
34.25	-1890.4	-1702
34.3125	-1892	-1702
34.375	-1892.8	-1702
34.4375	-1892	-1704.22
34.5	-1888.8	-1703.48
34.5625	-1888.8	-1705.7
34.625	-1888	-1705.7
34.6875	-1888	-1704.96
34.75	-1888.8	-1706.44
34.8125	-1889.6	-1707.18
34.875	-1891.2	-1707.18

Appendix 2. Supplementary materials for Chapter 5.

Table A2.1. Summary of morphological data for the Quaternary channel system. Morphological parameters include the depth of valley thalweg, magnitude of vertical aggradation (L_A) and lateral migration (L_M), L_M/L_A, and depositional ratio.

Valley distance /km	Depth of valley thalweg/m	Magnitude of Vertical aggradation (L_A)/m	Magnitude of Lateral migration (L_M)/m	L_M/L_A	Depositional ratio
0	-1113.6	102.02			
0.0625	-1117.6	103.06			
0.125	-1117.6	100.1			
0.1875	-1120	101.02			
0.25	-1124	102.06			
0.3125	-1127.2	103.04			
0.375	-1129.6	101			
0.4375	-1129.6	101.74			
0.5	-1132.8	101.98			
0.5625	-1133.6	99.82			
0.625	-1139.2	100.98			
0.6875	-1141.6	99.68			
0.75	-1142.4	94.56			
0.8125	-1143.2	100.54			
0.875	-1143.2	100.54			
0.9375	-1144	101.34			
1	-1143.2	102.02			
1.0625	-1141.6	98.94			
1.125	-1142.4	99.74			
1.1875	-1141.6	98.94			
1.25	-1141.6	98.94			
1.3125	-1142.4	96.04			
1.375	-1147.2	95.66			
1.4375	-1161.6	104.14			
1.5	-1168.8	104.68			
1.5625	-1168.8	102.46			
1.625	-1171.2	104.12			
1.6875	-1173.6	102.08			
1.75	-1176	103.74			
1.8125	-1180	105.52			
1.875	-1180.8	102.62			
1.9375	-1181.6	101.94			

Valley distance /km	Depth of valley thalweg/m	Magnitude of Vertical aggradation (L_A)/m	Magnitude of Lateral migration (L_M)/m	L_M/L_A	Depositional ratio
2	-1184	102.12			
2.0625	-1188	103.16			
2.125	-1193.6	108.76			
2.1875	-1194.4	108.08			
2.25	-1195.2	109.62			
2.3125	-1197.6	111.28			
2.375	-1198.4	108.38			
2.4375	-1205.6	111.88			
2.5	-1208	116.5			
2.5625	-1210.4	116.68			
2.625	-1213.6	119.14			
2.6875	-1217.6	120.92			
2.75	-1217.6	116.48			
2.8125	-1219.2	117.34			
2.875	-1220	115.92			
2.9375	-1223.2	116.9			
3	-1225.6	118.56			
3.0625	-1227.2	120.16			
3.125	-1226.4	115.66			
3.1875	-1228.8	120.28			
3.25	-1229.6	119.6			
3.3125	-1229.6	115.9			
3.375	-1232	119.78			
3.4375	-1235.2	105.96			
3.5	-1240.8	106.38			
3.5625	-1240.8	105.64			
3.625	-1240	106.32			
3.6875	-1241.6	107.92			
3.75	-1243.2	109.52			
3.8125	-1242.4	110.2			
3.875	-1240	107.8			
3.9375	-1239.2	107.74			
4	-1238.4	109.16			
4.0625	-1240	110.02			
4.125	-1240.8	110.82			
4.1875	-1242.4	111.68			

Valley distance /km	Depth of valley thalweg/m	Magnitude of Vertical aggradation (L_A)/m	Magnitude of Lateral migration (L_M)/m	L_M/L_A	Depositional ratio
4.25	-1256.8	126.08			
4.3125	-1259.2	129.22			
4.375	-1259.2	127.74			
4.4375	-1262.4	130.2			
4.5	-1263.2	127.3			
4.5625	-1266.4	125.32			
4.625	-1265.6	121.56			
4.6875	-1268.8	124.76			
4.75	-1271.2	127.9			
4.8125	-1272.8	128.02			
4.875	-1274.4	128.88			
4.9375	-1276.8	128.32			
5	-1277.6	124.68			
5.0625	-1280.8	124.18			
5.125	-1282.4	120.6			
5.1875	-1284.8	123			
5.25	-1286.4	120.9			
5.3125	-1288	122.5			
5.375	-1292	121.32			
5.4375	-1293.6	118.48			
5.5	-1296.8	120.2			
5.5625	-1300.8	120.5			
5.625	-1300	119.7			
5.6875	-1300	113.04			
5.75	-1300	110.82			
5.8125	-1300	111.56			
5.875	-1302.4	111			
5.9375	-1304.8	111.92			
6	-1307.2	110.62			
6.0625	-1311.2	113.14			
6.125	-1314.4	113.38			
6.1875	-1316	114.24			
6.25	-1319.2	115.96			
6.3125	-1319.2	115.22			
6.375	-1319.2	113			
6.4375	-1320	112.32			

Valley distance /km	Depth of valley thalweg/m	Magnitude of Vertical aggradation (L_A)/m	Magnitude of Lateral migration (L_M)/m	L_M/L_A	Depositional ratio
6.5	-1324	112.62			
6.5625	-1328	113.66			
6.625	-1328	113.66			
6.6875	-1328.8	115.2			
6.75	-1329.6	115.26			
6.8125	-1331.2	113.9			
6.875	-1331.2	113.9			
6.9375	-1332	113.22			
7	-1332.8	113.28			
7.0625	-1333.6	114.08			
7.125	-1336.8	112.84			
7.1875	-1339.2	113.76			
7.25	-1339.2	115.98			
7.3125	-1338.4	115.18			
7.375	-1340	116.04			
7.4375	-1341.6	116.9			
7.5	-1344	120.78			
7.5625	-1345.6	123.12			
7.625	-1345.6	123.86			
7.6875	-1345.6	126.08			
7.75	-1347.2	125.46			
7.8125	-1347.2	121.76			
7.875	-1350.4	123.48			
7.9375	-1353.6	125.94			
8	-1356.8	128.4			
8.0625	-1361.6	131.72			
8.125	-1366.4	132.82			
8.1875	-1366.4	135.04			
8.25	-1364	131.16			
8.3125	-1364.8	131.22			
8.375	-1369.6	134.54			
8.4375	-1368	130.72			
8.5	-1376.8	136.56			
8.5625	-1373.6	131.88			
8.625	-1374.4	131.2			
8.6875	-1377.6	130.7			

Valley distance /km	Depth of valley thalweg/m	Magnitude of Vertical aggradation (L_A)/m	Magnitude of Lateral migration (L_M)/m	L_M/L_A	Depositional ratio
8.75	-1382.4	131.06			
8.8125	-1383.2	130.38			
8.875	-1384.8	130.5			
8.9375	-1388	132.96			
9	-1390.4	130.18			
9.0625	-1390.4	125			
9.125	-1392.8	125.92			
9.1875	-1390.4	120.56			
9.25	-1396	125.42			
9.3125	-1402.4	129.6			
9.375	-1406.4	130.64			
9.4375	-1408	130.76			
9.5	-1410.4	131.68			
9.5625	-1410.4	130.2			
9.625	-1408.8	127.86			
9.6875	-1409.6	128.66			
9.75	-1410.4	127.24			
9.8125	-1413.6	128.22			
9.875	-1415.2	129.82			
9.9375	-1417.6	131.48			
10	-1419.2	130.86			
10.0625	-1415.2	126.12			
10.125	-1416	127.66			
10.1875	-1419.2	127.16			
10.25	-1421.6	131.78			
10.3125	-1421.6	130.3			
10.375	-1420.8	129.5			
10.4375	-1420.8	130.24			
10.5	-1420.8	130.98			
10.5625	-1422.4	130.36			
10.625	-1424.8	130.54			
10.6875	-1425.6	126.16			
10.75	-1426.4	124.74			
10.8125	-1428	124.86			
10.875	-1430.4	125.78			
10.9375	-1431.2	128.06			

Valley distance /km	Depth of valley thalweg/m	Magnitude of Vertical aggradation (L$_A$)/m	Magnitude of Lateral migration (L$_M$)/m	L$_M$/L$_A$	Depositional ratio
11	-1436.8	132.18			
11.0625	-1434.4	132			
11.125	-1436.8	129.96			
11.1875	-1438.4	129.34			
11.25	-1441.6	129.58			
11.3125	-1442.4	128.16			
11.375	-1442.4	128.16			
11.4375	-1442.4	128.16			
11.5	-1444.8	129.08			
11.5625	-1444.8	128.34			
11.625	-1440.8	123.6			
11.6875	-1447.2	129.26			
11.75	-1449.6	127.22			
11.8125	-1451.2	125.12			
11.875	-1452	125.18			
11.9375	-1456.8	129.98			
12	-1458.4	129.36			
12.0625	-1464	134.96			
12.125	-1464	137.92			
12.1875	-1464	140.88			
12.25	-1463.2	139.34			
12.3125	-1459.2	136.82			
12.375	-1460	136.88			
12.4375	-1462.4	138.54			
12.5	-1464	140.88			
12.5625	-1467.2	141.12			
12.625	-1467.2	141.86			
12.6875	-1468.8	139.76			
12.75	-1470.4	141.36			
12.8125	-1472	142.96			
12.875	-1475.2	143.2			
12.9375	-1476				
13	-1477.6	141.9			
13.0625					
13.125					
13.1875					

Valley distance /km	Depth of valley thalweg/m	Magnitude of Vertical aggradation (L_A)/m	Magnitude of Lateral migration (L_M)/m	L_M/L_A	Depositional ratio
13.25					
13.3125					
13.375					
13.4375					
13.5					
13.5625					
13.625					
13.6875					
13.75					
13.8125					
13.875					
13.9375					
14					
14.0625					
14.125					
14.1875					
14.25					
14.3125					
14.375					
14.4375					
14.5					
14.5625					
14.625					
14.6875					
14.75					
14.8125					
14.875					
14.9375					
15					
15.0625					
15.125					
15.1875					
15.25					
15.3125					
15.375					
15.4375					

Valley distance /km	Depth of valley thalweg/m	Magnitude of Vertical aggradation (L_A)/m	Magnitude of Lateral migration (L_M)/m	L_M/L_A	Depositional ratio
15.5					
15.5625					
15.625					
15.6875					
15.75	-1530.4	149.56			
15.8125	-1549.6	165.8			
15.875	-1551.2	164.44			
15.9375	-1552	163.76			
16	-1553.6	165.36			
16.0625	-1558.4	169.42			
16.125	-1562.4	171.94			
16.1875	-1563.2	171.26			
16.25	-1564	171.32			
16.3125	-1564.8	169.16			
16.375	-1566.4	170.76			
16.4375	-1568	173.84			
16.5	-1564.8	169.9			
16.5625	-1564.8	169.16			
16.625	-1564	167.62			
16.6875	-1563.2	169.78			
16.75	-1564	168.36			
16.8125	-1563.2	170.52			
16.875	-1564.8	173.6			
16.9375	-1575.2	185.48			
17	-1567.2	176			
17.0625	-1569.6	178.4			
17.125	-1572.8	183.08			
17.1875	-1566.4	174.46			
17.25	-1570.4	174.76			
17.3125	-1575.2	178.82			
17.375	-1576.8	176.72			
17.4375	-1577.6	174.56			
17.5	-1579.2	166.54			
17.5625	-1584	174.3			
17.625	-1585.6	180.34			
17.6875	-1584.8	181.02	500	2.76	

Valley distance /km	Depth of valley thalweg/m	Magnitude of Vertical aggradation (L_A)/m	Magnitude of Lateral migration (L_M)/m	L_M/L_A	Depositional ratio
17.75	-1580.8	174.06			
17.8125	-1577.6	171.6			
17.875	-1577.6	171.6			
17.9375	-1579.2	173.2			
18	-1580	172.52	600		0.72
18.0625	-1580.8	171.84			
18.125	-1582.4	174.18			
18.1875	-1583.2	176.46			
18.25	-1582.4	173.44			
18.3125	-1584	177.26			
18.375	-1587.2	178.24			
18.4375	-1584	175.78	607	3.45	
18.5	-1584.8	173.62			
18.5625	-1585.6	172.2			
18.625	-1583.2	169.8			
18.6875	-1585.6	170.72			
18.75	-1587.2	171.58			
18.8125	-1587.2	172.32			
18.875	-1588	171.64			
18.9375	-1590.4	171.08			
19	-1591.2	168.92	302		0.78
19.0625	-1591.2	170.4			
19.125	-1596.8	176			
19.1875	-1599.2	179.14			
19.25	-1600	181.42			
19.3125	-1601.6	180.8			
19.375	-1601.6	179.32			
19.4375	-1606.4	184.12			
19.5	-1608.8	184.3			
19.5625	-1610.4	183.68			
19.625	-1612	186.02			
19.6875	-1613.6	185.4			
19.75	-1614.4	183.98			
19.8125	-1615.2	182.56			
19.875	-1616.8	182.68			
19.9375	-1616.8	181.94			

Valley distance /km	Depth of valley thalweg/m	Magnitude of Vertical aggradation (L_A)/m	Magnitude of Lateral migration (L_M)/m	L_M/L_A	Depositional ratio
20	-1616.8	181.2	769		0.76
20.0625	-1617.6	179.78			
20.125	-1616	175.96			
20.1875	-1617.6	176.82			
20.25	-1618.4	175.4			
20.3125	-1617.6	173.86			
20.375	-1622.4	177.92			
20.4375	-1624	178.04			
20.5	-1623.2	173.54			
20.5625	-1624.8	173.66			
20.625	-1624.8	161.82			
20.6875	-1624	166.2			
20.75	-1626.4	170.08			
20.8125	-1628	166.5			
20.875	-1628	159.1	1261	7.93	
20.9375	-1628.8	162.12			
21	-1629.6	165.14	1235		0.77
21.0625	-1630.4	165.94			
21.125	-1631.2	163.04			
21.1875	-1630.4	160.02			
21.25	-1631.2	159.34			
21.3125	-1631.2	158.6			
21.375	-1632	161.62			
21.4375	-1632	161.62			
21.5	-1633.6	163.22			
21.5625	-1634.4	163.28			
21.625	-1632.8	162.42			
21.6875	-1635.2	165.56			
21.75	-1635.2	162.6			
21.8125	-1640.8	166.72			
21.875	-1640.8	166.72			
21.9375	-1644	172.88			
22	-1650.4	174.84	1621		0.85
22.0625	-1649.6	171.82			
22.125	-1654.4	175.14			
22.1875	-1655.2	172.98			

Valley distance /km	Depth of valley thalweg/m	Magnitude of Vertical aggradation (L$_A$)/m	Magnitude of Lateral migration (L$_M$)/m	L$_M$/L$_A$	Depositional ratio
22.25	-1655.2	172.24			
22.3125	-1655.2	172.98	1698	9.82	
22.375	-1656	170.82			
22.4375	-1656	171.56			
22.5	-1654.4	169.22			
22.5625	-1663.2	176.54			
22.625	-1668.8	147.36			
22.6875	-1669.6	147.42			
22.75	-1674.4	148.52			
22.8125	-1675.2	147.1			
22.875	-1674.4	140.38			
22.9375	-1676.8	138.34			
23	-1677.6	139.88			
23.0625	-1688.8	147.38			
23.125	-1683.2	142.52			
23.1875	-1684	140.36			
23.25	-1688	145.1			
23.3125	-1688	144.36			
23.375	-1692	146.14			
23.4375	-1691.2	144.6			
23.5	-1691.2	145.34			
23.5625	-1692.8	143.98	173	1.20	
23.625	-1694.4	143.36			
23.6875	-1699.2	149.64			
23.75	-1693.6	144.78			
23.8125	-1696.8	148.72			
23.875	-1700	151.92			
23.9375	-1699.2	151.12			
24	-1693.6	144.78	242		0.61
24.0625	-1692.8	143.24			
24.125	-1693.6	145.52			
24.1875	-1706.4	156.1			
24.25	-1707.2	159.12			
24.3125	-1705.6	153.08			
24.375	-1712.8	160.28			
24.4375	-1712	155.78			

Valley distance /km	Depth of valley thalweg/m	Magnitude of Vertical aggradation (L_A)/m	Magnitude of Lateral migration (L_M)/m	L_M/L_A	Depositional ratio
24.5	-1713.6	155.16			
24.5625	-1715.2	153.8			
24.625	-1716	153.12			
24.6875	-1717.6	155.46	193	1.24	
24.75	-1716	153.12			
24.8125	-1717.6	156.2			
24.875	-1716.8	156.14			
24.9375	-1718.4	157			
25	-1720	157.12	137		0.5
25.0625	-1720.8	157.92			
25.125	-1724.8	157.48			
25.1875	-1721.6	152.8			
25.25	-1725.6	153.84			
25.3125	-1727.2	156.92			
25.375	-1730.4	158.64			
25.4375	-1737.6	163.62			
25.5	-1735.2	161.96			
25.5625	-1737.6	164.36			
25.625	-1738.4	163.68	231	1.41	
25.6875	-1740	163.8			
25.75	-1733.6	157.4			
25.8125	-1737.6	160.66			
25.875	-1737.6	159.92			
25.9375	-1738.4	153.32			
26	-1744	161.88	141		0.48
26.0625	-1744	164.1			
26.125	-1745.6	163.48			
26.1875	-1746.4	163.54			
26.25	-1748.8	160.02			
26.3125	-1751.2	159.46			
26.375	-1753.6	157.42			
26.4375	-1756	158.34	366	2.31	
26.5	-1754.4	154.52			
26.5625	-1759.2	158.58			
26.625	-1758.4	157.78			
26.6875	-1760	158.64			

Valley distance /km	Depth of valley thalweg/m	Magnitude of Vertical aggradation (L$_A$)/m	Magnitude of Lateral migration (L$_M$)/m	L$_M$/L$_A$	Depositional ratio
26.75	-1760	156.42			
26.8125	-1758.4	146.68			
26.875	-1772.8	158.12			
26.9375	-1776.8	162.12			
27	-1778.4	162.24	268		0.49
27.0625	-1777.6	161.44			
27.125	-1776	157.62			
27.1875	-1774.4	156.76			
27.25	-1777.6	160.7	330	2.05	
27.3125	-1782.4	164.02			
27.375	-1780.8	160.2			
27.4375	-1782.4	158.1			
27.5	-1781.6	157.3			
27.5625	-1784.8	159.76			
27.625	-1787.2	158.46			
27.6875	-1795.2	162.02			
27.75	-1798.4	161.52			
27.8125	-1796.8	159.18			
27.875	-1796	159.12			
27.9375	-1797.6	160.72			
28	-1796.8	160.66	146		0.54
28.0625	-1798.4	162.26			
28.125	-1799.2	163.06			
28.1875	-1796.8	160.66			
28.25	-1796	159.12			
28.3125	-1799.2	163.8			
28.375	-1801.6	161.76	299	1.85	
28.4375	-1801.6	159.54			
28.5	-1804.8	156.82			
28.5625	-1808	156.32			
28.625	-1809.6	157.92			
28.6875	-1812	161.06			
28.75	-1815.2	165			
28.8125	-1818.4	165.98			
28.875	-1822.4	169.24			
28.9375	-1824.8	171.64			

Valley distance /km	Depth of valley thalweg/m	Magnitude of Vertical aggradation (L_A)/m	Magnitude of Lateral migration (L_M)/m	L_M/L_A	Depositional ratio
29	-1836.8	180.68	126		0.48
29.0625	-1847.2	190.34			
29.125	-1848	189.66			
29.1875	-1840.8	180.98	137	0.76	
29.25	-1832	172.92			
29.3125	-1836	176.18			
29.375	-1838.4	178.58			
29.4375	-1833.6	172.3			
29.5	-1834.4	171.62			
29.5625	-1835.2	171.68			
29.625	-1834.4	170.88			
29.6875	-1836.8	175.5			
29.75	-1832.8	171.5			
29.8125	-1828	164.48			
29.875	-1828	163.74			
29.9375	-1828.8	165.28			
30	-1830.4	166.14	158		0.49
30.0625	-1831.2	166.94			
30.125	-1840	177.22	161	0.91	
30.1875	-1841.6	176.6			
30.25	-1842.4	177.4			
30.3125	-1840.8	176.54			
30.375	-1840	175			
30.4375	-1837.6	172.6			
30.5	-1834.4	170.14			
30.5625	-1834.4	172.36			
30.625	-1834.4	171.62			
30.6875	-1834.4	171.62			
30.75	-1834.4	167.92			
30.8125	-1836.8	170.32			
30.875	-1836	168.78			
30.9375	-1839.2	170.5			
31	-1840.8	171.36	105		0.45
31.0625	-1841.6	173.64			
31.125	-1843.2	174.5			
31.1875	-1840.8	172.84			

Valley distance /km	Depth of valley thalweg/m	Magnitude of Vertical aggradation (L_A)/m	Magnitude of Lateral migration (L_M)/m	L_M/L_A	Depositional ratio
31.25	-1842.4	174.44			
31.3125	-1842.4	174.44			
31.375	-1843.2	175.24			
31.4375	-1842.4	173.7			
31.5	-1843.2	169.32			
31.5625	-1845.6	169.5			
31.625	-1847.2	169.62			
31.6875	-1848.8	169.74	264	1.56	
31.75	-1850.4	171.34			
31.8125	-1850.4	169.86			
31.875	-1852	169.24			
31.9375	-1856	172.5			
32	-1859.2	174.96	124		0.49
32.0625					
32.125					
32.1875	-1863.2	170.08			
32.25	-1866.4	173.28			
32.3125	-1874.4	180.54			
32.375	-1876	183.62			
32.4375	-1861.6	170.7			
32.5	-1861.6	168.48			
32.5625	-1861.6	168.48			
32.625	-1864	170.14	226	1.33	
32.6875	-1862.4	168.54			
32.75	-1865.6	174.7			
32.8125	-1864	174.58			
32.875	-1868.8	177.9			
32.9375	-1866.4	172.54			
33	-1865.6	171.74	66		0.32
33.0625	-1865.6	170.26			
33.125	-1864	170.88			
33.1875	-1878.4	183.8			
33.25	-1876.8	184.42			
33.3125	-1880.8	189.16			
33.375	-1876.8	185.16			
33.4375	-1880	187.62			

Valley distance /km	Depth of valley thalweg/m	Magnitude of Vertical aggradation (L_A)/m	Magnitude of Lateral migration (L_M)/m	L_M/L_A	Depositional ratio
33.5	-1882.4	188.54			
33.5625	-1884.8	190.94			
33.625	-1898.4	203.06			
33.6875	-1901.6	204.04			
33.75	-1890.4	191.36			
33.8125	-1887.2	188.16			
33.875	-1888.8	189.76			
33.9375	-1887.2	188.9			
34	-1888	188.96			
34.0625	-1888	188.22			
34.125	-1888	188.22			
34.1875	-1887.2	185.94			
34.25	-1890.4	188.4			
34.3125	-1892	190			
34.375	-1892.8	190.8			
34.4375	-1892	187.78			
34.5	-1888.8	185.32			
34.5625	-1888.8	183.1			
34.625	-1888	182.3			
34.6875	-1888	183.04			
34.75	-1888.8	182.36			
34.8125	-1889.6	182.42			
34.875	-1891.2	184.02			

Table A2.2. Summary of morphological data for the Quaternary channel system. Morphological parameters include Cross-sectional area of valley-fill deposits (CSA_{VF}) and valley (CSA_V), depositional ratio (CSA_{VF}/CSA_V), and magnitude of lateral migration (L_M).

Valley distance/km	CSA_{VF}/km^2	CSA_V/km^2	Depositional ratio (CSA_{VF}/CSA_V)	L_M/m
0				
1	0.150691	0.255802	0.589092345	
2	0.120344	0.218449	0.550902041	
3	0.030813	0.096539	0.319176706	
4	0.089047	0.157693	0.564685814	
5	0.100738	0.170393	0.591209733	
6	0.083286	0.160301	0.519560078	
7	0.145255	0.207305	0.700682569	
8	0.091181	0.144674	0.630251462	
9	0.101224	0.180376	0.561183306	
10	0.100981	0.186444	0.541615713	
11	0.02978	0.087341	0.340962435	
12	0.097655	0.177246	0.550957426	
13	0.149799	0.229496	0.652730331	
14	0.135026	0.220536	0.612262851	
15	0.151755	0.225427	0.673189103	
16	0.113793	0.179847	0.632721146	277
17				198
18	0.191765	0.265506	0.722262397	600
19	0.196271	0.253179	0.775226223	302
20	0.255914	0.335191	0.763487086	769
21	0.309917	0.401831	0.771262048	1235
22	0.365542	0.431202	0.847727979	1621
23	0.2282	0.399908	0.570631245	
24	0.138872	0.226424	0.613327209	242
25	0.141884	0.283733	0.500061678	137
26	0.144016	0.297392	0.484263195	141
27	0.136101	0.279469	0.486998558	268
28	0.104628	0.192257	0.544209054	146
29	0.086129	0.180781	0.476427279	126
30	0.081894	0.165813	0.493893724	158
31	0.071854	0.159526	0.450421875	105
32	0.097441	0.20076	0.48536063	124
33	0.053575	0.165804	0.323122482	66
34	0.210333	0.3367	0.624689635	

Appendix 3. Supplementary materials for Chapter 6.

Table A3.1. Summary of morphological data for the Pliocene-Quaternary channel system. Morphological parameters include width, height, and cross-sectional area (CSA).

Distance/km	Width/m	Height/m	CSA/km²
0			
0.0625			
0.125			
0.1875			
0.25			
0.3125	1274		
0.375	1235	279.16	
0.4375	1232	280.08	
0.5	1126	281.56	
0.5625	1001	275.88	
0.625	984	262.62	
0.6875	1085	265.26	
0.75	1278	269.88	
0.8125	1271	272.9	
0.875	1237	272.22	
0.9375	1295	270	
1	1284	269.32	0.255802
1.0625	1288	266.3	
1.125	1284	261.74	
1.1875	1304	258.1	
1.25	1307	254.34	
1.3125	1279	251.38	
1.375	1301	248.48	
1.4375	1343	251.06	
1.5	1377	263.98	
1.5625	1377	268.96	
1.625	1365	267.48	
1.6875	1349	269.14	
1.75	1327	270.06	
1.8125	1321	269.5	
1.875	1313	269.8	
1.9375	1299	266.16	
2	1282	264.74	0.218449
2.0625	1274	264.92	
2.125	1268	266.7	
2.1875	1246	270.82	
2.25	1257	269.4	

Distance/km	Width/m	Height/m	CSA/km²
2.3125	1261	267.24	
2.375	1219	268.9	
2.4375	1215	268.22	
2.5	1082	274.68	
2.5625	940	269.68	
2.625	900	258.02	
2.6875	892	264.92	
2.75	861	265.22	
2.8125	776	261.52	
2.875	765	256.46	
2.9375	772	254.3	
3	772	257.5	0.096539
3.0625	778	260.64	
3.125	743	261.5	
3.1875	734	255.52	
3.25	732	254.96	
3.3125	758	254.28	
3.375	856	252.8	
3.4375	885	252.98	
3.5	879	255.44	
3.5625	910	258.08	
3.625	950	256.6	
3.6875	977	255.06	
3.75	979	254.44	
3.8125	998	254.56	
3.875	1015	252.28	
3.9375	994	248.4	
4	1001	246.86	0.157693
4.0625	983	243.84	
4.125	995	243.22	
4.1875	984	241.06	
4.25	966	240.44	
4.3125	977	254.1	
4.375	1055	256.5	
4.4375	1216	257.98	
4.5	1237	264.14	
4.5625	1229	267.16	
4.625	1312	264.44	
4.6875	1184	265.12	
4.75	1170	258.7	
4.8125	1160	260.36	
4.875	1121	261.96	

Distance/km	Width/m	Height/m	CSA/km²
4.9375	1093	262.82	
5	1086	265.96	0.170393
5.0625	1057	267.5	
5.125	1020	269.96	
5.1875	957	270.08	
5.25	1029	266.56	
5.3125	1055	268.16	
5.375	1123	268.28	
5.4375	1030	273.02	
5.5	1004	267.96	
5.5625	1071	269.68	
5.625	1137	273.68	
5.6875	1179	275.1	
5.75	1208	273.62	
5.8125	1217	272.88	
5.875	1175	271.4	
5.9375	1161	271.58	
6	1132	273.98	0.160301
6.0625	1204	273.42	
6.125	1181	274.46	
6.1875	1226	276.92	
6.25	1259	277.78	
6.3125	1310	280.98	
6.375	1324	280.98	
6.4375	1079	279.5	
6.5	1046	266.24	
6.5625	1025	270.98	
6.625	1017	273.5	
6.6875	1079	270.54	
6.75	1054	265.42	
6.8125	1097	266.96	
6.875	1074	264.86	
6.9375	1097	264.12	
7	1108	264.92	0.207305
7.0625	1081	265.72	
7.125	1143	264.3	
7.1875	1155	266.76	
7.25	1152	268.42	
7.3125	1184	267.68	
7.375	1155	266.88	
7.4375	1148	268.48	
7.5	1206	267.86	

Distance/km	Width/m	Height/m	CSA/km²
7.5625	1270	269.52	
7.625	1192	267.42	
7.6875	1172	265.94	
7.75	1169	261.5	
7.8125	1135	260.14	
7.875	900	260.88	
7.9375	903	263.34	
8	923	265.8	0.144674
8.0625	942	271.22	
8.125	947	276.02	
8.1875	950	279.34	
8.25	988	277.86	
8.3125	961	276.2	
8.375	980	277	
8.4375	1028	282.54	
8.5	990	277.98	
8.5625	917	284.56	
8.625	876	278.4	
8.6875	962	268.84	
8.75	1037	272.78	
8.8125	1020	277.58	
8.875	1034	276.9	
8.9375	1023	277.02	
9	1012	278.74	0.180376
9.0625	1009	278.92	
9.125	1424	275.22	
9.1875	1439	295.38	
9.25	1255	301.86	
9.3125	1272	303.76	
9.375	1309	309.42	
9.4375	1306	312.68	
9.5	1313	304.66	
9.5625	1315	304.84	
9.625	1330	302.62	
9.6875	1264	297.32	
9.75	1217	294.42	
9.8125	1177	291.52	
9.875	1175	291.76	
9.9375	1259	291.88	
10	1261	292.8	0.186444
10.0625	1281	294.4	
10.125	1310	288.18	

Distance/km	Width/m	Height/m	CSA/km²
10.1875	1275	286.76	
10.25	937	286.26	
10.3125	997	275.34	
10.375	1037	276.08	
10.4375	981	276.76	
10.5	1103	277.5	
10.5625	1074	278.24	
10.625	1006	279.1	
10.6875	939	277.8	
10.75	934	274.9	
10.8125	916	271.26	
10.875	908	271.38	
10.9375	874	270.82	
11	834	268.66	0.087341
11.0625	770	275	
11.125	775	272.6	
11.1875	806	273.52	
11.25	849	275.86	
11.3125	877	279.8	
11.375	883	280.6	
11.4375	891	280.6	
11.5	1017	279.86	
11.5625	961	283	
11.625	970	280.78	
11.6875	1097	279.74	
11.75	1284	289.84	
11.8125	1326	295.2	
11.875	1348	296.8	
11.9375	1395	299.08	
12	1152	303.14	0.177246
12.0625	1185	289.2	
12.125	1201	294.8	
12.1875	1219	294.06	
12.25	1201	293.32	
12.3125	1206	291.04	
12.375	1210	284.08	
12.4375	1188	281.92	
12.5	1137	279.14	
12.5625	1017	277.04	
12.625	1034	275.8	
12.6875	1008	274.32	
12.75	941	272.96	

Distance/km	Width/m	Height/m	CSA/km²
12.8125	1306	270.86	
12.875	1353	273.94	
12.9375	1364	275.66	
13	1712	273.5	0.458460
13.0625	1680	288.48	
13.125	1828	305.9	
13.1875	1950	316.68	
13.25	1955	325.18	
13.3125	2121	334.54	
13.375	2127	343.96	
13.4375	2200	335.52	
13.5	2267	336.68	
13.5625	2127	321.04	
13.625	2230	316.66	
13.6875	2247	310.68	
13.75	2200	311.6	
13.8125	2235	329.14	
13.875	2369	335.66	
13.9375	2232	350.8	
14	2433	357.26	0.558103
14.0625	2345	362.74	
14.125	2376	352.4	
14.1875	2365	355.54	
14.25	2265	354.06	
14.3125	2238	355.54	
14.375	2294	350.8	
14.4375	2246	341.8	
14.5	2311	336	
14.5625	2329	334.58	
14.625	2326	335.5	
14.6875	2333	331.62	
14.75	2395	331.8	
14.8125	2458	330.32	
14.875	2403	333.46	
14.9375	2392	332.04	
15	2382	332.34	0.706487
15.0625	2402	336.22	
15.125	2305	337.32	
15.1875	2340	332.76	
15.25	2312	334.98	
15.3125	2295	329.06	
15.375	2239	327.7	

Distance/km	Width/m	Height/m	CSA/km²
15.4375	2239	326.22	
15.5	2204	324.06	
15.5625		319	
15.625		314.68	
15.6875		318.5	
15.75		319.92	
15.8125		318.38	
15.875		321.46	
15.9375		320.78	
16			0.713840
16.0625			
16.125			
16.1875			
16.25			
16.3125			
16.375			
16.4375			
16.5			
16.5625			
16.625			
16.6875			
16.75			
16.8125			
16.875			
16.9375			
17			
17.0625	3112		
17.125	3107	310.02	
17.1875	3186	313.16	
17.25	3246	314.76	
17.3125	3312	314.08	
17.375	3333	314.08	
17.4375	3338	315.68	
17.5	3386	314.88	
17.5625	3386	314.2	
17.625	3483	311.92	
17.6875	3459	311.18	
17.75	3503	307.3	
17.8125	3499	308.96	
17.875	3490	309.02	
17.9375	3551	309.14	
18	3551	308.46	0.904941

Distance/km	Width/m	Height/m	CSA/km²
18.0625	3607	310.18	
18.125	3581	308.58	
18.1875	3621	306.18	
18.25	3590	307.72	
18.3125	3647	307.72	
18.375	3638	309.38	
18.4375	3612	308.64	
18.5	3650	306.36	
18.5625	3625	308.02	
18.625	3690	309.68	
18.6875	3673	309.68	
18.75	3642	310.54	
18.8125	3616	312.14	
18.875	3651	317.8	
18.9375	3629	319.4	
19	3580	318.78	0.858614
19.0625	3450	318.1	
19.125	3344	316.68	
19.1875	3243	315.26	
19.25	3227	315.38	
19.3125	3241	317.04	
19.375	2879	318.02	
19.4375	2868	312.04	
19.5	2819	323.18	
19.5625	3130	326.32	
19.625	3260	316.9	
19.6875	3351	313.02	
19.75	3377	311.54	
19.8125	3425	310.12	
19.875	3468	307.22	
19.9375	3612	304.38	
20	3668	299.2	0.828541
20.0625	3742	296.92	
20.125	3742	293.9	
20.1875	3782	292.42	
20.25	3824	293.34	
20.3125	3715	296.54	
20.375	3742	293.64	
20.4375	3817	295.86	
20.5	3810	295.12	
20.5625	3837	296.78	
20.625	3919	297.58	

Distance/km	Width/m	Height/m	CSA/km²
20.6875	3952	298.38	
20.75	3980	296.16	
20.8125	3939	294.74	
20.875	3973	292.58	
20.9375	4095	290.36	
21	4217	289.74	0.995464
21.0625	4319	286.72	
21.125	4367	290.72	
21.1875	4421	291.58	
21.25	4543	291.64	
21.3125	4598	295.7	
21.375	4577	300.5	
21.4375	4638	303.08	
21.5	5148	297.78	
21.5625	5154	301.42	
21.625	5175	300.74	
21.6875	5257	298.52	
21.75	5304	298.58	
21.8125	5304	295.5	
21.875	5372	295.56	
21.9375	5467	294.08	
22	5766	298.26	1.218831
22.0625	5832	303.18	
22.125	5790	301.76	
22.1875	5866	305.02	
22.25	5840	311.48	
22.3125	5857	313.14	
22.375	5909	309.26	
22.4375	6002	315.72	
22.5	5959	310.24	
22.5625	5892	311.16	
22.625	5773	312.08	
22.6875	5959	309.8	
22.75	5790	312.26	
22.8125	5747	313.24	
22.875	5840	313.24	
22.9375	5695	309.24	
23	5594	306.96	1.221705
23.0625	5280	302.96	
23.125	5263	311.08	
23.1875	5170	310.1	
23.25	4915	306.96	

Distance/km	Width/m	Height/m	CSA/km²
23.3125	4669	296.74	
23.375	4567	319.2	
23.4375	4465	322.52	
23.5	4126	321.78	
23.5625	4000	324.98	
23.625	3905	322.7	
23.6875	3820	324.24	
23.75	2461	321.96	
23.8125	2309	322.82	
23.875	2156	324.42	
23.9375	2113	325.34	
24	2017	325.46	0.352194
24.0625	2105	325.52	
24.125	2105	325.58	
24.1875	2096	330.5	
24.25	1370	326.06	
24.3125	1390	292.96	
24.375	1398	291.6	
24.4375	1422	292.58	
24.5	1415	299.78	
24.5625	1383	293.68	
24.625	1543	284.24	
24.6875	1502	293.92	
24.75	1519	291.82	
24.8125	1519	283.2	
24.875	1585	295.34	
24.9375	1561	307.92	
25	1561	312.42	0.297392
25.0625	1658	321.72	
25.125	1550	319.5	
25.1875	1863	318.88	
25.25	1791	319.68	
25.3125	2142	319.86	
25.375	2187	321.52	
25.4375	2166	323.92	
25.5	2148	325.58	
25.5625	2107	322.5	
25.625	2100	328.04	
25.6875	2117	325.76	
25.75	2058	325.14	
25.8125	2058	323.66	
25.875	1982	321.32	

Distance/km	Width/m	Height/m	CSA/km²
25.9375	1982	334.24	
26	1721	337.5	0.279469
26.0625	1286	328.74	
26.125	1415	310.18	
26.1875	1453	314.5	
26.25	1432	311.42	
26.3125	1429	311.66	
26.375	1436	315.72	
26.4375	1411	315.6	
26.5	1443	316.46	
26.5625	1467	321.58	
26.625	1345	324.78	
26.6875	1283	324.22	
26.75	1318	332.96	
26.8125	1161	333.94	
26.875	1161	324.94	
26.9375	1161	320.44	
27	1165	323.52	0.192257
27.0625	1147	321.98	
27.125	1109	324.32	
27.1875	1081	316.98	
27.25	1105	312.36	
27.3125	1220	321.92	
27.375	1297	324.38	
27.4375	1265	326.78	
27.5	1192	324.56	
27.5625	1227	324.8	
27.625	1220	325.04	
27.6875	1220	322.94	
27.75	1164	320.16	
27.8125	1193	318.92	
27.875	1200	319.9	
27.9375	1164	323.9	
28	1199	326.3	0.180781
28.0625	1195	339.04	
28.125	1252	349.44	
28.1875	1224	350.24	
28.25	1241	341.56	
28.3125	1304	334.24	
28.375	1307	337.5	
28.4375	1384	339.9	
28.5	1310	336.58	

Distance/km	Width/m	Height/m	CSA/km²
28.5625	1227	338.86	
28.625	1213	332.26	
28.6875	1171	327.76	
28.75	1091	328.68	
28.8125	1102	322.46	
28.875	1060	314.7	
28.9375	1095	317.66	
29	1119	313.28	0.165813
29.0625	1150	314.14	
29.125	1227	315.68	
29.1875	1230	324.48	
29.25	1258	325.34	
29.3125	1241	325.4	
29.375	1258	322.32	
29.4375	1286	320.78	
29.5	1300	317.64	
29.5625	1008	314.44	
29.625	998	312.96	
29.6875	1095	301.12	
29.75	1091	301.86	
29.8125	1088	303.34	
29.875	1140	305	
29.9375	1130	303.46	
30	1161	306.66	0.159526
30.0625	1130	305.3	
30.125	998	312.76	
30.1875	998	314.36	
30.25	1015	311.22	
30.3125	1025	311.34	
30.375	1119	311.34	
30.4375	1234	301.78	
30.5	1262	302.46	
30.5625	1370	304.74	
30.625	1418	308.62	
30.6875	1432	309.48	
30.75	1415	311.08	
30.8125		309.72	
30.875	1408		
30.9375	1382	309.1	
31	1382	310.88	0.200760
31.0625	1342	311.86	
31.125	1312		

Distance/km	Width/m	Height/m	CSA/km²
31.1875			
31.25			
31.3125	1234		
31.375	1227	319.66	
31.4375	1272	320.52	
31.5	1351	306.12	
31.5625	1373	305.38	
31.625	1377	306.12	
31.6875	1349	307.04	
31.75	1328	305.44	
31.8125	1299	306.42	
31.875	1329	304.08	
31.9375	1344	308.88	
32	1527	307.22	0.165804
32.0625	1539	308.64	
32.125	1533	310.86	
32.1875	1488	308.52	
32.25	2755	322.18	
32.3125	2729	317.62	
32.375	2681	318.66	
32.4375	2699	313.18	
32.5	2684	314.16	
32.5625	2613	317.3	
32.625	2640	316.74	
32.6875	2537	330.34	
32.75	2471	332.06	
32.8125	2406	317.9	
32.875	2336	313.96	
32.9375	2233	311.86	
33	2173	308.78	
33.0625	2146	308.84	
33.125	2119	308.1	
33.1875	2090	310.32	
33.25	2038	309.52	
33.3125	1869	312.72	
33.375	1855	311.36	
33.4375	1835	310.68	
33.5	1846	308.4	
33.5625	1804	301.5	
33.625	1742	300.76	
33.6875	1794	298.48	
33.75	1811	297	

Distance/km	Width/m	Height/m	CSA/km²
33.8125	1770	294.84	
33.875		292.68	